





Een op intrinsieke kinetiek gebaseerde methodologie  
voor de multischaalmodellering van chemische reacties

An Intrinsic Kinetics Based Methodology  
for Multi-Scale Modeling of Chemical Reactions

Kenneth Toch

Promotoren: prof. dr. ir. J. W. Thybaut, prof. dr. ir. G. B. Marin  
Proefschrift ingediend tot het behalen van de graad van  
Doctor in de Ingenieurswetenschappen: Chemische Technologie

Vakgroep Chemische Proceskunde en Technische Chemie  
Voorzitter: prof. dr. ir. G. B. Marin  
Faculteit Ingenieurswetenschappen en Architectuur  
Academiejaar 2014 - 2015



ISBN 978-90-8578-751-8  
NUR 913, 952  
Wettelijk depot: D/2014/10.500/97

Promotoren:

Prof. Dr. Ir. Joris Thybaut	Universiteit Gent
Prof. Dr. Ir. Guy B. Marin	Universiteit Gent

Examencommissie:

Prof. Dr. Ir. Patrick De Baets, voorzitter	Universiteit Gent
Dr. Ir. Vladimir Galvita*, secretaris	Universiteit Gent
Dr. Ir. Michael Caracotsios*	(Northwestern University & Honeywell UOP)
Prof. Dr. Ir. Stijn van Hulle*	Universiteit Gent
Prof. Dr. Ir. Guy B. Marin, promotor	Universiteit Gent
Prof. Dr. Ir. Agustin Martinez	CSIC-ITQ
Prof. Dr. Ir. Mark Saeys	Universiteit Gent
Prof. Dr. Ir. Joris Thybaut*, promotor	Universiteit Gent

\* lees commissie

Universiteit Gent

Faculteit Ingenieurswetenschappen en Architectuur

Vakgroep Chemische Proceskunde en Technische Chemie

Laboratorium voor Chemische Techniek

Technologiepark 914

B-9052 Gent

België

Tel.: +32 (0)9 331 17 57

Fax: +32 (0)9 331 17 59

<http://www.lct.ugent.be>

This work was supported by the Research Board of Ghent University (BOF) , Shell and the 'Long Term Structural Methusalem Funding by the Flemish Government'

This work reports work undertaken in the context of the project "OCMOL, Oxidative Coupling of Methane followed by Oligomerization to Liquids". OCMOL is a Large Scale Collaborative Project supported by the European Commission in the 7th Framework Programme (GA n°228953). For further information about OCMOL see: <http://www.ocmol.eu> or <http://www.ocmol.com>.



# Acknowledgments

---

This has been an interesting period. Since five years I waited for this moment. Not that I wanted it to stop, but rather because it would be an accomplishment. Which accomplishment? A kinetic model? Some optimized catalyst? Regression analysis? Exciting statistics? I do not think so. Maybe it is being able to develop yourself. Getting to know yourself. Nobody said it was going to be easy. Everybody has his/her heights and lows, both scientifically as emotionally (during his PhD). Coping with these extrema and evolving into a better person, both scientifically as emotionally, is as important as publishing your latest findings in an international journal. And now, finally, I am here, writing these acknowledgments, being content with what I have accomplished.

There is a large number of people I'd like to acknowledge for their guidance and support throughout the last five years of my PhD research. First of all, I'd like to acknowledge prof. Guy B. Marin for allowing me to reach out higher than I could ever imagine. A warm thanks goes to prof. Joris W. Thybaut who believed in me to reach out higher than I could ever imagine. I thank both of you letting me participate in a large scale project. OCMOL has shown me around in some of Europe's nicest meeting rooms every six months. Most of all, it allowed me to interact with other people having different backgrounds but having the same goal. You also helped me improving my writing skills, although maybe at a slower rate than we would have liked. Next to this, I'd like to acknowledge Joris again for the professional relationship we have built up. Hopefully we can keep on exploiting it in the future!

I'd like to acknowledge the European Commission for supporting the Large Scale Collaborative Project "OCMOL, Oxidative Coupling of Methane followed by Oligomerization to Liquids", GA n°228953 for the work undertaken on ethene oligomerization. I'd like to acknowledge Shell for their support during the work performed on xylene isomerization. The Research Board of Ghent University is acknowledged for their funding of my first PhD

year. Finally, I'd also like to acknowledge the 'Long Term Structural Methusalem Funding by the Flemish Government'

Besides the thesis promoters and financial supporters, a lot of LCT people have contributed directly or indirectly to my accomplishment. Prof. Reyniers, looking back, I should have visited you more to discuss reaction mechanisms on ethene oligomerization. Nevertheless, thank you for the valuable input you've given me. Vladimir, Hilde and Evgeniy, thank you for guiding me in what I may call 'my neophyte': catalyst characterization.

I had the honor to go on this quest with several companions and end with friends. Bart, you started your PhD when I started my master thesis, so we know each other for the longest time. Thanks for all the scientific discussion and entertainment! Only a pity I did not beat you to the line! Kristof, thank you for being the devil's advocate and your unconditional enthusiasm. Jeroen, although we disagree on music, I think we can agree on our humor. Jonas, you always make me feel dumb, so thank you! Jolien, I hope you find the right acronyms and the way to your goal! Evelien, thank you for your cooperation during some side project, companionship to San-Francisco and the yummy snacks during the coffee breaks! Chetan and Luis, thanks for not laughing at me while doing the challenger course. Vaios, thank you for your companionship during all the OCMOL meetings and for teaching me your credo: '*relaaaax*'. Although Aaron and Kae have already left the building (together), I'd like to thank them for the great times we've spent together during the first years of my career at the LCT. I hope for everybody of the CaRE group and LCT that these kind of friendships might grow during your PhD and further career.

I'd like to thank the technical support during the last five years. Despite their workload, these guys always found the time to help me when I was in technical difficulties. Therefore: Thank you Bert, Brecht, Erwin, Georges, Hans, Jaimy, Marcel, Michaël and Tom.

Petra, Sarah, Kim and Kevin: thank you for helping me or at least pointing me in the right direction when I had some administrative difficulties.



Also, a number of squires joined me in my quest for a PhD. Wouter, Brecht, Julie and Jolien aided me either data acquisition, model construction or model discrimination.

Lastly, I'd like to thank the people who should be somewhere at the top of this list: my family. My parents showed me the possibilities in life. They gave me choices and I can only hope I make them proud. I was lucky enough to found an own family. Nele, I love you, thank you for walking this path with me. Your support was, is and will be an invaluable asset in our life. Our love resulted into two lovely boys (maybe more in the future, who knows?), let's hope we can give them the same chances as our parents gave us.

Kenneth

Fall 2014

Only now I've come to this moment in my life  
Fixing pieces to a puzzle with no defects



# Table of Contents

---

<b>Acknowledgments</b>	<b>i</b>
<b>Table of contents</b>	<b>v</b>
<b>List of figures</b>	<b>xiii</b>
<b>List of tables</b>	<b>xxix</b>
<b>List of symbols</b>	<b>xxxiii</b>
<b>Glossary of terms</b>	<b>xLi</b>
<b>Summary</b>	<b>xLvii</b>
<b>Samenvatting</b>	<b>Lix</b>
<b>Chapter 1 Introduction</b>	<b>1</b>
1.1 Multi-scale modeling	1
1.2 Single-Event MicroKinetic modeling	3
1.3 Model Based Catalyst Design	4
1.4 Introduction to the chemical reactions used for Model Based Catalyst Design and multi-scale modeling	5
1.4.1 <i>n</i> -Hexane hydrocracking: a case study	5
1.4.2 Ethene oligomerization: searching for sustainable fuels and chemicals	6
1.4.3 Xylene isomerization: meeting the world demand for polymer production	9
1.5 Scope of the thesis	10
1.6 References	11
<b>Chapter 2 Procedures</b>	<b>15</b>
2.1 Experimental	16
2.1.1 Catalysts	16
2.1.1.1 Pt/H-ZSM-5 for <i>n</i> -hexane hydroisomerization	16
2.1.1.2 Ni-SiO <sub>2</sub> -Al <sub>2</sub> O <sub>3</sub> for ethene oligomerization	16
2.1.1.3 Ni-Beta for ethene oligomerization	19
2.1.1.4 Pt/H-ZSM-5 for xylene isomerization	20

2.1.2	Reactor set-ups	20
2.1.2.1	Reactor set-up for n-hexane hydroisomerization	20
2.1.2.2	Reactor set-up for ethene oligomerization	21
2.1.2.3	Reactor set-up for experimental validation of the industrial reactor model for ethene oligomerization	22
2.1.2.4	Reactor set-up for xylene isomerization	22
2.1.3	Determination of outlet composition, flow rates, conversions, selectivities and yields	23
2.1.3.1	Outlet composition	23
2.1.3.2	Measured set-up flow rates	25
2.1.3.3	Mass and element balances	26
2.1.3.4	Outlet flow rates	26
2.1.3.5	Conversion, selectivities and yields	27
2.2	Modeling	28
2.2.1	A systematic methodology for kinetic modeling	28
2.2.1.1	Data analysis and model construction	29
2.2.1.2	Regression	30
2.2.1.3	Physical and statistical assessment	30
2.2.2	Reactor models	31
2.2.2.1	Continuous stirred tank reactor	31
2.2.2.2	Plug flow reactor	31
2.2.3	Parameter estimation	32
2.2.3.1	Isothermal vs. non-isothermal regression	32
2.2.3.2	Reparameterization of the Arrhenius and Van't Hoff equation	34
2.2.4	Statistical and physical assessment of the model and parameter estimates	34
2.2.5	Residual analysis	37
2.2.5.1	Parity diagram	37
2.2.5.2	Performance figure	38

2.2.5.3	Residual figure	39
2.2.5.4	Normal probability figure	40
2.2.6	Single-Event MicroKinetic (SEMK) methodology	41
2.3	References	42
<b>Chapter 3 Kinetic Modeling of <i>n</i>-Hexane Hydroisomerization on a Bifunctional zeolite</b>		<b>45</b>
3.1	Procedures	46
3.1.1	Experimental conditions	46
3.1.2	Reactor model	47
3.1.3	Parameter estimation	47
3.2	<i>n</i> -Hexane Hydroisomerization: experimental observations	48
3.3	<i>n</i> -Hexane Hydroisomerization: kinetic model development	50
3.3.1	Reaction network and catalytic cycle	50
3.3.2	Rate-equation derivation	55
3.4	<i>n</i> -Hexane Hydroisomerization: modeling	58
3.4.1	Isothermal regression	58
3.4.2	Non-isothermal regression	60
3.4.3	Model performance	63
3.5	Conclusions	66
3.6	References	67
<b>Chapter 4 Single-Event Modeling of Ethene Oligomerization on Ni-SiO<sub>2</sub>-Al<sub>2</sub>O<sub>3</sub></b>		<b>69</b>
4.1	Procedures	69
4.1.1	Experimental conditions	69
4.1.2	Definition of responses	70
4.2	Experimental investigation	70
4.3	SEMK model construction	74
4.3.1	Proposed mechanism for ethene oligomerization	74
4.3.1.1	Degenerate polymerization	75
4.3.1.2	Concerted coupling	76
4.3.1.3	SEMK reaction mechanism	77
4.3.2	Rate equations	78

4.3.3	Reaction network generation	81
4.3.4	Determination of the number of single events	81
4.4	Model regression and assessment	83
4.4.1	Identification, classification and determination of the model parameters	83
4.4.1.1	Physisorption	83
4.4.1.2	Nickel ion catalyzed oligomerization	84
4.4.1.3	Double bond isomerization	84
4.4.1.4	Estimation of the reaction enthalpies and activation energies	85
4.4.2	Revised model: fast and irreversible nickel ion activation	86
4.4.3	Model parameter assessment	87
4.4.4	Kinetic model performance	89
4.4.5	Physisorbed and chemisorbed species concentrations	91
4.5	Conclusions	94
4.6	References	95
<b>Chapter 5 Exploiting Bifunctional Heterogeneous Catalysts in Ethene Oligomerization:</b>		
<b>Guidelines for Rational Catalyst Design</b>		<b>97</b>
5.1	Procedures	98
5.1.1	Experimental conditions	98
5.1.2	Definition of responses	98
5.2	Ethene oligomerization on bifunctional catalysts: experimental investigation	99
5.3	Extension of the SEMK model for ethene oligomerization to bifunctional catalysts	103
5.3.1	Reaction network for ethene oligomerization on Ni-Beta zeolite	103
5.3.2	Physisorption in the zeolite pores	105
5.3.3	Metal-ion catalyzed elementary steps	107
5.3.4	Acid catalyzed elementary steps	107
5.3.5	Net rate of formation	108
5.4	Ethene oligomerization on bifunctional catalysts: assessment of acid activity	109
5.4.1	Determination of the model parameters	109
5.4.1.1	Pre-exponential factors	110

5.4.1.2	Activation energies and standard reaction enthalpies	110
5.4.1.3	Thermodynamic consistency for alkylation and cracking	111
5.4.1.4	Summary	112
5.4.2	Estimation of the model parameters	114
5.4.3	Kinetic model performance	117
5.5	Catalyst design guidelines for chemicals and fuel production from ethene oligomerization	119
5.5.1	Metal-ion versus acid catalyzed oligomerization: reaction path analysis	120
5.5.2	Strength and concentration of the acid sites	126
5.5.3	Ethene standard coordination enthalpy and nickel content	128
5.5.4	Physisorption parameters	129
5.6	Conclusions	131
5.7	References	132
<b>Chapter 6 Scale Up Chemicals and Fuel Production by Ethene Oligomerization: Industrial Reactor Design</b>		<b>135</b>
6.1	Experimental setup for reactor model validation	135
6.2	Multi-scale ethene oligomerization industrial reactor model	136
6.2.1	Reactor scale	138
6.2.1.1	Mass balance	139
6.2.1.2	Energy balance	139
6.2.1.3	Momentum balance	141
6.2.2	Catalyst pellet scale – liquid formation	142
6.2.3	Crystallite scale	144
6.2.3.1	Mass transfer limitations	144
6.2.3.2	Energy transfer limitations	147
6.2.4	Nanoscale – intrinsic kinetics description	147
6.2.5	Experimental validation of the reactor model	147
6.3	Design of an industrial oligomerization reactor	151
6.3.1	Effect of heating regime	152

6.3.2	Effect of the reactor geometry on the temperature profile and pressure drop	155
6.3.3	Effect of liquid formation on the conversion of ethene	156
6.3.4	Effect of the shape factor on the coverage profile of ethene in a catalyst particle	162
6.3.5	Final industrial reactor design	162
6.4	Conclusions	164
6.5	References	165
<b>Chapter 7 Catalyst Design for Ethylbenzene Dealkylation and Xylene Isomerization</b>		<b>167</b>
7.1	Procedures	167
7.1.1	Experimental conditions	167
7.1.2	Reactor model	168
7.1.3	Definition of responses	168
7.2	Xylene isomerization on Pt/H-ZSM-5: proposed reaction network and observed behavior	169
7.2.1	Elementary steps and reaction network of xylene isomerization on Pt/H-ZSM-5	170
7.2.1.1	Alkyl shift	170
7.2.1.2	Dealkylation	171
7.2.1.3	Transalkylation	171
7.2.1.4	Hydrogenation	172
7.2.1.5	Overall reaction network	172
7.2.2	Observed behavior of xylene isomerization on Pt/H-ZSM-5	174
7.3	The Single-Event MicroKinetic model for xylene isomerization on Pt/H-ZSM-5	175
7.3.1	Acid-catalyzed reaction rates	176
7.3.2	Hydrogenation rate	177
7.3.3	Net rates of formation	178
7.4	Xylene isomerization on Pt/H-ZSM-5: kinetic modeling	178
7.4.1	Determination of the model parameters	178
7.4.1.1	Calculation of the pre-exponential factors	179



7.4.1.2	Calculation of the physisorption parameters	180
7.4.1.3	Estimation of the activation energies and protonation enthalpy	181
7.4.2	Kinetic model performance	183
7.5	Discussion	185
7.6	Identification of an optimal catalyst for xylene isomerization	187
7.7	Conclusions	191
7.8	References	191
<b>Chapter 8 Conclusions and Future Work</b>		<b>193</b>
<b>Appendix A: Properties of Pure Components and Mixtures</b>		<b>197</b>
A.1	Pure component properties	197
A.1.1	Heat capacity for gasses	198
A.1.2	Heat capacity for liquids	198
A.1.3	Vapor pressure	199
A.2	Mixing rules for (critical) properties	199
A.2.1	Critical temperature	199
A.2.2	Critical volume of gas mixtures	200
A.2.3	Critical compressibility factor of gas mixtures	200
A.2.4	Critical pressure of gas mixtures	201
A.2.5	Molecular mass of mixtures	201
A.2.6	Acentric factor of mixtures	201
A.3	Volumetric flow rates	201
A.4	Molar volume	202
A.4.1	Molar volume of liquid components	202
A.4.2	Molar volume of liquid mixtures	202
A.5	Heat capacity of mixtures	203
A.5.1	Heat capacity of gas or liquid mixtures	203
A.5.2	Heat capacity of gas-liquid mixtures	203
A.6	Thermal conductivity	203
A.6.1	Thermal conductivity of gas components	203
A.6.2	Thermal conductivity of gas mixtures	205
A.6.3	Thermal conductivity of liquid components	205

A.6.4	Thermal conductivity of liquid mixtures	205
A.6.5	Thermal conductivity of gas-liquid mixtures	205
A.7	Viscosity	206
A.7.1	Viscosity of gas components	206
A.7.2	Viscosity of gas mixtures	207
A.7.3	Viscosity of liquid components	208
A.7.4	Viscosity of liquid mixtures	209
A.7.5	Viscosity of gas-liquid mixtures	210
A.8	Surface tension	210
A.8.1	Surface tension of liquid components	210
A.8.2	Surface tension of liquid mixtures	210
A.9	References	210

# List of figures

---

- Figure 1-1: Multi-scale approach of reaction engineering as envisioned by the Laboratory of Chemical Technology, Ghent University [4].
- Figure 1-2: Model based catalyst design [17]
- Figure 1-3: literature survey (Web of Knowledge) using the key words: Topic=((ethene ) AND (oligomerization OR oligomerisation OR dimerization OR dimerisation)) AND (heterogenous OR heterogeneous OR silica OR alumina) as accessed on September 1st , 2014; full line: cumulative number of articles as function of year; dotted line: number of articles published.
- Figure 2-1: FTIR spectra of CO adsorbed on the amorphous Ni-SiO<sub>2</sub>-Al<sub>2</sub>O<sub>3</sub> at 293 K during CO adsorption (a) and after CO adsorption (b-c). Sample (b) has been pretreated for 8 hours at 773 K under flowing He. Sample (c) has been pretreated for 8 hours at 773 K under flowing H<sub>2</sub>.
- Figure 2-2: Recorder TCD signal of H<sub>2</sub>-TPR of the amorphous Ni-SiO<sub>2</sub>-Al<sub>2</sub>O<sub>3</sub> under 5%H<sub>2</sub>/Ar at a temperature increase of 10 K min<sup>-1</sup>.
- Figure 2-3: Proposed procedure for kinetic modeling
- Figure 2-4: Arrhenius plot for the unreparameterized Arrhenius relation (left) and the reparameterized Arrhenius relation (right).
- Figure 2-5: Parity diagrams for 4 theoretical cases: (a) adequate model with a normal distributed error with expected value equal to zero, (b) inadequate model with a normal distributed error with expected value equal to zero, (c) adequate model with a two-tailed *t*-distributed error and (d) adequate model with a normal distributed error with expected value equal to three
- Figure 2-6: Residual figures for 4 theoretical cases: (a) adequate model with a normal distributed error with expected value equal to zero, (b) inadequate model with a normal distributed error with expected value equal to zero, (c) adequate model with a two-tailed *t*-distributed error and (d) adequate model with a normal distributed error with expected value equal to three.

- Figure 2-7: Normal probability figures for 4 theoretical cases: (a) adequate model with a normal distributed error with expected value equal to zero, (b) inadequate model with a normal distributed error with expected value equal to zero, (c) adequate model with a two-tailed *t*-distributed error and (d) adequate model with a normal distributed error with expected value equal to three
- Figure 3-1: Schematic overview of (ideal) hydroisomerization of *n*-hexane over a bifunctional zeolite
- Figure 3-2: *n*-Hexane conversion on Pt/H-ZSM-5 catalyst as a function of the temperature at different hydrogen to *n*-hexane molar inlet ratio and total pressures. Symbols correspond to experimental observations, lines correspond to model simulations, i.e., Eqs. 3-1 to 3-3, in which the net rates of formation are given by Eqs. 3-4 to 3-6 using the parameters from Table 3-4. ●, full line:  $F_{\text{H}_2}^0 / F_{\text{C}_6}^0 = 50 \text{ mol mol}^{-1}$ ,  $p_{\text{tot}} = 1.0 \text{ MPa}$ ; ■, dashed line:  $F_{\text{H}_2}^0 / F_{\text{C}_6}^0 = 100 \text{ mol mol}^{-1}$ ,  $p_{\text{tot}} = 1.0 \text{ MPa}$ ; ▲, dotted line:  $F_{\text{H}_2}^0 / F_{\text{C}_6}^0 = 50 \text{ mol mol}^{-1}$ ,  $p_{\text{tot}} = 2.0 \text{ MPa}$ .
- Figure 3-3: *n*-Hexane hydroisomerization product selectivity on Pt/H-ZSM-5 catalyst as a function of the conversion. Symbols correspond to experimental observations, lines correspond to model simulations, i.e., Eqs. 3-1 to 3-3, in which the net rates of formation are given by Eqs. 3-4 to 3-6 using the parameters from Table 3-4. ●, full line: 2MP; ■, dashed line: 3MP; ▲, dotted line: propane.
- Figure 3-4: Molar ratio of 2MP to 3MP as function of *n*-C<sub>6</sub> conversion on Pt/H-ZSM-5 catalyst. The dotted line represents the calculated thermodynamic equilibrium. The higher conversions were obtained mainly due to higher reaction temperatures and, hence, the shift of the thermodynamic equilibrium.
- Figure 3-5: Simplified reaction scheme of *n*-hexane hydroisomerization on a bifunctional catalyst
- Figure 3-6: Alternative, simplified reaction scheme of *n*-hexane hydroisomerization on a bifunctional catalyst

- Figure 3-7: Normal probability figure for the molar outlet flow rate of 3MP determined by solving the set of Eqs. 3-1 to 3-3, in which the net rates of formation are based upon the alternative reaction scheme given in Figure 3-6.
- Figure 3-8: Physisorption equilibrium of *n*-hexane, 2MP and 3MP in the zeolite pores
- Figure 3-9: (de-)Hydrogenation equilibrium between a physisorbed *n*-hexane, 2MP and 3MP molecule and one of their corresponding alkene
- Figure 3-10: (de-)Protonation equilibrium between *n*-hexylene, 2-methyl-pentylene and 3-methyl-pentylene and (one of) their corresponding carbenium ions
- Figure 3-11: pcp-branching of a hexyl to 2- and 3-methyl-pentyl
- Figure 3-12: Cracking via  $\beta$ -scission of a 2-methyl-pentyl to propylene and propyl
- Figure 3-13: Arrhenius plot,  $\ln(k_{comp})$  and  $\ln(K^{phys})$  as function of the reciprocal of temperature for which  $k_{comp}$  and  $K^{phys}$  are obtained from Table 3-2.
- Figure 3-14: Parity diagram for the molar outlet flow rate of 2MP (●), 3MP (■) and propane (▲) determined by solving the set of Eqs. 3-1 to 3-3, in which the net rates of formation are given by Eqs. 3-4 to 3-6 using the parameters from Table 3-4.
- Figure 3-15: Residual figures for the molar outlet flow rate of 2MP (top), 3MP (middle) and propane (bottom) as function of pressure (left) and temperature (right) determined by solving the set of Eqs. 3-1 to 3-3, in which the net rates of formation are given by Eqs. 3-4 to 3-6 using the parameters from Table 3-4.
- Figure 3-16: Normal probability figure for the molar outlet flow rate of 2MP determined by solving the set of Eqs. 3-1 to 3-3, in which the net rates of formation are given by Eqs. 3-4 to 3-6 using the parameters from Table 3-4.
- Figure 3-17: Normal probability figure for the molar outlet flow rate of 3MP determined by solving the set of Eqs. 3-1 to 3-3, in which the net rates of formation are given by Eqs. 3-4 to 3-6 using the parameters from Table 3-4.
- Figure 3-18: Normal probability figure for the molar outlet flow rate of propane determined by solving the set of Eqs. 3-1 to 3-3, in which the net rates of formation are given by Eqs. 3-4 to 3-6 using the parameters from Table 3-4.
- Figure 4-1: Ethene oligomerization product yields on 1.8wt% Ni-SiO<sub>2</sub>-Al<sub>2</sub>O<sub>3</sub> as function of ethene conversion. Symbols correspond to experimental data, lines correspond to model simulations, i.e., by integration of Eq. 2-21, with the

corresponding net rates of formation as given by Eq. 4-27 and the parameter values as reported in Table 4-4; ●, full line: butene; ▲, dashed line: hexene.

Figure 4-2: Experimental product distribution: molar fraction as function of carbon number. The full line shows the linear trend of the logarithm of the molar fraction of the components as function of their carbon number.

Figure 4-3: Ethene conversion on 1.8wt% Ni-SiO<sub>2</sub>-Al<sub>2</sub>O<sub>3</sub> as function of space-time at different temperatures, at 3.5MPa total pressure and an ethene inlet partial pressure equal to 0.35 MPa. Symbols correspond to experimental data, lines correspond to model simulations, i.e., by integration of Eq. 2-21, with the corresponding net rates of formation as given by Eq. 4-27 and the parameter values as reported in Table 4-4; ●, full line: 443 K; ■, dash-dotted line: 473 K; ▲, dashed line: 493 K.

Figure 4-4: Ethene conversion on 1.8wt% Ni-SiO<sub>2</sub>-Al<sub>2</sub>O<sub>3</sub> as function of space-time at different inlet ethene partial pressures, at 3.5 MPa total pressure and at 473K. Symbols correspond to experimental data, lines correspond to model simulations, i.e., by integration of Eq. 2-21, with the corresponding net rates of formation as given by Eq. 4-27 and the parameter values as reported in Table 4-4; ●, full line: 0.15 MPa; ■, dash-dotted line: 0.25 MPa; ▲, dashed line: 0.35 MPa.

Figure 4-5: Ethene oligomerization rate on 1.8wt% Ni-SiO<sub>2</sub>-Al<sub>2</sub>O<sub>3</sub> as function of ethene inlet partial pressure at different space-times and temperatures. Symbols correspond to experimental data, lines are determined by linear regression for each set of experimental conditions indicating the first order dependency on the reaction rate of the ethene inlet partial pressure; ●: 4.8 kg<sub>cat</sub> s mol<sub>C<sub>2</sub></sub><sup>-1</sup> and 473 K; ○: 7.2 kg<sub>cat</sub> s mol<sub>C<sub>2</sub></sub><sup>-1</sup> and 473 K; ■: 4.8 kg<sub>cat</sub> s mol<sub>C<sub>2</sub></sub><sup>-1</sup> and 503 K; □: 7.2 kg<sub>cat</sub> s mol<sub>C<sub>2</sub></sub><sup>-1</sup> and 503 K.

Figure 4-6: Proposed mechanism for ethene oligomerization on a heterogeneous nickel-based catalyst based on degenerated polymerization, (\*) the multi-elementary step isomerization is depicted as a elementary step for not to overload the figure.

Figure 4-7: Proposed mechanism for ethene oligomerization on a heterogeneous nickel catalyst based on concerted coupling

- Figure 4-8: Theoretical ASF distributions given by Eq. 4-28 for different chain growth probabilities  $\alpha$ . Full lines:  $\alpha_{ref}$ , dashed lines:  $1.15 \alpha_{ref}$ , dotted lines:  $1.30 \alpha_{ref}$ . Left:  $\alpha_{ref} = 0.1$ , middle:  $\alpha_{ref} = 0.3$ , right:  $\alpha_{ref} = 0.5$ .
- Figure 4-9: Residual diagrams for the molar outlet flow rate of butene as function of temperature (a), inlet partial pressure of ethene (b), space-time (c) and molar flow rate of butene (d). Residuals are determined by integration of Eq. 2-21, with the corresponding net rates of formation, Eq. 4-27 and the parameter values reported in Table 4-4.
- Figure 4-10: Residual diagrams for the molar outlet flow rate of ethene (a), hexene (b), octene (c) and 1-butene (d) as function of inlet partial pressure of ethene. Residual are determined by integration of Eq. 2-21, with the corresponding net rates of formation, Eq. 4-27 and the parameter values reported in Table 4-4.
- Figure 4-11: Catalyst occupancy by physisorbed species and the corresponding physisorbed fractions as a function of space-time at 473 K and an inlet ethene partial pressure equal to 0.35 MPa, calculated by integration of Eq. 2-21, with the corresponding net rates of formation, Eq. 4-27 and the parameter values reported in Table 4-4. Full line: catalyst occupancy by physisorbed species, dotted line: physisorbed fraction of ethene, short-dashed line: physisorbed fraction of butene, long-dashed line: physisorbed fraction of hexene, dashed dotted line: physisorbed fraction of octene.
- Figure 4-12: Catalyst occupancy by physisorbed species and the corresponding physisorbed fractions as a function of temperature at an inlet ethene partial pressure equal to 0.35 MPa at 13.4% conversion, calculated by integration of Eq. 2-21, with the corresponding net rates of formation, Eq. 4-27 and the parameter values reported in Table 4-4. Full line: catalyst occupancy by physisorbed species, dotted line: physisorbed fraction of ethene, short-dashed line: physisorbed fraction of butene, long-dashed line: physisorbed fraction of hexene, dashed dotted line: physisorbed fraction of octene.
- Figure 4-13: Catalyst occupancy by physisorbed species and the corresponding physisorbed fractions as a function of the inlet ethene partial pressure at 473 K, at 13.4% conversion, calculated by integration of Eq. 2-21, with the

corresponding net rates of formation, Eq. 4-27 and the parameter values reported in Table 4-4. Full line: catalyst occupancy by physisorbed species, dotted line: physisorbed fraction of ethene, short-dashed line: physisorbed fraction of butene, long-dashed line: physisorbed fraction of hexene, dashed dotted line: physisorbed fraction of octene.

Figure 5-1: Ethene conversion and butene and hexene selectivity on 4.9wt% Ni-Beta as function of time-on-stream at 523 K,  $10.2 \text{ kg}_{\text{cat}} \text{ s mol}^{-1}$ , 2.5 MPa total pressure and an ethene inlet partial pressure equal to 0.25 MPa. Symbols correspond to experimental observations, lines are the exponential trend lines to determine the ethene conversion and product selectivities at zero hour time-on-stream. ●, full line: conversion, left axis; ▲, dashed line: butene selectivity, right axis; ■, dotted line: hexene selectivity, right axis.

Figure 5-2: Ethene conversion and butene and hexene selectivity on 4.9wt% Ni-Beta as function of space-time at 523 K, 3.0MPa total pressure and an ethene inlet partial pressure equal to 0.35 MPa. Symbols correspond to experimental observations, lines correspond to model simulations, i.e., integration of Eq. 2-21, with the corresponding net rates of formation as given by Eq. 5-15 and the parameter values as reported in Tables 5-5 and 5-6; ●, full line: conversion, left axis; ▲, dashed line: butene selectivity, right axis; ■, dotted line: hexene selectivity, right axis.

Figure 5-3: Propene and pentene selectivity on 4.9wt% Ni-Beta as function of space-time at 523 K, 3.0 MPa total pressure and an ethene inlet partial pressure equal to 0.35 MPa. Symbols correspond to experimental observations, lines correspond to model simulations, i.e., integration of Eq. 2-21, with the corresponding net rates of formation as given by Eq. 5-15 and the parameter values as reported in Tables 5-5 and 5-6 ●, full line: propene; ▲, dashed line: pentene. M

Figure 5-4: Ethene conversion and propene and pentene selectivity on 4.9wt% Ni-Beta as function of temperature at  $10.5 \text{ kg}_{\text{cat}} \text{ s mol}^{-1}$ , 3.0 MPa total pressure and an ethene inlet partial pressure equal to 0.35 MPa. Symbols correspond to experimental observations, lines correspond to model simulations, i.e., integration of Eq. 2-21, with the corresponding net rates of formation as



given by Eq. 5-15 and the parameter values as reported in Tables 5-5 and 5-6; ●, full line: conversion, left axis; ▲, dashed line: propene selectivity, right axis; ■, dotted line: pentene selectivity, right axis.

Figure 5-5: Schematic representation of the ethene oligomerization reaction network involving Ni-ion oligomerization and acid catalyzed alkylation, isomerization and cracking.

Figure 5-6: Energy diagram for alkylation and  $\beta$ -scission

Figure 5-7: Simulated ethene oligomerization rates as function of space-time at 473 K and an inlet ethene partial pressure of 0.34 MPa. Full line: Ni-Beta zeolite, as determined by the model given by integration of Eq. 2-21 in which the net rates of formation is given by Eq. 5-15 with the parameter values given in Tables 5-5 and 5-6. Dashed line: Ni-SiO<sub>2</sub>-Al<sub>2</sub>O<sub>3</sub> as determined by the model given by integration of Eq. 2-21 in which the net rates of formation is given by Eq. 4-27 with the parameter values given in Table 4-4.

Figure 5-8: Parity diagrams for the molar outlet flow rate of ethene (a), propene (b), butene (c), pentene (d) and hexene (e) as determined by integration of Eq. 2-21, with the corresponding net rates of formation, Eq. 5-15 and the parameter values reported in Tables 5-5 and 5-6.

Figure 5-9: Residual figures for the molar outlet flow rate of propene (a) and butene (b) as function of temperature as determined by integration of Eq. 2-21, with the corresponding net rates of formation, Eq. 5-15 and the parameter values reported in Tables 5-5 and 5-6.

Figure 5-10: Normal probability figures for the molar outlet flow rate of propene (a) and butene (b) as determined by integration of Eq. 2-21, with the corresponding net rates of formation, Eq. 5-15 and the parameter values reported in Tables 5-5 and 5-6.

Figure 5-11: Ethene conversion and selectivity towards linear 1-alkenes (full line), gasoline (dotted line) and propene (dashed line) on Ni-Beta as function of space-time at 503 K and an ethene inlet partial pressure of 1.0 MPa as obtained by integration of Eq. 2-21, with the corresponding net rates of formation, Eq. 5-15 and the parameter values reported in Tables 5-5 and 5-6.

Figure 5-12: Selectivity towards linear 1-alkenes (full line), gasoline (dotted line) and propene (dashed line) as function of conversion on Ni-Beta at 503 K and an ethene inlet partial pressure of 1.0 MPa as obtained by integration of Eq. 2-21, with the corresponding net rates of formation, Eq. 5-15 and the parameter values reported in Tables 5-5 and 5-6.

Figure 5-13: Reaction path analysis for ethene oligomerization on Ni-Beta at 503 K, an ethene inlet partial pressure of 1.0 MPa and a conversion of 1% (a), 50% (b), 70% (c) and 99% (d), see also Figures 5-11 and 5-12. The model simulations were obtained by integration of Eq. 2-21, with the corresponding net rates of formation, Eq. 5-15 and the parameter values reported in Tables 5-5 and 5-6. The alkenes are lumped per carbon number. The height of the horizontal line in these circle is proportional to the mass fraction of the corresponding alkene lump. If no line is visible it indicates that the corresponding mass fraction is very small, i.e., less than 1%. However, these lump may still significantly contribute to the product formation. Additionally, alkene lumps in watermark indicate that its mass fraction is less than 0.1%. The vertical gray-scale code is used to differentiate between the different structural isomers, i.e., white: linear alkenes, light grey: monobranched alkenes and dark grey: dibranched alkenes. The surface area taken by these colors is proportional to the mass fraction of each structural isomer in the alkene lump. The color of the arrows indicate the reaction family: blue = metal-ion oligomerization, red = acid alkylation, green =  $\beta$ -scission. pcp-branching and alkyl shift are not explicitly shown as they only change the isomer distribution within an alkene lump. The size of the arrow is linearly proportional to the rate of the corresponding step. The numbers at the arrow head indicate the fraction of the lump which is produced via the corresponding step while numbers next to the arrow shaft indicate the fraction of the lump which is consumed via this step.

Figure 5-14: Selectivity towards linear 1-alkenes (full line), gasoline (dotted line) and propene (dashed line) as function of temperature at an ethene inlet partial pressure of 1.0 MPa and a conversion of 50% as obtained by integration of

Eq. 2-21, with the corresponding net rates of formation as given by Eq. 5-15 and the parameter values as reported in Tables 5-5 and 5-6.

Figure 5-15: Reaction path analysis for ethene oligomerization on Ni-Beta at 50% ethene conversion, an ethene inlet partial pressure of 1.0 MPa and 443 K (a), 483 K (b), 523 K (c) and 573 K (d), corresponding with (a), (b), (c) and (d) in Figure 5-14. The model simulations were obtained by integration of Eq. 2-21, with the corresponding net rates of formation, Eq. 5-15 and the parameter values reported in Tables 5-5 and 5-6. The alkenes are lumped per carbon number. The height of the horizontal line in these circle is proportional to the mass fraction of the corresponding alkene lump. If no line is visible it indicates that the corresponding mass fraction is very small, i.e., less than 1%. However, these lump may still significantly contribute to the product formation. Additionally, alkene lumps in watermark indicate that its mass fraction is less than 0.1%. The vertical gray-scale code is used to differentiate between the different structural isomers, i.e., white: linear alkenes, light grey: monobranched alkenes and dark grey: dibranched alkenes. The surface area taken by these colors is proportional to the mass fraction of each structural isomer in the alkene lump. The color of the arrows indicate the reaction family: blue = metal-ion oligomerization, red = acid alkylation, green =  $\beta$ -scission. pcp-branching and alkyl shift are not explicitly shown as they only change the isomer distribution within an alkene lump. The size of the arrow is linearly proportional to the rate of the corresponding step. The numbers at the arrow head indicate the fraction of the lump which is produced via the corresponding step while numbers next to the arrow shaft indicate the fraction of the lump which is consumed via this step.

Figure 5-16: Selectivity towards linear 1-alkenes (full line), gasoline (dotted line) and propene (dashed line) on Ni-Beta as function of alkene standard protonation enthalpy (s) at 50% ethene conversion, 503 K and an ethene inlet partial pressure of 1.0 MPa as obtained by integration of Eq. 2-21, with the corresponding net rates of formation as given by Eq. 5-15 and the parameter values as reported in Tables 5-5 and 5-6. The alkene standard protonation

enthalpy for the formation of tertiary carbenium ions is determined to be 30  $\text{kJ mol}^{-1}$  more negative than that of secondary carbenium ion formation.

Figure 5-17: Reaction path analysis for ethene oligomerization on Ni-Beta at 50% ethene conversion, 503 K, an ethene inlet partial pressure of 1.0 MPa and an alkene standard protonation enthalpy ( $\Delta H_p$ ) equal to  $-80 \text{ kJ mol}^{-1}$ . The alkene standard protonation enthalpy for the formation of tertiary carbenium ions is determined to be  $30 \text{ kJ mol}^{-1}$  less. The model simulations were obtained by integration of Eq. 2-21, with the corresponding net rates of formation, Eq. 5-15 and the parameter values reported in Tables 5-5 and 5-6. The alkenes are lumped per carbon number. The height of the horizontal line in these circles is proportional to the mass fraction of the corresponding alkene lump. If no line is visible it indicates that the corresponding mass fraction is very small, i.e., less than 1%. However, these lumps may still significantly contribute to the product formation. Additionally, alkenes in watermark indicate that its mass fraction is less than 0.1%. The vertical gray-scale code is used to differentiate between the different structural isomers, i.e., white: linear alkenes, light grey: monobranched alkenes and dark grey: dibranched alkenes. The surface area taken by these colors is proportional to the mass fraction of each structural isomer in the alkene lump. The color of the arrows indicates the reaction family: blue = metal-ion oligomerization, red = acid alkylation, green =  $\beta$ -scission.  $\text{pcp}$ -branching and alkyl shift are not explicitly shown as they only change the isomer distribution within an alkene lump. The size of the arrow is linearly proportional to the rate of the corresponding step. The numbers at the arrow head indicate the fraction of the lump which is produced via the corresponding step while numbers next to the arrow shaft indicate the fraction of the lump which is consumed via this step.

Figure 5-18: Selectivity towards linear 1-alkenes (full line), gasoline (dotted line) and propene (dashed line) on Ni-Beta as function of acid site concentration ( $\Delta H_p$ ) at 50% ethene conversion, 503 K and an ethene inlet partial pressure of 1.0 MPa as obtained by integration of Eq. 2-21, with the corresponding net rates of formation as given by Eq. 5-15 and the parameter values as reported in Tables 5-5 and 5-6.

- Figure 5-19: Selectivity towards linear 1-alkenes (full line), gasoline (dotted line) and propene (dashed line) on Ni-Beta as function of ethene standard coordination enthalpy at a nickel-ion site at 50% ethene conversion, 503 K and an ethene inlet partial pressure of 1.0 MPa as obtained by integration of Eq. 2-21, with the corresponding net rates of formation as given by Eq. 5-15 and the parameter values as reported in Tables 5-5 and 5-6.
- Figure 5-20: Selectivity towards linear 1-alkenes (full line), gasoline (dotted line) and propene (dashed line) on Ni-Beta as function of nickel content at 50% ethene conversion, 503 K and an ethene inlet partial pressure of 1.0 MPa as obtained by integration of Eq. 2-21, with the corresponding net rates of formation as given by Eq. 5-15 and the parameter values as reported in Tables 5-5 and 5-6.
- Figure 5-21: Selectivity towards linear 1-alkenes (full line), gasoline (dotted line) and propene (dashed line) on Ni-USY as function of temperature at an ethene inlet partial pressure of 1.0 MPa and a conversion of 50% as obtained by integration of Eq. 2-21, with the corresponding net rates of formation as given by Eq. 5-15 and the parameter values as reported in Tables 5-5 and 5-6.
- Figure 5-22: Selectivity towards linear 1-alkenes (full line), gasoline (dotted line) and propene (dashed line) as function of conversion on Ni-USY at 503 K and an ethene inlet partial pressure of 1.0 MPa as obtained by integration of Eq. 2-21, with the corresponding net rates of formation as given by Eq. 5-15 and the parameter values as reported in Tables 5-5 and 5-6.
- Figure 6-1: Graphical representation of the industrial reactor model for the heterogeneous, bifunctional catalyst ethene oligomerization.
- Figure 6-2: Mathematical representation of the industrial reactor model for the heterogeneous, bifunctional catalyst ethene oligomerization.
- Figure 6-3: Fractional coverage of ethene in a catalyst particle as function of the number of mesh points, used for discretizing the partial differential equations describing these profiles, at the reactor inlet (no conversion): full line: 3 mesh points, small dashed line: 5 mesh points, dotted line: 10 mesh points. The inlet temperature is equal to 503 K, the inlet partial pressure and molar flow rate of ethene is equal resp. 1.0 MPa and. The diffusion coefficient for ethene is taken equal to  $10^{-16} \text{ m}^2 \text{ s}^{-1}$  for illustration purposes.

- Figure 6-4: Time needed to determine the initial concentration profile as function of the number of mesh points, used for discretizing the partial differential equations describing these profiles, at the reactor inlet (no conversion). The inlet temperature is equal to 503 K, the inlet partial pressure and molar flow rate of ethene is equal resp. 1.0 MPa and  $37.2 \text{ mol s}^{-1}$ . The catalyst used is Ni-Beta. The diffusion coefficient for ethene is taken equal to  $10^{-16} \text{ m}^2 \text{ s}^{-1}$  for illustration purposes.
- Figure 6-5: Ethene conversion as function of space-time on Ni-SiO<sub>2</sub>-Al<sub>2</sub>O<sub>3</sub> at 493 K, 3.5 MPa total pressure and 2.6 MPa inlet ethene pressure; black line: simulation results as obtained using the simulation model for an industrial oligomerization reactor, see equations 6-3, 6-6 and 6-14.
- Figure 6-6: Ethene conversion on Ni-SiO<sub>2</sub>-Al<sub>2</sub>O<sub>3</sub> as function of temperature at  $48.0 \text{ kg}_{\text{cat}} \text{ s mol}_{\text{C}_2}^{-1}$ , 3.5 MPa total pressure and 2.6 MPa inlet ethene pressure; black line: simulation results as obtained using the simulation model for an industrial oligomerization reactor, see equations 6-3, 6-6 and 6-14.
- Figure 6-7: Ethene conversion on Ni-SiO<sub>2</sub>-Al<sub>2</sub>O<sub>3</sub> as function of ethene inlet molar fraction at  $48.0 \text{ kg}_{\text{cat}} \text{ s mol}_{\text{C}_2}^{-1}$ , 493 K and 3.5 MPa total pressure; black line: simulation results as obtained using the simulation model for an industrial oligomerization reactor, see equations 6-3, 6-6 and 6-14.
- Figure 6-8: Ethene conversion on Ni-SiO<sub>2</sub>-Al<sub>2</sub>O<sub>3</sub> as function of total pressure at  $22.4 \text{ kg}_{\text{cat}} \text{ s mol}_{\text{C}_2}^{-1}$ , 493 K and 2.6 MPa inlet ethene pressure; black line: simulation results as obtained using the simulation model for an industrial oligomerization reactor, see equations 6-3, 6-6 and 6-14.
- Figure 6-9: Temperature increase during operation of the pilot plant reactor using the Ni-SiO<sub>2</sub>-Al<sub>2</sub>O<sub>3</sub> as function of the dimensionless reactor length as obtained using the simulation model for an industrial oligomerization reactor, see equations 6-3, 6-6 and 6-14, at 3.5 MPa total pressure and 2.6 MPa inlet ethene pressure for different reactor wall temperatures: full line: 443 K, dotted line: 453 K, dashed line: 473 K, dashed-dotted line: 493 K. The inlet temperature was taken equal to the reactor wall temperature.
- Figure 6-10: Ethene conversion (left axis) and reactor temperature (right) as function of the Ni-Beta catalyst mass, i.e., axial reactor coordinate as obtained using the

simulation model for an industrial oligomerization reactor, see equations 6-3, 6-6 and 6-14, at 503 K inlet temperature, 1.0 MPa inlet ethene pressure and an inlet ethene molar flow rate equal to  $37.2 \text{ mol s}^{-1}$ , full line: isothermal case, dashed lines: adiabatic case.

Figure 6-11: Reactor temperature (left axis) and product yield (right) as function of the Ni-Beta catalyst mass, i.e., axial reactor coordinate as obtained using the simulation model for an adiabatic industrial oligomerization reactor, see equations 6-3, 6-6 and 6-14, at 503 K inlet temperature, 1.0 MPa inlet ethene pressure and an inlet ethene molar flow rate equal to  $37.2 \text{ mol s}^{-1}$ , full line, left axis: reactor temperature; full line, right axis: 1-alkene yield; dashed line: propene yield; dotted line: gasoline yield.

Figure 6-12: Reactor temperature as function of axial reactor coordinate as obtained using the simulation model for an adiabatic industrial oligomerization reactor, see equations 6-3, 6-6 and 6-14, at 503 K inlet temperature, 1.0 MPa inlet ethene pressure and an inlet ethene molar flow rate equal to  $37.2 \text{ mol s}^{-1}$ , full line: Ni-Beta, dashed lines: Ni-SiO<sub>2</sub>-Al<sub>2</sub>O<sub>3</sub>.

Figure 6-13: Reactor temperature (left axis) and heat produced (right axis) as function of the Ni-Beta catalyst mass, i.e., axial reactor coordinate as obtained using the simulation model for a heat exchanging industrial oligomerization reactor, see equations 6-3, 6-6 and 6-14, at 503 K inlet temperature, a constant cooling medium temperature of 503 K, 1.0 MPa inlet ethene pressure and an inlet ethene molar flow rate equal to  $37.2 \text{ mol s}^{-1}$ , full line: reactor temperature, dashed line: produced heat.

Figure 6-14: Reactor temperature as function of the Ni-Beta catalyst mass, i.e., axial reactor coordinate as obtained using the simulation model for a heat exchanging industrial oligomerization reactor with varying length to diameter ratio ( $L_r/d_r$ ), see equations 6-3, 6-6 and 6-14, at 503 K inlet temperature, 1.0 MPa inlet ethene pressure and an inlet ethene molar flow rate equal to  $37.2 \text{ mol s}^{-1}$ , full line:  $L_r/d_r = 15$ , dashed line:  $L_r/d_r = 10$ , dotted line:  $L_r/d_r = 8$ , dashed-dotted line:  $L_r/d_r = 5$ .

Figure 6-15: Pressure drop as function of the catalyst pellet to reactor diameter ratio as obtained using the simulation model for an isothermal industrial

oligomerization reactor using the Ni-Beta catalyst, see equations 6-3, 6-6 and 6-14, at 503 K inlet temperature, 1.0 MPa inlet ethene pressure and an inlet ethene molar flow rate equal to  $37.2 \text{ mol s}^{-1}$ .

Figure 6-16: Ethene conversion as function of the catalyst mass, i.e., axial reactor coordinate as obtained using the simulation model for an isothermal industrial oligomerization reactor see equations 6-3, 6-6 and 6-14, for a Ni-Beta catalyst containing only Ni-ion sites (type I and III) at 393 K inlet temperature, 10.0 MPa inlet ethene pressure and an inlet ethene molar flow rate equal to  $37.2 \text{ mol s}^{-1}$ . Full line: ignoring liquid formation, dashed line:  $A_{\text{macro}} = 100 A_{\text{micro}}$  (type I), dotted line:  $A_{\text{micro}} = 100 A_{\text{macro}}$  (type III)

Figure 6-17: Ethene conversion (left) and wetting efficiency and phase molar gas fraction (right) as function of the catalyst mass, i.e., axial reactor coordinate as obtained using the simulation model for an isothermal industrial oligomerization reactor see equations 6-3, 6-6 and 6-14, for a Ni-Beta catalyst containing only Ni-ion sites having a macroporous surface area which highly exceeds the microporous surface area, i.e.,  $A_{\text{macro}} = 100 A_{\text{micro}}$  (type I), at 393 K inlet temperature, 10.0 MPa inlet ethene pressure and an inlet ethene molar flow rate equal to  $37.2 \text{ mol s}^{-1}$ . Full line: ethene conversion, dashed line: molar gas phase fraction, dotted line: wetting efficiency

Figure 6-18: Ethene conversion (left) and wetting efficiency and phase molar gas fraction (right) as function of the catalyst mass, i.e., axial reactor coordinate as obtained using the simulation model for an isothermal industrial oligomerization reactor see equations 6-3, 6-6 and 6-14, for a Ni-Beta catalyst containing only Ni-ion sites having a microporous surface area which highly exceeds the macroporous surface area, i.e.,  $A_{\text{micro}} = 100 A_{\text{macro}}$  (type III), at 393 K inlet temperature, 10.0 MPa inlet ethene pressure and an inlet ethene molar flow rate equal to  $37.2 \text{ mol s}^{-1}$ . Full line: ethene conversion, dashed line: molar gas phase fraction, dotted line: wetting efficiency

Figure 6-19: Ethene conversion as function of the catalyst mass, i.e., axial reactor coordinate as obtained using the simulation model for an isothermal industrial oligomerization reactor see equations 6-3, 6-6 and 6-14, for a Ni-Beta catalyst containing acid and Ni-ion sites (type II and IV) at 393 K inlet



temperature, 10.0 MPa inlet ethene pressure and an inlet ethene molar flow rate equal to  $37.2 \text{ mol s}^{-1}$ . Full line: ignoring liquid formation, dashed line:  $A_{\text{macro}} = 100 A_{\text{micro}}$  (type II), dotted line:  $A_{\text{micro}} = 100 A_{\text{macro}}$  (type IV)

Figure 6-20: 1-alkene selectivity as function of ethene conversion using the simulation model for an isothermal industrial oligomerization reactor see equations 6-3, 6-6 and 6-14, for a Ni-Beta catalyst containing acid and Ni-ion sites (type II and IV) at 393 K inlet temperature, 10.0 MPa inlet ethene pressure and an inlet ethene molar flow rate equal to  $37.2 \text{ mol s}^{-1}$ . Full line: ignoring liquid formation, dashed line:  $A_{\text{macro}} = 100 A_{\text{micro}}$  (type II), dotted line:  $A_{\text{micro}} = 100 A_{\text{macro}}$  (type IV)

Figure 6-21: Propene selectivity as function of ethene conversion using the simulation model for an isothermal industrial oligomerization reactor see equations 6-3, 6-6 and 6-14, for a Ni-Beta catalyst containing acid and Ni-ion sites (type II and IV) at 393 K inlet temperature, 10.0 MPa inlet ethene pressure and an inlet ethene molar flow rate equal to  $37.2 \text{ mol s}^{-1}$ . Full line: ignoring liquid formation, dashed line:  $A_{\text{macro}} = 100 A_{\text{micro}}$  (type II), dotted line:  $A_{\text{micro}} = 100 A_{\text{macro}}$  (type IV)

Figure 6-22: Fractional coverage of ethene in a Ni-Beta catalyst particle as function of the shape factor  $s$ , at the reactor inlet (no conversion): full line: slab ( $s=0$ ), dotted line: cylinder ( $s=1$ ), dashed line: sphere ( $s=2$ ). The inlet temperature is equal to 503 K, the inlet partial pressure and molar flow rate of ethene is equal resp. 1.0 MPa and. The diffusion coefficient for ethene is taken equal to  $10^{-16} \text{ m}^2 \text{ s}^{-1}$  for illustration purposes.

Figure 6-23: Ethene conversion (left axis) and reactor temperature (right) as function of the Ni-Beta catalyst mass, i.e., axial reactor coordinate as obtained using the simulation model for an adiabatic industrial oligomerization reactor, see equations 6-3, 6-6 and 6-14, at 573 K inlet temperature, 3.5 MPa inlet ethene pressure and an inlet ethene molar flow rate equal to  $37.2 \text{ mol s}^{-1}$

Figure 6-24: Product yield as function of the Ni-Beta catalyst mass, i.e., axial reactor coordinate as obtained using the simulation model for an adiabatic industrial oligomerization reactor, see equations 6-3, 6-6 and 6-14, at 573 K inlet temperature, 3.5 MPa inlet ethene pressure and an inlet ethene molar flow

rate equal to  $37.2 \text{ mol s}^{-1}$ ; full line: 1- alkenes, dashed line: propene, dotted line: gasoline.

Figure 7-1: Schematic representation of alkyl shift of a dialkyl substituted aromatic component

Figure 7-2: Schematic overview of dealkylation of an alkyl substituted aromatic component

Figure 7-3: Schematic overview of transalkylation between two metaxylene molecules

Figure 7-4: Schematic overview of the total hydrogenation of a dialkyl substituted aromatic component

Figure 7-5: Schematic representation of the reaction network for xylene isomerization on a bifunctional catalyst. A gas phase aromatic component can physisorb on the catalyst surface followed by a possible interaction with either acid or metal sites. Depending on the nature of the active site, acid catalyzed isomerization or scission or metal catalyzed hydrogenation occurs. Products formed leave the active sites and desorb from the catalyst surface.

Figure 7-6: Parity diagrams for the responses of the kinetic model for xylene isomerization on a bifunctional Pt/H-ZSM-5 catalyst: conversion of ethylbenzene (a), benzene selectivity (b), conversion of xylene (c), mass fraction of toluene (d), mass fraction of  $C_9+$ -components (e) and approach to equilibrium (ate) of paraxylene (f). The parity diagrams are obtained using equations 1 to 4 with the molar outlet flow rates determined by the kinetic model consisting of the reactor model, see Eq. 2-21, the reaction rate equations, see Eqs. 7-12 to 7-14, and the net rates of formation, see Eqs. 7-15 to 7-17. See Table 7-6 for the estimated parameter values and their 95% confidence interval.

Figure 7-7: Simulated approach to equilibrium for paraxylene (a), benzene yield (b), xylene conversion (c) and profit function  $\Psi=ab/c$  (d) as function of protonation enthalpy at the reaction conditions as defined in Table 7-9. Full line: at 673 K and 1.0 MPa; dotted line: at 653 K and 1 MPa; dashed line: 633 K and 1.0 MPa.

# List of tables

- 
- Table 2-1: Properties of the Pt/H-ZSM-5 catalyst used for *n*-hexane hydroisomerization
- Table 2-2: Properties of the Ni-SiO<sub>2</sub>-Al<sub>2</sub>O<sub>3</sub> catalyst used for ethene oligomerization
- Table 2-3: Properties of the Ni-Beta catalyst used for ethene oligomerization
- Table 2-4: Properties of the Pt/H-ZSM-5 catalyst used for xylene isomerization
- Table 3-1: Range of experimental conditions for *n*-hexane hydroisomerization on Pt/H-ZSM-5
- Table 3-2: Parameter estimates and corresponding 95% confidence interval as function of temperature determined by isothermal regression to the experimental data of the kinetic model given by the set of Eqs. 3-1 to 3-3, in which the net rates of formation are given by Eqs. 3-4 to 3-6. Not statistically significant parameters are indicated in italics.
- Table 3-3: Determined values of the pre-exponential factor, kinetic/equilibrium coefficient at average temperature, i.e., 531.48 K, and activation energy and reaction enthalpy by the isothermal regression and the Arrhenius plot, see Figure 3-12.
- Table 3-4: Parameter estimates, corresponding approximate 95% individual confidence interval and *t* values of the kinetic/equilibrium coefficients at average temperature and activation energies and reaction enthalpy determined by non-isothermal regression to the experimental data of the kinetic model given by the set of Eqs. 3-1 to 3-3, in which the net rates of formation are given by Eqs. 3-4 to 3-6.
- Table 3-5: Binary correlation coefficient matrix as determined by non-isothermal regression to the experimental data of the kinetic model given by the set of Eqs. 3-1 to 3-3, in which the net rates of formation are given by Eqs. 3-4 to 3-6.
- Table 4-1: Ranges of experimental conditions for ethene oligomerization on Ni-SiO<sub>2</sub>-Al<sub>2</sub>O<sub>3</sub>

- Table 4-2: Reaction steps and kinetic parameters for ethene oligomerization on a heterogeneous nickel containing catalyst for the degenerate polymerization and concerted coupling mechanism
- Table 4-3: External, internal and global symmetry numbers and number of chiral atoms of the reactant species considered in the reaction network
- Table 4-4: Reaction enthalpies and activation energies as well as statistical performance indicators, all at 95% confidence level, determined by non-linear regression of the model given by integration of Eq. 2-21 to the experimental data measured at the range of operating conditions given in Table 4-1. Left: according to the original kinetic model given for which the net rates of formation are given by Eq. 4-16; right: according to the revised kinetic model given for which the net rates of formation are given by Eq. 4-27.
- Table 4-5: Chain growth probability  $\alpha$  as function of temperature as determined by Eqs. 4-12 and 4-13 calculated with the parameter values reported in Table 4-4.
- Table 4-6: Binary correlation coefficient matrix as determined by non-linear regression by integration of Eq. 2-21, with the corresponding net rates of formation, Eq. 4-27, to the experimental data measured at the operating conditions given in Table 4-1.
- Table 5-1: Range of investigated experimental conditions for ethene oligomerization on Ni-Beta
- Table 5-2: Overview of the reaction networks generated with ReNGeP for regression, reaction pathway analysis and catalyst design purposes.
- Table 5-3: Selection of the reference alkenes considered in Eq. 5-13
- Table 5-4: Overview of the kinetic and catalyst descriptors to be determined for the Single-Event MicroKinetic model for ethene oligomerization on Ni-Beta zeolite.
- Table 5-5: Catalyst descriptors as well as statistical performance indicators, all at 95% confidence level, determined by non-linear regression of the model given by integration of Eq. 2-21 in which the net rates of formation are given by Eq. 5-15 to the experimental data measured at the operating conditions given in Table 5-1. (a): values from [14] and (b): values from [9, 10]

- Table 5-6: Kinetic descriptors used during the non-linear regression of the model given by integration of Eq. 2-21 in which the net rates of formation are given by Eq. 5-15 to the experimental data measured at the operating conditions given in Table 5-1. (a): values from Table 4-4, (b): values from [9, 10] and (c): determined via thermodynamic considerations
- Table 6-1: Overview of the catalyst types simulated to study the effect of liquid formation on the observed kinetics for ethene oligomerization.
- Table 7-1: Range of investigated experimental conditions for xylene isomerization on Pt/H-ZSM-5
- Table 7-2: Molar fractions of the components at the inlet and the outlet of the reactor for xylene isomerization on a bifunctional Pt/H-ZSM-5 catalyst
- Table 7-3: Calculated pre-exponential factors for methyl shift, dealkylation and transalkylation using Eqs. 7-22 to 7-24 at 623.15K.
- Table 7-4: Pre-exponential factors for the hydrogenation kinetics based on a Langmuir Hinshelwood/Hougen Watson type rate equation as used in the kinetic model for xylene isomerization on a bifunctional Pt/H-ZSM-5 catalyst [16]
- Table 7-5: Physisorption enthalpies for linear alkanes and aromatic components on USY and ZSM-5 zeolite. Physisorption enthalpies for linear alkanes on USY and ZSM-5 zeolite and for aromatics on USY zeolite are reported by Denayer [24]. Physisorption enthalpies for aromatics on ZSM-5 as used in the kinetic model for xylene isomerization on a bifunctional Pt/H-ZSM-5 catalyst are calculated via (\*) and (\*\*).
- Table 7-6: Parameter estimates with their 95% confidence intervals and corresponding t and F values obtained after regression of the kinetic model of xylene isomerization to the experimental data obtained on a bifunctional Pt/H-ZSM-5 catalyst in which for the hydrogenation kinetics the first hydrogen addition is taken as the rate determining step ( $i=1$ ). Literature reported values and ranges are included for comparison. The model consists of the reactor model, see Eq. 2-21, the reaction rate equations, see Eqs. 7-12 to 7-14, and the net rates of formation, see Eqs. 7-15 to 7-17. Values denoted with \* are taken from literature and are not estimated.

- Table 7-7: Correlation coefficient matrix from the regression of the experimental data to the proposed kinetic model for xylene isomerization on a bifunctional Pt/H-ZSM-5 catalyst. The model consists of the reactor model, see Eq. 2-21, the reaction rate equations, see Eqs. 7-12 to 7-14, and the net rates of formation, see Eqs. 7-15 to 7-17. The protonation enthalpy not included as estimated parameter.
- Table 7-8: Relative pre-exponential factors as determined in the kinetic model for xylene isomerization on a bifunctional Pt/H-ZSM-5 catalyst, linked to the changes in entropy during the formation of the transition state
- Table 7-9: Reaction conditions used in the investigation of the effect of the protonation enthalpy and the total acid site concentration on the simulated catalyst performance. The model consists of the reactor model, see Eq. 2-21, the reaction rate equations, see Eqs. 7-12 to 7-14, and the net rates of formation, see Eqs. 7-15 to 7-17. All parameter estimates, except the value for the protonation enthalpy, from Table 7-6 are used as input for the simulations.
- Table 9-1: Critical and other properties of the linear 1-alkenes used as reference components, \* determined by extrapolation
- Table 9-2: Coefficients for the determination of the heat capacity of the reference components, see Eq. 9-1.
- Table 9-3: Coefficients for the determination of the vapor pressure of the reference components, see Eqs. 9-3 and 9-4, \* determined by extrapolation
- Table 9-4: Coefficients used in the determination of the molar volume of a pure liquid components, see Eqs. 9-25 to 9-27.
- Table 9-5: Coefficients used to determine  $B_i$  to calculate the thermal conductivity of a gas component, see Eq. 9-43.
- Table 9-6: Coefficient used for the determination of the thermal conductivity of a liquid olefin, see Eq. 9-44.
- Table 9-7: Coefficients used to determine  $E_i$  to calculate the viscosity of a gas component, see Eq. 9-57.

# List of symbols

---

## Roman symbols

$a_t$ (e.g. $a_c$ )	number of $t$ atoms (e.g. carbon number)	[-]
$A$	peak surface area	[-]
$A$	pre-exponential factor	[variable]
$A$	surface area / cross-sectional area	[m <sup>2</sup> ]
$ATE$	approach to equilibrium	[-]
$\underline{b}$	model parameter vector	
$C_{H^+}$	acid site concentration	[mol g <sub>cat</sub> <sup>-1</sup> ]
$C_i$	concentration of component $i$	[mol g <sub>cat</sub> <sup>-1</sup> ]
$C_p$	heat capacity	[J K <sup>-1</sup> ]
$CF$	calibration factor	[variable]
$d$	diameter	[m]
$d.f.$	degrees of freedom	[-]
$e$	error	[variable]
$e_t$	element $t$	
$E(i)$	expected value of $i$	[variable]
$E_a$	activation energy	[J mol <sup>-1</sup> ]
$f$	friction factor	[-]
$F$	molar flow rate	[mol s <sup>-1</sup> ]
$F_a$	F-value resulting from the adequacy test	[-]
$F_s$	F-value resulting from the significance test	[-]
$g$	gravitational acceleration	[m <sup>3</sup> kg <sup>-1</sup> s <sup>-2</sup> ]
$Ga$	Galileo number	[-]
$h$	Planck's constant	[J s]
$H$	Henry coefficient	[mol g <sup>-1</sup> Pa <sup>-1</sup> ]

$\Delta H$	enthalpy change	[J mol <sup>-1</sup> ]
$i$	counter	
$j$	counter	
$J_m$	mass flux	[g m <sup>-2</sup> s <sup>-1</sup> ]
$k$	rate coefficient	[variable]
$\tilde{k}$	single-event rate coefficient	[variable]
$k_B$	Boltzmann constant	[J K <sup>-1</sup> ]
$K$	equilibrium coefficient	[variable]
$l$	counter	
$L$	length	[m]
$\dot{m}$	mass flow rate	[g s <sup>-1</sup> ]
$M$	molecular mass	[g mol <sup>-1</sup> ]
$n_b$	number of fixed beds	[-]
$n_{chir}$	number of chiral atoms	[-]
$n_{comp}$	number of components	[-]
$n_{dbi}$	number of double bound isomers	[-]
$n_e$	number of single events	[-]
$n_e(i)$	number of repeat experiments at the $i^{\text{th}}$ set of reaction conditions	[-]
$n_{exp}$	number of experiments	[-]
$n_{mesh}$	number of mesh points	[-]
$n_{ole}$	number of olefins	[-]
$n_{par}$	number of parameters	[-]
$n_r$	number of reactions	[-]
$n_{resp}$	number of responses	[-]
$Ni^{(+)}$	nickel-ion species	
$p_i$	particle pressure of component $i$	[Pa]
$Q$	power	[W]
$Q$	volumetric flow rate	[m <sup>3</sup> s <sup>-1</sup> ]



$r$	reaction rate	$[\text{mol s}^{-1} \text{g}_{\text{cat}}^{-1}]$
$R$	net rate of formation	$[\text{mol s}^{-1} \text{g}_{\text{cat}}^{-1}]$
$R$	universal gas constant	$[\text{J mol}^{-1} \text{K}^{-1}]$
$R^2$	multiple correlation coefficient	[-]
$Re$	Reynolds number	[-]
$s$	shape factor	[-]
$s(b_i)$	standard deviation of parameter $b_i$	[variable]
$\Delta S$	entropy change	$[\text{J mol}^{-1} \text{K}^{-1}]$
$S_{i,j}$	selectivity for component $i$ coming from component $j$	[-]
$SSQ$	sum of squares	[variable]
$t(b_i)$	t-value for parameter $b_i$	[-]
$T$	temperature	[K]
$u_s$	superficial velocity	$[\text{m s}^{-1}]$
$V(\underline{b})$	(co-)variance of parameter vector $\underline{b}$	[variable]
$V_m$	molar volume	$[\text{m}^3 \text{mol}^{-1}]$
$V_p$	pore volume	$[\text{m}^3 \text{g}_{\text{cat}}^{-1}]$
$w$	mass fraction	$[\text{g g}^{-1}]$
$w$	statistical weight	[-]
$W$	catalyst mass	[g]
$We$	Weber number	[-]
$X$	conversion	[-]
$y_i$	molar fraction of component $i$ in the gas phase	$[\text{mol mol}^{-1}]$
$Y_{i,j}$	experimental value of the $j^{\text{th}}$ response of the $i^{\text{th}}$ experiment	[variable]
$\hat{Y}_{i,j}$	calculated value of the $j^{\text{th}}$ response of the $i^{\text{th}}$ experiment	[variable]

## Greek symbols

$\alpha$	chain growth probability	[-]
$\alpha$	heat transfer coefficient	[W m <sup>-2</sup> K <sup>-1</sup> ]
$\alpha_j^i$	stoichiometric coefficient with respect to component $i$ for reaction $j$	[-]
$\underline{\beta}$	real parameter vector	
$\gamma$	combined chain growth probability	[-]
$\varepsilon$	bed porosity	[-]
$\eta$	catalyst effectiveness	[-]
$\eta_w$	wetting efficiency	[-]
$\theta$	fractional occupancy	[-]
$\lambda$	thermal conductivity	[W m <sup>-1</sup> K <sup>-1</sup> ]
$\mu$	dynamic viscosity	[Pa s]
$\rho$	mass density	[g m <sup>-3</sup> ]
$\rho_{i,j}$	binary correlation coefficient between parameter $i$ and $j$	[-]
$\sigma$	standard deviation	[variable]
$\sigma$	surface tension	[N m <sup>-1</sup> ]
$\sigma$	symmetry numbers	[-]
$\sigma_{ii}^2$	covariance of response $i$	[variable]
$\varphi$	molar gas fraction	[mol mol <sup>-1</sup> ]
$\varphi_e$	element balance	[-]
$\varphi_m$	mass balance	[-]
$\xi$	dimensionless distance	[-]

## Subscripts

<i>2MP</i>	2-methyl-pentane
<i>3MP</i>	3-methyl-pentane
<i>aro</i>	aromatic
<i>A</i>	aromatic
<i>b</i>	catalyst bed
<i>B</i>	benzene
<i>c</i>	catalyst crystallite
<i>car</i>	carbenium ion
<i>comp</i>	composite
<i>exp</i>	experimental
<i>ext</i>	external
<i>f</i>	fluidum
<i>f</i>	formation
<i>gl</i>	global
<i>int</i>	internal
<i>is</i>	internal standard
<i>LOF</i>	lack of fit
<i>m</i>	mean
<i>m</i>	metal
<i>MX</i>	meta-xylene
<i>naft</i>	naphthalene
<i>o</i>	non-micro porous
<i>ole</i>	olefin
<i>OX</i>	ortho-xylene
<i>p</i>	catalyst pellet
<i>p</i>	micro porous
<i>PE</i>	pure-error
<i>PX</i>	paraxylene
<i>r</i>	reaction

<i>r</i>	reactor
<i>r</i>	reduced
<i>ref</i>	reference
<i>REG</i>	regression
<i>RES</i>	residual
<i>sim</i>	simulated
<i>tot</i>	total
<i>TOL</i>	toluene
<i>XYL</i>	xylene

## Superscripts

$+$	carbenium ion
$\neq$	transition state
$0$	inlet
$0$	standard
$2p$	two-phase
$a$	activation
$as$	alkyl shift
$bs$	beta-scission
$c$	coordination
$chem$	chemisorption
$da$	dealkylation
$deh$	dehydrogenation
$eq$	equilibrium
$f$	forward
$g$	gas
$hyd$	hydrogenation
$ins$	insertion
$iso$	isomerization
$l$	liquid
$ms$	methyl shift
$pcp$	protonated-cyclo-propyl branching
$phys$	physisorption
$pr$	protonation
$r$	reactant
$r$	reverse
$s$	surface
$sat$	saturation
$ta$	transalkylation
$ter$	termination

*trans* translational  
*wall* wall

# Glossary of terms

---

Activation energy	For an elementary step, the difference in internal energy between transition state and reactants. A measure for the temperature dependence of the rate coefficient.
Active sites	Groups at the surface of a solid or enzyme, responsible for their catalytic activity.
Adsorption	The preferential concentration of a species at the interface between two phases. Adherence of the atoms, ions or molecules of a gas or liquid to the surface of another substance.
Arrhenius relation	Expresses the dependence of a rate coefficient $k$ corresponding with a chemical reaction on the temperature $T$ and activation energy, $E_a$ : $k = A \exp(E_a/RT)$ with $R$ is the universal gas constant, $T$ the temperature and $A$ the pre-exponential factor.
Catalyst	A source of active centers regenerated at the end of a closed reaction sequence..
Chemisorption	Also known as chemical adsorption. Adsorption in which the forces involved are valence forces of the same kind as those operating in the formation of chemical compounds. Chemisorption strongly depends on the surface and the sorptive, and only one layer of chemisorbed molecules is formed. Its energy of adsorption is the same order of magnitude as in chemical reactions, and the adsorption may be activated.
Conversion	Measure for the amount of a reactant that has been transformed into products as a result of a chemical reaction.
Deactivation	The decrease in conversion in a catalytic reaction with time of run under constant reaction conditions.

Elementary step	The irreducible act of reaction in which reactants are transformed into products directly, i.e., without passing through an intermediate that is susceptible to isolation.
Effectiveness factor	Ratio of actual reaction rate for a porous catalyst to reaction rate that would be observed if the total surface area throughout the catalyst interior were exposed to a fluid of the same composition and temperature as that found at the outside of the particle.
Gas Chromatography (GC)	The process in which the components of a mixture are separated from one another by injecting the sample into a carrier gas which is passing through a column or over a bed of packing with different affinities for adsorptive of the components to be separated.
Group contribution method	A technique to estimate and predict thermodynamic and other properties from molecular structures, i.e., atoms, atomic groups, bond type etc.
Intermediate	Is formed from a reactant and transforms into a product during a chemical reaction. The intermediate is often a short-lived and unstable species that cannot directly be detected during a reaction.
Internal diffusion	Also called intraparticle diffusion. Motion of atoms within the particles of a solid phase that has a sufficiently large porosity to allow this motion.
Intraparticle diffusion	Motion of atoms or molecules in between particles of a solid phase
Langmuir-Hinshelwood-Hougen-Watson (LHHW) mechanism	It is assumed that both reactants must be adsorbed on the catalyst in order to react. Normally adsorption-desorption steps are essentially at equilibrium and a surface step is rate-determining. Adsorption steps can also be rate-determining.
Mechanism	A sequence of elementary steps in which reactants are converted into products, through the formation of intermediates.
Network	When several single reactions take place in a system, these parallel and consecutive reactions constitute a network.



Normal probability figure	A 2-dimensional scatter plot in which the ordered residuals, i.e., residuals ordered from lowest to highest value, are displayed against the theoretical quantile values, which are points dividing the cumulative distribution function into equal portions.
Objective function	Is a function used during optimization problems which have to be minimized or maximized by choosing the best set of variables which determines the values of this function.
Pseudo-steady state	Its mathematical expression is that the time rate of change of the concentration of all active centres in a reaction sequence is equal to zero
Parameter estimation	Process of estimating the parameters of a relation between independent and dependent variables as to describe a chemical reaction as good as possible.
Parity diagram	A 2-dimensional scatter plot in which the model calculated values of the responses are displayed against the experimentally observed values
Performance figure	In a performance figure, the response values, both experimentally observed as well as model calculated ones, are displayed against an independent variables, e.g., conversion as a function of space-time.
Physisorption	Also known as physical adsorption. Adsorption in which the forces involved are intermolecular forces (van der Waals forces) of the same kind as those responsible for deviation from ideal gas behavior or real gases at the condensation of vapors, and which do not involve a significant change in the electronic orbital patterns of the species involved. Physisorption usually occurs at temperatures near the boiling point of adsorbate, and multilayer can occur. The heat of adsorption is usually significantly less than 40 kJ/mol.
Porosity	A measure of the void spaces in a material, expressed as the ratio of the volume of voids to the total volume of the material.
Pre-exponential factor	The temperature-independent factor of a rate coefficient, also called the frequency factor.

Reaction family	Classification of elementary reaction steps on the basis of same features
Reaction rate	The number of moles of a component created by a chemical reaction per unit of time, volume or catalyst weight.
Rate-determining step	If, in a reaction sequence, consisting of $n$ steps, $(n-1)$ steps are reversible and if the rate of each of these $(n-1)$ steps potentially larger in either direction than the rate of the $n$ th step, the latter is said to be rate-determining. The rate-determining step need not be reversible.
Residual plot	A 2-dimensional scatter plot in which the residuals, i.e., the differences between the model simulated values and the observed values, are put against the independent (or dependent) variable values.
Single Event MicroKinetics	Single Event MicroKinetics: A kinetic modeling concept in which elementary steps are grouped into reaction families mainly based on enthalpic/energetic considerations. By accounting for the symmetry effects of reactant and transition state a unique, single-event rate coefficient suffices per reaction family. As a result, the number of adjustable parameters is greatly reduced. (abbrev.: SEMK)
Steady state	A system in steady-state has certain properties that are time-independent.
Surface coverage	Ratio of the amount of adsorbed substance to the monolayer capacity (also, sometimes defined for metals as the ratio of the number of adsorbed atoms or groups to the number of metal surface atoms).
Support	Also called carrier. Material, usually of high surface area, on which the active catalytic material, present as the minor component, is dispersed. The support may be catalytically inert, but it may contribute to the overall catalytic activity.
Surface coverage	Ratio of the amount of adsorbed substance to the monolayer capacity

---

Steady state	A system in steady-state has certain properties that are time-independent.
Transition state	Also called activated complex.. The configuration of highest potential energy along the path of lowest energy between reactants and products.
Transition state theory	Theory to calculate the rate of an elementary reaction from a knowledge of the properties of the reacting components and their concentrations. Differs from collision theory in that it takes into account the internal structure of reactant components.

---



# Summary

---

Kinetic modeling provides chemical engineers with a useful tool for process control, reaction mechanism elucidation, catalyst design and industrial reactor optimization. The development of a systematic methodology for the construction of such models will be a valuable asset. It will increase the fundamental understanding of the underlying chemistry and promotes communication between researchers with an industrial and academic background. In this work, such a systematic methodology was developed.

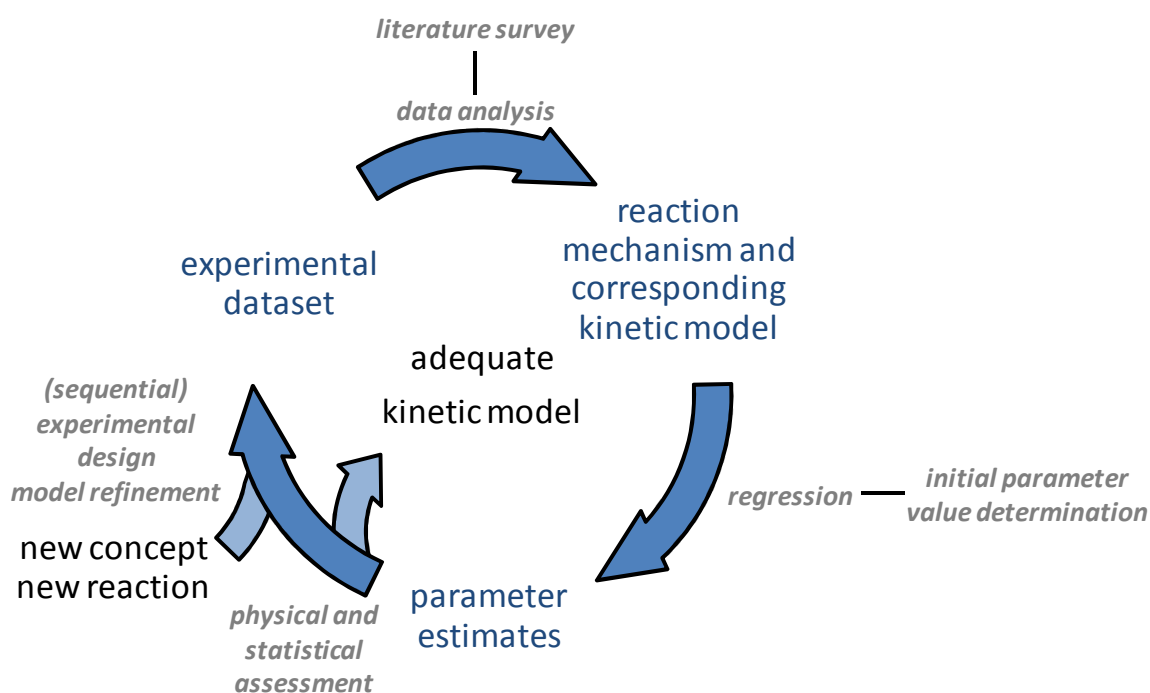


Figure 1: Proposed procedure for kinetic modeling

The methodology is presented in Figure 1. Although most of the concepts used are already known for several decades, the actual integration into a single methodology is rather unique. It starts from intrinsic kinetic data obtained from a well-designed experimental campaign. These data are supposed not to reflect any other phenomena than the reaction kinetics, i.e., so-called *intrinsic* kinetics are concerned. Additional phenomena, such as transport limitations, phase effects, may occur when extrapolating the intrinsic kinetics towards more realistic, industrial conditions and are typically accounted for *a posteriori* in the model construction via suitable correlations [1]. From the intrinsic kinetics experimental data

complemented with a literature survey, possible reaction mechanism(s) and the corresponding (micro)kinetic model(s) can be constructed. These models contain a variety of unknown parameters. While some of these can potentially be determined from independent characterization measurements, other parameters such as pre-exponential factors and activation energies typically have to be assessed via regression of the kinetic model to the experimental data, see Figure 1. Subsequently, the resulting parameter estimates are evaluated for their physical meaning and statistical significance. Upon a positive evaluation of the parameter estimates and when the kinetic model is both globally significant and capable of describing the experimental data adequately, the procedure is considered to have converged. If not, the model should be refined, which can be achieved via a mere reformulation of the model or, alternatively, may comprise an additional set of experimental measurements, eventually planned via a sequential experimental design, see Figure 1.

With the gradual increase of computational resources over the last decades, kinetic models have gradually become more complex, i.e., ranging from power-law over Langmuir-Hinshelwood/Hougen-Watson to microkinetic models. Also industrially, where rather simple models suffice for process control around a stable operating point, the advantages of such detailed microkinetic models are recognized, e.g., with respect to rational catalyst design and industrial reactor optimization. In order to reduce the number of parameters in microkinetic models, the Single-Event MicroKinetic (SEMK) methodology can be employed [2]. The fundamental character of this methodology makes that the model parameters have a precise physical meaning and, hence, that a distinction can be made between so-called catalyst and kinetic descriptors. Catalyst descriptors are model parameters which are directly related to catalyst properties, e.g., acid strength of the active site, pore volume... Kinetic descriptors are parameters which are directly related to the reaction families and are independent of the catalyst used, e.g., activation energies [3].

As part of the present work, the intrinsic kinetics based methodology implemented in a multi-scale modeling suite was applied successfully to three different, industrially relevant chemical reactions, i.e., *n*-hexane hydroisomerization, ethene oligomerization and xylene isomerization.

## *n*-Hexane hydroisomerization

*n*-Hexane hydroisomerization on Pt/H-ZSM-5 proved to be an excellent case study owing to the limited number of components and reaction steps involved. A good trade-off was found between the physical meaning and statistical significance of the model as a whole and the individual parameter estimates through the use of Langmuir-Hinshelwood/Hougen-Watson (LHHW) type rate equations. Limited deviations between the experimental and simulated outlet molar flow rates could be attributed to internal mass transport effects. It led to the model formally not being adequate, however, for the illustrative purposes of the case study, it would be beyond the scope to actually account for these transport effects in detail. This has been the subject of a separate investigation [4].

## Ethene oligomerization

Next, the methodology has been applied to ethene oligomerization on different heterogeneous, bifunctional catalysts. This reaction has been investigated within the framework of the EU FP7 IP OCMOL, i.e., Oxidative Coupling of Methane followed by Oligomerization to Liquids, which aims at economically exploiting stranded natural gas reserves [5]. Ethene oligomerization is already performed industrially using homogeneous Ni catalysts [6]. Besides the use of ecologically unfriendly solvents, the product distribution cannot be tuned easily with this family of catalysts [7]. The use of heterogeneous catalysts opens up opportunities in this respect and was explored in this work. These heterogeneous catalysts contain a nickel-ion and acid sites. The acid sites are provided by the support, e.g., amorphous SiO<sub>2</sub>-Al<sub>2</sub>O<sub>3</sub> and Beta zeolite. Ethene is not easily protonated under the relative mild reaction conditions applied as relative unstable primary carbenium ions are necessarily involved. Instead, ethene dimerizes on the nickel-ion sites after which the resulting butenes protonate and undergo acid catalyzed alkylation, isomerization and cracking, as illustrated in Figure 2.

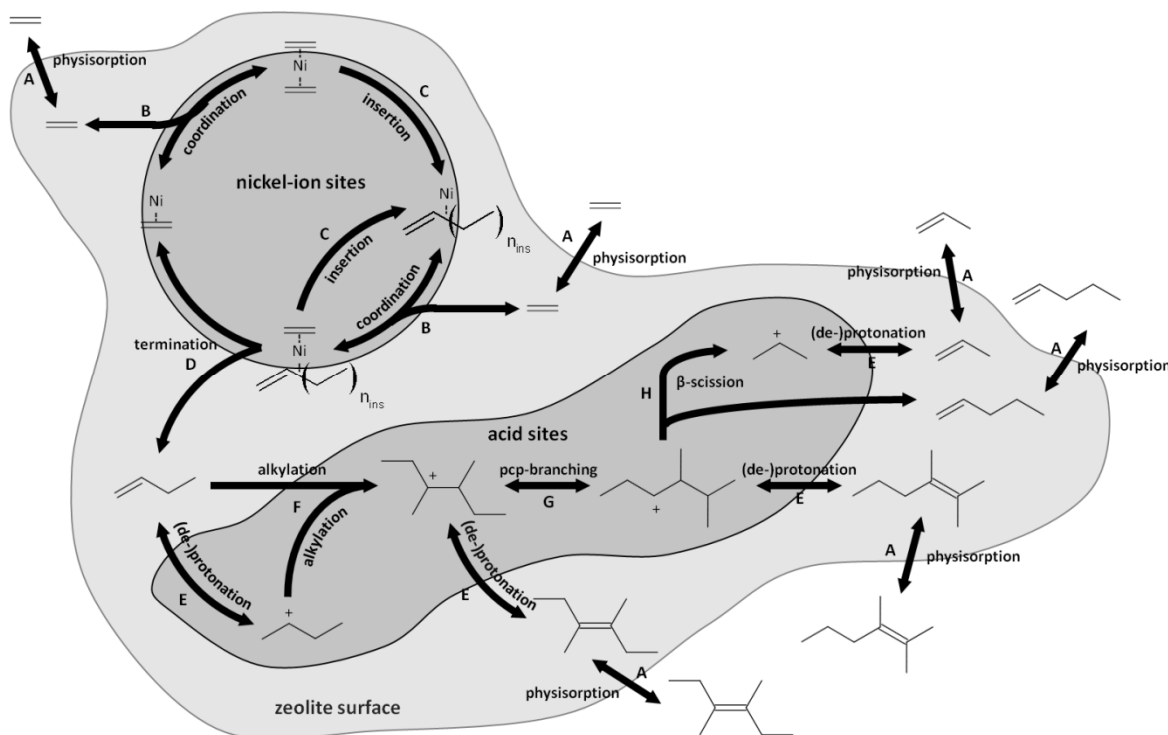


**Figure 2: Schematic representation of the ethene oligomerization reaction network involving Ni-ion oligomerization and acid catalyzed alkylation, isomerization and cracking.**

An experimental campaign was devised in which an intrinsic ethene oligomerization kinetics dataset was acquired on two different catalysts, i.e., an amorphous Ni-SiO<sub>2</sub>-Al<sub>2</sub>O<sub>3</sub> and a Ni-Beta zeolite. The amorphous Ni-SiO<sub>2</sub>-Al<sub>2</sub>O<sub>3</sub> gave rise to an Anderson-Schulz-Flory (ASF) product distribution essentially limited to butenes and hexenes. Additionally, the product distribution was independent of the reaction conditions applied, see Figure 3. Catalyst characterization indicated that only weak acid sites were present on the Ni-SiO<sub>2</sub>-Al<sub>2</sub>O<sub>3</sub>, which were assumed not to be capable of catalyzing reaction steps such as alkylation and cracking. Hence, oligomerization, c.q., dimerization, originated only from reaction on the nickel-ion sites. Based upon the experimental observations, a microkinetic model was constructed inspired by reaction mechanisms described in literature for homogeneous catalysts, i.e., degenerated polymerization and concerted coupling [8, 9]. Although no decisive answer could be given with respect to the actual mechanism occurring on the heterogeneous catalysts, the experimental results tended to favor the degenerated polymerization mechanism due to the temperature independency of the product distribution as well as its ASF character. In order to reduce the number of parameters, the SEMK methodology was employed [2]. The regression of the microkinetic model to the experimental data was successful. The difference in activation energies for chain growth and



termination was about  $10 \text{ kJ mol}^{-1}$  and the pre-exponential factors for both steps are equal which led to a low chain growth probability of 0.1 and the simulated product distributions being practically constant in the investigated temperature range. The model could adequately predict the experimental observations, see Figures 3 and 4.

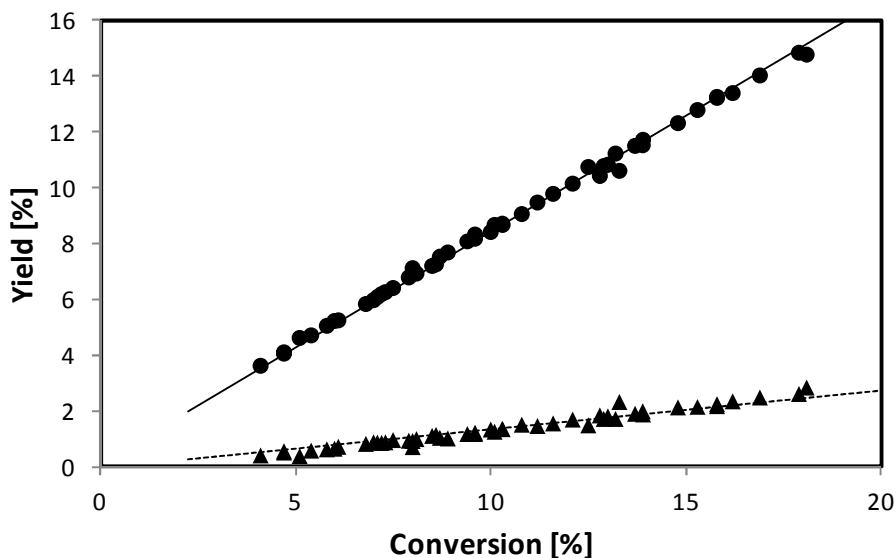


Figure 3: Ethene oligomerization product yields on 1.8wt% Ni-SiO<sub>2</sub>-Al<sub>2</sub>O<sub>3</sub> as function of ethene conversion. Symbols correspond to experimental data, lines correspond to model simulations, i.e., by integration of Eq. 2-21, with the corresponding net rates of formation as given by Eq. 4-27 and the parameter values as reported in Table 4-4; ●, full line: butene; ▲, dashed line: hexene.

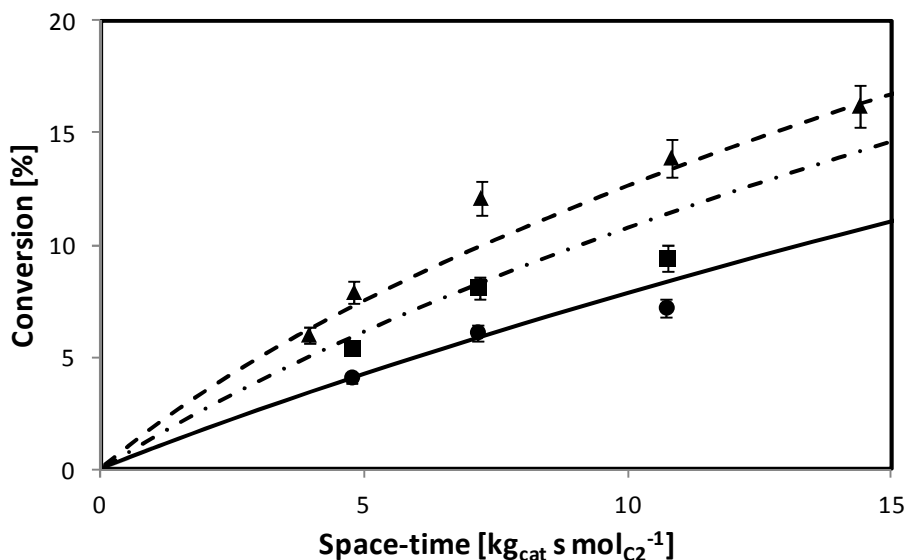
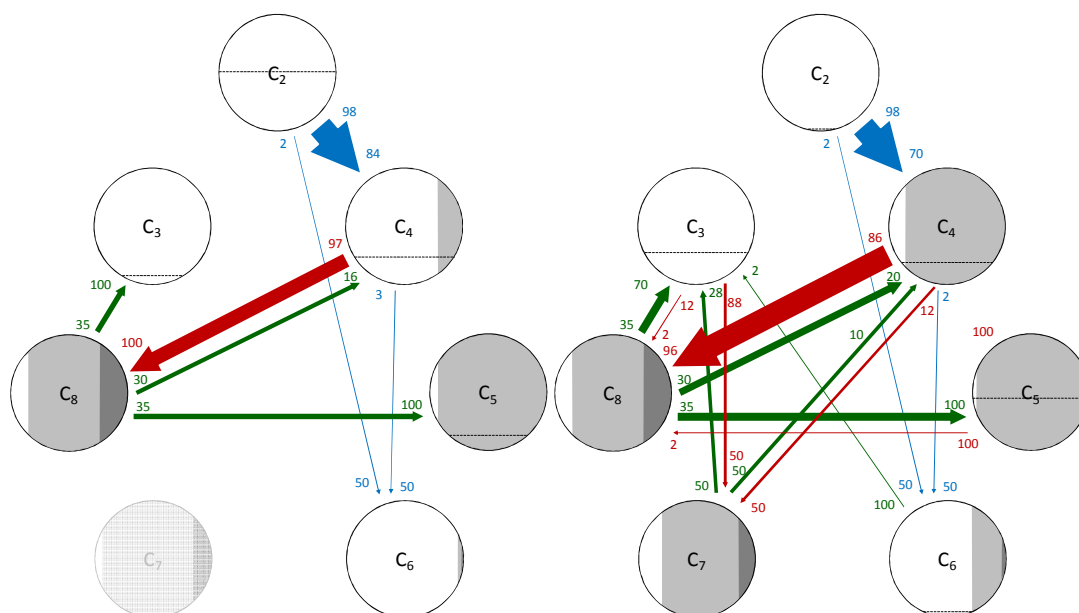


Figure 4: Ethene conversion on 1.8wt% Ni-SiO<sub>2</sub>-Al<sub>2</sub>O<sub>3</sub> as function of space-time at different inlet ethene partial pressures, at 3.5 MPa total pressure and at 473 K. Symbols correspond to experimental data, lines correspond to model simulations, i.e., by integration of Eq. 2-21, with the corresponding net rates of formation as given by Eq. 4-27 and the parameter values as reported in Table 4-4; ●, full line: 0.15 MPa; ■, dash-dotted line: 0.25 MPa; ▲, dashed line: 0.35 MPa.

The data acquired on the Ni-Beta zeolite indicated acid site activity by the production of odd carbon numbered alkenes. The SEMK model was extended with acid catalyzed steps such as (de-)protonation, alkylation, isomerization and cracking, which resulted in more than 20 unknown parameters. However, most of these parameters were kinetic descriptors and could be retrieved from literature or calculated from thermodynamic considerations. Only 2 catalyst descriptors needed to be estimated which resulted in a physically meaningful and statistically significant model and parameters. Based upon this model, a reaction path analysis was performed, vide Figure 5. At low conversion, ethene dimerization on the nickel-ion sites is the dominant pathway, see Figure 5(left). With increasing conversion, the butenes produced are protonated and mainly undergo alkylation towards octene. Octene instantaneously isomerizes and cracks, resulting in a considerable C<sub>3</sub>-C<sub>5</sub> fraction, Figure 5(right).



**Figure 5: Reaction path analysis for ethene oligomerization on Ni-Beta at 503 K, an ethene inlet partial pressure of 1.0 MPa and a conversion of 50% (left) and 99% (right). The model simulations were obtained by integration of Eq. 2-21, with the corresponding net rates of formation, Eq. 5-14 and the parameter values reported in Tables 5-5 and 5-6. The alkenes are lumped per carbon number. The height of the horizontal line in these circle is proportional to the mass fraction of the corresponding alkene lump. If no line is visible it indicates that the corresponding mass fraction is very small, i.e., less than 1%. However, these lump may still significantly contribute to the product formation. Additionally, alkene lumps in watermark indicate that its mass fraction is less than 0.1%. The vertical gray-scale code is used to differentiate between the different structural isomers, i.e., white: linear alkenes, light grey: monobranched alkenes and dark grey: dibranched alkenes. The surface area taken by these colors is proportional to the mass fraction of each structural isomer in the alkene lump. The color of the arrows indicate the reaction family: blue = metal-ion oligomerization, red = acid alkylation, green =  $\beta$ -scission. pcp-branching and alkyl shift are not explicitly shown as they only change the isomer distribution within an alkene lump. The size of the arrow is linearly proportional to the rate of the corresponding step. The numbers at the arrow head indicate the fraction of the lump which is produced via the corresponding step while numbers next to the arrow shaft indicate the fraction of the lump which is consumed via this step.**

Additionally, guidelines were proposed for tuning the catalyst properties in order to maximize the yield toward some valuable product fractions, i.e., 1-alkenes, propene and gasoline. Figure 6 shows the effect of changing acid site concentrations on the product distribution at 50% conversion while maintaining a constant nickel-ion concentration. For a low concentration of acid sites, mostly 1-alkenes are produced originating from oligomerization on the nickel-ion sites. With increasing acid site concentration, the oligomers are isomerized and cracked on the acid sites, leading to a gasoline and propene fraction.

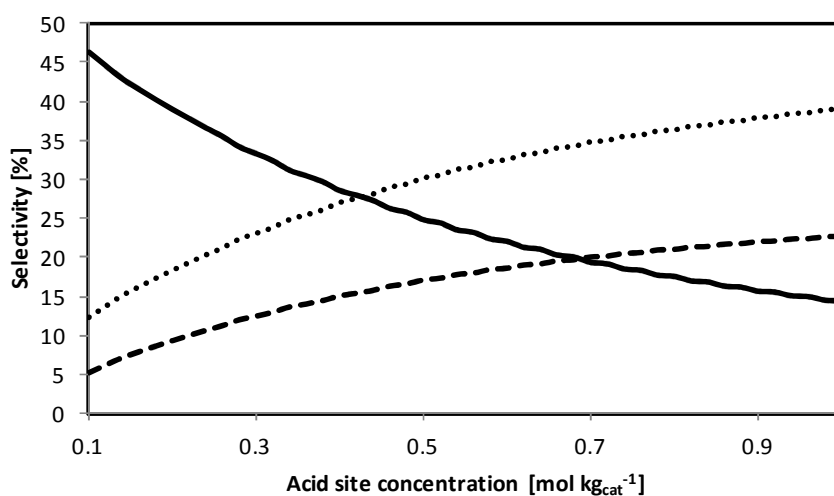


**Figure 6: Selectivity towards linear 1-alkenes (full line), gasoline (dotted line) and propene (dashed line) on Ni-Beta as function of acid site concentration at 50% ethene conversion, 503 K and an ethene inlet partial pressure of 1.0 MPa as obtained by integration of Eq. 2-21, with the corresponding net rates of formation as given by Eq. 5-14 and the parameter values as reported in Tables 5-5 and 5-6.**

Similar effects were observed when increasing the acid strength of the active sites, decreasing the nickel-ion concentration and decreasing the ethene standard coordination enthalpy. The effect of changing the physisorption parameters was also investigated. A too strong physisorption of the heavier components leads to a rapid saturation of the catalyst surface, resulting in a decrease in ethene oligomerization rate.

The SEMK model for ethene oligomerization was also integrated in an industrial reactor model, see Figure 7. The model is capable of describing a multi fixed bed reactor which is operated isothermally, adiabatically or via continuous heat exchange. The pressure drop due to friction in the fixed beds can be determined. Liquid formation due to condensation of heavy oligomers is also incorporated, as well as intra-crystalline transport limitations. The

industrial reactor model was validated with experiments performed by CEPESA (Compañía Española de Petróleos S.A.) using their oligomerization demonstration set-up at more extreme conditions compared to the lab-scale data against which the SEMK model had been regressed. The effect of the heating regime, reactor geometry, liquid formation and intracrystallite diffusion on the observed performance was investigated via model simulations. Based upon the range of operating conditions of the OCMOL process [5], an industrial reactor was designed. Aiming at an annual capacity of 30 kTon ethene and 95% ethene conversion, a reactor with a length and internal diameter of resp. 10 and 1 m is required. Operating the reactor at 573 K and 3.5 MPa using the Ni-Beta catalyst as investigated in this work should lead to a 1-alkene yield of 4%, a propene yield of 30% and a gasoline yield of 40%.

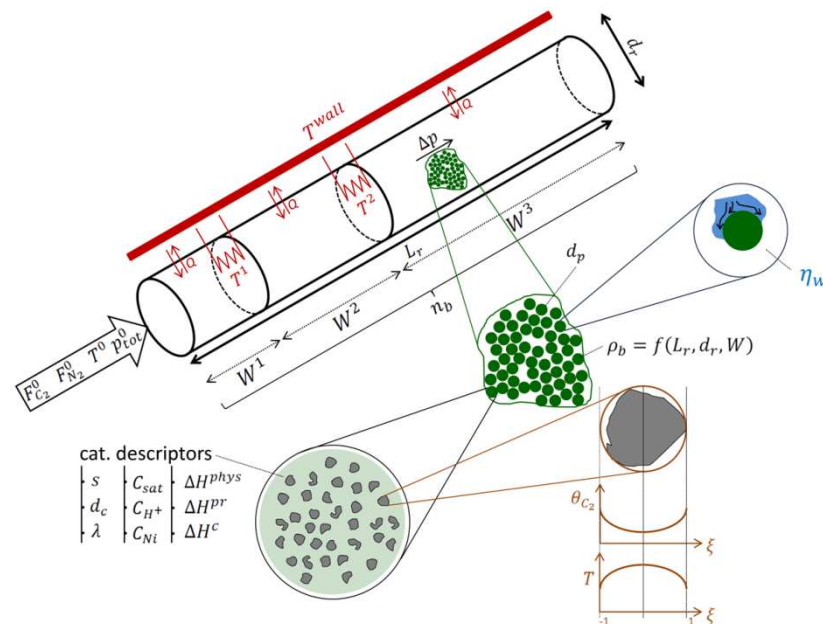
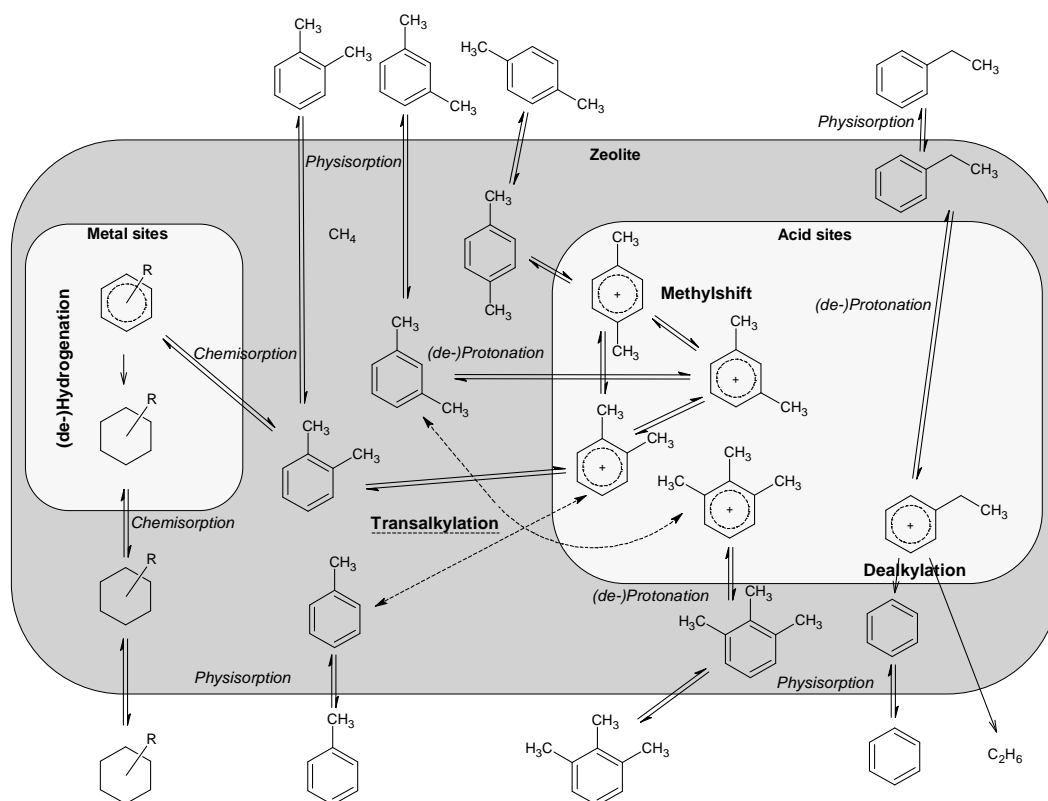


Figure 7: Graphical representation of the industrial reactor model for the heterogeneous, bifunctional catalyzed ethene oligomerization.

## Xylene isomerization

Xylene isomerization is an important reaction in the production of polymers, c.q., polyethylenetereftalate (PET) [10] and is used for increasing the paraxylene content of the xylenes mixture coming from catalytic reforming, gasoil pyrolysis and toluene disproportionation [11]. Typically, a bifunctional catalyst is used for this reaction, e.g., Pt/H-ZSM-5. The acid sites catalyze methylshift, transalkylation and dealkylation, see Figure 8,

while the noble metal decreases coke formation but also hydrogenates a small fraction of the aromatic feed components, see Figure 8.



**Figure 8: Schematic representation of the reaction network for xylene isomerization on a bifunctional catalyst. A gas phase aromatic component can physisorb on the catalyst surface followed by a possible interaction with either acid or metal sites. Depending on the nature of the active site, acid catalyzed isomerization or scission or metal catalyzed hydrogenation occurs. Products formed leave the active sites and desorb from the catalyst surface.**

In order to elucidate and quantify the main reaction pathways, a SEMK model was constructed. A limited, but well-designed experimental dataset on an industrially developed Pt/H-ZSM-5 was provided by Shell for model evaluation through regression. The model could adequately describe the experimental data and was subsequently used to identify the constraints for an optimal Pt/H-ZSM-5 catalyst, as illustrated in Figure 9. It maps the value of a 'profit' function  $\psi$ , defined by valuable product yields and losses, as a function of the standard protonation enthalpy, which is a measure of the average acid strength of the active sites [12]. On a catalyst containing only weak acid sites, corresponding to a standard protonation enthalpy less negative than  $-60 \text{ kJ mol}^{-1}$ , few activity is observed corresponding to a low 'profit'. With increasing acid strength of the active sites, corresponding to standard protonation enthalpies between  $-60$  and  $-80 \text{ kJ mol}^{-1}$ , the profit function increases because the para-xylene and benzene yield increases. With even stronger acid sites, corresponding

to standard protonation enthalpies beyond  $-80$  to  $-85$   $\text{kJ mol}^{-1}$ , xylene is being converted into other aromatic fractions, leading to a decrease of the ‘profit’ function. At even more negative standard protonation enthalpies, below  $-90$   $\text{kJ mol}^{-1}$ , the benzene yield also decreases leading to an even more pronounced decrease of the profit function  $\psi$ . The investigated industrial Pt/H-ZSM-5 catalyst, with an estimated standard protonation enthalpy amounting to  $-86.8$   $\text{kJ mol}^{-1}$  was located very near to the optimal range and, hence, exhibited practically the desired steady-state kinetics behavior.

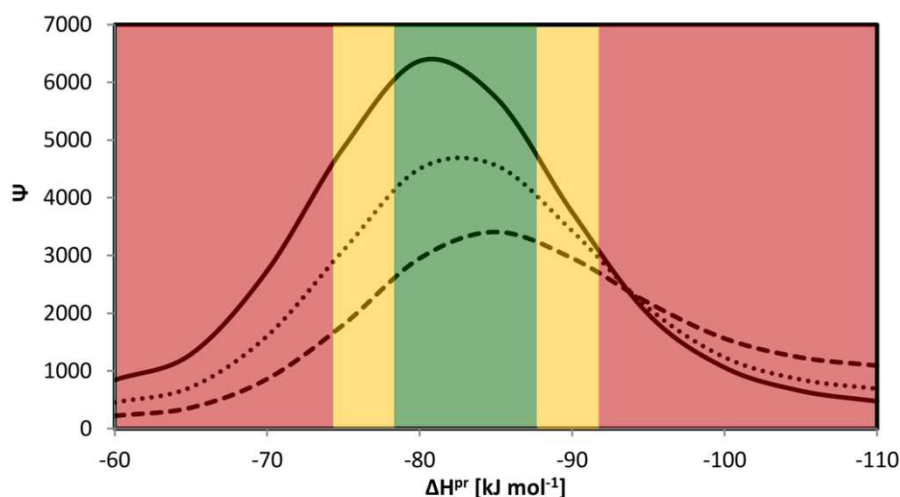


**Figure 9: Simulated profit function as function of protonation enthalpy at the reaction conditions as defined in Table 7-9. Full line: at 673 K and 1.0 MPa; dotted line: at 653 K and 1 MPa; dashed line: 633 K and 1.0 MPa.**

## Conclusions

The developed methodology proved its versatility by successfully modeling three different and industrially relevant reactions. Intrinsic kinetics were used to construct and regress the corresponding kinetic models. In order to reduce the number of adjustable parameters, the SEMK methodology was applied. The resulting (micro)kinetic models had a clear physical meaning and were statistically significant. The SEMK models were used for multi-scale modeling, i.e., rational catalyst design and industrial reactor simulation, which allow a more efficient optimization of the corresponding industrial processes.

## References

- [1] G.F. Froment, K.B. Bischoff, J. De Wilde, Chemical reactor analysis and design, 2010.
- [2] G.F. Froment, Catalysis Today. 52 (1999) 153-163.
- [3] J.W. Thybaut, G.B. Marin, Journal of Catalysis. 308 (2013) 352-362.
- [4] B.D. Vandegheuchte, J.W. Thybaut, G.B. Marin, Ind. Eng. Chem. Res. (2014).

- [5] <http://www.ocmol.eu/>, 2014.
- [6] Ullmann's Encyclopedia of Industrial Chemistry (2014).
- [7] P.T. Anastas, M.M. Kirchhoff, T.C. Williamson, Applied Catalysis a-General. 221 (2001) 3-13.
- [8] C. Lepetit, J.Y. Carriat, C. Bennett, Applied Catalysis a-General. 123 (1995) 289-300.
- [9] S.M. Pillai, M. Ravindranathan, S. Sivaram, Chemical Reviews. 86 (1986) 353-399.
- [10] Ullmann's Encyclopedia of Industrial Chemistry, 6th ed.
- [11] Kirk-Othmer Encyclopaedia of Chemical Technology, 4th ed.
- [12] J.W. Thybaut, G.B. Marin, G.V. Baron, P.A. Jacobs, J.A. Martens, Journal of Catalysis. 202 (2001) 324-339.

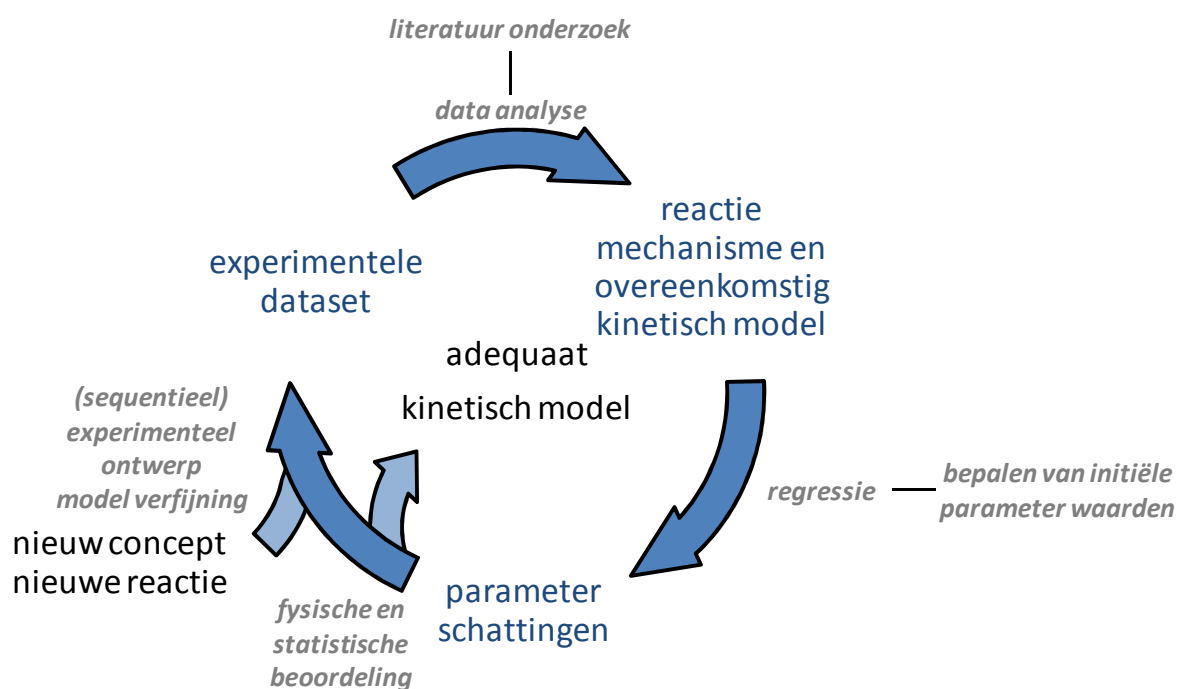




# Samenvatting

---

Kinetische modellen vormen voor chemisch ingenieurs een handig instrument met het oog op procescontrole, opheldering van reactiemechanismen, katalysatorontwerp en optimalisatie van industriële reactoren. De ontwikkeling van een systematische methodologie voor het opstellen van zulke modellen kan een waardevolle troef zijn. Immers, dergelijke modellen verhogen het fundamenteel begrip van de onderliggende chemie in de bestudeerde reacties en bevorderen de communicatie tussen onderzoekers met een industriële en academische achtergrond. In dit werk werd een dergelijke systematische methodologie ontwikkeld.



Figuur 1: Voorgestelde procedure voor kinetisch modelleren

De ontwikkelde methodologie is voorgesteld in Figuur 1. Alhoewel de gebruikte concepten reeds enkele decennia gekend zijn, is de integratie ervan vrij uniek. De methodologie vertrekt van intrinsieke kinetische data verkregen via een goed ontworpen experimentele campagne. Deze data zijn verondersteld bepaald te zijn door geen enkel ander verschijnsel dan de zogenaamde 'intrinsieke' reactiekinetiek zelf. Bijkomende fenomenen zoals

transportoverdracht en fase-effecten kunnen potentieel snelheidslimiterend worden bij extrapolatie naar realistische, industriële condities en worden bij voorkeur *a posteriori* in rekening gebracht via de gepaste correlaties [1]. De intrinsieke kinetische experimentele data, aangevuld met een literatuuronderzoek, leiden typisch tot één of, bij gebrek aan eensgezindheid, tot meerdere mogelijke reactiemechanismen waarvoor overeenkomstige kinetische modellen kunnen worden opgesteld. Deze kinetische modellen bevatten verschillende onbekende parameters. Een aantal van deze parameters worden typisch bepaald aan de hand van onafhankelijke karakteriseringsexperimenten. Voor andere parameters, zoals b.v. de pre-exponentiële factoren, is het mogelijk om, gebaseerd op principiële overwegingen, een grootteorde vast te leggen, terwijl de waarden voor een laatste stel van parameters zoals de activeringsenergieën, worden bepaald met behulp van regressie, zie Figuur 1. Vervolgens worden de verkregen parameters beoordeeld naar hun fysische betekenis en statistische significantie. Na een positieve beoordeling van de individuele parameterschattingen en het globale model, wordt de procedure beschouwd als afgelopen, zeker als het model tevens als adequaat geëvalueerd wordt. In het ander geval moet het kinetische model worden verfijnd. Dit kan aan de hand van een herformulering van het model of via het uitvoeren van een aantal bijkomende experimenten, eventueel via sequentieel experimenteel ontwerp, zie Figuur 1.

Gedurende de laatste decennia zijn de computationele middelen gestaag toegenomen waardoor de kinetische modellen complexer werden. Een duidelijke evolutie van machtswet over Langmuir-Hinshelwood/Hougen-Watson tot microkinetische modellen heeft zich in de loop der jaren voltrokken. Industrieel gezien volstaan eenvoudige modellen voor procescontrole rond een welbepaald, stabiel werkingspunt. Echter, de voordelen van gedetailleerde, microkinetische modellen worden steeds meer duidelijk voor de industrie, met name rationeel katalysatorontwerp en optimalisatie van industriële reactoren. Om het aantal parameters in microkinetische modellen in de hand te houden wordt typisch gebruik gemaakt van de *Single-Event MicroKinetic* (SEMK) methodologie [2]. Het fundamenteel karakter van deze methodologie zorgt ervoor dat de modelparameters een duidelijke fysische betekenis hebben en dat een onderscheid wordt gemaakt tussen zogenaamde kinetische en katalysatordescriptoren. Katalysatordescriptoren zijn modelparameters die in direct verband staan met katalysatoreigenschappen zoals de zuursterkte, porievolume, etc.

Kinetische descriptors zijn modelparameters die specifiek rekening houden met de beschouwde reactiefamilies en die katalysatoronafhankelijk zijn. Vaak zijn activeringsenergieën een voorbeeld van kinetische descriptors [3].

In het kader van dit doctoraat is de methodologie voor de ontwikkeling van modellen voor intrinsieke kinetiek met succes toegepast op drie verschillende en industrieel relevante chemische reacties: *n*-hexaanhydroïsomerasie, etheen oligomerisatie en xyleen isomerisatie. Bovendien werden deze modellen gebaseerd op een intrinsieke kinetiek geïmplementeerd in een multischaalomgeving die katalysatorontwerp en/of reactoroptimalisatie binnen handbereik brachten.

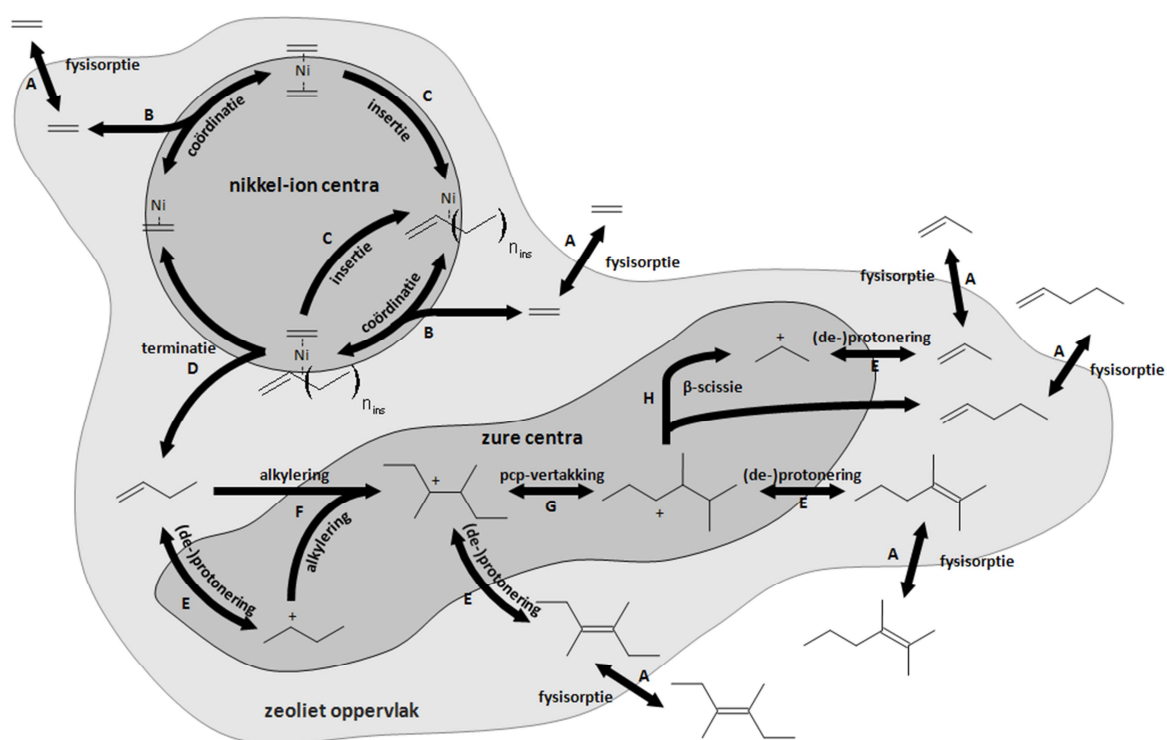
## *n*-Hexaanhydroïsomerasie

*n*-Hexaanhydroïsomerasie op Pt/H-ZSM-5 is gebleken een uitstekende gevalstudie te zijn dankzij het beperkte aantal parameters en reactiestappen. Een goed compromis werd bereikt tussen fysische betekenis en statistische significantie van het globale model en de individuele parameters gebruik makende van Langmuir-Hinshelwood/Hougen-Watson (LHHW) type snelheidsvergelijkingen. Een beperkte afwijking tussen de experimentele en gesimuleerde uitlaat molaire debieten kon worden toegewezen aan interne massatransporeffecten. Formeel leidde dit tot een inadequaat model, maar het gedetailleerd in rekening brengen van deze interne massatransporeffecten overstijgt echter de doelstellingen die met deze gevalstudie beoogd werden en is ondertussen gerapporteerd als een afzonderlijk onderzoek [4].

## Etheenoligomerisatie

Vervolgens is de methodologie toegepast op etheenoligomerisatie op verschillende heterogene, bifunctionele katalysatoren. Deze reactie is onderzocht binnen het kader van het EU-FP7 gefinancierde project OCMOL '*Oxidative Coupling of Methane followed by Oligomerization to Liquids*'. Het OCMOL-project is gericht op het economisch exploiteren van 'gestrande' gasreserves [5]. Etheenoligomerisatie wordt reeds industrieel toegepast met behulp van homogene Ni katalysatoren [6]. Naast het gebruik van milieuvriendelijke solventen kan de productdistributie in een dergelijke, homogene procesuitvoering maar

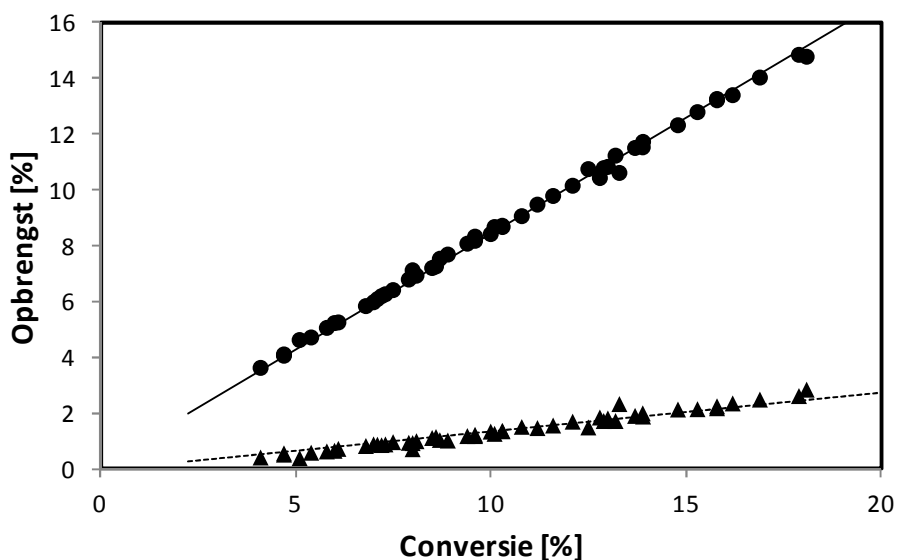
moelijk worden bijgesteld [7]. Het gebruik van heterogene katalysatoren opent veelbelovende perspectieven in dit verband en is onderzocht in dit werk. Deze heterogene katalysatoren bevatten zowel nickel-ion als zure centra. De zure centra zijn afkomstig van de drager, b.v., amorf  $\text{SiO}_2\text{-Al}_2\text{O}_3$  en Beta zeoliet. Etheen wordt maar moeilijk geprotoneerd bij de relatief milde reactiecondities omdat het aanleiding geeft tot relatief onstabiele, primaire carbeniumionen. In plaats daarvan dimeriseert etheen op de nickel-ion centra waarna de geproduceerde butenen protoneren en reacties ondergaan op de zure centra zoals alkylering, isomerisatie en kalking, zie Figuur 2.



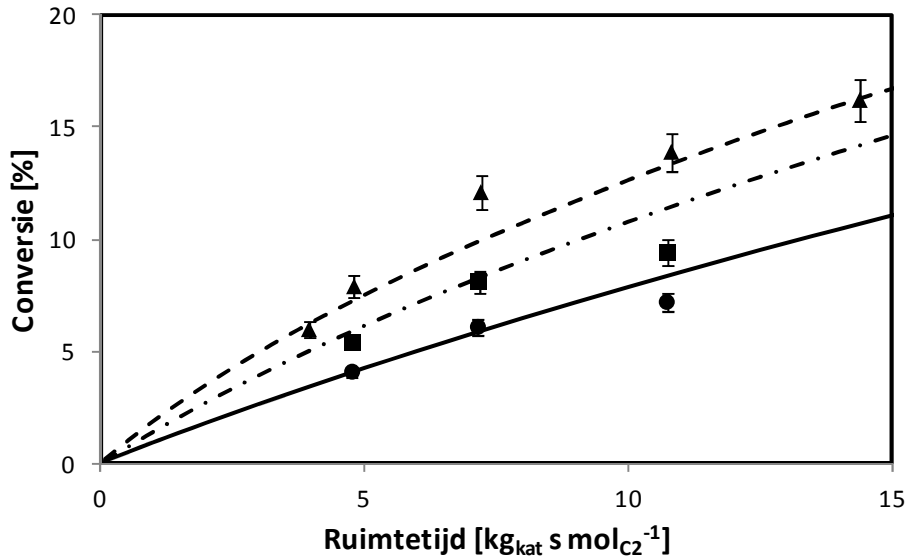
**Figuur 2: Schematische voorstelling van het reactienetwerk voor etheenoligomerisatie via Ni-ion oligomerisatie en alkylering, isomerisatie en kalking gekatalyseerd door de zure centra.**

Een experimentele campagne werd uitgevoerd om een intrinsiek kinetische dataset te verwerven op twee verschillende katalysatoren, nl., een amorf  $\text{Ni-SiO}_2\text{-Al}_2\text{O}_3$  en een Ni-Beta zeoliet. De amorf  $\text{Ni-SiO}_2\text{-Al}_2\text{O}_3$  leidde tot een Anderson-Schulz-Flory (ASF) productdistributie, vooral bestaande uit buteen en hexeen. De productdistributie was bovendien onafhankelijk van de gebruikte reactiecondities, zie Figuur 3. Katalysator karakterisering toonde aan dat de zure centra op amorf  $\text{Ni-SiO}_2\text{-Al}_2\text{O}_3$  zwak van aard waren en dus niet in staat om reactiestappen zoals alkylering en kalking te katalyseren. Dit betekende dat oligomerisatie, in dit geval vooral dimerisatie, alleen werd veroorzaakt

door de nickel-ion centra. Gebaseerd op de experimentele waarnemingen werd een microkinetisch model opgesteld, geïnspireerd op reactiemechanismen voor homogene katalyse zoals beschreven in de literatuur, nl., degeneratieve polymerisatie en gecoördineerde koppeling [8, 9]. Er kon geen uitsluitsel worden gegeven over welk mechanisme effectief doorging op de heterogene katalysatoren. Echter, de temperatuursonafhankelijkheid van de productdistributie en het ASF karakter ervan zorgden voor een voorkeur voor het degeneratievepolymerisatiemechanisme. Om het aantal parameters te beperken werd de SEMK methodologie toegepast. De regressie van het kinetisch model aan de experimentele data kende een positieve uitkomst. Het verschil in activeringsenergieën voor ketengroei en terminatie was beperkt tot  $10 \text{ kJ mol}^{-1}$  en de pre-exponentiële factoren voor beide stappen waren identiek. Dit leidde tot een lage ketengroeiopprobabiliteit en gesimuleerde productdistributies die onafhankelijk waren in het beschouwde temperatuursgebied. Het model was in staat om de experimentele waarnemingen adequaat te voorspellen, zie Figuren 3 en 4.

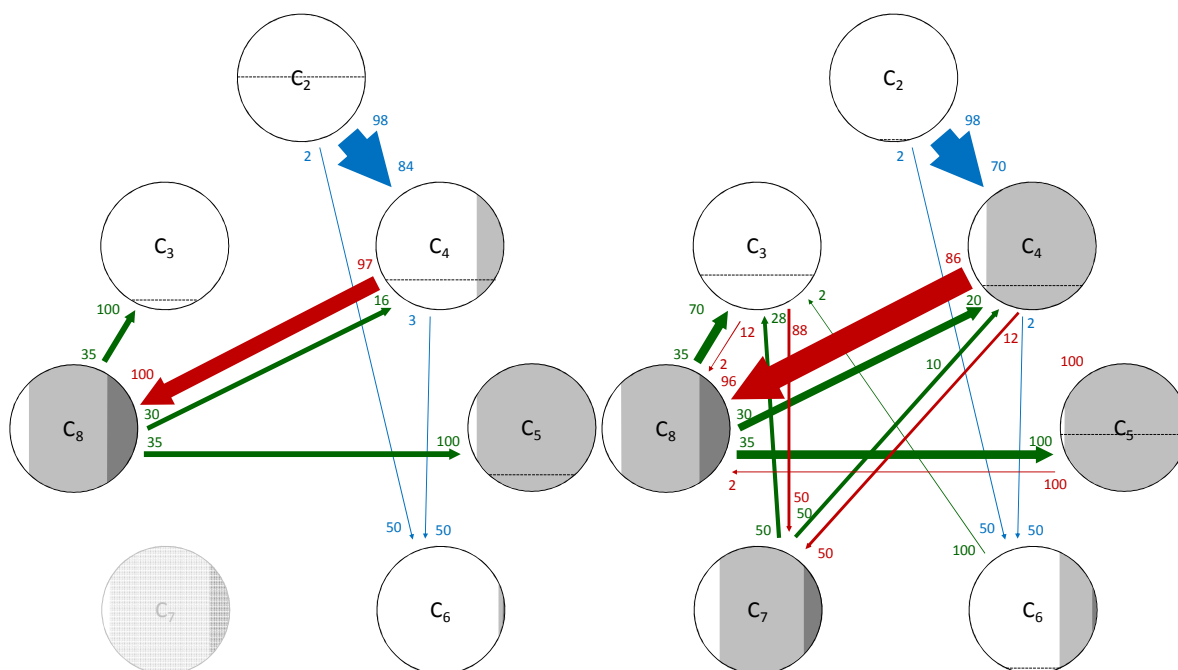


Figuur 3: Productopbrengsten van etheenoligomerisatie op 1.8m% Ni-SiO<sub>2</sub>-Al<sub>2</sub>O<sub>3</sub> als functie van de etheenconversie. Symbolen stemmen overeen met experimentele data, lijnen met modelsimulaties, nl., via integratie van vgl. 2-21 waarin de netto-vormingssnelheden gegeven zijn door vgl. 4-27 met de parameterwaarden zoals in Tabel 4-4; ●, volle lijn: buteen; ▲, onderbroken lijn: hexeen.



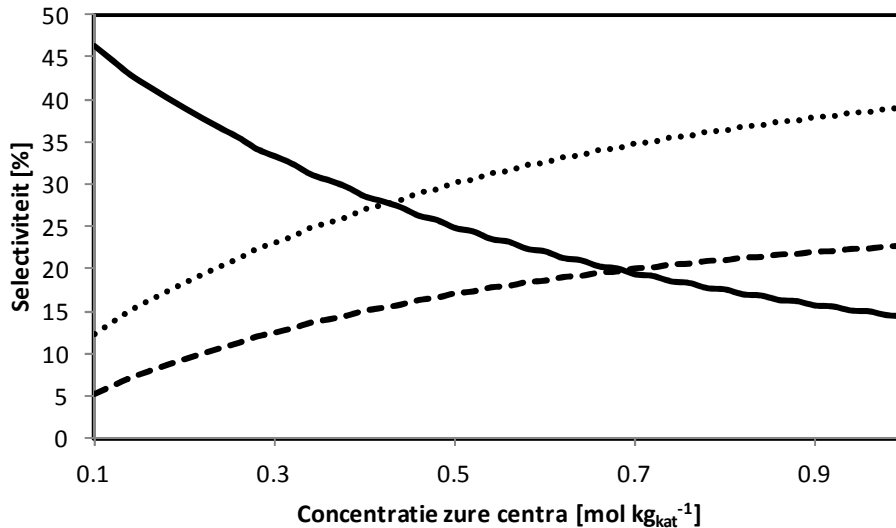
**Figuur 4:** Etheen conversie door etheenoligomerisatie op 1.8m% Ni-SiO<sub>2</sub>-Al<sub>2</sub>O<sub>3</sub> als functie van de ruimtetijd bij verschillende inlaat etheen partiële drukkens, bij een totale druk van 3.5 MPa en 473 K. Symbolen stemmen overeen met experimentele data, lijnen met modelsimulaties, nl., via integratie van vgl. 2-21 waarin de netto-vormingssnelheden gegeven zijn door vgl. 4-27 met de parameterwaarden zoals in Tabel 4-4; ●, volle lijn: 0.15 MPa; ■, onderbroken-stippel lijn: 0.25 MPa; ▲, onderbroken lijn: 0.35 MPa.

De Ni-Beta zeoliet vertoonde activiteit van de zure centra door de productie van alkenen met een oneven koolstofgetal, zelfs al waren de corresponderende opbrengsten eerder gering. Het SEMK model werd uitgebreid met elementaire stappen zoals (de-)protonering, alkylering, isomerisatie en kalking, gekatalyseerd door zure centra. Dit resulteerde in meer dan 20 onbekende parameters. Het gros van deze parameters waren kinetische descriptoren waarvoor equivalente waarden konden gevonden worden in de literatuur of die konden worden berekend aan de hand van thermodynamische overwegingen. Slechts 2 katalysatordescriptoren moesten nog geschat m.b.v. modelregressie en dit resulteerde in fysische betekenisvolle en statistisch significante parameters en model. Gebaseerd op dit model werd een reactiepad analyse uitgevoerd, zie Figuur 5. Bij lage conversie wordt het reactienetwerk gedomineerd door etheen dimerisatie op de nickel-ion centra, zie Figuur 5 (links). Met toenemende conversie protoneren de geproduceerde butenen, hetgeen leidt tot alkyleringsreacties en de vorming van octeen. Octeen isomeriseert vervolgens snel gevolgd door kalking, resulterend in een aanzienlijke C<sub>3</sub>-C<sub>5</sub> fractie, zie Figuur 5 (rechts).



**Figuur 5: Reactiepadanalyse van etheenoligomerisatie op Ni-Beta bij 503 K, een inlaat etheenpartieeldruk van 1.0 MPa en een conversie van 50% (links) en 99% (rechts). De modelsimulaties zijn verkregen via integratie van vgl. 2-21 waarin de netto-vormingssnelheden gegeven zijn door vgl. 5-15 met de parameterwaarden zoals in Tabellen 5-5 en 5-6. De alkenen zijn gegroepeerd per koolstofgetal. De hoogte van de horizontale lijn in de cirkels is proportioneel met de massafractie van de overeenkomstige alkeengroep. Als de horizontale lijn niet zichtbaar is, is de massafractie van de overeenkomstige alkeen groep kleiner dan 1%. Echter, deze groepen kunnen wel significant bijdragen tot de vorming van andere producten. Bovendien worden de alkeengroepen die een massafractie hebben van minder dan 0.1% weergegeven in watermerk. De verticale grijswaardeschaal differentieert tussen de verschillende structurele isomeren, nl., wit: lineaire alkenen, lichtgrijs: mono-vertakte alkenen, donkergrijs: di-vertakte alkenen. De oppervlakte ingenomen door deze kleuren is proportioneel met de massafractie van elk structurele isomeer in de alkeengroep. De kleur van een pijl duidt de reactie familie aan: blauw = metaal-ion gekatalyseerde oligomerisatie, rood = alkylering gekatalyseerd door een zuur centrum, groen =  $\beta$ -scissie. PCP-vertakkingen en alkylverschuivingen zijn niet expliciet weergegeven omdat deze enkel de verdeling van de structurele isomeren beïnvloeden binnen eenzelfde alkeengroep. De grootte van een pijl is proportioneel met de snelheid van de overeenkomstige stap. Het getal aan de pijlpunt duidt de fractie van de groep aan die wordt geproduceerd via de overeenkomstige stap. Het getal aan de pijlstaart duidt de fractie van de groep aan die verdwijnt via de overeenkomstige stap.**

Gebaseerd op deze reactiepad analyse, zijn richtlijnen voorgesteld om de katalysatoreigenschappen aan te passen om de opbrengst naar bepaalde, waardevolle productfracties te maximaliseren, b.v., 1-alkenen, propaan en benzine. Figuur 6 toont het effect van de verandering van de concentratie aan zure centra op de productdistributie bij 50% conversie bij eenzelfde nickel-ion concentratie. Bij een lage concentratie aan zure centra worden vooral 1-alkenen geproduceerd via oligomerisatie op de nickel-ion centra. Met toenemende concentratie aan zure centra worden de gevormde oligomeren meer geïsoomiseerd en gekraakt op de zure centra wat leidt tot een toename van de benzine en propaanfractie.



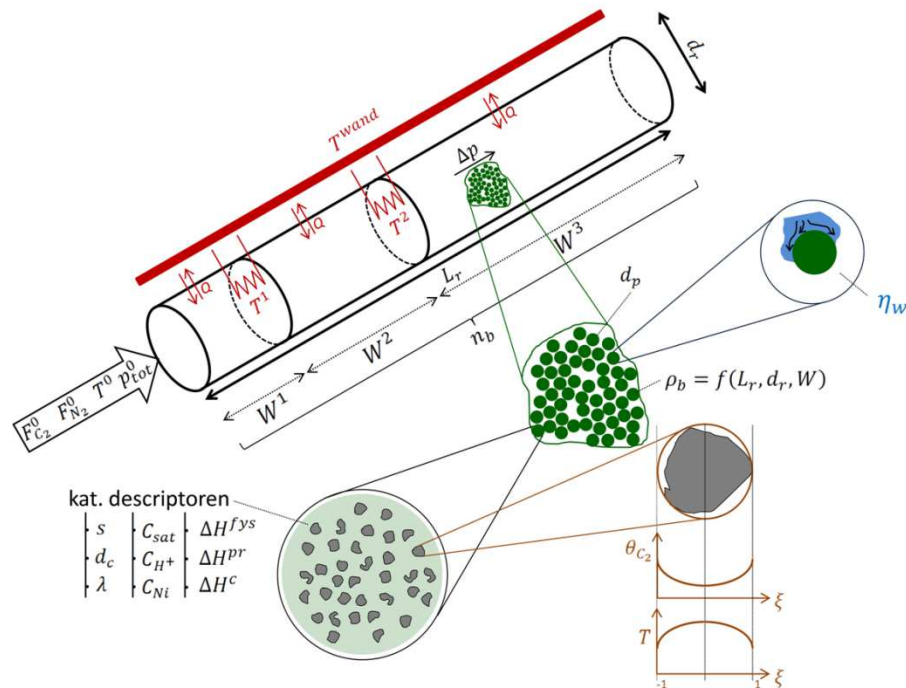
**Figuur 6:** Selectiviteit naar 1-alkenen (volle lijn), benzine (stippellijn) en propeen (gestreepte lijn) op Ni-Beta als functie van de concentratie aan zure centra bij 50% etheenconversie, 503 K en een inlaat etheenpartieeldruk van 1.0 MPa. De resultaten zijn verkregen door integratie van vgl. 2-21 waarin de netto-vormingssnelheden gegeven zijn door vgl. 5-15 met de parameter waarden zoals in Tabellen 5-5 en 5-6.

Gelijkaardige effecten werden waargenomen bij stijgende zuursterkte, dalende concentratie aan nickel-ion centra en dalende etheen standaard coördinatie enthalpie. Het effect van een verandering in fysisorptieparameters werd ook onderzocht. Een te sterke fysisorptie van de zwaardere componenten leidt tot een snelle saturatie van het katalysatoroppervlak en een daling van de etheenoligomerisatiesnelheid.

Het SEMK-model voor etheenoligomerisatie is tevens geïntegreerd in een multi-schaalmodel voor een industriële reactor, zie Figuur 7. Dit model is in staat om een multi-vastbedreactor te beschrijven die zowel isotherm, adiabatisch en via warmte-uitwisseling kan worden bedreven. De drukval als gevolg van wrijving met het vast bed kan worden bepaald. Vloeistofvorming door condensatie van zware oligomeren is eveneens opgenomen, net als intrakristallijne transportlimitaties. Het industriële reactor model is gevalideerd a.h.v. een stel experimenten uitgevoerd door CEPESA (Compañía Española de Petróleos S.A.) gebruikmakende van hun oligomerisatie demonstratie-eenheid. Deze testen werden uitgevoerd bij meer extreme reactiecondities dan toegepast bij de acquisitie van de laboschaaldata gebruikt voor het opstellen van het intrinsiek kinetische model. Het effect van het verwarmingsregime, de reactorgeometrie, vloeistofvorming en intrakristallijne diffusie op de waargenomen performantie is onderzocht a.h.v. modelsimulaties. Een industriële reactor is ontworpen gebaseerd op het bereik van reactiecondities voor het



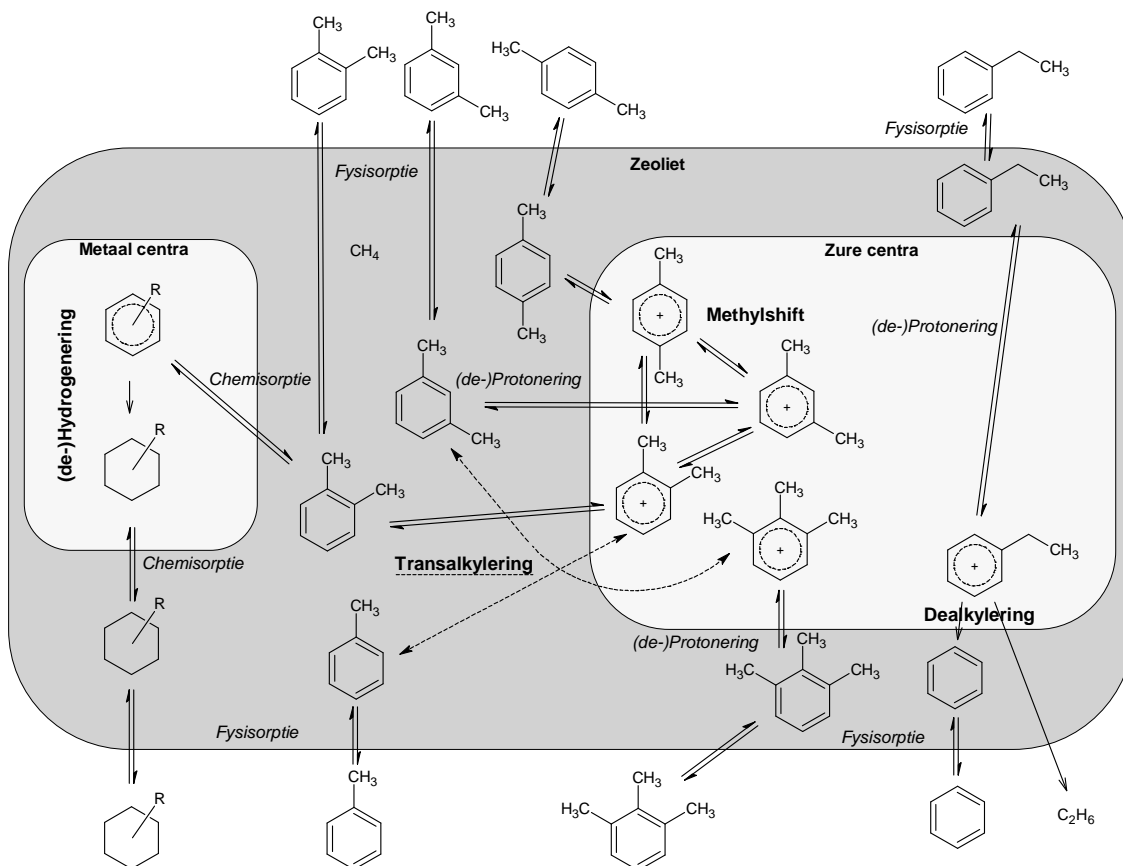
OCMOL proces [5]. Een jaarlijkse capaciteit van 30 kTon etheen en een conversie van 95% werden voorgesteld als ontwerpparameters. Dit leidde tot een reactor van ca. 10 m lang en 1 m in diameter. Indien de reactor adiabatisch wordt bedreven met inlaattemperatuur en etheendruk van respectievelijk 573 K en 3.5 MPa met de Ni-Beta zeoliet, wordt een 1-alkeen opbrengst verkregen van 4%. Voor propaan en benzine bedraagt dit resp. 30% en 40%.



Figuur 7: Grafische voorstelling van het industriële reactormodel voor de heterogeen, bifunctioneel gekatalyseerde etheen oligomerisatie.

## Xyleenisomerisatie

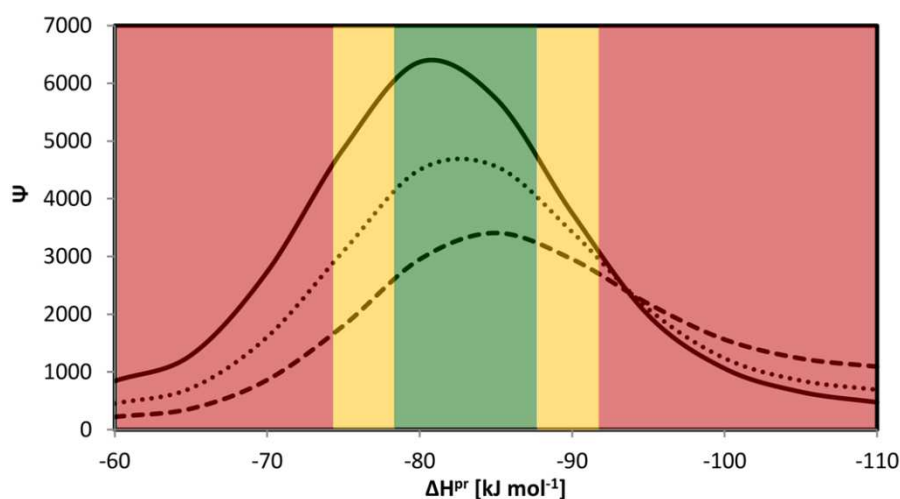
Xyleenisomerisatie is een belangrijke reactie voor de productie van monomeren die gebruikt worden voor een belangrijk polymeer, nl., polyethyleentereftalaat (PET) [10]. Xyleenisomerisatie en wordt ingezet om de paraxyleenhoeveelheid te verhogen in xyleen mengsels komende van katalytisch reformen, pyrolyse van gasolie en toluen disproportionering [11]. Typisch wordt een bifunctionele katalysator gebruikt voor deze reactie, b.v., Pt/H-ZSM-5. De zure centra katalyseren methylverschuivingen, transalkylerings- en dealkyleringsreacties, zie Figuur 8. Het edelmetaal, in dit geval Pt, vermindert de cokesvorming maar leidt tevens tot de hydrogenering van een kleine fractie aan aromaten, zie Figuur 8.



**Figuur 8: Schematische voorstelling van het reactienetwerk voor xyleenisomerisatie op een bifunctionele katalysator. Een gasfasecomponent kan fysisorberen op het katalysatoroppervlak, gevolgd door een mogelijke interactie met ofwel de zure als metallische centra. Afhankelijk van het type actief centrum, ondergaat de component isomerisatie of scissie op de zure centra of hydrogenering op de metallische centra. De gevormde producten verlaten de actieve centra en desorberen van het katalysatoroppervlak.**

Om de voornaamste reactiepaden te bepalen, is een SEMK model opgesteld. Een beperkte, maar goed ontworpen experimentele dataset op een industriële Pt/H-ZSM-5 was door Shell aangereikt en werd gebruikt voor modelevaluatie en -regressie. Het resulterende model kon de experimentele data adequaat beschrijven en werd vervolgens gebruikt om optimale Pt/H-ZSM-5 eigenschappen te bepalen, zie Figuur 9. Figuur 9 toont de waarde van een 'opbrengst'functie  $\psi$  als functie van de standaard protoneringsenthalpie. Deze standaard protoneringsenthalpie is een maat voor de gemiddelde zuursterkte van de actieve centra [12]. De 'opbrengst'functie is gedefinieerd a.h.v. opbrengst en verlies van waardevolle producten. Op een katalysator met zwak zure centra, overeenkomstig met een standaard protoneringsenthalpie lager dan  $-60 \text{ kJ mol}^{-1}$ , wordt er slechts weinig activiteit waargenomen, wat overeenkomt met een lage 'opbrengst'. Met toenemende zuursterkte van de actieve centra, d.i. tussen  $-60$  en  $-80 \text{ kJ mol}^{-1}$ , neemt de 'opbrengst'functie toe door een toenemende opbrengst aan paraxyleen en benzeen. Met nog sterkere zure centra, nl.,

tussen  $-80$  en  $-85$   $\text{kJ mol}^{-1}$ , wordt xyleen omgezet naar andere aromaten. Dit resulteert in een daling van de 'opbrengst'functie. Bij een nog meer negatieve standaard protoneringsenthalpie, nl., lager dan  $-90$   $\text{kJ mol}^{-1}$ , daalt eveneens de opbrengst van benzeen. Dit leidt tot een verdere daling van de 'opbrengst'functie  $\psi$ . De geschatte standaard protoneringsenthalpie van de industrieel gebruikte Pt/H-ZSM-5 katalysator bedroeg  $-86.8$   $\text{kJ mol}^{-1}$ , hetgeen heel nauw aansluit bij het bepaalde, optimale bereik.



**Figuur 9:** Gesimuleerde 'opbrengst' als functie van de standaard protoneringsenthalpie bij de reactiecondities gegeven in Tabel 7-9. Volle lijn: bij 673 K en 1.0 MPa; stippellijn: bij 653 K en 1.0 MPa; onderbroken lijn: bij 633 K en 1.0 MPa.

## Besluit

De ontwikkelde methodologie voor het opstellen van modellen voor een intrinsieke kinetiek heeft zijn veelzijdigheid aangetoond a.h.v. verschillende, industrieel relevante reacties. Hierbij moest telkens slechts een minimum aan modelparameters bepaald worden via regressie aan een experimentele dataset, onder meer dankzij het gebruik van de SEMK methodologie. De resulterende (micro)kinetische modellen hadden een duidelijke fysische betekenis en waren statistisch significant. De SEMK modellen werden ingezet voor multischaalmodellering: rationeel katalysatorontwerp en de simulatie van industriële reactoren. Dit laat toe om de overeenkomstige industriële processen op een meer efficiënte manier te optimaliseren.

## Referenties

- [1] G.F. Froment, K.B. Bischoff, J. De Wilde, Chemical reactor analysis and design, 2010.
- [2] G.F. Froment, Catalysis Today. 52 (1999) 153-163.
- [3] J.W. Thybaut, G.B. Marin, Journal of Catalysis. 308 (2013) 352-362.

- [4] B.D. Vandegehuchte, J.W. Thybaut, G.B. Marin, *Ind. Eng. Chem. Res.* (2014).
- [5] <http://www.ocmol.eu/>, 2014.
- [6] *Ullmann's Encyclopedia of Industrial Chemistry* (2014).
- [7] P.T. Anastas, M.M. Kirchoff, T.C. Williamson, *Applied Catalysis a-General*. 221 (2001) 3-13.
- [8] C. Lepetit, J.Y. Carriat, C. Bennett, *Applied Catalysis a-General*. 123 (1995) 289-300.
- [9] S.M. Pillai, M. Ravindranathan, S. Sivaram, *Chemical Reviews*. 86 (1986) 353-399.
- [10] *Ullmann's Encyclopedia of Industrial Chemistry*, 6th ed.
- [11] *Kirk-Othmer Encyclopediae of Chemical Technology*, 4th ed.
- [12] J.W. Thybaut, G.B. Marin, G.V. Baron, P.A. Jacobs, J.A. Martens, *Journal of Catalysis*. 202 (2001) 324-339.

# Chapter 1

## Introduction

---

Among other aspects, chemical reaction and reactor engineering focuses on the development of comprehensive models, accounting for net production rates based on intrinsic chemical kinetics as well as for transport phenomena at the catalyst pellet and the reactor scale [1, 2]. Reactor integration into an overall plant and the corresponding optimization heavily rely on adequate reactor and kinetic models which should, hence, be an essential element in the toolbox mastered by chemical engineers. It offers strategic advantages for engineers to adopt a systematic methodology when constructing such a model. This leads to an increased understanding of the occurring phenomena and facilitates academic and industrial communication between researchers in a similar field. Such a systematic methodology is proposed in this work, which is aimed at acquiring adequate kinetic models with a sound physical meaning and a justifiable statistical significance starting from intrinsic kinetic data.

### 1.1 Multi-scale modeling

At the Laboratory of Chemical Technology at Ghent University, chemical engineering is approached in a multi-scale ideology as depicted in Figure 1-1. As can be seen in Figure 1-1, kinetics are situated centrally between the fundamental phenomena occurring at the catalyst scale and the applied phenomena at the reactor scale. In order to elucidate the underlying reaction mechanisms and design corresponding industrial reactors, an adequate mathematical representation of the occurring chemical kinetics is necessary. Several types of kinetic models can be considered, i.e., power laws, Langmuir-Hinshelwood/Hougen-Watson (*LHHW*), Eley-Rideal, Mars-van Krevelen, lumped models and detailed mechanistic models... [3]. The order in which they are presented corresponds with increasing level of detail and complexity in the model as well as of CPU time needed when performing the model simulations. While for industrial process simulations, 'easy-to-use' models such as

power laws and even *LHHW* models are preferred because of their simplicity and the adequacy of interpolation in the range of experimental conditions for which they have been constructed, academics tend to choose for the other side of the spectrum aiming at a detailed understanding of the occurring phenomena.

With increasing computational resources, detailed mechanistic and microkinetic models are being noticed by industry. The construction of such microkinetic models does require more effort but allows the user for safe extrapolation, even relative far from the range of reaction conditions in which the experimental campaign was performed. Additionally, the parameters may have clear physical meaning and can be considered as catalyst and kinetic descriptors which can be regarded as properties of resp. the catalyst used and the reactions occurring. If so, guidelines might be proposed for model based catalyst design and optimization, see section 1.2.

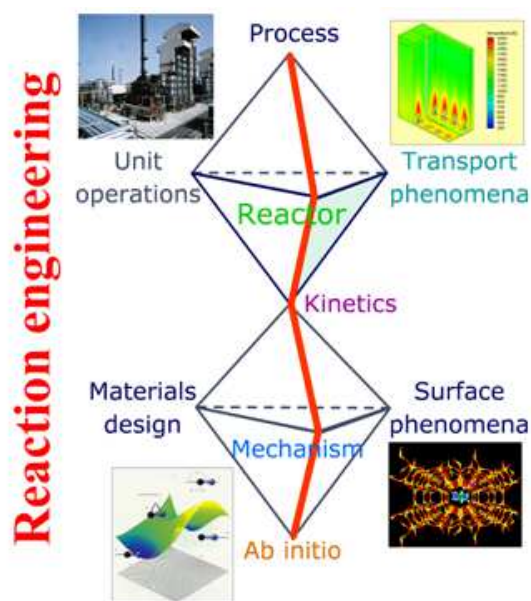


**Figure 1-1: Multi-scale approach of reaction engineering as envisioned by the Laboratory of Chemical Technology, Ghent University [4].**

This work is focused on establishing a systematic methodology for the kinetic modeling of complex chemical reactions while pursuing a trade-off between ‘industrial efficiency’ and ‘academic elucidation’. Within this methodology, the kinetic information is retrieved via so-called intrinsic kinetic data. The acquisition of such data occurs in the absence of transport limitations, such as of mass and heat. Specific attention should be paid to this intrinsic kinetic character of the data when an experimental campaign is designed [5], since

transport limitations may conceal and bias the experimental observations. The modeling of transport limited data relies on more complex expressions and, more importantly, requires additional model parameters which enhance the degrees of freedom of the model and, hence, potentially jeopardize the sound statistical and physical meaning of the final parameter estimates. For industrial reactor modeling purposes, the required transport phenomena are typically accounted for via the proper correlations [1].

In order to obtain a kinetic model with both a sound statistical and physical interpretation, simple power law and even *LHHW* kinetics tend to be insufficient. Microkinetic models, which meet these requirements, often contain a gargantuan amount of components, intermediates and elementary steps, which allows for rational catalyst design. However, this requires more computational effort to determine the unknown kinetic and catalyst descriptors. In this work, in order to decrease the computational effort needed to solve these microkinetic models, the Single-Event MicroKinetic (SEMK) methodology has been applied, see section 1.2. As will be clear from this work, such a microkinetic approach could yield adequate kinetic models with a clear physiochemical meaning, allowing for optimization at smaller and larger scale, i.e., resp. catalyst and reactor scale. The systematic methodology developed in this work and the following multi scale modeling and optimization will be illustrated with several industrially relevant reactions used for the production of chemicals and fuels employing bifunctional catalysts such as *n*-hexane hydrocracking, see section 1.4.1 and chapter 3, ethene oligomerization, see section 1.4.2 and chapters 4, 5 and 6, and xylene isomerization, see section 1.4.3 and chapter 7.

## 1.2 Single-Event MicroKinetic modeling

The *SEMK* methodology is ideally suited for the detailed kinetic modelling of reactions in complex mixtures [6]. Rather than lumping species into pseudo components, reaction families are defined to reduce the number of model parameters. Per reaction family a unique rate coefficient denoted as “single-event” rate coefficient, is defined. To calculate the actual rate coefficient of an elementary step, the single-event rate coefficient is multiplied with the number of single events. The latter accounts for the number of indistinguishable manners in which an elementary step can occur and depends on the structural differences between the reactants and the transition state. This methodology is

already applied successfully to acid, metal and bifunctional catalyzed reactions, i.e., hydroconversion [7, 8], alkylation [9], catalytic cracking [10], catalytic reforming [11], methanol to olefins [12, 13], Fischer-Tropsch synthesis [14], hydrogenation of aromatics [15] and xylene isomerization [16]. Within such SEMK models, a distinction is made between kinetic and catalyst descriptors, the former are reaction specific and catalyst independent, e.g., activation energies and pre-exponential factors while the latter take into account the effect of the catalyst properties, e.g., acid site strength through the protonation enthalpy, while the former are reaction specific and catalyst independent, e.g., activation energies and pre-exponential factors. When both types of model parameters have been quantified, an optimal catalyst can be designed by the optimization of a cost function, e.g., defined by the product yield, within a specified range of operating conditions, as a function of the catalyst descriptors [16, 17], hence, bringing model based catalyst design within reach, see section 1.2.

### 1.3 Model Based Catalyst Design

A schematic overview of model based catalyst design is given in Figure 1-2. Traditionally, an optimal catalyst is being identified via a number of iterations between the synthesis of consecutive generations in a catalyst library and the analysis of the performance testing results in the corresponding activity library, see the forward and reverse arrow of step 2 in Figure 1-2. Model based catalyst design quantifies the information contained in the activity library through the kinetic and catalyst descriptors in the adequate microkinetic models that are constructed. By '*in-silico*' determination of optimal catalyst descriptor values, see section 1.2 and step 4 in Figure 1-2, guidelines are proposed for synthesizing a new generation catalyst library. As such, model based catalyst design allows a more rational approach in catalyst design and optimization.



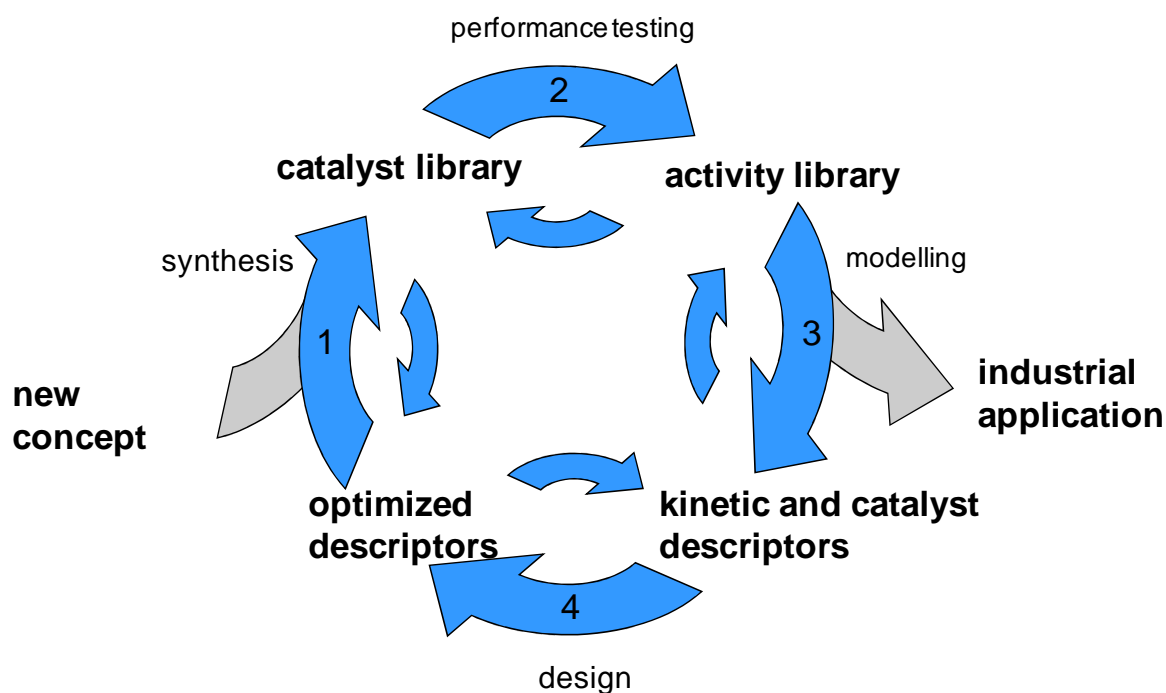


Figure 1-2: Model based catalyst design [17]

## 1.4 Introduction to the chemical reactions used for Model Based Catalyst Design and multi-scale modeling

In total, three relevant industrial chemical reactions have been modeled by applying the methodology described in previous sections, i.e., *n*-hexane hydroisomerization, ethene oligomerization and xylene isomerization. *n*-Hexane hydroisomerization is considered as a case study in which the methodology is illustrated. For ethene oligomerization, a microkinetic model is constructed based upon intrinsic kinetic data. This microkinetic model is used for multi-scale modeling, i.e., model based catalyst design and industrial reactor optimization. A microkinetic model has been constructed for xylene isomerization based upon a limited, but well-designed experimental data set obtained from Shell. The resulting knowledge is used to provide guidelines for the optimization of the industrially used xylene isomerization catalyst.

### 1.4.1 *n*-Hexane hydrocracking: a case study

*n*-Hexane hydroisomerization over a bifunctional zeolite is used in this work as a case study to illustrate the systematic methodology developed for kinetic modeling as developed in this work. This model reaction only entails a limited reaction network for which the

mechanism is well-established [18-24]. While the acid function provided by the H-ZSM-5 zeolite framework provokes the skeletal rearrangement and cracking, the metal function enables operating at moderate temperatures in the range between 200°C to 300°C while avoiding deactivation by coking. In order to acquire the most details as possible about the acid catalyzed reaction mechanism, the experimental investigation was performed at gas phase conditions under which ideal hydrocracking occurs [20, 22, 23, 25-29]. When performing experiments within such a range of operating conditions, the acid catalyzed reactions are rate determining, leading to specific kinetic behavior, e.g., exhibiting a maximum isomer yield.

The goal of modeling the hydroisomerization of *n*-hexane over a bifunctional catalyst is twofold:

1. illustrate the systematic methodology proposed for kinetic modeling.
2. develop a kinetic model exhibiting an adequate balance between statistical significance and physical meaning.

This case study is an ideal exercise for engineering students and young professionals new to the field of chemical reaction engineering and has been successfully used during several modeling courses at Ghent University and international workshops.

### 1.4.2 Ethene oligomerization: searching for sustainable fuels and chemicals

The pursuit of so-called 'sustainable' fuels and chemicals has never assumed such a global character as today. With increasing environmental concern and corresponding legislation as well as crude oil depletion, new feedstocks and processes are screened for their economic potential while accounting for their environmental impact. Shale gas and oil, tar sands and stranded gas are exploited to aid in the transition to non-conventional hydrocarbon sources. Of these hydrocarbon sources, stranded gas is the most promising for the transition to sustainable processes.

Natural gas reservoirs are considered to be stranded when their commercial exploitation is impossible. For such, typically small, reservoirs several projects are investigating the application of gas-to-liquid technologies, e.g., *Next-GTL* [30], *CARENA* [31], *DEMCAMER* [32] and *OCMOL* [33]. The present work has been performed within the framework of *OCMOL*

which is the acronym for 'Oxidative Coupling of Methane followed by the Oligomerization to Liquids' [33]. It is aimed at to use heterogeneous catalysts in order to improve the process' sustainability by nullifying the need for environmental unfriendly solvents and decreasing the energy requirements for solvent recuperation [34].

In the first step of this integrated process, methane originating from stranded gas or biogas is oxidatively coupled to form ethene. In a subsequent step, the latter is oligomerized and transformed into liquid fuels, e.g., gasoline, or chemicals such as linear 1-alkenes and propene. The latter could be an important asset when shale gas is used as feed to the *OCMOL* process. Shale gas processing leads to a product slate primarily composed of ethene rather than propene which, hence, indirectly affects the production of polypropylene and other propene derivatives [35].

Ethene is not susceptible to acid catalysis under the mild reaction conditions, i.e., at temperatures 523 K, used in this work, because it necessarily requires the involvement of primary carbenium ions. However, in the presence of nickel-ions, ethene is readily dimerized to butene which, in turn, can undergo further acid catalyzed steps via secondary carbenium ions .

Ethene oligomerization is a well-established reaction which, in a homogeneously catalyzed process configuration, has already been implemented at the industrial scale [36]. Commonly used catalysts such as trialkylammonium and nickel complexes, typically lead to linear 1-alkenes [37]. While 1-alkenes are high-value products, these processes offer little flexibility in tuning the product distribution to respond to potential fluctuations in market demands for fuels and chemicals. Additionally, the use of homogeneous catalysts is inherently coupled to the use of environmentally unfriendly solvents and an extensive energy consumption for their recuperation [34]. The use of heterogeneous catalysts may help to overcome these disadvantages. Nowadays it is attempted to immobilize active sites for ethene oligomerization on a heterogeneous support, hence, avoiding further catalyst separation. Active metals such as nickel [38, 39] or chromium [40, 41] are then deposited on acidic supports such as zeolites or silica-alumina. The acid sites of these supports catalyze the further reactions of the dimers, i.e., butenes, produced at the metal sites and guarantee the desired product flexibility. The use of specific zeolite framework structures such as ZSM-5 or ZSM-22 enables a further tuning of the product yields [7, 42].

First efforts on the heterogeneously catalyzed dimerization of ethene by Kimura et al. [43] who used a nickel oxide-silica catalyst, date back to the beginning of the 70's. Within the next two decades, a few articles were published, see Figure 1-3 In the late 80's and early 90's the subject gained more interest. Since 1990, about 10 articles per year have been published on ethene oligomerization. Especially, the group of Scurrrell [44-47] and Hulea [48-52] performed exhaustive work on ethene oligomerization on various silica-aluminas. Up to now, however, no work has been reported on the detailed kinetic modeling of ethene oligomerization on a silica alumina comprising a metal ion function.

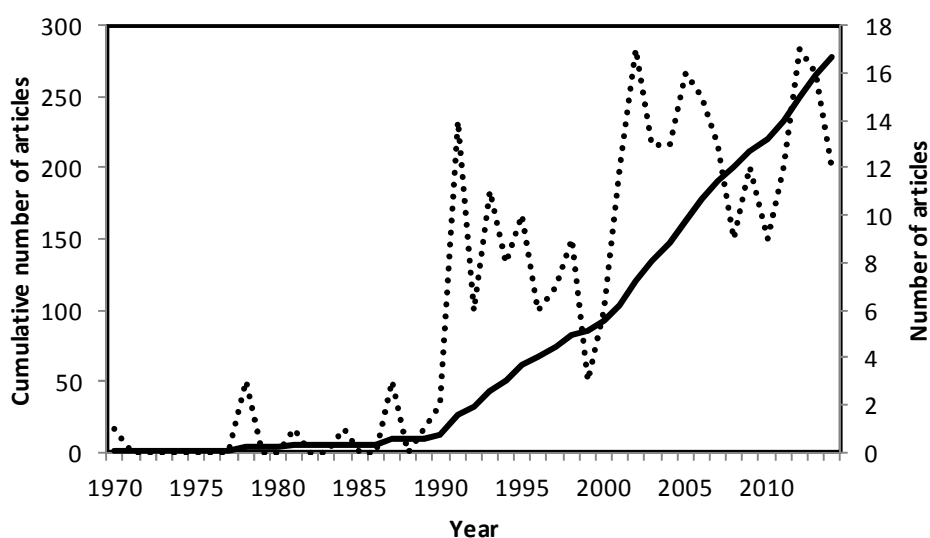


**Figure 1-3: literature survey (Web of Knowledge) using the key words: Topic=((ethene OR ethylene) AND (oligomerization OR oligomerisation OR dimerization OR dimerisation)) AND (heterogenous OR heterogeneous OR silica OR alumina) as accessed on September 1<sup>st</sup>, 2014; full line: cumulative number of articles as function of year; dotted line: number of articles published.**

The goal of modeling the bifunctional, heterogeneously catalyzed oligomerization of ethene is threefold:

1. elucidate the reaction mechanism and determine the main reaction pathways
2. use this knowledge to design 'in-silico' an ethene oligomerization catalyst which enhances the yield towards valuable products, e.g., gasoline
3. develop an industrial reactor model accounting for phenomena which are normally not encountered in lab-scale set-ups, e.g., transport phenomena and liquid formation. This industrial reactor model will be used to design an industrial ethene oligomerization reactor.

### 1.4.3 Xylene isomerization: meeting the world demand for polymer production

During the last decades, thermoplastic polymers have become very important. They have proven their flexibility, durability and broad application area. One of the most common thermoplastic polymers is PET – polyethylenetereftalate. The main uses for this polymer are in synthetic fibers, beverage bottles, food and other containers, films and foils [53]. The key building blocks of this polymer are ethylene and tereftalic acid. The latter is formed by partial oxidation of paraxylene, which, as a raw material, is generally co-produced with other xylene isomers, i.e., metaxylene and orthoxylene. Ethylbenzene is usually present as well in such xylene mixtures. All these components exhibit very similar boiling points. Conventional xylene mixtures produced by catalytic reforming, gasoil pyrolysis, toluene disproportionation or from charcoal, contain an excess of metaxylene and a deficit of paraxylene in comparison with the global market demand. Metaxylene, which is economically and industrially less interesting, typically makes up about two thirds of such mixtures, while at least 70% is required as paraxylene [54]. Additionally, a large amount of the orthoxylene is needed for the production of plasticizers through phthalic anhydride [53]. Isomerization processes in which the less valuable products are transformed into the desired isomers, play a pivotal role in matching the market demand while preventing xylene losses.

Xylene isomerization is an acid-catalyzed process which makes use of either amorphous silica-aluminates, zeolites or metal oxides. Nowadays, mostly zeolite based isomerization processes are commercialized because of the broad range in which the catalyst properties can be tuned, i.e., shape selectivity, acid site density, surface area,... [53, 54]. The use of a metallic function such as platinum provides a bifunctional character to the zeolite which suppresses deactivation in the presence of hydrogen.

First efforts related to kinetic modelling of xylene isomerization on H-ZSM-5 were reported in 1995 by Liang et al. [55] who proposed a kinetic model for toluene disproportionation on ZSM-5, including diffusion phenomena. In 1996 Morin et al. [56] constructed a kinetic model for xylene isomerization on HY zeolites. Ilyas and Al-Khattaf [57-61] performed kinetic measurements and correspondingly constructed a kinetic model for xylene isomerization on both USY and H-ZSM-5 zeolites. Gonzalez et al. [62] constructed a quadratic model for the

isomerization of xylenes over a Pt/mordenite catalyst. More recently, some authors published on the use of a membrane reactor [63-67] or a moving bed reactor [68] for the isomerization of xylene. Despite the major industrial interest and relevance of the subject, no entirely fundamental kinetic modeling methodology, such as the Single-Event MicroKinetics (SEMK), has been applied to xylene isomerization yet.

The goal of modeling the isomerization of xylene is threefold:

1. SEMK model construction based upon a limited, but well-designed experimental data set obtained from Shell.
2. reaction mechanism elucidation and reaction pathway analysis
3. use this knowledge to provide guidelines for the optimization of the industrially used xylene isomerization catalyst

### 1.5 Scope of the thesis

In this work, the multi-scale modeling approach of the Laboratory of Chemical Technology is approached starting from a systematic methodology. This systematic methodology is based on intrinsic kinetics which are used to determine the catalyst and kinetic descriptors by regression. This should result in an adequate microkinetic model which has a sound physical meaning and a justifiable statistical significance. Using these microkinetic models, new catalyst can be tailored 'in-silico'. Similarly, industrial reactors can be designed and optimized by including phenomena which are occurring and influencing the kinetics at larger scales. This multi-scale modeling approach has been illustrated by and applied to three industrial relevant chemical reactions, i.e., *n*-hexane hydroisomerization, ethene oligomerization and xylene isomerization.

The scope of the thesis can be summarized in the following bullet points:

- a. To develop a systematic methodology for (kinetic) modelling (chapter 2, section )
- b. Apply the developed methodology for modeling industrially relevant reactions:
  - i. *n*-hexane hydroisomerization (chapter 3)
  - ii. ethene oligomerization (chapter 4, 5 and 6)
  - iii. xylene isomerization (chapter 7)

- c. Illustrate the benefits of (Single-Event) MicroKinetic modeling towards multi scale modeling:
  - i. Catalyst design (chapter 5 and 7)
  - ii. Industrial reactor design (chapter 6)

## 1.6 References

- [1] G.F. Froment, K.B. Bischoff, J. De Wilde, Chemical reactor analysis and design, 2010.
- [2] G.B. Marin, G.S. Yablonsky, Kinetics of Chemical Reactions: Decoding Complexity, 2011.
- [3] A.N.R. Bos, L. Lefferts, G.B. Marin, M.H.G.M. Steijns, Applied Catalysis a-General. 160 (1997) 185-190.
- [4] <http://www.lct.ugent.be/>, 2014.
- [5] R.J. Berger, E.H. Stitt, G.B. Marin, F. Kapteijn, J.A. Moulijn, Catech. 5 (2001) 30-60.
- [6] G.F. Froment, Catalysis Today. 52 (1999) 153-163.
- [7] C.S.L. Narasimhan, J.W. Thybaut, G.B. Marin, P.A. Jacobs, J.A. Martens, J.F. Denayer, G.V. Baron, Journal of Catalysis. 220 (2003) 399-413.
- [8] J.W. Thybaut, I.R. Choudhury, J.F. Denayer, G.V. Baron, P.A. Jacobs, J.A. Martens, G.B. Marin, Topics in Catalysis. 52 (2009) 1251-1260.
- [9] J.M. Martinis, G.F. Froment, Industrial & Engineering Chemistry Research. 45 (2006) 954-967.
- [10] R. Quintana-Solorzano, J.W. Thybaut, P. Galtier, G.B. Marin, Catalysis Today. 150 (2010) 319-331.
- [11] R. Sotelo-Boyas, G.F. Froment, Industrial & Engineering Chemistry Research. 48 (2009) 1107-1119.
- [12] T.Y. Park, G.F. Froment, Industrial & Engineering Chemistry Research. 40 (2001) 4187-4196.
- [13] T.Y. Park, G.F. Froment, Industrial & Engineering Chemistry Research. 40 (2001) 4172-4186.
- [14] G. Lozano-Blanco, J.W. Thybaut, K. Surla, P. Galtier, G.B. Marin, Industrial & Engineering Chemistry Research. 47 (2008) 5879-5891.
- [15] T. Bera, J.W. Thybaut, G.B. Marin, Industrial & Engineering Chemistry Research. 50 (2011) 12933-12945.
- [16] K. Toch, J.W. Thybaut, B.D. Vandegheuchte, C.S.L. Narasimhan, L. Domokos, G.B. Marin, Applied Catalysis a-General. 425-426 (2012) 130-144.
- [17] J.W. Thybaut, G.B. Marin, Journal of Catalysis. 308 (2013) 352-362.
- [18] J.F. Allain, P. Magnoux, P. Schulz, M. Guisnet, Applied Catalysis a-General. 152 (1997) 221-235.
- [19] M.A. Baltanas, G.F. Froment, Computers & Chemical Engineering. 9 (1985) 71-81.
- [20] M.A. Baltanas, H. Vansina, G.F. Froment, Industrial & Engineering Chemistry Product Research and Development. 22 (1983) 531-539.
- [21] G.G. Martens, J.W. Thybaut, G.B. Marin, Industrial & Engineering Chemistry Research. 40 (2001) 1832-1844.
- [22] M. Steijns, G. Froment, P. Jacobs, J. Uytterhoeven, J. Weitkamp, Industrial & Engineering Chemistry Product Research and Development. 20 (1981) 654-660.

- [23] M. Steijns, G.F. Froment, *Industrial & Engineering Chemistry Product Research and Development*. 20 (1981) 660-668.
- [24] A. vandeRunstraat, J. vanGrondelle, R.A. vanSanten, *Industrial & Engineering Chemistry Research*. 36 (1997) 3116-3125.
- [25] C.S. Raghuvver, J.W. Thybaut, R. De Bruycker, K. Metaxas, T. Bera, G.B. Marin, *Fuel*. 125 206-218.
- [26] J.W. Thybaut, C.S.L. Narasimhan, J.F. Denayer, G.V. Baron, P.A. Jacobs, J.A. Martens, G.B. Marin, *Industrial & Engineering Chemistry Research*. 44 (2005) 5159-5169.
- [27] J.W. Thybaut, C.S.L. Narasimhan, G.B. Marin, *Catalysis Today*. 111 (2006) 94-102.
- [28] H. Vansina, M.A. Baltanas, G.F. Froment, *Industrial & Engineering Chemistry Product Research and Development*. 22 (1983) 526-531.
- [29] J. Weitkamp, *Erdol & Kohle Erdgas Petrochemie*. 31 (1978) 13-22.
- [30] [http://cordis.europa.eu/project/rcn/93080\\_en.html](http://cordis.europa.eu/project/rcn/93080_en.html), 2014.
- [31] <http://www.carenafp7.eu/>, 2014.
- [32] <http://www.demcamer.org/>, 2014.
- [33] <http://www.ocmol.eu/>, 2014.
- [34] P.T. Anastas, M.M. Kirchoff, T.C. Williamson, *Applied Catalysis a-General*. 221 (2001) 3-13.
- [35] T.K. Swift, M.G. Moore, *Chemical Engineering Progress*. 109 (2013) 24-28.
- [36] *Ullmann's Encyclopedia of Industrial Chemistry* (2014).
- [37] J.J. Spivey, D.E. Resasco, A.G. Dixon, M. Boudart, *Catalysis*, 1999.
- [38] R. Abeywickrema, M.A. Bennett, K.J. Cavell, M. Kony, A.F. Masters, A.G. Webb, *Journal of the Chemical Society-Dalton Transactions* (1993) 59-68.
- [39] L.X. Pei, X.M. Liu, H.Y. Gao, Q. Wu, *Applied Organometallic Chemistry*. 23 (2009) 455-459.
- [40] N. Peulecke, B.H. Muller, S. Peitz, B.R. Aluri, U. Rosenthal, A. Wohl, W. Muller, M.H. Al-Hazmi, F.M. Mosa, *Chemcatchem*. 2 (2010) 1079-1081.
- [41] P.Y. Qiu, R.H. Cheng, Z. Liu, B.P. Liu, B. Tumanskii, M.S. Eisen, *Journal of Organometallic Chemistry*. 699 (2012) 48-55.
- [42] C.S.L. Narasimhan, J.W. Thybaut, J.A. Martens, P.A. Jacobs, J.F. Denayer, G.B. Marin, *Journal of Physical Chemistry B*. 110 (2006) 6750-6758.
- [43] K. Kimura, H. Ai, A. Ozaki, *Journal of Catalysis*. 18 (1970) 271-&.
- [44] J. Heveling, C.P. Nicolaidis, M.S. Scurrell, *Abstracts of Papers of the American Chemical Society*. 202 (1991) 8-Petr.
- [45] J. Heveling, C.P. Nicolaidis, M.S. Scurrell, *Journal of the Chemical Society-Chemical Communications* (1991) 126-127.
- [46] J. Heveling, C.P. Nicolaidis, M.S. Scurrell, *Applied Catalysis a-General*. 173 (1998) 1-9.
- [47] J. Heveling, C.P. Nicolaidis, M.S. Scurrell, *Catalysis Letters*. 95 (2004) 87-91.
- [48] V. Hulea, F. Fajula, *Journal of Catalysis*. 225 (2004) 213-222.
- [49] M. Lallemand, A. Finiels, F. Fajula, V. Hulea, *Applied Catalysis a-General*. 301 (2006) 196-201.
- [50] M. Lallemand, A. Finiels, F. Fajula, V. Hulea, *Journal of Physical Chemistry C*. 113 (2009) 20360-20364.
- [51] M. Lallemand, A. Finiels, F. Fajula, V. Hulea, *Chemical Engineering Journal*. 172 (2011) 1078-1082.
- [52] M. Lallemand, O.A. Rusu, E. Dumitriu, A. Finiels, F. Fajula, V. Hulea, *Applied Catalysis a-General*. 338 (2008) 37-43.



- 
- [53] Ullmann's Encyclopedia of Industrial Chemistry, 6th ed.
- [54] Kirk-Othmer Encyclopediae of Chemical Technology, 4th ed.
- [55] W.G. Liang, S.Y. Chen, S.Y. Peng, Chemical Engineering Science. 50 (1995) 2391-2396.
- [56] S. Morin, N.S. Gnep, M. Guisnet, Journal of Catalysis. 159 (1996) 296-304.
- [57] S. Al-Khattaf, A. Iliyas, A. Al-Amer, T. Inui, Journal of Molecular Catalysis a-Chemical. 225 (2005) 117-124.
- [58] S. Al-Khattaf, N.M. Tukur, A. Al-Amer, Industrial & Engineering Chemistry Research. 44 (2005) 7957-7968.
- [59] A. Iliyas, S. Al-Khattaf, Applied Catalysis a-General. 269 (2004) 225-236.
- [60] A. Iliyas, S. Al-Khattaf, Industrial & Engineering Chemistry Research. 43 (2004) 1349-1358.
- [61] A. Iliyas, S. Al-Khattaf, Chemical Engineering Journal. 107 (2005) 127-132.
- [62] H. Gonzalez, A. Rodriguez, L. Cedeno, J. Ramirez, J. Aracil, Industrial & Engineering Chemistry Research. 35 (1996) 3964-3972.
- [63] A.L. Deshayes, E.E. Miro, G.I. Horowitz, Chemical Engineering Journal. 122 (2006) 149-157.
- [64] A.M. Tarditi, G.I. Horowitz, E.A. Lombardo, Catalysis Letters. 123 (2008) 7-15.
- [65] A.M. Tarditi, S. Irusta, E.A. Lombardo, Chemical Engineering Journal. 122 (2006) 167-174.
- [66] Y.F. Yeong, A.Z. Abdullah, A.L. Ahmad, S. Bhatia, Chemical Engineering Journal. 157 (2010) 579-589.
- [67] C. Zhang, Z. Hong, X.H. Gu, Z.X. Zhong, W.Q. Jin, N.P. Xu, Industrial & Engineering Chemistry Research. 48 (2009) 4293-4299.
- [68] M. Minceva, P.S. Gomes, V. Meshko, A.E. Rodrigues, Chemical Engineering Journal. 140 (2008) 305-323.



# Chapter 2

## Procedures

---

This chapter gives an overview of all experimental and modeling procedures applied in this work. In total, four different experimental set-ups were used for the acquisition of kinetic data. Two experimental set-ups were located at two different industrial partners. One was used to experimentally validate the industrial reactor model for ethene oligomerization, see Chapter 6, while the other was used to acquire the intrinsic kinetic dataset for xylene isomerization on Pt/H-ZSM-5, see Chapter 7. The two other experimental set-ups were situated at the Laboratory of Chemical Technology at Ghent University, i.e., a CSTR type Berty reactor set-up and a HTK-1 plug flow reactor set-up. The Berty set-up was used for the *n*-hexane hydroisomerization experiments on a Pt/H-ZSM-5 catalyst different from the one used in the xylene isomerization experiments. The High-Throughput Kinetic Set-up, *HTK-1*, was used for the acquisition of intrinsic ethene oligomerization data on an amorphous Ni-SiO<sub>2</sub>-Al<sub>2</sub>O<sub>3</sub> and a Ni-Beta catalyst. A discussion on these catalysts and experimental set-ups is given in resp. sections 2.1.1 and 2.1.2. The results from such typical experimental campaign are raw data which have to be reconciliated before they can be used for (micro)kinetic modeling purposes. The procedure of transforming this raw data into useable numbers is described in section 2.1.3.

A systematic methodology to adequately model the observed kinetics was proposed, see section 2.2.1, and was applied throughout this thesis. Mathematical models are at hand for any of the considered reactors, see section 2.2.2, and are used in the determination of unknown parameters via model regression to experimental data, see section 2.2.3. The regression results were evaluated based on their physical meaning and statistical significance as described in sections 2.2.4 and 2.2.5. Single-Event MicroKinetics are used throughout this work to describe complex chemical reactions. A short overview is given in section 2.2.6. Lastly, if the kinetic model was able to adequately describe the experimental

data, a reaction path analysis could be performed to support the elucidation of the underlying chemistry [1].

## 2.1 Experimental

### 2.1.1 Catalysts

#### 2.1.1.1 Pt/H-ZSM-5 for *n*-hexane hydroisomerization

The Pt/H-ZSM-5 catalyst used for *n*-hexane hydroisomerization experiments was synthesized according a literature reported recipe [2]. Table 2-1 gives an overview of its most relevant properties. Prior to the experimentation, the catalyst was reduced in situ under flowing hydrogen at atmospheric pressure and 673 K during at least 4 hours.

**Table 2-1: Properties of the Pt/H-ZSM-5 catalyst used for *n*-hexane hydroisomerization**

Pt content [wt%]	Acid site concentration [mol kg <sub>cat</sub> <sup>-1</sup> ]	Si/Al-ratio [-]	BET surface area [10 <sup>3</sup> m <sup>2</sup> kg <sub>cat</sub> <sup>-1</sup> ]	Micropore surface area [10 <sup>3</sup> m <sup>3</sup> kg <sub>cat</sub> <sup>-1</sup> ]
0.98	0.12	137	467	0.182

#### 2.1.1.2 Ni-SiO<sub>2</sub>-Al<sub>2</sub>O<sub>3</sub> for ethene oligomerization

The Ni impregnated amorphous SiO<sub>2</sub>-Al<sub>2</sub>O<sub>3</sub> used for ethene oligomerization experiments was synthesized by Johnson Matthey according to the procedures as reported by Heveling et al. [3]. The aluminum, silicium and Ni content were verified by inductively coupled plasma atomic emission spectroscopy, i.e., *ICP-AES*, using a Thermo Jarrell Ash IRIS, see Table 2-2. The BET surface area and the micropore surface area were determined by N<sub>2</sub> physisorption at 77 K using a Micromeritics Gemini V Series. The acid site concentration was determined by ammonia temperature programmed desorption, i.e., *NH<sub>3</sub>-TPD*, using a Micromeritics AutoChem II in a temperature range from 293 K to 923 K. Only weak acid sites were detected, i.e., ammonia desorption only occurred in the temperature range from 473 to 523 K.

**Table 2-2: Properties of the Ni-SiO<sub>2</sub>-Al<sub>2</sub>O<sub>3</sub> catalyst used for ethene oligomerization**

Ni content [wt%]	Acid site		BET surface area [10 <sup>3</sup> m <sup>2</sup> kg <sub>cat</sub> <sup>-1</sup> ]	Micropore surface area [10 <sup>3</sup> m <sup>2</sup> kg <sub>cat</sub> <sup>-1</sup> ]
	concentration (weak) [mol kg <sub>cat</sub> <sup>-1</sup> ]	Si/Al ratio [-]		
1.8	0.80	0.21	199	17.8

Efforts to elucidate the nature of the active site for ethene oligomerization were made. Ni<sup>0</sup>, isolated Ni<sup>+</sup> or Ni<sup>2+</sup> species and into lesser extent NiO, are known to be catalytically active for ethene oligomerization [4]. XPS measurements of the Ni-SiO<sub>2</sub>-Al<sub>2</sub>O<sub>3</sub> catalyst showed the presence of Ni<sup>2+</sup> species, i.e., either isolated Ni<sup>2+</sup> or NiO. Diffuse reflectance infrared fourier transform (DRIFT) spectroscopy of adsorbed CO was performed on the Ni-SiO<sub>2</sub>-Al<sub>2</sub>O<sub>3</sub> using a Bruker Tensor 27 with a Specac environmental cell. Two different pretreatments were given to the catalyst, i.e., 8 hours at 773 K under flowing He and 8 hours at 773 K under flowing H<sub>2</sub>. A similar pretreatment, except for the temperature, i.e., 573 K instead of 773 K, was also applied but yielded the same results. Figure 2-1a shows a typical IR spectrum recorded while CO was adsorbed at 293 K. The two peaks at 2180 and 2120 cm<sup>-1</sup> can be assigned to gas phase CO [5]. The peaks between 2060 and 2000 cm<sup>-1</sup> cannot be attributed to gas phase CO, but could possibly indicate the presence of Ni<sup>0</sup>-CO or a binuclear bridging Ni<sup>+</sup> complex, i.e., Ni<sup>+</sup>-(CO)<sub>2</sub> [4, 6]. When the CO gas flow was changed for He, both catalyst samples showed a similar IR spectrum, see Figure 2-1b and Figure 2-1c. It must be noted that these peaks disappeared slowly over time, indicating a slow desorption of CO from the nickel sites. The peaks at 2180 cm<sup>-1</sup> and 2120 cm<sup>-1</sup> indicate the presence of resp. Ni<sup>2+</sup>-(CO) and Ni<sup>+</sup>-(CO) species.

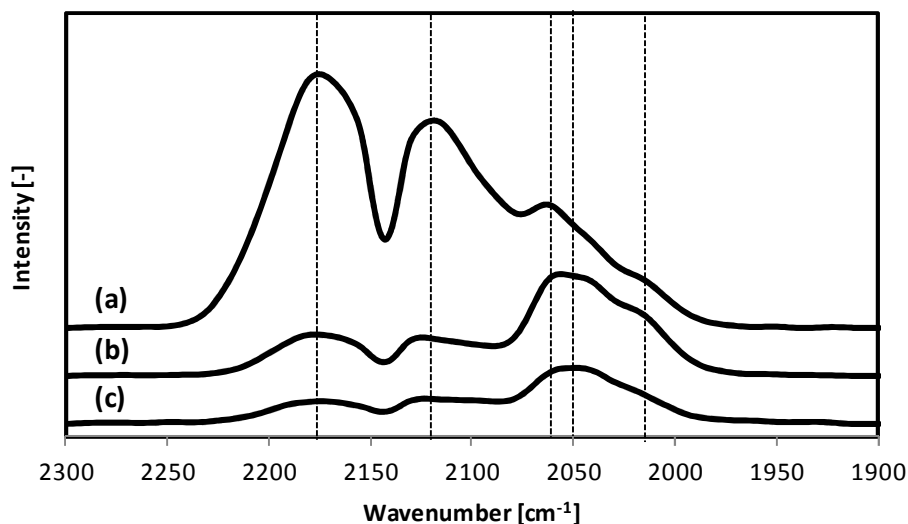


**Figure 2-1: FTIR spectra of CO adsorbed on the amorphous Ni-SiO<sub>2</sub>-Al<sub>2</sub>O<sub>3</sub> at 293 K during CO adsorption (a) and after CO adsorption (b-c). Sample (b) has been pretreated for 8 hours at 773 K under flowing He. Sample (c) has been pretreated for 8 hours at 773 K under flowing H<sub>2</sub>.**

A H<sub>2</sub>-TPR was recorded of the Ni-SiO<sub>2</sub>-Al<sub>2</sub>O<sub>3</sub> catalyst using the Micromeritics AutoChem II as described previously. Before reduction, the sample was pretreated under inert atmosphere, i.e., Ar, at elevated temperature, i.e., 773 K in order to remove all adsorbed components from the catalyst surface. After cooling down to room temperature, the sample was reduced under a 5%H<sub>2</sub>/Ar flow at a temperature increase of 10 K min<sup>-1</sup> up to 1273 K. A small peak in the range of 500 to 600 K was observed which could be attributed to bulk NiO species. At higher temperatures, there was no indication of additional reduction.

A H<sub>2</sub> pulse chemisorption experiment using the Micromeritics AutoChem II was performed at 293 K on the reduced Ni-SiO<sub>2</sub>-Al<sub>2</sub>O<sub>3</sub> sample resulting from the H<sub>2</sub>-TPR to determine the metal dispersion and mean particle diameter. There was a very limited to no uptake of hydrogen which indicated that Ni<sup>0</sup> or NiO is either not present or heavily clustered resulting in particle diameters larger than 15 nm. However, XRD analysis of the catalyst revealed no Ni diffraction peaks which indicates the absence of Ni<sup>0</sup> or NiO clusters or, at least the absence of Ni particles larger than 3 nm.

Additionally, a CO pulse chemisorption was performed using the Micromeritics AutoChem II at 293 K. Before chemisorption, the sample was pretreated under inert atmosphere, i.e., He, at elevated temperature, i.e., 773 K in order to remove all adsorbed components from the catalyst surface. However, this did not result in quantitative information on the dispersion due to slow release of CO from the Ni species as observed during the CO-FTIR

measurements. After several CO pulses until the corresponding peak surface areas did not change anymore, it was assumed that the Ni species were saturated with CO. On this sample, a TPD was performed. The volume of CO gas released was used to determine the dispersion. Depending on the configuration assumed, i.e., linear or a binuclear bridging Ni complex, the dispersion was equal to resp. 140% and 70%.

Concluding, the H<sub>2</sub> pulse chemisorption experiment showed that the amount of Ni<sup>0</sup> or NiO is negligible, even after reduction of the catalyst at high temperature. This could be attributed to individual Ni species which are in an exchange position and are difficult reduced. This would explain the high dispersion as determined by CO pulse chemisorption and the XRD analysis. The nature of these Ni species could not be specified via DRIFT of CO adsorption on the catalyst, i.e., Ni<sup>2+</sup> or Ni<sup>+</sup>, but XPS measurement indicated the presence of mainly Ni<sup>2+</sup> species. On top of that, the pretreatment of the catalyst at elevated temperature under inert flow can also lead to the reduction of Ni<sup>2+</sup> to Ni<sup>+</sup> via a dehydration mechanism [4], so the determination of the actual active site is not a sinecure.

### 2.1.1.3 Ni-Beta for ethene oligomerization

The Ni-Beta zeolite used for ethene oligomerization experiments was synthesized at CSIC-ITQ [7]. An elemental analysis was performed by ICP-AES to determine the nickel content, i.e., 4.9 wt%, and Si/Al-ratio, i.e., 12.5. An XRD analysis of the catalyst showed the presence of NiO particles. Via N<sub>2</sub> adsorption experiments at 77K, the BET surface area and micropore volume were determined to amount to resp. 458 m<sup>2</sup> g<sup>-1</sup> and 0.135 cm<sup>3</sup> g<sup>-1</sup>. The acid site concentration equals 6.3 · 10<sup>-4</sup> mol g<sup>-1</sup> as measured by NH<sub>3</sub>-TPD. The nature of the active sites on this catalyst has already been elucidated in literature [7]. An overview of the Ni-Beta zeolite properties is given in Table 2-3. A more detailed discussion on the Ni-Beta catalyst can be found in [7].

**Table 2-3: Properties of the Ni-Beta catalyst used for ethene oligomerization**

Ni content [wt%]	Acid site concentration [mol kg <sub>cat</sub> <sup>-1</sup> ]	Si/Al ratio [-]	BET surface area [10 <sup>3</sup> m <sup>2</sup> kg <sub>cat</sub> <sup>-1</sup> ]	Micropore volume [10 <sup>3</sup> m <sup>3</sup> kg <sub>cat</sub> <sup>-1</sup> ]
4.9	0.63	12.5	458	135

#### 2.1.1.4 Pt/H-ZSM-5 for xylene isomerization

The Pt/H-ZSM-5 catalyst used for xylene isomerization experiments was prepared by an industrial partner using a ZSM-5 with a silica to alumina ratio of 80 available from Zeolyst. The zeolite was mixed with a silica binder and extruded into a cylinder form with a diameter of 1.6 mm. After calcination the extrudates were pore volume impregnated to achieve a Pt loading of 200 ppmw. The catalyst obtained was characterized by  $^{27}\text{Al}$  MAS NMR and IR spectroscopy, i.e., analyzing both the OH region and H/D exchange spectra. The results validated the theoretically expected acid site concentration in the catalyst, i.e.  $0.35 \text{ mol kg}^{-1}$  [8]. Laser ablation inductively couple plasma mass spectrometry (LA-ICP-MS) measurements having a spatial resolution of  $30 \mu\text{m}$  indicated only minor variations in the Pt loading from the edge to the centre of the cross section of the extrudates.

**Table 2-4: Properties of the Pt/H-ZSM-5 catalyst used for xylene isomerization**

Pt content [ppmw]	Acid site concentration [ $\text{mol kg}_{\text{cat}}^{-1}$ ]	Si/Al ratio [-]
200	0.35	80

## 2.1.2 Reactor set-ups

#### 2.1.2.1 Reactor set-up for *n*-hexane hydroisomerization

The *n*-hexane hydroisomerization experiments were performed in a Berty reactor set-up at the LCT at Ghent University. It is a gas-phase continuous stirred tank reactor (CSTR). Prior to entering the reactor, *n*-hexane and hydrogen are mixed in an evaporator/pre-heater to ensure that the reactor feed is completely gaseous. The *n*-hexane feed flow rate is verified by monitoring the mass of the feed reservoir. Methane is added to the reactor effluent as an internal standard for analytical and mass and carbon balance verification purposes. After reaching steady state operation after ca. 1 hour, a sample is taken via a 6-way valve and is injected on a HP Series II 5890 instrument with a 50 m (id = 0.25 mm) RSL-150 column with a  $0.25 \mu\text{m}$  poly(dimethylsiloxane) film for GC analysis. More details on the Berty reactor and set-up can be found in literature [9-11].



### 2.1.2.2 Reactor set-up for ethene oligomerization

The oligomerization experiments were performed in the *HTK-1* set-up available at the *LCT* at Ghent University. It comprises 8 plug flow reactors, each with an internal diameter of 0.011 m and a total length of 0.811 m [12]. Each reactor pair is placed in a heating jacket, capable of reaching 923 K, and the temperature is controlled at three points throughout each individual reactor using either a multipoint thermocouple at the outer side of the reactor wall or in the centre of the reactor, i.e., the catalyst bed. The pressure is regulated via a back-pressure regulator, operating up to 20 MPa. Prior to loading it into the reactor, the catalyst powder was pressed into flakes and crushed again into pellets with a diameter of 300  $\mu\text{m}$  to 560  $\mu\text{m}$  to avoid mass transport limitations at the pellet scale [13]. For each run, 0.5 to 1.0 g of the catalyst was physically mixed with inert material of a similar diameter. To avoid heat transport limitations in the case of ethene oligomerization, it was determined that the bed should only contain about 10wt% of active material [13]. Non-porous sintered  $\alpha\text{-Al}_2\text{O}_3$  was used as inert material and was also placed in front of the catalyst bed to assure a homogeneous inlet flow pattern and to enhance the preheating of the reactor inlet flow. The relatively high thermal conductivity of the  $\alpha\text{-Al}_2\text{O}_3$ , i.e.,  $\pm 30 \text{ W m}^{-1} \text{ K}^{-1}$ , also ensured a smooth and sufficient heat removal from the catalyst bed.

After catalyst loading, the catalyst was pre-treated in situ under a nitrogen flow with a space-time of  $4 \text{ kg}_{\text{cat}} \text{ s mol}_{\text{N}_2}^{-1}$ , at atmospheric pressure and 573 K for several hours. After this period, the reactor was cooled down to the required reaction temperature under the same nitrogen flow rate as during the pre-treatment and at atmospheric pressure.

During reaction, care was taken to work at gas phase conditions, even in the analysis section operating at atmospheric pressure and heat traced up to 313 K. The inlet feed contained 10 to 20 mol% of ethene, diluted with nitrogen. Methane was also sent in small quantities as internal standard. Each of the feed flow rates is individually controlled using thermal mass flow controllers.

The effluent analysis occurred on-line using an Agilent 3000 micro-GC. This gas chromatograph contains 4 parallel columns each being connected to a thermal conductivity detector (*TCD*). Two of these channels sufficed to completely analyze the reactor effluent. On the first column, i.e., a PLOT U (8 m x 0.32 mm), methane, ethene and nitrogen were quantitatively determined. On the second column, i.e., an OV-1 (10 m x 0.15 mm x 2.0  $\mu\text{m}$ ), ethene and the oligomerization products were quantitatively determined. It was possible to

separate all butene isomers, i.e., 1-butene and 2-cis and 2-trans butene. The higher alkenes formed were detected as a lump per carbon number since the internal isomers could not be separated on the columns used. Ethene was used as a reference component between both columns [14].

### ***2.1.2.3 Reactor set-up for experimental validation of the industrial reactor model for ethene oligomerization***

The experimental data used to validate the industrial reactor simulation model were oligomerization demonstration unit constructed at CEPESA. The unit consists of one fixed bed reactor which can be heated by an electrical furnace. The reactor is capable of operating at temperatures up to 823 K and pressures up to 5.0 MPa. Three gasses can be independently fed to the reactor inlet after preheating. The reactor temperature could be kept within 2 K of the temperature set-point. The product stream is cooled down and sent to a knock-out drum at atmospheric pressure which separates the reactor effluent into a gaseous and liquid fraction. The liquid flow rate is monitored by a weighing scale while the gas flow rate is measured by a wet gas meter. The gas flow is analyzed online using a Varian 3800 gas chromatograph while the liquid phase is analyzed off-line.

### ***2.1.2.4 Reactor set-up for xylene isomerization***

The xylene isomerization experiments were performed using in a gas phase reactor set-up with a down flow reactor on a gram scale available at Shell. The catalyst was mixed with inert material and loaded in the isothermal section of the reactor. After catalyst reduction at atmospheric conditions, the reactor was pressurized and an industrial feedstock corresponding to a paraxylene extracted recycle feed to a BTX unit was introduced while ensuring proper vaporization of the feedstock upstream of the reactor.

The products were analyzed on-line, while maintaining vapor phase conditions, and were also collected, at a lower temperature, in the depressurized section of the unit in a gas-liquid separator/condenser for off-line analysis and further product identification and evaluation. During analysis a proper separation between hydrocarbons up to C<sub>12</sub> was achieved, i.e., with grouping of paraffins, isoparaffins, olefins and aromatic molecules per carbon number, including the quantitative separation of the xylene isomers using a combination of suitable columns and FID/TCD detectors.

## 2.1.3 Determination of outlet composition, flow rates, conversions, selectivities and yields

For every experimental campaign performed within this work, the outlet flow consisted only of a gas phase and was analysed via gas chromatography. The raw data obtained from a gas chromatography, i.e., the peak surface areas were translated into the corresponding outlet flow rates, see section 2.1.3.1. Error analysis [15] has shown that the recommended procedure to calculate conversion, selectivities and product yields, is as follows:

1. Measured set-up outlet flow rates
2. Verification of mass balance(s)
3. Application of normalization method to calculate conversions and selectivities

First, the outlet flow rates are measured directly or indirectly, see section 2.1.3.2. From these measured set-up flow rates, the mass and elemental balances are verified, see section 2.1.3.3. If the mass and elemental balances are closed within 5%, the outlet flow rates are determined via the normalization method, see section 2.1.3.4. Normalizing the outlet flow rates leads to closed mass and element balances. Indirectly, it is assumed that the error on the balances are proportionally distributed over all flow rates. However, the error on the balances could be situated in the flow rate of a limited number of different components. Therefore, it should be verified that the balances are closed within 5% in order to minimize these effects on the further calculations. Finally, these 'normalized' outlet flow rates are used to calculate conversion, selectivities and product yields, see section 2.1.3.5.

### **2.1.3.1 Outlet composition**

As mentioned in previous paragraph, the set-up outlet composition obtained during the experimental campaigns always comprised either a gas phase or both gas and liquid phase and was determined using gas chromatography. Due to the component specific nature of the detectors used, i.e., FID and TCD, calibration factors are used to relate the measured peak surface areas  $A$  with the flow composition. In this work, the calibration factors were based upon work done by Dietz [16]. A calibration factor,  $CF$ , gives the relationship between a molar quantity and the measured peak area and is defined as their ratio. Depending on the experimental campaign, only one or several detectors were used. The next two

paragraphs explain how to determine the effluent composition in terms of molar fractions of a set-up operating at gas phase conditions for both cases.

- One detector

Ideally, the gas outlet composition is determined with only one detector when all components are qualitatively and quantitatively separated on the preceding column(s). Using the calibration factors,  $CF$ , the relative molar composition of the set-up gas outlet composition is calculated via:

$$y_k = \frac{A_k \cdot CF_k}{\sum_{j=1}^{n_{comp}} A_j \cdot CF_j} \quad 2-1$$

in which  $A_k$  is the peak surface area obtained from raw GC data. Subscripts  $k$  stands for component  $k$ . For the liquid composition,  $x_k$ , a similar relationship holds.

- Multiple detectors

When multiple detectors are used for determining the composition of a stream, several reference components, common to at least two of them are necessary to allow quantitative detection if not all components are visible on a single detector. In this work, a single reference component was visible on all detectors, see section 2.1.2.2. On each detector  $i$ , the relative molar fraction of component  $k$ ,  $y_k^i$  can be obtained by applying equation 2-1. Since the molar fraction of every component on a detector is determined relatively to every other component on that detector, the injection time or volume and detector type and settings will not influence this composition. Imagine the molar outlet flow rate of the reference component,  $F_{ref}$ , to be known. The molar outlet flow rate of a gas phase component can be related to that of the reference component:

$$F_k = F_{ref} \frac{y_k^i}{y_{ref}^i} \quad 2-2$$

The molar outlet fraction of component  $k$  is calculated as:

$$y_k = \frac{F_k}{\sum_{j=1}^{n_{comp}} F_j} \quad 2-3$$

Substituting equation 2-2 in equation 2-3 results in an expression for  $y_k$ , independent from

$F_{ref}$ :

$$y_k = \frac{F_{ref} \frac{y_k^i}{y_{ref}^i}}{\sum_{j=1}^{n_{comp}} F_{ref} \frac{y_j^i}{y_{ref}^i}} = \frac{\frac{y_k^i}{y_{ref}^i}}{\sum_{j=1}^{n_{comp}} \frac{y_j^i}{y_{ref}^i}} \quad 2-4$$

Of course, in the denominator each component should be considered only once.

Substituting equation 2-1 in equation 2-4 results in:

$$y_k = \frac{\frac{A_k^i \cdot CF_k}{A_{ref}^i \cdot CF_{ref}}}{\sum_{j=1}^{n_{comp}} \frac{A_j^i \cdot CF_j}{A_{ref}^i \cdot CF_{ref}}} \quad 2-5$$

Again, one and only one surface area should be considered per component over all parallel columns.

### 2.1.3.2 Measured set-up flow rates

To measure the set-up gas outlet flow rates, an internal standard was fed. The internal standard remained entirely in the gas phase, hence, the outlet molar flow rate of every component could be determined when the molar fraction of the component and the total molar outlet flow rate is known. The latter was calculated via the known inlet,  $F_{is}^0$ , and, thus, outlet flow rate of the internal standard:

$$F_k = \frac{F_{is}^0}{y_{is}} \cdot y_k \quad 2-6$$

To measure the set-up liquid outlet flow rates, a scale was used to follow up the mass flow rate  $\dot{m}^l$  and is calculated as:

$$F_k^l = x_k \cdot \frac{\dot{m}^l}{\sum_{j=1}^{n_{comp}} x_j \cdot M_j} \quad 2-7$$

with  $M_j$  the molecular mass of component  $j$ .

### 2.1.3.3 Mass and element balances

When the gas and/or liquid mass flow rates are measured either directly or indirectly, the mass and element balances, resp.  $\varphi_m$  and  $\varphi_e$  are verified:

$$\varphi_m = \frac{\dot{m}}{\dot{m}^0} \quad 2-8$$

$$\varphi_e = \frac{F_{e_t}}{F_{e_t}^0} \quad 2-9$$

By introducing the molar outlet flow rates of every component in each phase, the mass and element balances, e.g. for element  $t$ , can be written as:

$$\varphi_m = \frac{\sum_{j=1}^{n_{comp}} F_j^l \cdot M_j + \sum_{j=1}^{n_{comp}} F_j^g \cdot M_j}{\sum_{j=1}^{n_{comp}} F_j^0 \cdot M_j} \quad 2-10$$

$$\varphi_{e_t} = \frac{\sum_{j=1}^{n_{comp}} a_{t,j} \cdot F_j^l + \sum_{j=1}^{n_{comp}} a_{t,j} \cdot F_j^g}{\sum_{j=1}^{n_{comp}} a_{t,j} \cdot F_j^0} \quad 2-11$$

with  $a_{t,j}$  the number of element  $t$  in component  $j$ .

### 2.1.3.4 Outlet flow rates

The normalization method assumes a closed mass balance which should be verified before being applied. In case only a gas phase is present and the mass balance is assumed to be closed, i.e.

$$\dot{m}^0 = \dot{m} \quad 2-12$$

Equation 2-12 can be rewritten as:

$$\sum_{j=0}^{n_{comp}} F_j^0 \cdot M_j = \sum_{j=0}^{n_{comp}} F_j \cdot M_j \quad 2-13$$

and

$$F_{tot}^0 \sum_{j=0}^{n_{comp}} y_j^0 \cdot M_j = F_{tot} \sum_{j=0}^{n_{comp}} y_j \cdot M_j \quad 2-14$$

Solving this equation to  $F_{tot}$  gives:

$$F_k = y_k \cdot F_{tot}^0 \cdot \frac{\sum_{j=1}^{n_{comp}} y_j^0 \cdot M_j}{\sum_{j=1}^{n_{comp}} y_j \cdot M_j} \quad 2-15$$

If both a gas and liquid phase were present at the set-up outlet, a set of two equations should be solved simultaneously, e.g., the mass and an element balance:

$$\begin{aligned} \dot{m}^0 &= \dot{m}^l + \dot{m}^g \\ F^{l,0} \cdot \sum_{j=1}^{n_{comp}} x_j^0 \cdot M_j + F^{g,0} \cdot \sum_{j=1}^{n_{comp}} y_j^0 \cdot M_j &= F^l \cdot \sum_{j=1}^{n_{comp}} x_j \cdot M_j + F^g \cdot \sum_{j=1}^{n_{comp}} y_j \cdot M_j \end{aligned} \quad 2-16$$

and

$$\begin{aligned} F_{e_k}^0 &= F_{e_k}^l + F_{e_k}^g \\ F^{l,0} \cdot \sum_{j=1}^{n_{comp}} x_j^0 \cdot a_{k,j} + F^{g,0} \cdot \sum_{j=1}^{n_{comp}} y_j^0 \cdot a_{k,j} &= F^l \cdot \sum_{j=1}^{n_{comp}} x_j \cdot a_{k,j} + F^g \cdot \sum_{j=1}^{n_{comp}} y_j \cdot a_{k,j} \end{aligned} \quad 2-17$$

### 2.1.3.5 Conversion, selectivities and yields

The conversion of feed component  $k$ ,  $X_k$ , is defined on a molar basis:

$$X_k = \frac{F_k^0 - F_k}{F_k^0} \quad 2-18$$

The selectivity towards component  $k$  is defined on an elemental basis such as carbon, oxygen, hydrogen or even nitrogen, see Chen Qi [15]. The selectivity for component  $k$  originating from component  $v$  based on the element  $e_t$  is defined as:

$$S_{k,v} = \frac{a_{t,k} \cdot (F_k - F_k^0)}{a_{t,v} \cdot (F_v^0 - F_v)} \quad 2-19$$

with  $F_k^0$  the molar inlet flow rate of component  $k$ ,  $F_v$  the molar outlet flow rate of feed component  $v$  and  $a_{t,k}$  the number of  $t$  atoms in component  $k$ . Physically, this definition of selectivity can be translated as the fraction of element  $e_t$  being transferred to product  $k$  from  $v$  at a certain conversion of  $v$ . The product yields are determined on mass basis by multiplication of the conversion and the aforementioned product selectivities.

## 2.2 Modeling

### 2.2.1 A systematic methodology for kinetic modeling

The kinetic modeling of chemical reactions requires the combination of different fields of expertise, e.g., optimization theory [17], parameter estimation [18] and chemical reactor and reaction engineering [19, 20]. Several authors, e.g., Box et al., Froment et al., Buzzi-Ferraris et al., Stewart et al. ... have reported general techniques and methodologies for this purpose. For example, several methods for multiresponse parameter estimation by applying Bayesian theory [21-23] or least squares are reported [24]. The reformulation and analysis of kinetic models, including the handling of outliers, model discrimination and experimental design is also extensively discussed [25-27]. With the increased use of computers in the course of previous decades, a number of regression software packages were specifically developed for chemical kinetics modeling [28-30]. While all literature cited excels in describing these techniques, no work seems to be available which combines these techniques in an applied manner, i.e., from data processing to an adequate kinetic model.

In this section, a systematic methodology for chemical kinetics modeling is proposed. It aims at maximizing the amount of information that can be retrieved while minimizing the effort. The model that is most closely corresponding to the physical reality is likely to be much more complex than the statistically most relevant one. It is important to acquire a good balance between what is physically meaningful and statistically required. The parameters obtained by regression should have a clear physical meaning with confidence intervals of an acceptable size, i.e., at least inferior to the parameter value itself [31]. Also, the model adequacy should be verified to evaluate the extent to which the model exhibits systematic deviations from the experimental observations.

The methodology comprises three main steps after having acquired the experimental data: data analysis, regression and a physical and statistical assessment, see Figure 2-2. Model discrimination and sequential experimental design are potential add-ons that are incorporated in the figure but not further addressed in the present work.



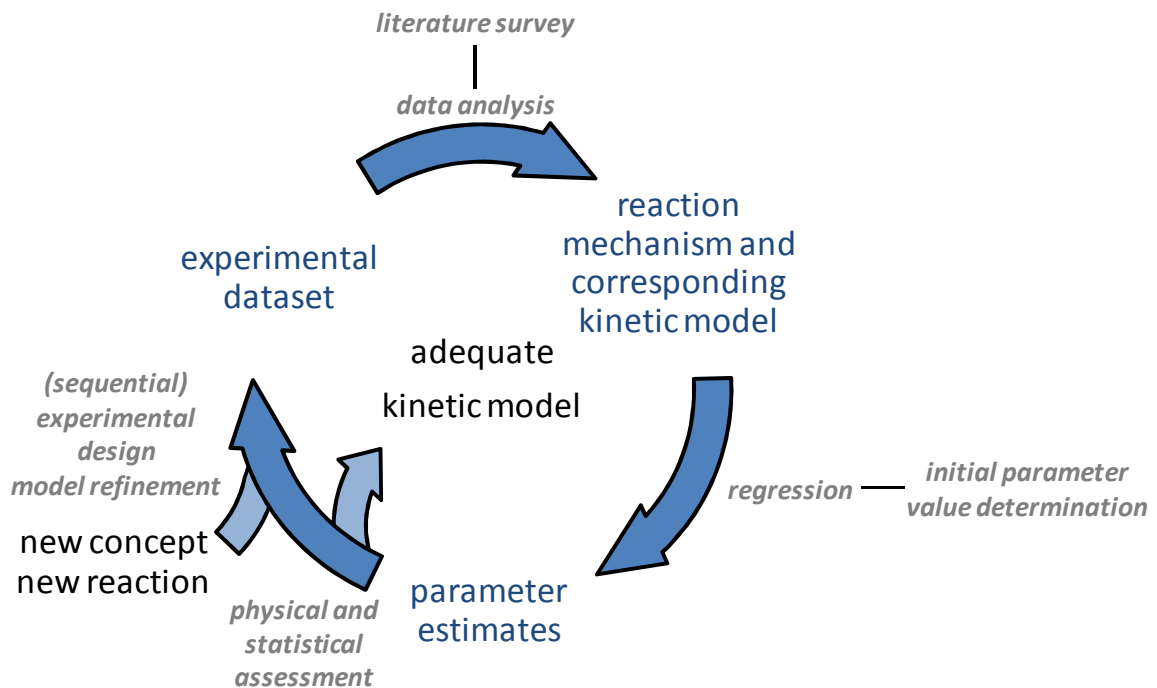


Figure 2-2: Proposed procedure for kinetic modeling

### 2.2.1.1 Data analysis and model construction

Prior to setting up a kinetic model, experimental data are needed which contain the necessary information to construct a kinetic model and to determine the corresponding kinetic parameters, see Figure 2-2.

One option to extract the valuable information from the experimental data is to plot the dependent variables, e.g., molar outlet flow rates, conversions, selectivities, as function of the independent variables such as reaction temperature, inlet partial pressures, space-time... The observed trend as function of the independent variables can then be used to evaluate apparently required functional relationships and corresponding potential reaction mechanisms [25].

A more specific option for information extraction is to apply the method of initial rates [19]. Several kinetic models may be proposed depending on which of the elementary steps is considered to be rate determining, e.g., adsorption, desorption or surface reaction. Within the method of initial rates, differential experimental data, i.e., data obtained at conversion and space-time close to zero, are plotted against the independent variables, more particularly the reactant partial pressure or the total pressure. The trend obtained is compared to that exhibited by the different models which can lead to an initial model discrimination. Other methods are also reported in literature which are based on the use of

so-called intrinsic parameters, i.e., obtained when rewriting the rate expressions in terms of fractional coverages [32].

As indicated by Figure 2-2, from the knowledge gained by data analysis and literature, a reaction network and mechanism can be constructed and the corresponding rate-equations are derived .

### **2.2.1.2 Regression**

After the data analysis and model construction, the model(s) can be regressed to the experimental data. However, due to the typical non-linear character of kinetic models, it is important to have good initial guesses for the parameter estimates. If the initial guesses for the parameter estimates are too remote from the true values, the optimization routine might end up in a local extremum. Good initial parameter values can be obtained by linearization of the model, e.g., through an isothermal regression, see section 2.2.3.1, or from a literature survey or ab-initio calculations [33].

During regression, typically a residual sum of squares is minimized or a probability density function is maximized. The objective function should be carefully defined in accordance with the problem formulation and may require the introduction of weights [26]. In order to identify the optimum of the objective function, various optimization routines are available in literature such as the Rosenbrock [34] and Levenberg-Marquardt algorithm [35].

### **2.2.1.3 Physical and statistical assessment**

Having performed the regression, the model performance and corresponding parameters, should be evaluated, see Figure 2-2. These tests are two-fold, i.e., assessing the physical meaning and verifying statistical significance.

For the model, the physical meaning and statistical significance can be assessed by analyzing the residuals, as described in section 2.2.5. The parity diagram and residual and normal probability figure are mostly used to determine the statistical significance while the performance figure is used to assess the physical meaning of the model. Additionally, statistical tests can be performed for model significance and adequacy, see section 2.2.4.

For the kinetic parameters, also both the physical meaning and statistical significance should be investigated. The first can be done by verifying if the values obtained are in line with what can be expected on physical grounds, e.g., the reaction order estimated is sensible, the activation energy obtained has a positive value... The latter is assessed by the actual value of

the parameter estimate in combination with the corresponding confidence interval, which should not include zero. If so, this parameter is deemed to be statistically insignificant and could be excluded from the kinetic model. It must be kept in mind, however, that a statistically insignificant parameter does not necessarily correspond to a step that does not contribute to the model. Such a parameter may correspond to a step which is so fast that the actual rate is irrelevant, as long as it is sufficiently high compared to the other elementary steps in the reaction mechanism.

All these assessments can be used to determine any shortcomings in the model, which may be, but not limited to, missing reaction steps or whether the set of parameter values obtained is only a local optimum. Therefore, the kinetic model can be reformulated based on the assessment or additional experiments can be performed, preferentially via sequential experimental design, see Figure 2-2. If both the physical and statistical significance are fulfilled and, hence, no additions or corrections to the model are necessary, the procedure is considered to be converged and the modeling as finalized.

## 2.2.2 Reactor models

### 2.2.2.1 *Continuous stirred tank reactor*

For a steady-state ideal continuous stirred tank reactor, the outlet molar flow rates are described by a set of algebraic equations:

$$F_i = F_i^0 + R_i W \quad i = 1 \dots n_{comp} \quad 2-20$$

with  $W$  the catalyst mass and  $R_i$  the net rate of formation of component  $i$ . This set of differential equations is solved by DDASPK [36].

### 2.2.2.2 *Plug flow reactor*

For a steady-state ideal plug flow reactor, the molar flow rates in a point of the reactor are described by a set of differential equations:

$$\frac{dF_i}{dW} = R_i \quad i = 1 \dots n_{comp} \quad 2-21$$

This set of differential equations is solved by DDASPK [36] with the following initial conditions:

$$W = 0 \rightarrow F_i = F_i^0 \quad 2-22$$

Inert components, e.g., nitrogen, are not explicitly accounted for in this set of differential equations since the net rate of formation of these components equals zero.

## 2.2.3 Parameter estimation

The model parameter vector  $\underline{b}$  was estimated by the minimization of the weighted sum of squared residuals,  $SSQ$ :

$$SSQ = \sum_{i=1}^{n_{\text{exp}}} \sum_{j=1}^{n_{\text{resp}}} w_j (\hat{Y}_{i,j} - Y_{i,j})^2 \xrightarrow{b} \text{Min} \quad 2-23$$

in which  $n_{\text{exp}}$  and  $n_{\text{resp}}$  are resp. the number of experiments and responses,  $w_j$  the statistical weight attributed to response  $j$ , and  $\hat{Y}_{i,j}$  and  $Y_{i,j}$  resp. the corresponding model calculated and experimental response value. The statistical weights were determined from the inverse of the covariance matrix of the experimental errors:

$$w_j = \frac{1}{\sigma_{jj}^2} = \left[ \frac{\sum_{i=1}^{n_{\text{exp}}} (\hat{Y}_{i,j} - Y_{i,j})^2}{n_{\text{exp}} \cdot n_{\text{resp}} - n_{\text{par}}} \right]^{-1} \quad 2-24$$

By adjusting the value for the parameter vector  $\underline{b}$ , while minimizing the  $SSQ$ ,  $\underline{b}$  will converge to the true parameter vector  $\underline{\beta}$ . The  $SSQ$  minimization was performed by use of a Rosenbrock [34] followed by a Levenberg-Marquardt algorithm [35]. The former is more robust against divergence and is used for bringing the parameter values in the neighborhood of the optimal parameters while the latter is applied for reaching the true minimum of the  $SSQ$ .

### 2.2.3.1 Isothermal vs. non-isothermal regression

When performing a regression, the goal is to determine the set of optimal parameters corresponding to the global minimum of the objective function. In many cases, the objective function also contains several local extrema. It is possible that, by choosing a certain set of initial parameter values, the final set of parameters obtained from regression is situated in a local minimum. Sometimes, this will not be evident from the model performance since it may seem to be adequate. This is more likely the case in highly non-linear models, e.g.,

when using the Arrhenius or van 't Hoff relation for describing the temperature dependence of a rate or equilibrium coefficient.

If sufficient isothermal kinetic data, i.e., a subset of kinetic data in which the temperature is constant, are available, a regression per temperature to these subset(s) of experimental data can be performed. This is also denoted as isothermal regression. This has several advantages. Firstly, per rate coefficient only one parameter needs to be estimated rather than two, i.e., the rate coefficient itself, rather than the pre-exponential factor and the reaction enthalpy or activation energy. Secondly, the regression of an isothermal model which can be linearized, results in a linear regression for which a priori no initial estimates are required. By performing the isothermal regression, a value for each rate and/or equilibrium coefficient is obtained at every temperature. The coefficients obtained at every temperature can then be used to construct so-called Arrhenius and van 't Hoff plots, see resp. equation 2-25 and 2-26.

$$k = A \exp\left(-\frac{E_a}{RT}\right) \xrightarrow{\ln} \ln(k) = \ln(A) - \frac{E_a}{R} \frac{1}{T} \quad 2-25$$

$$K = A \exp\left(\frac{\Delta H}{RT}\right) \xrightarrow{\ln} \ln(K) = \ln(A) + \frac{\Delta H}{R} \frac{1}{T} \quad 2-26$$

Linear regression of these isothermally determined parameter estimates yields a value for the slope and intercept which are a measure for resp. the activation energy or reaction enthalpy and pre-exponential factor, see equation 2-27.

$$\sum_{i=1}^{n_{par}} \left( k_i - A \exp\left(-\frac{E_a}{RT}\right) \right)^2 \xrightarrow{A, E_a} Min \quad 2-27$$

These values typically serve as initial parameter values in the non-isothermal regression in which all data are simultaneously assessed and where the Arrhenius and van 't Hoff relationships are directly implemented. This last regression is typically considered to be the actual one since the parameters are estimated based on the minimization of the residual sum of squares of the directly observed values, see equation 2-28.

$$\sum_{i=1}^{n_{exp}} \left( F_i - \hat{F}_i \right)^2 \xrightarrow{A, E_a} Min \quad 2-28$$

This is the only regression which is supposed to allow determining the global extremum of the objective function, however, the above described procedure starting with isothermal regressions provides the most suitable initial guesses for this non-isothermal regression.

### 2.2.3.2 Reparameterization of the Arrhenius and Van't Hoff equation

In the Arrhenius and van 't Hoff relation, a pronounced correlation is typically found between the pre-exponential factor and activation energy or reaction enthalpy. To overcome the corresponding regression issues, reparameterized versions of these relations are used in which the rate or equilibrium coefficient at the mean temperature is used, see resp. equation 2-29 and 2-30 [37]. The concept of reparameterization is also illustrated in Figure 2-4. The 'classical', unreparameterized and reparameterized Arrhenius relation is used in resp. the left and right Arrhenius plot in Figure 2-4 to determine the kinetic parameters. In case of the unreparameterized Arrhenius relation it is clear that the activation energy, i.e., the slope of the line, will compensate for the pre-exponential factor value, i.e., the intersection with the y-axis (at  $x = 0$ ). In contrast to this, with the reparameterized Arrhenius relation, a change of the rate coefficient at mean temperature cannot be compensated by any change in activation energy.

$$k = k_{T_m} \cdot \exp\left(-\frac{E_a}{R}\left(\frac{1}{T} - \frac{1}{T_m}\right)\right) \quad 2-29$$

$$K = K_{T_m} \cdot \exp\left(\frac{\Delta H}{R}\left(\frac{1}{T} - \frac{1}{T_m}\right)\right) \quad 2-30$$

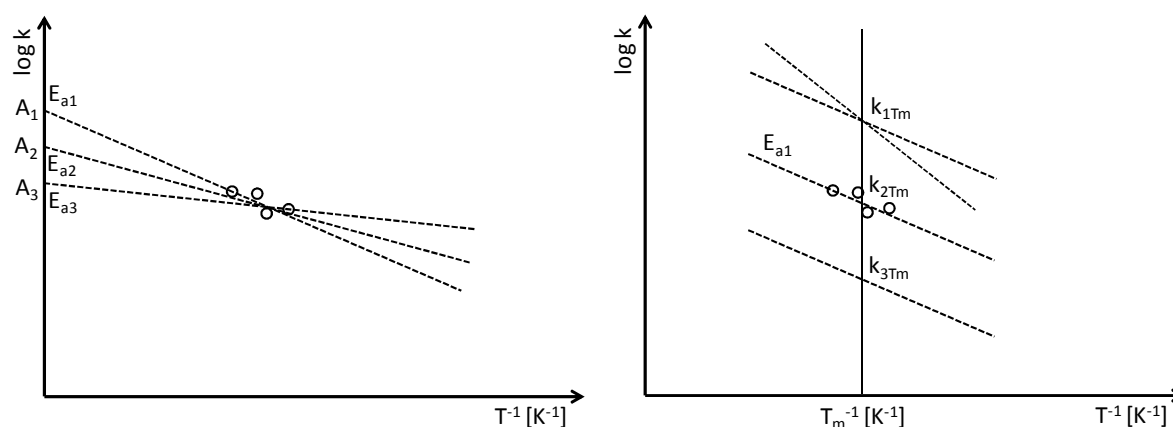


Figure 2-3: Arrhenius plot for the unreparameterized Arrhenius relation (left) and the reparameterized Arrhenius relation (right).

## 2.2.4 Statistical and physical assessment of the model and parameter estimates

The model significance is typically verified by testing the null hypothesis that all parameters would simultaneously be equal to zero, via an  $F$  test [24, 30]. In this  $F$  test, the ratio of the

mean regression sum of squares and the mean residual sum of squares is taken, see equation 2-28.

$$F_s = \frac{\frac{SSQ_{REG}}{d.f. \cdot REG}}{\frac{SSQ_{RES}}{d.f. \cdot RES}} = \frac{\frac{\sum_{i=1}^{n_{resp}} \sum_{j=1}^{n_{exp}} \hat{Y}_{i,j}^2}{n_{par}}}{\frac{\sum_{i=1}^{n_{resp}} \sum_{j=1}^{n_{exp}} (Y_{i,j} - \hat{Y}_{i,j})^2}{n_{exp} n_{resp} - n_{par}}} \quad 2-31$$

If the calculated value exceeds the tabulated  $F$  value at a selected confidence level, e.g., 95%, with the corresponding degrees of freedom, the null hypothesis is rejected and the model is deemed to be significant. In practice, the above mentioned null hypothesis is easily rejected, and, hence, for having a reliable assessment of the model significance, the calculated  $F$  values should at the very least be of the order of magnitude of 100.

The model's adequacy is assessed by evaluating if the deviation between the experimental observations and model prediction can be attributed solely to experimental errors and not to a lack-of-fit of the model. If a lack-of-fit is present, systematic deviations between the model calculated and observed values occur. The model's adequacy is determined by partitioning the residuals' sum of squares, i.e., the difference between model calculated and observed values, into a pure-error sum of squares,  $SSQ_{PE}$ , as determined by repeat experiments, and a lack-of-fit sum of squares,  $SSQ_{LOF}$  [37]:

$$SSQ_{RES} = SSQ_{LOF} + SSQ_{PE} \quad 2-32$$

The pure-error sum of squares is determined by repeat experiments as follows:

$$SSQ_{PE} = \sum_{i=1}^k \sum_{j=1}^{n_{resp}} \sum_{l=1}^{n_e(i)} (y_{j,l}^{(i)} - \bar{y}_j^{(i)})^2 \quad 2-33$$

with  $k$  the number of different sets of repeat experiments,  $n_e(i)$  the number of repeat experiments at the  $i^{\text{th}}$  set of repeat experiments,  $y_{j,l}^{(i)}$  the  $i^{\text{th}}$  experimental observation corresponding to the  $j^{\text{th}}$  set of repeat experiments and the  $j^{\text{th}}$  response and  $\bar{y}_j^{(i)}$  the average value of the  $i^{\text{th}}$  set of repeat experiments and the  $j^{\text{th}}$  response. The corresponding degrees of freedom are given by:

$$d.f. \cdot PE = n_{resp} \sum_{i=1}^k (n_e(i) - 1) \quad 2-34$$

The ratio of the lack-of-fit and pure-error sum of squares follows an  $F$  distribution with the corresponding degrees of freedom under the hypothesis that the model is adequate, see equation 2-35.

$$F_a = \frac{\frac{SSQ_{LOF}}{d.f. \cdot LOF}}{\frac{SSQ_{PE}}{d.f. \cdot PE}} \quad 2-35$$

If the calculated  $F$  value exceeds the corresponding tabulated  $F$  value, the model is not adequate. In contrast to the test for the global significance of the model, the model adequacy test is very difficult to be fulfilled, particularly for models that are non linear in the parameters.

The significance of every individual parameter is tested by means of a  $t$  test. In most cases, the value against which a parameter estimate is tested is zero. It is, hence, tested, if the confidence interval comprises the zero value or not. The  $t$  value is calculated by the ratio of the parameter value and its standard deviation  $s(b_i)$ :

$$t(b_i) = \frac{b_i}{s(b_i)} \quad 2-36$$

If the calculated value exceeds the tabulated value at a selected confidence level, e.g., 95%, with  $n_{exp} \cdot n_{resp} - n_{par}$  degrees of freedom, the parameter is considered to be significantly different from zero. In practice, good  $t$  values are in the order of 10 to 100.

The binary correlation coefficient between two parameters  $i$  and  $j$  is calculated via the (co-)variances of these parameters,  $V(b)$ , see equation 2-37. Two parameters  $i$  and  $j$  are strongly correlated if  $|\rho_{i,j}| \geq 0.95$ .

$$\rho_{i,j} = \frac{V(b)_{i,j}}{\sqrt{V(b)_{i,i} V(b)_{j,j}}} \quad 2-37$$

Besides a statistical assessment of the model and the parameter estimates, the physical significance of both should be evaluated. The physical meaning of the model is reflected in the qualitative prediction of the effect of changing reaction conditions. Additionally, the model should not result in physically unrealistic predictions. The physical meaning of the individual parameter estimates can be determined by validating if the order of magnitude of the parameter value and its sign are acceptable. If needed, literature reported values can assist in this.



## 2.2.5 Residual analysis

Model performance can be assessed using statistical tests such as the  $F$  test for the model adequacy if an estimate of the error variance is available from repetition experiments. Another method is to perform a residual analysis in which it is verified to what extent the residuals adopt the assumed behavior for the experimental error, i.e., a zero mean and constant variance. A residual is the numerical difference between the simulated and the experimental values. Residual analysis is a general term in which, among others, the following tools can be included: parity diagrams, performance figures, residual figures and normal probability figures. All these tools are illustrated in what follows making use of a theoretical example, according to the very simple model  $y = x$ . Of course in the 'measured' variable  $y$  an experimental error  $e$  is included. 4 models are proposed to simulate the response  $y$  as a function of the independent variable  $x$  and the error  $e$ :

$$\begin{array}{llll}
 \text{(a)} & y = x + e & x = \{0 \dots 100\} & e \propto N(0, \sigma = 5) \\
 \text{(b)} & y = ax^2 + x + e & x = \{0 \dots 100\} & e \propto N(0, \sigma = 5) \quad a = 0.07 \\
 \text{(c)} & y = x + e & x = \{0 \dots 100\} & e \propto t(5) \\
 \text{(d)} & y = x + e & x = \{0 \dots 100\} & e \propto N(3, \sigma = 5)
 \end{array}$$

The reference model is represented by model (a), i.e., the adequate model predicting  $y$ , in which the error,  $e$ , is normally distributed with expected value 0 and a constant variance  $\sigma$ . (b) is an inadequate model due to a redundant quadratic term. (c) represents a model without a systematic deviation in which the error is not normally distributed, but according to a two-tailed  $t$ -distribution with the number of degrees of freedom equal to 5. Finally, (d) is an inadequate model with a normally distributed error with a systematic deviation amounting to 3.

### 2.2.5.1 Parity diagram

A parity diagram is a 2-dimensional scatter plot in which the model calculated values of the responses are displayed against the experimentally observed values. Investigating the distribution of the scatter points around the first bisector allows determining the model's adequacy and the error distribution. If the model is adequate and the assumptions made with respect to the experimental error are valid, meaning that the errors are distributed normally with an expected value of zero and a constant standard deviation, the model

calculated values should be distributed normally around this first bisector, see Figure 2-5(a). For a non-adequate model the simulated values exhibit a systematic deviation, see Figure 2-5(b). A non-normal statistical distribution of the experimental errors which resembles a normal distribution, e.g., a 2-tailed  $t$ -distribution, can lead to a seemingly acceptable parity diagram although the error distribution assumptions are not valid, see Figure 2-5(c). If the experimental error is normally distributed with an expected value  $E(e)$  different from zero, the model calculated values will be normally distributed around the imaginary line constructed  $E(e)$  units transposed above the first bisector, see Figure 2-5(d).

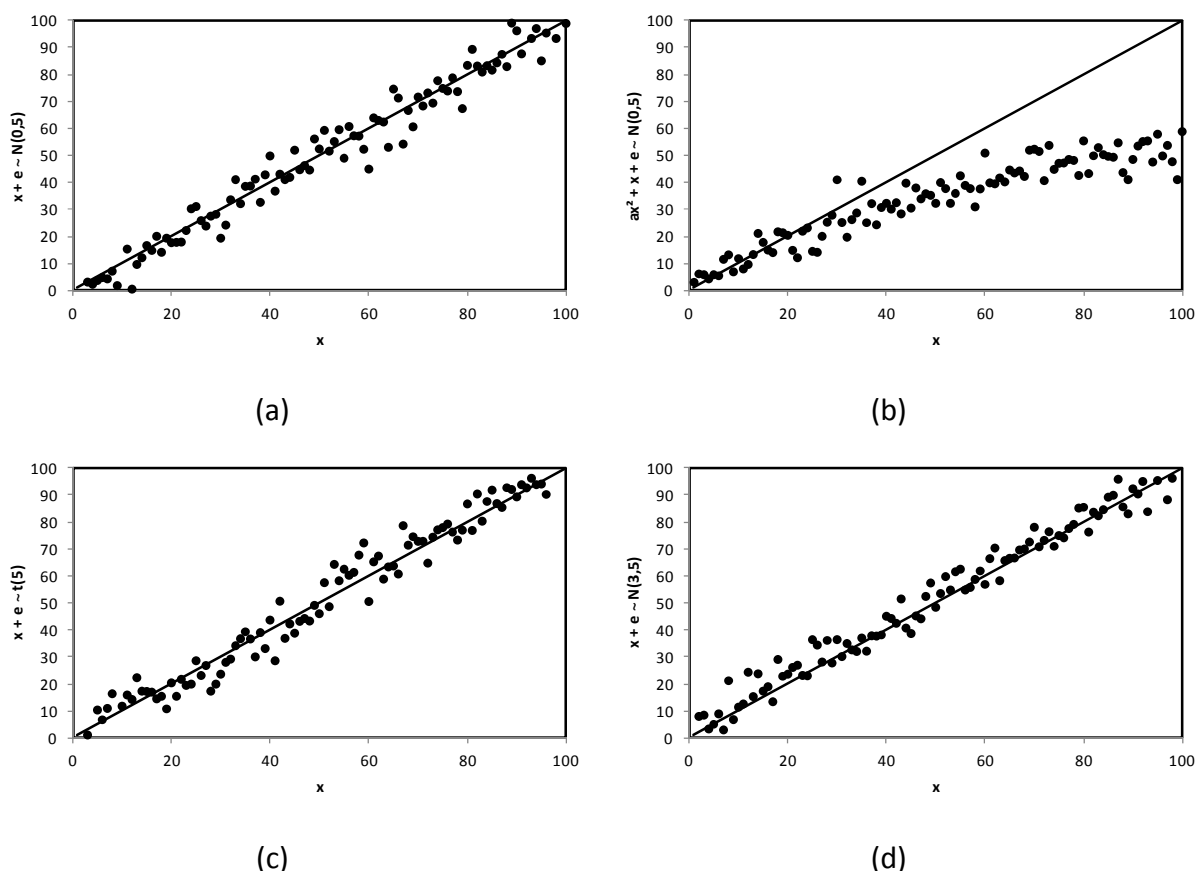


**Figure 2-4: Parity diagrams for 4 theoretical cases: (a) adequate model with a normal distributed error with expected value equal to zero, (b) inadequate model with a normal distributed error with expected value equal to zero, (c) adequate model with a two-tailed  $t$ -distributed error and (d) adequate model with a normal distributed error with expected value equal to three**

### 2.2.5.2 Performance figure

In a performance figure, the response values, both experimentally observed as well as model calculated ones, are displayed against an independent variables, e.g., conversion as a function of space-time. The experimental values are represented by symbols including an indication of the error on the measurement, e.g., a variance determined from repetition

experiments, while the model calculated values are plotted as a continuous function. Such a performance figure typically provides more detailed information on the agreement between model simulations and experimental data compared to a parity diagram. From a performance figure, the effect of the reaction conditions on the simulated values and the corresponding residuals can be thoroughly analyzed while a parity diagram integrates all this information in a single figure.

### ***2.2.5.3 Residual figure***

A residual figure is a 2-dimensional scatter plot in which the residuals, i.e., the differences between the model simulated values and the observed values, are put against the independent (or dependent) variable values. It contains mainly information on the occurrence of systematic deviations, i.e., the model adequacy. Information on the error distribution can also be obtained from these figures. If the experimental error is normally distributed, the residuals should be distributed normally over the x-axis in these residual figures, see Figure 2-6(a). If the model is adequate, systematic deviations from this normal distribution as function of the independent variable values are absent. If present, they can provide strategic information on the origin of the model inadequacy. For example, a systematic increase of the residual of a product outlet flow rate as function of the reaction temperature can indicate that an activation energy determining the production rate of this product is too high. Other model inadequacies, e.g., redundant terms in the model equation, can also be indicated by these plots, see Figure 2-6(b). Deviations from the standard normal distribution are also sometimes detectable, see Figure 2-6(d).

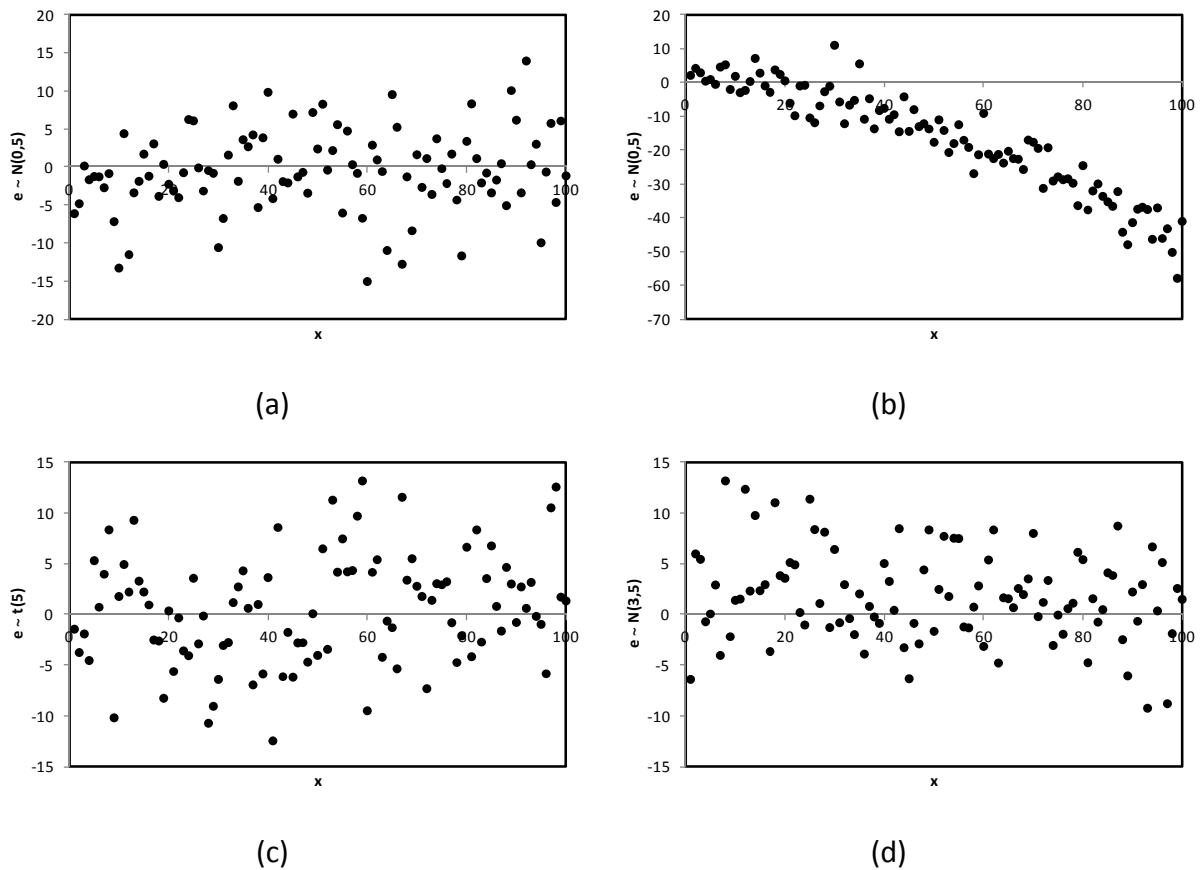


**Figure 2-5: Residual figures for 4 theoretical cases: (a) adequate model with a normal distributed error with expected value equal to zero, (b) inadequate model with a normal distributed error with expected value equal to zero, (c) adequate model with a two-tailed  $t$ -distributed error and (d) adequate model with a normal distributed error with expected value equal to three.**

#### **2.2.5.4 Normal probability figure**

A normal probability figure is a 2-dimensional scatter plot in which the ordered residuals, i.e., residuals ordered from lowest to highest value, are displayed against the theoretical quantile values, which are points dividing the cumulative distribution function into equal portions. It provides the most objective information on the error distribution. If linear regression of these points leads to an adequate result, e.g.,  $R^2 > 0.97$  [38], the error is considered to be normally distributed with an expected value equal to zero, see Figure 2-7(a). A non-adequate model, i.e., a model containing systematic deviations, can still lead to near acceptable linear regression results of the normal probability figure based upon the  $R^2$  value, see Figure 2-7(b). However; visually these shortcomings are more easily noticeable. Non-normal error distributions are fairly easily detected by the construction of a normal probability figure. If the error is distributed according to a two-tailed  $t$  distribution, pronounced deviations as a result of these tails will be present in the normal probability figure due to the nature of this distribution, as is clearly indicated in Figure 2-7(c). Another

example is given in Figure 2-7(d) where the expected value of the error is different from zero. A model leading to a normal probability plot from which it is concluded that the residuals are normally distributed will typically also be evaluated as an adequate model. It should be noted, however, that such a correspondence between the interpretation of a normal probability plot and the model adequacy test cannot be mathematically demonstrated, but that it can be expected to hold for all practical purposes.

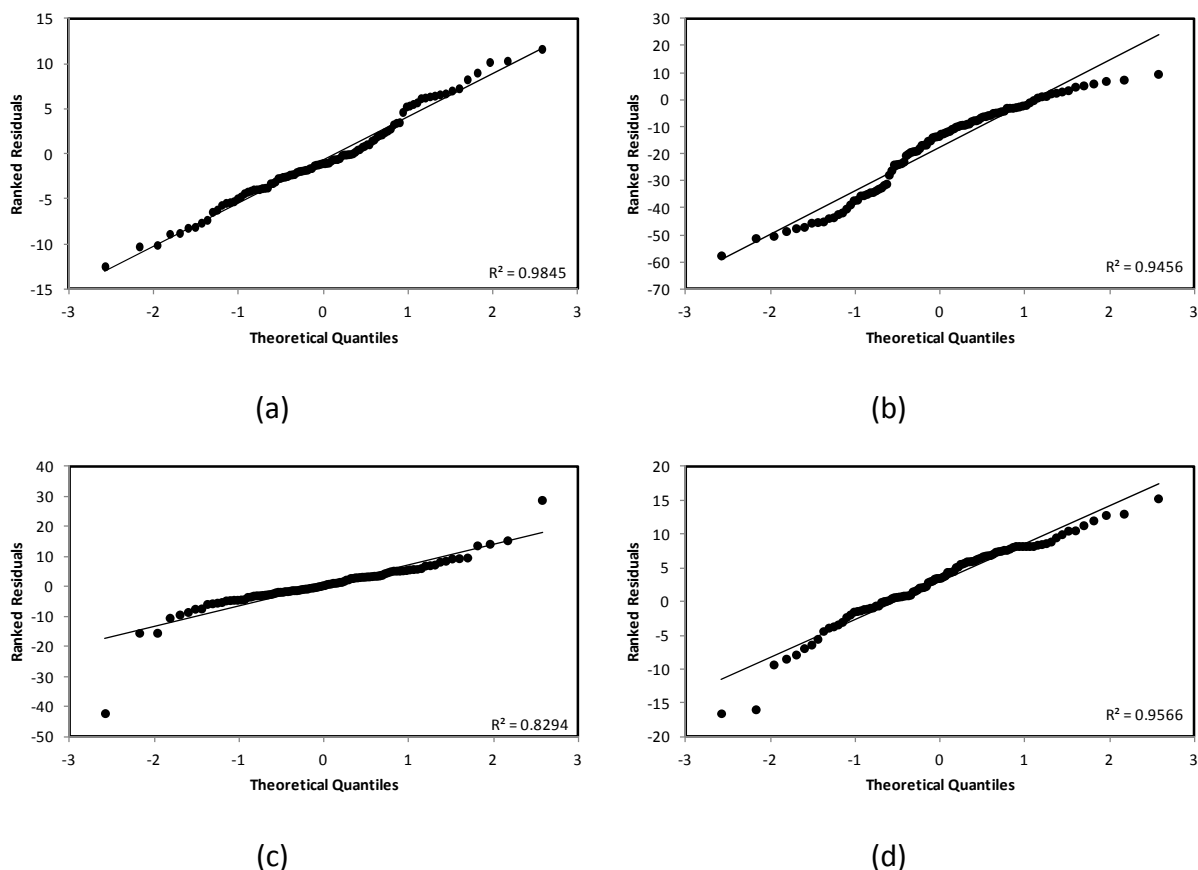


**Figure 2-6: Normal probability figures for 4 theoretical cases: (a) adequate model with a normal distributed error with expected value equal to zero, (b) inadequate model with a normal distributed error with expected value equal to zero, (c) adequate model with a two-tailed  $t$ -distributed error and (d) adequate model with a normal distributed error with expected value equal to three**

## 2.2.6 Single-Event MicroKinetic (SEMK) methodology

In the Single-Event MicroKinetic methodology, a unique single-event rate coefficient  $\tilde{k}$  is assigned to each elementary reaction family. The single-event rate coefficient is assumed to only depend on the reaction family of the elementary step, e.g., 1,2-alkyl shift, alkylation... and the types of carbenium ions involved. This is obtained by explicitly accounting for the symmetry of the transition state and of the reactants:

$$k = n_e \cdot \tilde{k} \quad 3-38$$

with,  $n_e$ , the number of single events defined as the ratio of the global symmetry number  $\sigma_{gl}$  of the reactant to that of the transition state:

$$n_e = \frac{\sigma_{gl}^r}{\sigma_{gl}^\ddagger} \quad 3-39$$

The global symmetry number  $\sigma_{gl}$  is calculated as follows:

$$\sigma_{gl} = \frac{\sigma_{int}\sigma_{ext}}{2^{n_{chir}}} \quad 3-40$$

with  $\sigma_{int}$  and  $\sigma_{ext}$  being, respectively, the internal and external symmetry number and  $n_{chir}$  the number of chiral atoms. Using this single event concept, the number of rate coefficients required to describe the chemical kinetics in complex mixtures is reduced drastically. This is described more extensively in previous work [39-43].

The fundamental character of the model makes that the model parameters have a precise physical meaning and, hence, that a distinction can be made between so-called catalyst and kinetic descriptors. Catalyst descriptors are model parameters which are directly related to catalyst properties, e.g., acid site strength, pore volume... Where possible, catalyst characterization techniques such as  $\text{NH}_3\text{-TPD}$ ,  $\text{BET}$  measurements... can be used to determine the catalyst descriptors independently from the reaction kinetics and, hence, the kinetic descriptors. The latter are parameters which are directly related to the reaction families and are independent of the catalyst used, e.g., activation energies [42].

## 2.3 References

- [1] P. Kumar, J.W. Thybaut, S. Teketel, S. Svelle, P. Beato, U. Olsbye, G.B. Marin, *Catalysis Today*. 215 (2013) 224-232.
- [2] H. Robson, *Verified Synthesis of Zeolitic Materials*, Elsevier, 2001.
- [3] J. Heveling, C.P. Nicolaidis, M.S. Scurrill, *Applied Catalysis a-General*. 173 (1998) 1-9.
- [4] A. Finiels, F. Fajula, V. Hulea, *Catalysis Science & Technology*. 4 (2014) 2412-2426.
- [5] NIST Standard Reference Database Number 69.
- [6] A. Sarkar, D. Seth, M. Jiang, F.T.T. Ng, G.L. Rempel, *Topics in Catalysis*. 57 (2014) 730-740.
- [7] A. Martinez, M.A. Arribas, P. Concepcion, S. Moussa, *Applied Catalysis a-General*. 467 (2013) 509-518.
- [8] R. Van Borm, A. Aerts, M.F. Reyniers, J.A. Martens, G.B. Marin, *Industrial & Engineering Chemistry Research*. 49 (2010) 6815-6823.
- [9] J.M. Berty, *Chemical Engineering Progress*. 70 (1974) 78-85.
- [10] M. Steijns, G. Froment, P. Jacobs, J. Uytterhoeven, J. Weitkamp, *Industrial & Engineering Chemistry Product Research and Development*. 20 (1981) 654-660.

- [11] M. Steijns, G.F. Froment, *Industrial & Engineering Chemistry Product Research and Development*. 20 (1981) 660-668.
- [12] N. Navidi, J.W. Thybaut, G.B. Marin, *Applied Catalysis a-General*. 469 (2014) 357-366.
- [13] R.J. Berger, E.H. Stitt, G.B. Marin, F. Kapteijn, J.A. Moulijn, *Cattech*. 5 (2001) 30-60.
- [14] K.M. Van Geem, S.P. Pyl, M.F. Reyniers, J. Vercammen, J. Beens, G.B. Marin, *Journal of Chromatography A*. 1217 (2010) 6623-6633.
- [15] Q. Chen, Internal report Eindhoven University of Technology - Final Version (1992).
- [16] W.A. Dietz, *Journal of Gas Chromatography*. 5 (1967) 68-&.
- [17] T.F. Edgar, D.M. Himmelblau, L. Lasdon, *Optimization of Chemical Processes*, McGraw-Hill Higher Education, 2001.
- [18] Y. Bard, *Nonlinear Parameter Estimation*, Academic Press, 1974.
- [19] G.F. Froment, K.B. Bischoff, J. De Wilde, *Chemical reactor analysis and design*, 2010.
- [20] G.B. Marin, G.S. Yablonsky, *Kinetics of Chemical Reactions: Decoding Complexity*, 2011.
- [21] G.E.P. Box, N.R. Draper, *Biometrika*. 52 (1965) 355.
- [22] M.J. Box, N.R. Draper, *Annals of Mathematical Statistics*. 41 (1970) 1391.
- [23] M.J. Box, N.R. Draper, W.G. Hunter, *Technometrics*. 12 (1970) 613.
- [24] G.F. Froment, L.H. Hosten, in: J. Anderson, M. Boudart (Eds.), *Catalysis Science and Technology*, 1981.
- [25] G. Buzzi-Ferraris, *Catalysis Today*. 52 (1999) 125-132.
- [26] G. Buzzi-Ferraris, F. Manenti, *Chemical Engineering Science*. 64 (2009) 1061-1074.
- [27] G. Buzzi-Ferraris, F. Manenti, *Computers & Chemical Engineering*. 34 (2010) 1904-1906.
- [28] BzzMath: Numerical libraries in C++, <http://www.chem.polimi.it/homes/gbuzzi>.
- [29] G. Buzzi-Ferraris, F. Manenti, 22 European Symposium on Computer Aided Process Engineering. 30 (2012) 1312-1316.
- [30] W.E. Stewart, M. Caracotsios, *Computer-Aided Modeling of Reactive Systems*, John Wiley & Sons, Inc., 2008.
- [31] M. Boudart, *Industrie Chimique Belge-Belgische Chemische Industrie*. 31 (1966) 74.
- [32] J.R. Kittrell, R. Mezaki, *Aiche Journal*. 13 (1967) 389.
- [33] A. vandeRunstraat, J. vanGrondelle, R.A. vanSanten, *Industrial & Engineering Chemistry Research*. 36 (1997) 3116-3125.
- [34] H.H. Rosenbrock, *Computer Journal*. 3 (1960) 175-184.
- [35] D.W. Marquardt, *Journal of the Society for Industrial and Applied Mathematics*. 11 (1963) 431-441.
- [36] Netlib, <http://www.netlib.org>, (2012).
- [37] J.R. Kittrell, *Advances of Chemical Engineering*. 8 (1970).
- [38] Athena Visual Studio, Web page <http://www.athenavisual.com/>.
- [39] G.G. Martens, G.B. Marin, J.A. Martens, P.A. Jacobs, G.V. Baroni, *Journal of Catalysis*. 195 (2000) 253-267.
- [40] G.D. Svoboda, E. Vynckier, B. Debrabandere, G.F. Froment, *Industrial & Engineering Chemistry Research*. 34 (1995) 3793-3800.
- [41] J.W. Thybaut, G.B. Marin, *Chemical Engineering & Technology*. 26 (2003) 509-514.
- [42] J.W. Thybaut, G.B. Marin, *Journal of Catalysis*. 308 (2013) 352-362.
- [43] J.W. Thybaut, G.B. Marin, G.V. Baron, P.A. Jacobs, J.A. Martens, *Journal of Catalysis*. 202 (2001) 324-339.





# Chapter 3

## Kinetic Modeling of *n*-Hexane Hydroisomerization on a Bifunctional zeolite

---

In this chapter, the systematic methodology developed in chapter 2 is demonstrated by applying it to a model reaction involving a limited reaction network and an established reaction mechanism, i.e., *n*-hexane hydroisomerization over a bifunctional zeolite such as platinum impregnated H-ZSM-5 [1-7]. While the acid function provided by the H-ZSM-5 zeolite framework provokes skeletal rearrangement and cracking, the metal function enables operating at relatively low temperatures and avoiding deactivation by coking. In order to acquire the most details as possible about the acid catalyzed reaction mechanism, the experimental investigation was performed at gas phase conditions under which ideal hydrocracking occurs [3, 5, 6, 8-12]. When performing experiments within such a range of operating conditions, the acid catalyzed reactions are rate determining, leading to specific kinetic behavior, e.g., exhibiting a maximum in the isomer yield. The hydroisomerization reaction mechanism has already been discussed extensively in the literature [9, 13]. A short recapitulation is given in Figure 3-1. In a first step, gas phase alkanes are physically adsorbed within the catalyst pores where they are subsequently dehydrogenated at the metal, i.e., platinum, sites. The produced alkenes desorb from the metal sites and diffuse towards the acid sites where they are protonated to form reactive carbenium ions. These carbenium ions undergo isomerization and cracking reactions. The product carbenium ions are converted

into the corresponding, observable gas phase alkanes via the sequence of elementary steps described above in the reverse sense.

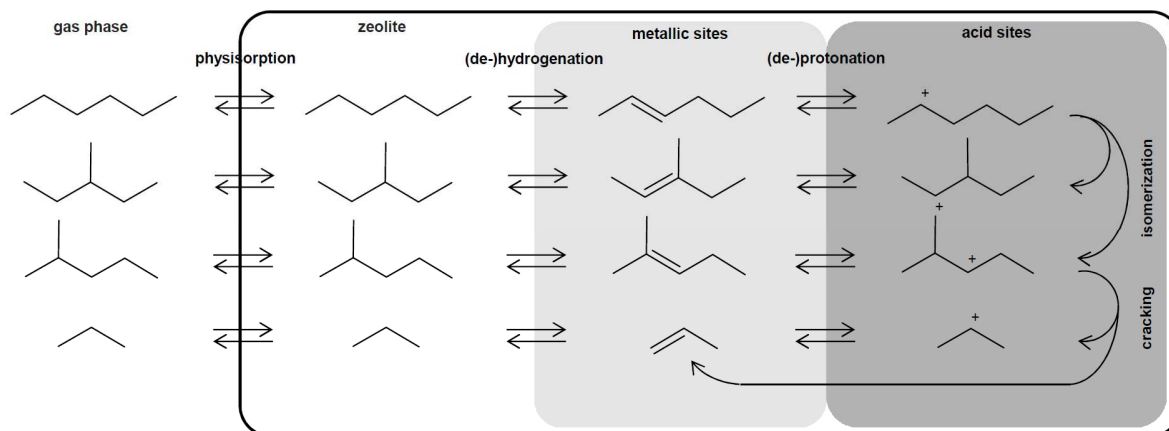


Figure 3-1: Schematic overview of (ideal) hydroisomerization of *n*-hexane over a bifunctional zeolite

## 3.1 Procedures

### 3.1.1 Experimental conditions

The experimental dataset was acquired on a Pt/H-ZSM-5 using the Berty reactor described in sections 2.1.1.1 and 2.1.2.1. The temperature and total pressure ranged from 493 to 573 K and 1.0 to 2.0 MPa with a molar inlet hydrogen to hydrocarbon ratio amounting from 50 to 100 mol mol<sup>-1</sup> at a space-time of 191.0 kg<sub>cat</sub> s mol<sub>C<sub>6</sub></sub><sup>-1</sup>. These reaction conditions were chosen such that intrinsic kinetics were measured [14]. External diffusion limitations were absent with the corresponding efficiency exceeding 0.998. The Weisz-Prater criterion to determine internal diffusion limitations was only narrowly satisfied with a corresponding efficiency close to 0.95. Taking into account possible diffusion effects was beyond the scope of this case study due to its complexity, but probably decreased the adequacy of the resulting model. Temperature gradients, both at reactor and catalyst pellet scale, were always below 0.5 K. All partial pressures were sufficiently below the corresponding vapor pressures which ensured that no condensation occurred. Also, it was experimentally verified that ideal hydrocracking occurred [3, 5, 6, 9, 11, 12], see section 3.2. During experimentation, catalyst deactivation was not observed. For the complete experimental dataset, a single catalyst batch was used, i.e., 4.88 g. In total, 36 experiments were performed at 24 unique sets of experimental conditions. Table 3-1 gives an overview of the range of experimental conditions applied for *n*-hexane hydroisomerization.

**Table 3-1: Range of experimental conditions for *n*-hexane hydroisomerization on Pt/H-ZSM-5**

Temperature [K]	Total pressure [MPa]	Hydrogen to hydrocarbon feed ratio [mol mol <sup>-1</sup> ]	Space time [kg <sub>cat</sub> s mol <sub>C<sub>2</sub></sub> <sup>-1</sup> ]
493 – 573	1.00 – 2.00	50 – 100	191.0

### 3.1.2 Reactor model

For modeling purposes, the reactor is considered as an ideal *CSTR* as described in section 2.2.2.1.

The *CSTR* is described by a set of algebraic equations for the components in the reaction mixture:

$$F_i = F_i^0 + R_i W \quad i = 2MP, 3MP \text{ and } C_3 \quad 3-1$$

with  $W$  the catalyst mass and  $R_i$  the net rate of formation of component  $i$ , see equations 3-4 to 3-6 in section 3.3.1. In order to eliminate any linear dependence in the set of reactor balance equations, the carbon and hydrogen balances were used to calculate the hydrogen and *n*-hexane molar flow rate, see resp. equation 3-2 and 3-3.

$$F_{nC6} = F_{nC6}^0 - F_{2MP} - F_{3MP} - \frac{F_{C3}}{2} \quad 3-2$$

$$F_{H_2} = F_{H_2}^0 - \frac{F_{C3}}{2} \quad 3-3$$

### 3.1.3 Parameter estimation

The regression was performed with a commercially available software package, i.e., Athena Visual Studio [15, 16]. In this software package, Bayesian estimation is conventionally used for multiresponse regression purposes [17]. Differences amounting to at least one order of magnitude occur between the responses. Via Bayesian estimation, it is statistically assured that every response, and even each measurement within a response, is equally accounted for. The assumptions made within this package lead to an optimization criterion which is equivalent to generalized least squares, *GLS*. Using a *CSTR* typically leads to the direct determination of the reaction rates and, hence, these could be used as responses in the objective function. However, using the molar outlet flow rates calculated from a *CSTR* mass balance eliminates the double use of the measurements, i.e., as experimental observations (reaction rate) and as independent variables (reactor concentrations or partial pressures). In total, 3 responses are considered, i.e., the molar outlet flow rate of the products: 2-methyl pentane (2MP), 3-methyl pentane (3MP), and propane ( $C_3$ ). The molar outlet flow rate of

the reactants, i.e., *n*-hexane and hydrogen were not taken into account into the regression. These flow rates were determined from the product outlet flow rates using resp. a carbon and hydrogen balance. This was justified because the experimental data is normalized before being used for further analysis and regression, see section 2.1.3.

### 3.2 *n*-Hexane Hydroisomerization: experimental observations

In the entire range of operating conditions, so-called ideal hydrocracking behavior was observed [3, 5, 6, 8-12]. With increasing temperature, i.e., from 493 to 573 K, the *n*-hexane conversion increased with the temperature, from ca. 20% to ca. 80%, see Figure 3-2. A higher inlet hydrogen to *n*-hexane molar ratio and/or total pressure resulted in a decrease of the conversion, see Figure 3-2. If the hydrogenation reaction is in quasi-equilibrium and the inlet hydrogen to *n*-hexane molar ratio and/or total pressure increases, this equilibrium is shifted towards the alkanes and, hence, less *n*-hexane is converted [9].

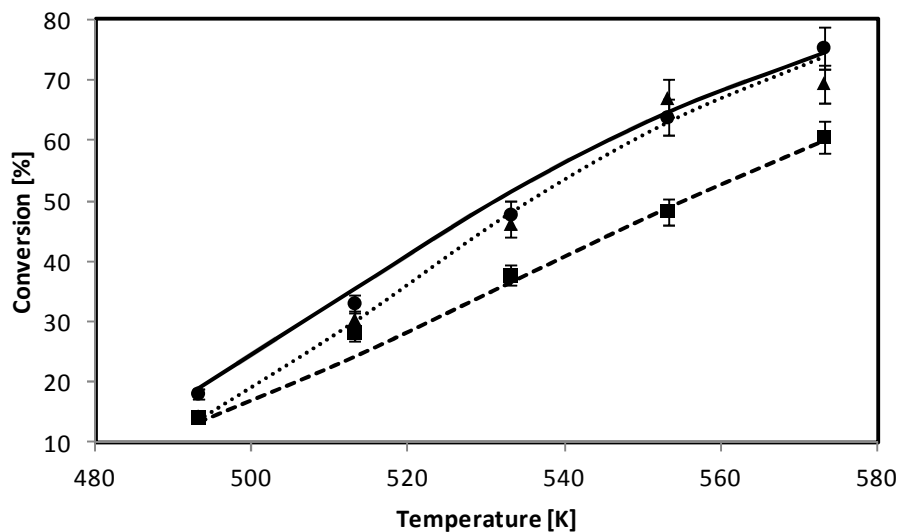


**Figure 3-2:** *n*-Hexane hydroisomerization conversion on Pt/H-ZSM-5 catalyst as a function of the temperature at different hydrogen to *n*-hexane molar inlet ratio and total pressures. Symbols correspond to experimental observations, lines correspond to model simulations, i.e., Eqs. 3-1 to 3-3, in which the net rates of formation are given by Eqs. 3-4 to 3-6 using the parameters from Table 3-4. ●, full line:  $F_{\text{H}_2}^0 / F_{\text{C}_6}^0 = 50 \text{ mol mol}^{-1}$ ,  $p_{\text{tot}} = 1.0 \text{ MPa}$ ; ■, dashed line:  $F_{\text{H}_2}^0 / F_{\text{C}_6}^0 = 100 \text{ mol mol}^{-1}$ ,  $p_{\text{tot}} = 1.0 \text{ MPa}$ ; ▲, dotted line:  $F_{\text{H}_2}^0 / F_{\text{C}_6}^0 = 50 \text{ mol mol}^{-1}$ ,  $p_{\text{tot}} = 2.0 \text{ MPa}$ .

In Figure 3-3, the product selectivity as function of the *n*-hexane conversion is given. At low conversions, almost exclusively isomerization via protonated cyclopropyl (pcp) branching occurs to 2MP and 3MP. In general, the ratio of 2MP and 3MP is close to 2 at *n*-hexane

conversions below 50% after which it decreases to the thermodynamic equilibrium, i.e., around 1.5, see Figure 3-4. The higher molar ratio of 2MP to 3MP than expected from kinetic considerations can be attributed to the occurrence of intracrystalline diffusion effects [18], the latter also being confirmed by the absence of di-branched components. The critical diameter of 2MP amounts to 0.54 nm [19] and is slightly smaller than that of 3MP, i.e., 0.56 nm [18]. This difference in critical diameter and spatial structure can indeed lead to a difference in diffusivity in the medium sized pores of the ZSM-5 zeolite investigated in this work [18].

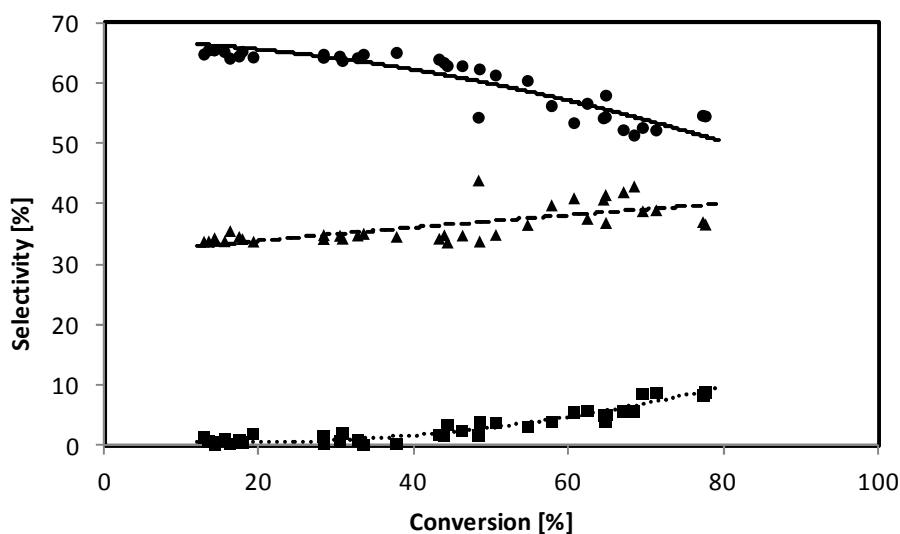


Figure 3-3: *n*-Hexane hydroisomerization product selectivity on Pt/H-ZSM-5 catalyst as a function of the conversion. Symbols correspond to experimental observations, lines correspond to model simulations, i.e., Eqs. 3-1 to 3-3, in which the net rates of formation are given by Eqs. 3-4 to 3-6 using the parameters from Table 3-4. ●, full line: 2MP; ■, dashed line: 3MP; ▲, dotted line: propane.

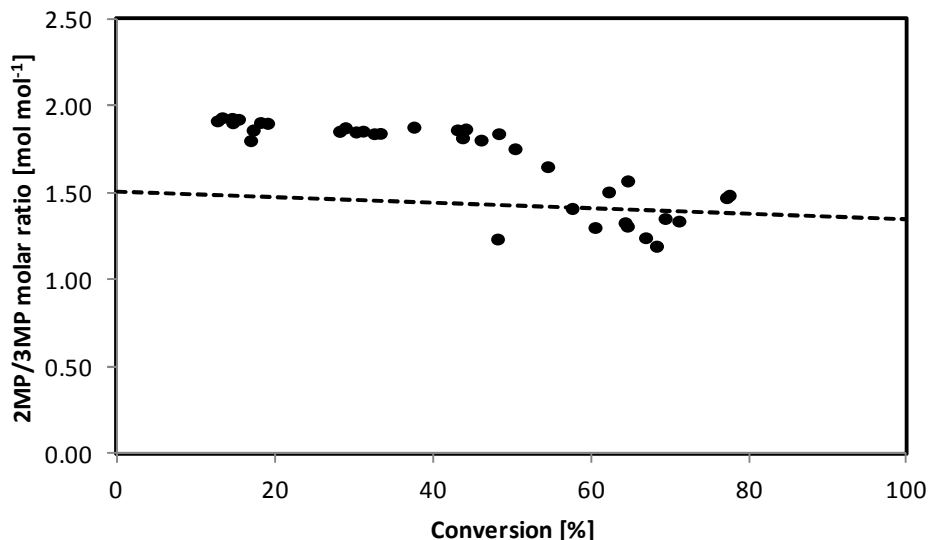


Figure 3-4: Molar ratio of 2MP to 3MP as function of *n*-C<sub>6</sub> conversion on Pt/H-ZSM-5 catalyst. The dotted line represents the calculated thermodynamic equilibrium. The higher conversions were obtained mainly due to higher reaction temperatures and, hence, the shift of the thermodynamic equilibrium.

With increasing conversion, the relative importance of cracking via  $\beta$ -scission increases, as seen by the increasing propane yield, up to 8%, see Figure 3-3. This also results in a decrease of 2MP selectivity in favor of propane, since, the latter can only be formed from 2MP and not from 3MP according to the classical carbenium ion chemistry.

### 3.3 *n*-Hexane Hydroisomerization: kinetic model development

#### 3.3.1 Reaction network and catalytic cycle

In this section, a reaction network for *n*-hexane hydrocracking on a bifunctional catalyst is proposed based on the experimental observations and the corresponding catalytic cycle is constructed. Within the scope of this work, intracrystalline diffusion is not explicitly accounted for.

First the global reaction network is constructed, see Figure 3-5. Experimentally, three reaction products are observed: 2MP, 3MP and propane. Mechanistically, 2MP and 3MP can be formed from hexane via Protonated CycloPropane (PCP) branching, i.e., resp. via  $r^{pcp(1)}$  and  $r^{pcp(2)}$  in a single catalytic cycle. Propane formation from 2MP via  $\beta$ -scission, i.e.,  $r^{bs}$ , is the only cracking route in hexane hydroconversion which does not involve a primary

carbenium ion and, hence, the only one which occurs to an appreciable extent under the reaction conditions applied.

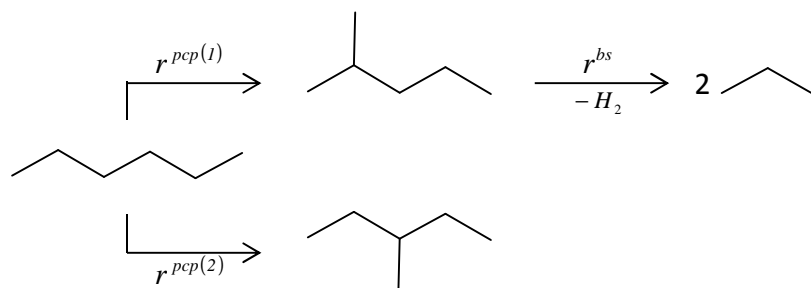


**Figure 3-5: Simplified reaction scheme of *n*-hexane hydroisomerization on a bifunctional catalyst**

As an alternative, the following reaction scheme could also be proposed for the hydroisomerization of *n*-hexane on Pt/H-ZSM-5, see Figure 3-6. For this reaction scheme it is assumed that the reaction rate of PCP branching of *n*-hexane towards 2MP and 3MP is equal, i.e.,  $r^{pcp}$ . This is justified by the same transition state through which the formation of 2MP and 3MP by pcp-branching is occurring. To account for the difference between the conversion to 2MP and 3MP, an additional isomerization step from 3MP to 2MP via an alkylshift is assumed, i.e.,  $r^{as}$ . However, after regression, statistical tests showed that using this alternative reaction scheme led to a globally less significant and less adequate model. In addition, with the normal probability figures, it was determined that the residuals were not normally distributed, see Figure 3-7. An extended discussion of these results is beyond the scope of this work. The use of one of the  $C_6$  isomers as a (co-)feed during experiments could also lead to a better understanding of the underlying chemistry and, hence, the corresponding reaction network.

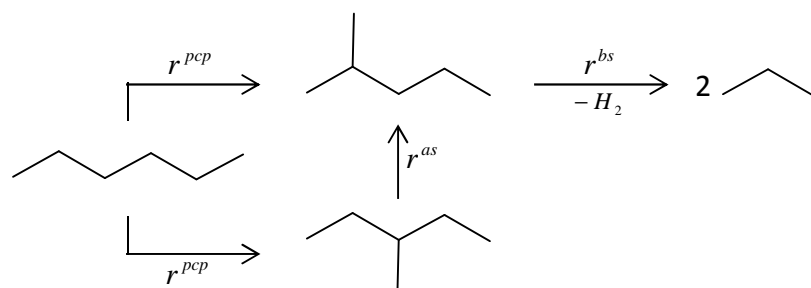


**Figure 3-6: Alternative reaction scheme of *n*-hexane hydroisomerization on a bifunctional catalyst**

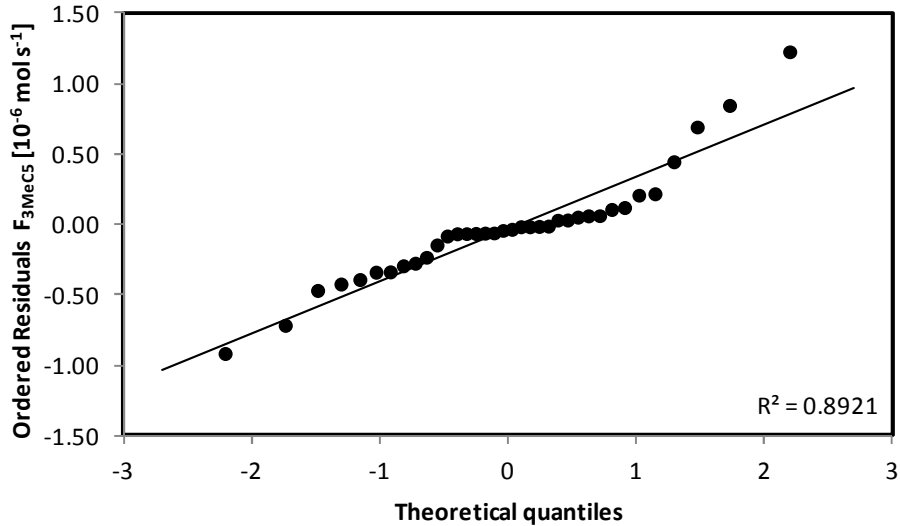


**Figure 3-7: Normal probability figure for the molar outlet flow rate of 3MP determined by solving the set of Eqs. 3-1 to 3-3, in which the net rates of formation are based upon the alternative reaction scheme given in Figure 3-6.**

The net rate of formation of all the components, i.e., *n*-hexane, 2MP, 3MP, propane and hydrogen is obtained from the rate of the individual reactions by accounting for the stoichiometry in the global reaction network, see Figure 3-5:

$$R_{nC_6} = -r^{pcp(1)} - r^{pcp(2)} \quad 3-4$$

$$R_{2MP} = r^{pcp(1)} - r^{bs} \quad 3-5$$

$$R_{3MP} = r^{pcp2} \quad 3-6$$

$$R_{C_3} = 2r^{bs} \quad 3-7$$

$$R_{H_2} = -r^{bs} \quad 3-8$$

Experimentally, the *n*-hexane conversion decreased with increasing total pressure and inlet hydrogen to *n*-hexane molar ratio, see section 3.2. As mentioned before, this is indicative of the occurrence of ideal hydrocracking, such that the following hypotheses can be made with respect to the catalytic cycle comprised by each of the steps in the global reaction network:

**Hypothesis 1:** The reactions on the acid sites, e.g., PCP branching and cracking, are rate determining within a catalytic cycle while all the other steps, i.e., sorption, (de-)hydrogenation and (de-)protonation are in quasi-equilibrium [3, 5, 6, 9, 11, 12].



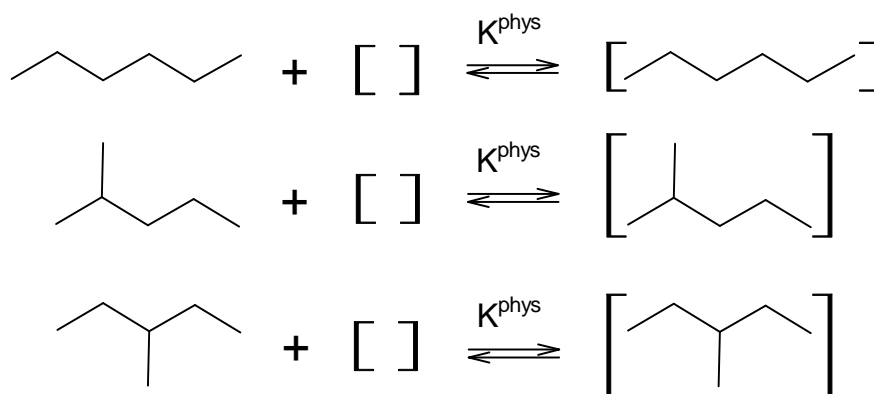
The difference in physisorption between the C<sub>6</sub> alkanes is expected to be negligible due to their structural resemblance. Additionally, the amount of propane adsorbed is negligible compared to that of C<sub>6</sub> alkanes due to its lower carbon number [20].

**Hypothesis 2:** All C<sub>6</sub> hydrocarbons are considered to interact in an identical manner with an adsorption site, i.e., the physisorption enthalpy and entropy are identical.

**Hypothesis 3:** The cracking product, propane, is instantaneously released to the gas phase, i.e., it does not physisorb in the zeolite pores.

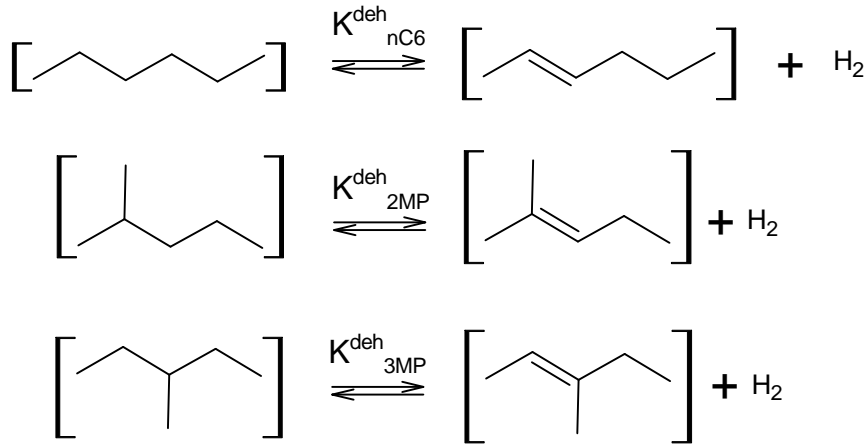
In a first step, gas phase C<sub>6</sub> alkanes physisorb with the zeolite framework at a physisorption site [ ]. This physical adsorption is quantified via an equilibrium coefficient  $K^{phys}$  (hypothesis 1-3), see

Figure 3-8:



**Figure 3-8: Physisorption equilibrium of *n*-hexane, 2MP and 3MP in the zeolite pores**

Secondly, the alkanes diffuse to and chemisorb onto a metallic site, i.e., Pt. On this site, the alkanes are dehydrogenated yielding a corresponding alkene and hydrogen which is accounted for via the equilibrium coefficient  $K^{deh}$  (hypothesis 1), see Figure 3-9. Implicitly, it is assumed that the alkenes can desorb from the zeolite pores to the gas phase in a similar way as the alkanes. However, the amount of physisorbed as well as gas phase alkenes is negligibly small compared to the alkanes due to the quasi-equilibrium of the hydrogenation under a hydrogen excess. As a result these alkenes are not explicitly accounted for in any of the mass or site balances.



**Figure 3-9: (de-)Hydrogenation equilibrium between a physisorbed *n*-hexane, 2MP and 3MP molecule and one of their corresponding alkene**

No hydrogen physisorption is considered in the zeolite pores due its low molecular mass. As a result, the bulk gas phase partial pressure of hydrogen is used in the calculation of the (de-)hydrogenation equilibrium in the zeolite pores. The metallic sites are not explicitly accounted for in the model given the quasi-equilibration that is assumed for the (de-)hydrogenation reactions (hypothesis 1).

Hypothesis 4: No hydrogen physisorption is considered.

The alkenes can protonate at the acid sites yielding a reactive carbenium ion via  $K_{pr}$  (hypothesis 1), see Figure 3-10.

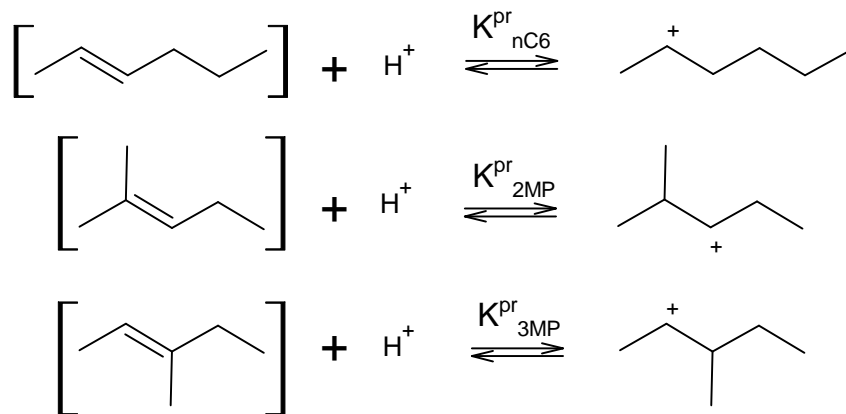


**Figure 3-10: (de-)Protonation equilibrium between *n*-hexylene, 2-methyl-pentylene and 3-methyl-pentylene and (one of) their corresponding carbenium ions**

The reactive *n*-hexyl ion subsequently undergoes isomerization reactions. Due to the linear structure of the ion this is limited to PCP branching. 2- and 3-methyl-pentyl can be formed via resp. the rate-determining steps  $k^{pcp(1)}$  and  $k^{pcp(2)}$  (hypothesis 1), see Figure 3-11.

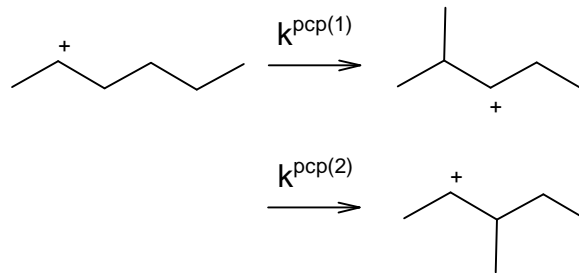


Figure 3-11: pcp-branching of a hexyl to 2- and 3-methyl-pentyl

The 2-methyl-pentyl can react by cracking towards propylene and a propyl in via  $r^{bs}$  (hypothesis 1), see Figure 3-12.

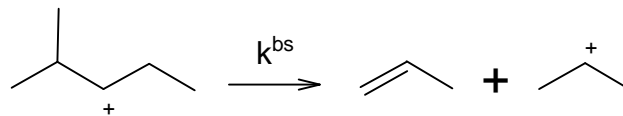


Figure 3-12: Cracking via  $\beta$ -scission of a 2-methyl-pentyl to propylene and propyl

It is assumed that the number of carbenium ions is negligible compared to the total number of acid sites [21]. This means that the number of free sites approach the total number of acid sites, and, hence, no acid site balance needs to be accounted for.

Hypothesis 5: The number of carbenium ions is negligible compared to the total number of acid sites.

### 3.3.2 Rate-equation derivation

Based upon the global reaction network proposed in section 3.3.1, three catalytic cycles with a clearly identified rate-determining step need to be accounted for, i.e., the acid catalyzed isomerization of  $n$ -hexane into 2MP and 3MP as well as the cracking of 2MP to propane. Following the law of mass action, the reaction rate for these three steps can be written as:

$$r^{pcp(1)} = k^{pcp(1)} C_{nC_6^+} \quad 3-9$$

$$r^{pcp(2)} = k^{pcp(2)} C_{nC_6^+} \quad 3-10$$

$$r^{bs} = k^{bs} C_{2MP^+} \quad 3-11$$

In these equations, the hexyl and 2-methyl-pentyl ion concentration, i.e., resp.  $C_{nC_6^+}$  and  $C_{2MP^+}$ , are not directly observable and have to be related to the corresponding gas phase partial pressures based on the hypotheses formulated in the previous section. Via the

protonation equilibrium, the carbenium ion concentration can be expressed in terms of the physisorbed alkene concentration:

$$K_{nC_6}^{pr} = \frac{C_{nC_6^+}}{C_{nC_6}^{phys} C_{H^+}} \quad 3-12$$

Under hypothesis 5, the concentration of free acid sites,  $C_{H^+,free}$ , approaches the total acid site concentration,  $C_{H^+}$ , under all reaction conditions. The alkene concentration is calculated via the hydrogenation equilibrium:

$$K_{nC_6}^{deh} = \frac{C_{nC_6}^{phys} P_{H_2}}{C_{nC_6}^{phys}} \quad 3-13$$

The concentration of the physisorbed alkanes, e.g.,  $C_{nC_6}^{phys}$  is calculated via the physisorption equilibria:

$$K^{phys} = \frac{C_{nC_6}^{phys}}{P_{nC_6} C_{free}^{phys}} \quad 3-14$$

Lastly, the concentration of free physisorption sites, i.e.,  $C_{free}^{phys}$ , is determined via a physisorption site balance (hypotheses 1-4):

$$C_{tot}^{phys} = C_{free}^{phys} + C_{nC_6}^{phys} + C_{2MP}^{phys} + C_{3MP}^{phys} \quad 3-15$$

By substituting the physisorbed alkanes concentration in equation 3-15 with the corresponding equilibria, the concentration of free physisorption sites is given by the following Langmuir isotherm:

$$C_{free}^{phys} = \frac{C_{tot}^{phys}}{1 + K_{phys} (P_{nC_6} + P_{2MP} + P_{3MP})} \quad 3-16$$

Combining equation 3-9 to equation 3-16 leads to the following expressions for the rate determining steps in terms of observable partial pressures and adjustable model parameters only:

$$r^{pcp(1)} = \frac{K^{phys} K_{nC_6}^{deh} K_{nC_6}^{pr} k^{pcp(1)} C_{H^+} C_{tot}^{phys} \frac{P_{nC_6}}{P_{H_2}}}{1 + K^{phys} (P_{nC_6} + P_{2MP} + P_{3MP})} \quad 3-17$$

$$r^{pcp(2)} = \frac{K^{phys} K_{nC_6}^{deh} K_{nC_6}^{pr} k^{pcp(2)} C_{H^+} C_{tot}^{phys} \frac{P_{nC_6}}{P_{H_2}}}{1 + K^{phys} (P_{nC_6} + P_{2MP} + P_{3MP})} \quad 3-18$$

$$r^{bs} = \frac{K^{phys} K_{2MP}^{deh} K_{2MP}^{pr} k^{bs} C_{H^+} C_{tot}^{phys} \frac{P_{2MP}}{P_{H_2}}}{1 + K^{phys} (P_{nC_6} + P_{2MP} + P_{3MP})} \quad 3-19$$

A product of several parameters occurs in the numerator of these rate expressions. In order to avoid a pronounced correlation between these parameters, they are lumped into a single, composite rate coefficient:

$$K^{phys} K_{nC_6}^{deh} K_{nC_6}^{pr} k^{pcp(1)} C_{H^+} C_{tot}^{phys} = k_{comp}^{pcp(1)} \quad 3-20$$

$$K^{phys} K_{nC_6}^{deh} K_{nC_6}^{pr} k^{pcp(2)} C_{H^+} C_{tot}^{phys} = k_{comp}^{pcp(2)} \quad 3-21$$

$$K^{phys} K_{2MP}^{deh} K_{2MP}^{pr} k^{bs} C_{H^+} C_{tot}^{phys} = k_{comp}^{bs} \quad 3-22$$

Of course, it may be possible to assess the catalyst descriptors such as  $C_{H^+}$  and  $C_{tot}^{phys}$  via separate, dedicated measurements. It is, however, beyond the scope of the present work aiming at a systematic methodology to further elaborate on this, and, hence, these descriptors are incorporated into the lumped rate coefficients. The final rate expressions used in the modeling of the *n*-hexane hydroconversion kinetics in terms of adjustable parameters, i.e.,  $k_{comp}^{pcp(1)}$ ,  $k_{comp}^{pcp(2)}$ ,  $k_{comp}^{bs}$  and  $K^{phys}$ , hence, become:

$$r^{pcp(1)} = \frac{k_{comp}^{pcp(1)} \frac{P_{nC_6}}{P_{H_2}}}{1 + K^{phys} (P_{nC_6} + P_{2MP} + P_{3MP})} \quad 3-23$$

$$r^{pcp(2)} = \frac{k_{comp}^{pcp(2)} \frac{P_{nC_6}}{P_{H_2}}}{1 + K^{phys} (P_{nC_6} + P_{2MP} + P_{3MP})} \quad 3-24$$

$$r^{bs} = \frac{k_{comp}^{bs} \frac{P_{2MP}}{P_{H_2}}}{1 + K^{phys} (P_{nC_6} + P_{2MP} + P_{3MP})} \quad 3-25$$

From these reaction rates, the net rate of formation of all the components, i.e., *n*-hexane, 2MP, 3MP, propane and hydrogen can be determined using equation 3-4 to 3-8.

## 3.4 *n*-Hexane Hydroisomerization: modeling

### 3.4.1 Isothermal regression

An isothermal regression at each of the investigated temperatures has been performed and yielded the estimates for the 4 rate coefficients, i.e.,  $k_{comp}^{pcp(1)}$ ,  $k_{comp}^{pcp(2)}$ ,  $k_{comp}^{bs}$  and  $K^{phys}$  and the corresponding individual 95% confidence intervals as reported in Table 3-2.

**Table 3-2: Parameter estimates and corresponding 95% confidence interval as function of temperature determined by isothermal regression to the experimental data of the kinetic model given by the set of Eqs. 3-1 to 3-3, in which the net rates of formation are given by Eqs. 3-4 to 3-6. Not statistically significant parameters are indicated in italics.**

Temperature [K]	493	513	533	553	573
$k_{comp}^{pcp(1)}$ [ $10^{-6}$ mol s <sup>-1</sup> kg <sub>cat</sub> <sup>-1</sup> ]	72.9 ± 11.8	150.6 ± 40.8	215.8 ± 51.3	281.1 ± 48.7	566.9 ± 158.9
$k_{comp}^{pcp(2)}$ [ $10^{-6}$ mol s <sup>-1</sup> kg <sub>cat</sub> <sup>-1</sup> ]	37.9 ± 6.4	80.2 ± 22.8	113.1 ± 28.2	189.2 ± 33.5	358.5 ± 101.9
$k_{comp}^{bs}$ [ $10^{-6}$ mol s <sup>-1</sup> kg <sub>cat</sub> <sup>-1</sup> ]	8.9 ± 8.9	8.4 ± 12.9	17.9 ± 9.0	23.6 ± 6.3	52.1 ± 16.0
$K^{phys}$ [ $10^{-5}$ Pa <sup>-1</sup> ]	4.0 ± 1.3	2.8 ± 2.0	1.2 ± 1.4	-0.2 ± 0.7	1.1 ± 1.6
$F_s$	676.8 (4.3)	264.3 (4.6)	327.3 (4.5)	506.9 (4.5)	283.1 (4.5)
number of data points	9	6	7	7	7

The PCP branching rate coefficients increase with the temperature while the ratio of both rate coefficients, i.e.,  $\frac{k_{comp}^{pcp(1)}}{k_{comp}^{pcp(2)}}$ , decreases from ca. 2.0 to 1.5 with increasing temperature from 493 to 573 K. This indicates that the composite activation energy of  $k_{comp}^{pcp(1)}$  is smaller than that of  $k_{comp}^{pcp(2)}$ . Both catalytic cycles include the same elementary steps in which a secondary carbenium ion undergoes PCP branching leading to another secondary carbenium ion and, hence, it could be expected that the activation energies are identical. Intracrystalline diffusion phenomena are considered to be at the origin of this deviation, as explained in section 3.2. With increasing conversion, especially at higher temperatures, 2MP and 3MP are produced in amounts corresponding to thermodynamic equilibrium. Hence,

the rate coefficient of PCP branching towards 3MP has to increase faster with the temperature than that leading to 2MP, resulting in a higher activation energy of the former. The limited cracking at lower temperatures leads to a difficult determination of the corresponding rate coefficient. As a result, its value is sometimes not significantly estimated, i.e., the confidence interval includes zero as a possible parameter value. However, with increasing temperature, cracking becomes more important and, hence, the corresponding rate coefficient,  $k_{comp}^{bs}$ , increases and can be estimated significantly from 533 K onwards.

The opposite holds true for the physisorption equilibrium coefficient  $K^{phys}$ . Physisorption is an exothermic step and, hence, it is most pronounced at lower temperatures. As a result, also the corresponding physisorption coefficient is statistically most significantly determined in the lower temperature range which is evident from the higher  $t$  values (not shown) and the corresponding relatively more narrow confidence intervals. At higher temperatures, the physisorption equilibrium coefficient adopts such a small value that in the adsorption term in equation 3-23 to 3-25,  $K^{phys} (p_{nC_6} + p_{2MeC_5} + p_{3MeC_5})$  becomes negligible compared to 1 and it becomes impossible to estimate the physisorption coefficient significantly.

Plotting the logarithm of the estimates for the composite rate coefficients against the reciprocal of temperature results in an Arrhenius plot, see Figure 3-13. For the Arrhenius plot, also the statistically non-significant estimates have been included as long as their value was physically meaningful. The slope of the trend lines, corresponding to  $\frac{E_a}{R}$  or  $\frac{-\Delta H^{phys}}{R}$ , and the intercept with the y-axis, corresponding to  $\ln(A)$  allow determining the initial guesses for the non-isothermal regression as reported in Table 3-3.

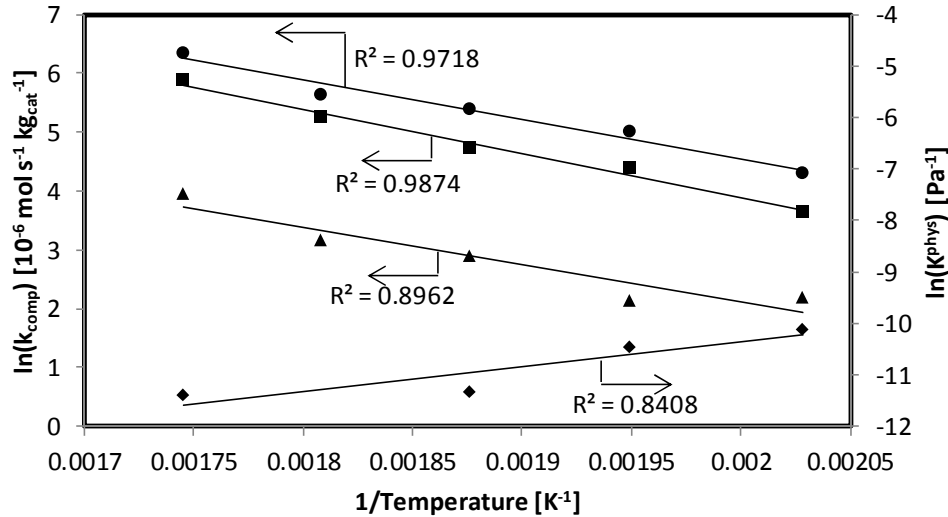


Figure 3-13: Arrhenius plot,  $\ln(k_{comp})$  and  $\ln(K^{phys})$  as function of the reciprocal of temperature for which  $k_{comp}$  and  $K^{phys}$  are obtained from Table 3-2.

Table 3-3: Determined values of the pre-exponential factor, kinetic/equilibrium coefficient at average temperature, i.e., 531.48 K, and activation energy and reaction enthalpy by the isothermal regression and the Arrhenius plot, see Figure 3-13.

	A [mol s <sup>-1</sup> kg <sub>cat</sub> <sup>-1</sup> or 10 <sup>-9</sup> Pa <sup>-1</sup> ]	k <sub>Tm</sub> or K <sub>Tm</sub> [10 <sup>-6</sup> mol s <sup>-1</sup> kg <sub>cat</sub> <sup>-1</sup> or 10 <sup>-5</sup> Pa <sup>-1</sup> ]	E <sub>a</sub> or ΔH <sup>phys</sup> [kJ mol <sup>-1</sup> ]
$k_{comp}^{pcp(1)}$	59.1	206.6	55.5
$k_{comp}^{pcp(2)}$	116.5	118.4	62.8
$k_{comp}^{bs}$	2.8	17.5	53.0
$K^{phys}$	2.0	1.8	-40.0

### 3.4.2 Non-isothermal regression

Starting from the initial estimates reported in Table 3-3, the values of the kinetic and equilibrium coefficients at average temperature, i.e., 531.48 K, and activation energies and physisorption enthalpy were estimated via non-isothermal regression with simultaneously considering all data that have been measured as reported in Table 3-4.



**Table 3-4: Parameter estimates, corresponding approximate 95% individual confidence interval and  $t$  values of the kinetic/equilibrium coefficients at average temperature and activation energies and reaction enthalpy determined by non-isothermal regression to the experimental data of the kinetic model given by the set of Eqs. 3-1 to 3-3, in which the net rates of formation are given by Eqs. 3-4 to 3-6.**

	$k_{T_m,comp}$ or $K_{Tm}$ [ $10^{-6} \text{ mol s}^{-1} \text{ kg}_{cat}^{-1}$ or $10^{-5} \text{ Pa}^{-1}$ ]	$t$ value  tabulated value: 2.0	$E_{a,comp}$ or $\Delta H^{phys}$ [ $\text{kJ mol}^{-1}$ ]	$t$ value  tabulated value: 2.0
$k_{comp}^{pcp(1)}$	$200.0 \pm 22.8$	18.5	$53.5 \pm 7.1$	15.9
$k_{comp}^{pcp(2)}$	$114.5 \pm 13.7$	17.6	$61.4 \pm 7.8$	16.6
$k_{comp}^{bs}$	$14.6 \pm 2.4$	12.7	$68.0 \pm 9.7$	14.8
$K^{phys}$	$1.0 \pm 0.6$	3.3	$-88.6 \pm 28.0$	6.8

The model has a higher  $F$  value for the global significance of the regression than the corresponding tabulated  $F$  value, i.e., 2365 compared to 3.9. All parameters are estimated significantly, as reflected by their confidence interval and corresponding  $t$  value exceeding the tabulated  $t$  value. The coefficients concerning cracking,  $k_{comp}^{bs}$ , and physisorption,  $K^{phys}$ , have the widest confidence intervals. As discussed in section 3.4.1, the information contained in the data corresponding to these parameters is constrained to the higher respectively lower temperature range. Literature values for the activation energies of PCP branching and cracking are difficult to find due to their composite nature. However, the physisorption enthalpy estimate, i.e.,  $88 \text{ kJ mol}^{-1}$ , corresponds rather well to physisorption studies of n-hexane on ZSM-5, i.e.,  $70\text{-}80 \text{ kJ mol}^{-1}$  [7, 22, 23]. A different activation energy for PCP branching to 2MP and 3MP was obtained, i.e., resp.  $53$  and  $61 \text{ kJ mol}^{-1}$ . This composed activation energy comprises the physisorption enthalpy, the dehydrogenation enthalpy, the protonation enthalpy and the activation energy of the elementary step. The physisorption enthalpy is estimated to be ca.  $-90 \text{ kJ mol}^{-1}$ , the dehydrogenation enthalpy is determined by thermodynamic calculations to be ca.  $100 \text{ kJ mol}^{-1}$  and protonation enthalpies are reported to be within the range of ca.  $-70$  to  $-90 \text{ kJ mol}^{-1}$  [7, 13]. The activation energy for PCP branching (s,s) is reported to be equal to ca.  $110\text{-}130 \text{ kJ mol}^{-1}$  [7, 13]. From the parameter estimates, the activation energy for PCP branching (s,s) amounts to  $120\text{-}140 \text{ kJ mol}^{-1}$  which corresponds rather well to the literature values. The occurrence of diffusion effects is not pronounced since this would lead to an observed activation energy

which is much smaller [24]. The activation energy for cracking is estimated to be the highest, i.e.,  $68 \text{ kJ mol}^{-1}$ , as expected since propane is a secondary product and is only formed in the higher temperature range.

The F value for the model adequacy was determined at 1.75 which slightly exceeds the tabulated value at 95% significance with resp. 67 and 33 degrees of freedom, i.e., 1.69. This means that, statistically, the model is found to be marginally inadequate, i.e., some deviations between the model calculated and observed values are present which cannot be solely attributed to experimental errors. As stated in section 2.2.4, the test for the model adequacy is a quite severe test. It can, hence, be concluded that the model performs quite fair within the investigated range of operating conditions, but that extrapolations should be approached with sufficient care.

Table 3-5 shows the binary correlation coefficient matrix obtained from the non-isothermal regression. No binary correlation coefficients higher than 0.95 are obtained and, hence, the kinetic parameters can be considered to be uncorrelated. A maximum binary correlation coefficient of 0.92 occurs obtained between  $k_{T_m,comp}^{pcp(1)}$  and  $k_{T_m,comp}^{pcp(2)}$ . Both parameters are closely related since both represent the simultaneous formation of an isomerization product from *n*-hexane.

**Table 3-5: Binary correlation coefficient matrix as determined by non-isothermal regression to the experimental data of the kinetic model given by the set of Eqs. 3-1 to 3-3, in which the net rates of formation are given by Eqs. 3-4 to 3-6.**

	$k_{T_m,comp}^{pcp(1)}$	$k_{T_m,comp}^{pcp(2)}$	$k_{T_m,comp}^{bs}$	$K_{T_m}^{phys}$	$E_{a,comp}^{pcp(1)}$	$E_{a,comp}^{pcp(2)}$	$E_{a,comp}^{bs}$	$\Delta H^{phys}$
$k_{T_m,comp}^{pcp(1)}$	1.00	0.92	0.60	0.90	-0.72	-0.62	-0.41	0.36
$k_{T_m,comp}^{pcp(2)}$	0.92	1.00	0.57	0.85	-0.65	-0.72	-0.39	0.34
$k_{T_m,comp}^{bs}$	0.60	0.57	1.00	0.63	-0.36	-0.33	-0.92	0.40
$K_{T_m}^{phys}$	0.90	0.85	0.63	1.00	-0.54	-0.49	-0.39	0.65
$E_{a,comp}^{pcp(1)}$	-0.72	-0.65	-0.36	-0.54	1.00	0.87	0.26	0.18
$E_{a,comp}^{pcp(2)}$	-0.62	-0.72	-0.33	-0.49	0.87	1.00	0.26	0.17
$E_{a,comp}^{bs}$	-0.41	-0.39	-0.92	-0.39	0.26	0.26	1.00	-0.18
$\Delta H^{phys}$	0.36	0.34	0.40	0.65	0.18	0.17	-0.18	1.00

### 3.4.3 Model performance

An initial visual assessment of the model's performance can be made from Figure 3-2 and Figure 3-3. It is clear that the model is able to simulate the observed trends very well. In Figure 3-14, the parity diagram of the three responses, i.e., the three reaction products: 2MP, 3MP and propane, are shown. For all three components, the simulated points are distributed uniformly around the first bisector of the parity diagram, indicating that no pronounced systematic deviations occur between model simulations and experimental data. For the propane response, however, at low outlet flow rates, which are corresponding to the experiments at lowest temperatures, the largest relative deviations are obtained which is agreement with the wider confidence intervals of estimates for the cracking rate coefficients at these temperatures, as discussed in section 3.4.1.

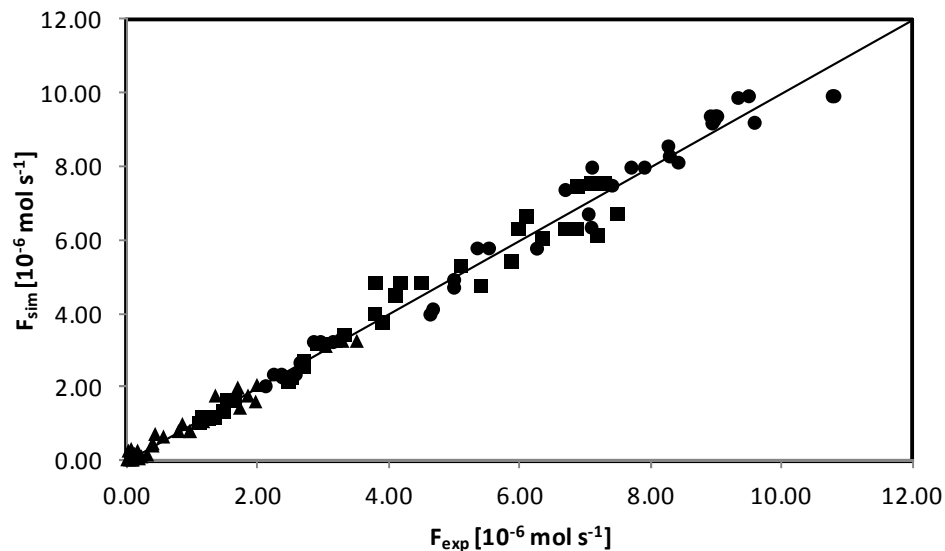


**Figure 3-14: Parity diagram for the molar outlet flow rate of 2MP (●), 3MP (■) and propane (▲) determined by solving the set of Eqs. 3-1 to 3-3, in which the net rates of formation are given by Eqs. 3-4 to 3-6 using the parameters from Table 3-4.**

The behavior of the responses' residuals which are expected to approach the true experimental error does also not exhibit any particular trend with the operating conditions, i.e., temperature and pressure, as shown by the residual figures, see Figure 3-15. For all responses and operating conditions, the residuals are normally distributed around the x-axis indicating no lack of fit by the model and the normal distribution of the experimental error with expected value equal to zero. However, based on the experimental error determined

by repeat experiments, the variance is slightly higher than expected as indicated by the  $F$  value for the model adequacy.

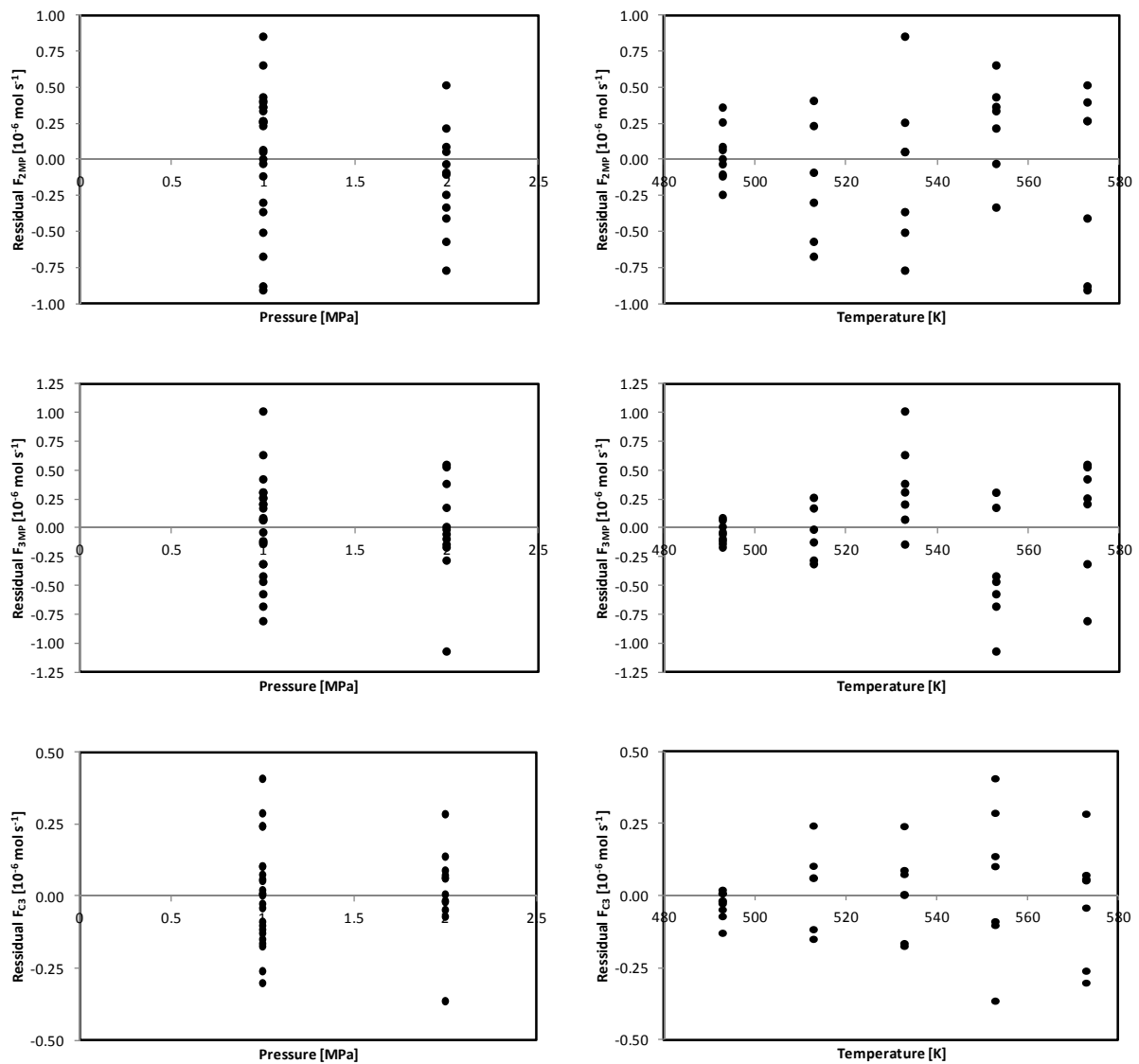


**Figure 3-15:** Residual figures for the molar outlet flow rate of 2MP (top), 3MP (middle) and propane (bottom) as function of pressure (left) and temperature (right) determined by solving the set of Eqs. 3-1 to 3-3, in which the net rates of formation are given by Eqs. 3-4 to 3-6 using the parameters from Table 3-4.

Figures 3-16 to 3-18 show the normal probability figures for each response. For all three responses, the linear regression of the ranked residuals to the theoretical quantiles leads to a  $R^2$ -value exceeding 0.97. Also a visual inspection of the normal probability figures show that the experimental error is distributed normally.

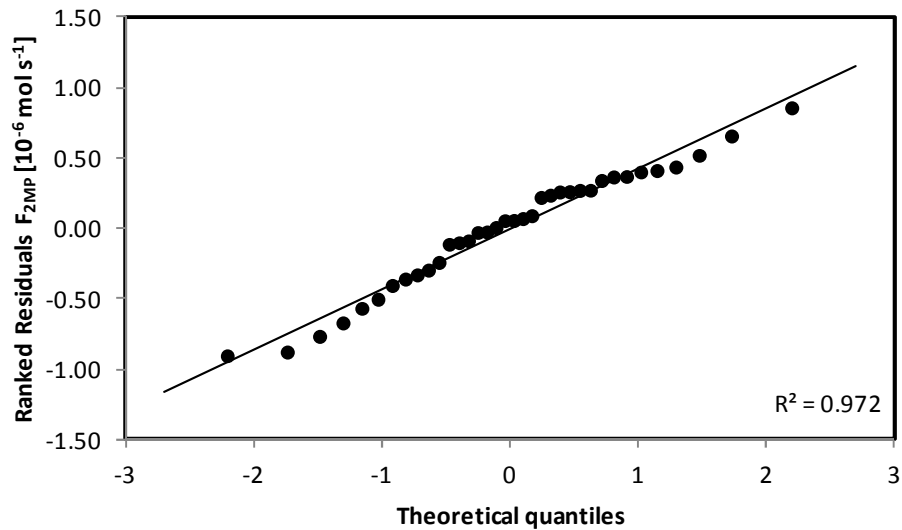


Figure 3-16: Normal probability figure for the molar outlet flow rate of 2MP determined by solving the set of Eqs. 3-1 to 3-3, in which the net rates of formation are given by Eqs. 3-4 to 3-6 using the parameters from Table 3-4.

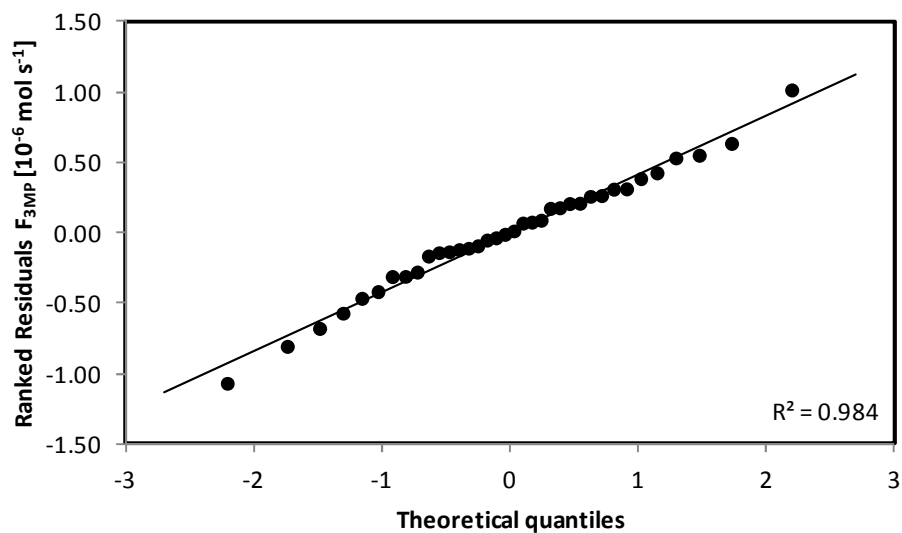


Figure 3-17: Normal probability figure for the molar outlet flow rate of 3MP determined by solving the set of Eqs. 3-1 to 3-3, in which the net rates of formation are given by Eqs. 3-4 to 3-6 using the parameters from Table 3-4.

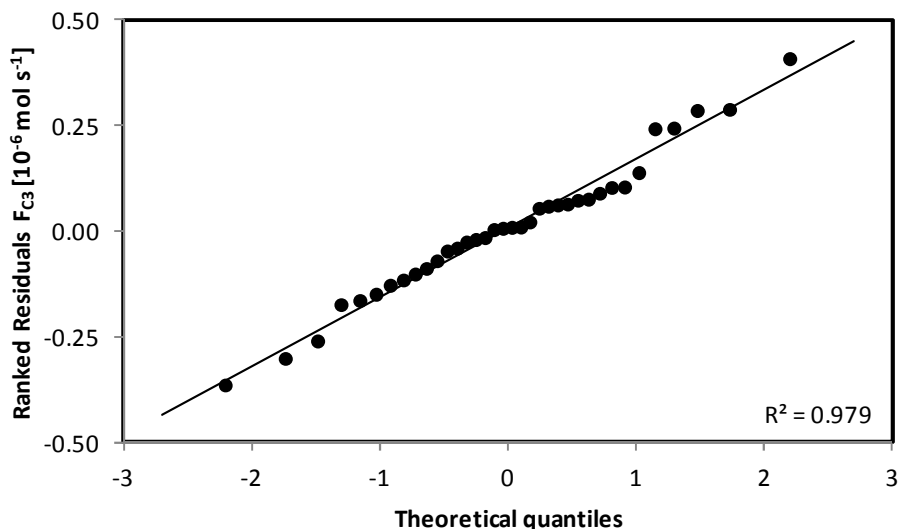


Figure 3-18: Normal probability figure for the molar outlet flow rate of propane determined by solving the set of Eqs. 3-1 to 3-3, in which the net rates of formation are given by Eqs. 3-4 to 3-6 using the parameters from Table 3-4.

### 3.5 Conclusions

The developed methodology for kinetic modeling was successfully applied to *n*-hexane hydroisomerization over a bifunctional catalyst, i.e., Pt/H-ZSM-5. The kinetic model obtained was able to describe the experimental data very satisfactory. However, the variance of the residuals could not only be attributed to experimental error as repeat experiments and the test for model adequacy have revealed. All parameter estimates obtained could be traced back in terms of the phenomena that were actually occurring. The values of the composite activation energies for PCP branching and  $\beta$ -scission were determined to be statistically significant. The composite activation energy for  $\beta$ -scission was higher than those of PCP branching, hence, the production of cracked products, i.e., propane, is regarded as a secondary reaction which is only becoming important at higher temperatures, as experimentally observed. The composite activation energy for PCP branching towards 3MP exceeds that of the reaction leading to 2MP, which resulted from the experimental observation that the 2MP to 3MP molar ratio decreases with increasing temperature. This could be due to intracrystalline diffusion effects in the medium pore sized MFI support. This support is selective to the formation of 2MP at lower conversions. The physisorption enthalpy for the  $C_6$  components corresponds well with reported values from literature.

## 3.6 References

- [1] J.F. Allain, P. Magnoux, P. Schulz, M. Guisnet, *Applied Catalysis a-General*. 152 (1997) 221-235.
- [2] M.A. Baltanas, G.F. Froment, *Computers & Chemical Engineering*. 9 (1985) 71-81.
- [3] M.A. Baltanas, H. Vansina, G.F. Froment, *Industrial & Engineering Chemistry Product Research and Development*. 22 (1983) 531-539.
- [4] G.G. Martens, J.W. Thybaut, G.B. Marin, *Industrial & Engineering Chemistry Research*. 40 (2001) 1832-1844.
- [5] M. Steijns, G. Froment, P. Jacobs, J. Uytterhoeven, J. Weitkamp, *Industrial & Engineering Chemistry Product Research and Development*. 20 (1981) 654-660.
- [6] M. Steijns, G.F. Froment, *Industrial & Engineering Chemistry Product Research and Development*. 20 (1981) 660-668.
- [7] A. vandeRunstraat, J. vanGrondelle, R.A. vanSanten, *Industrial & Engineering Chemistry Research*. 36 (1997) 3116-3125.
- [8] C.S. Raghuvver, J.W. Thybaut, R. De Bruycker, K. Metaxas, T. Bera, G.B. Marin, *Fuel*. 125 206-218.
- [9] J.W. Thybaut, C.S.L. Narasimhan, J.F. Denayer, G.V. Baron, P.A. Jacobs, J.A. Martens, G.B. Marin, *Industrial & Engineering Chemistry Research*. 44 (2005) 5159-5169.
- [10] J.W. Thybaut, C.S.L. Narasimhan, G.B. Marin, *Catalysis Today*. 111 (2006) 94-102.
- [11] H. Vansina, M.A. Baltanas, G.F. Froment, *Industrial & Engineering Chemistry Product Research and Development*. 22 (1983) 526-531.
- [12] J. Weitkamp, *Erdol & Kohle Erdgas Petrochemie*. 31 (1978) 13-22.
- [13] B.D. Vandegheuchte, J.W. Thybaut, A. Martinez, M.A. Arribas, G.B. Marin, *Applied Catalysis A: General*. 441-442 (2012) 10-20.
- [14] EUROKIN\_fixed-bed\_html, EUROKIN spreadsheet on requirements for measurement of intrinsic kinetics in the gas-solid fixed-bed reactor, 2012.
- [15] Athena Visual Studio, Web page <http://www.athenavisual.com/>.
- [16] W.E. Stewart, M. Caracotsios, *Computer-Aided Modeling of Reactive Systems*, John Wiley & Sons, Inc., 2008.
- [17] Y. Bard, *Nonlinear Parameter Estimation*, Academic Press, 1974.
- [18] V.R. Choudhary, D.B. Akolekar, *Journal of Catalysis*. 117 (1989) 542-548.
- [19] A.F.P. Ferreira, M.C. Mittelmeijer-Hazeleger, J.V.D. Bergh, S. Aguado, J.C. Jansen, G. Rothenberg, A.E. Rodrigues, F. Kapteijn, *Microporous and Mesoporous Materials*. 170 (2013) 26-35.
- [20] J.F.M. Denayer, G.V. Baron, *Adsorption-Journal of the International Adsorption Society*. 3 (1997) 251-265.
- [21] J.W. Thybaut, G.B. Marin, G.V. Baron, P.A. Jacobs, J.A. Martens, *Journal of Catalysis*. 202 (2001) 324-339.
- [22] W. Makowski, D. Majda, *Applied Surface Science*. 252 (2005) 707-715.
- [23] S. Savitz, A.L. Myers, R.J. Gorte, D. White, *Journal of the American Chemical Society*. 120 (1998) 5701-5703.
- [24] G.F. Froment, K.B. Bischoff, J. De Wilde, *Chemical reactor analysis and design*, 2010.





# Chapter 4

## Single-Event Modeling of Ethene Oligomerization on Ni-SiO<sub>2</sub>-Al<sub>2</sub>O<sub>3</sub>

---

In this chapter, ethene oligomerization on an amorphous nickel silica-alumina catalyst was investigated experimentally as well as by SEMK modeling. Due to the catalyst's amorphous structure, no specific pore geometry or framework related effects needed to be considered. In addition, the catalyst used had only rather weak acid sites and, hence, the observed ethene oligomerization, c.q., dimerization, originated exclusively from the nickel ion sites. This allowed to specifically determine the metal ion kinetics. The high selectivity towards butenes of these nickel ion sites will be exploited in chapter 5 by adding a stronger acidic function within a tailored pore structure aiming at selectively converting the butenes toward heavier and highly branched alkenes.

### 4.1 Procedures

#### 4.1.1 Experimental conditions

The experimental dataset was obtained on a Ni-SiO<sub>2</sub>-Al<sub>2</sub>O<sub>3</sub> catalyst using the *HTK-1* set-up as described in resp. section 2.1.1.2 and 2.1.2.2. Initially, when sending ethene to a fresh catalyst bed, the temperature in the catalyst bed increased for ca. 10 K over 2 to 3 minutes, after which the temperature again decreased to the set point, see also section 4.4.2. After a period of ca. 1 hour, steady state was obtained and the effluent was analysed. No

deactivation was observed during a time-on-stream of 8 hours. Only components up to carbon number 8 were detected.

Both the carbon and mass balance were verified using methane as an internal standard and were closed within  $\pm 5\%$ . The molar outlet flow rates were normalized assuming a closed carbon balance for further data interpretation and kinetic modeling. The range of investigated experimental conditions was chosen such that intrinsic kinetics could be measured, see section 2.1.2.2, and is given in Table 4-1.

**Table 4-1: Range of experimental conditions for ethene oligomerization on Ni-SiO<sub>2</sub>-Al<sub>2</sub>O<sub>3</sub>**

Temperature	Total pressure	Ethene partial pressure	Space time
[K]	[MPa]	[MPa]	[kg <sub>cat</sub> s mol <sub>C<sub>2</sub></sub> <sup>-1</sup> ]
443 – 503	1.50 – 3.50	0.15 – 0.35	4.8 – 14.4

### 4.1.2 Definition of responses

In total, 5 responses were experimentally determined, i.e., the molar outlet flow rates of ethene,  $F_{C_2}$ , 1-butene,  $F_{1-C_4}$ , a lump of butenes, including 1-butene,  $F_{C_4}$ , a lump of hexenes,  $F_{C_6}$ , and a lump of octenes,  $F_{C_8}$ . Thermodynamic equilibrium was reached within the C<sub>4</sub> fraction, see section 4.2 and, hence, the outlet molar flow rate of 1-butene was thermodynamically correlated with the lumped molar outlet flow rate of the butenes. In the model, the molar outlet flow rate of 1-butene was determined via the thermodynamic equilibrium, see section 4.4.1.3. Despite the independent observation of both responses, i.e., the molar outlet flow rates of 1-butene,  $F_{1-C_4}$ , and the lump of butenes,  $F_{C_4}$ , the former was omitted from the SSQ.

## 4.2 Experimental investigation

The experimental investigation comprised 51 experiments and was performed in the range of conditions given by Table 4-1. Of these 51 experiments, 11 were repeat experiments, from which a relative experimental error amounting to 6.0% was determined. Only linear, even carbon numbered components, up to octenes, were detected in which butenes were the main products, see Figure 4-1. The selectivity towards butene, hexene and octene amounted to resp. 80-90%, 10-15% and 1-5%. The products followed an Anderson-Schulz-Flory (ASF) distribution, as shown by the linear relationship of the logarithm of the molar fraction as function of the carbon number, see Figure 4-2. The active metal ion sites mainly

dimerized ethene to butene while only a limited amount of butene further reacted towards hexene and octene. The butene and hexene product yields exhibited a linear trend with the ethene conversion, independent of the operating conditions used, see Figure 4-1. This showed that the ratio of chain growth to termination, similar to polymerization kinetics, see section 4.3.1, was constant for all reaction conditions applied. Such a trend, together with the absence of odd-carbon numbered product alkenes, which would have been the result from acid catalyzed cracking reactions, and the results from the  $NH_3$ -TPD measurements, indicated that the only active sites on the catalyst were the metal ion sites. The metal ion sites acted primarily as dimerization sites and to a limited extent also as trimerization sites. If acid catalyzed reactions, i.e., acid catalyzed oligomerization in particular, would have occurred, the butene yield would have increased less than proportional with the conversion due to additional consumption of butenes by dimerization to octene on the acid sites. This would have resulted in a deviation from the ASF product distribution [1]. In addition, odd-carbon numbered products would have been produced.

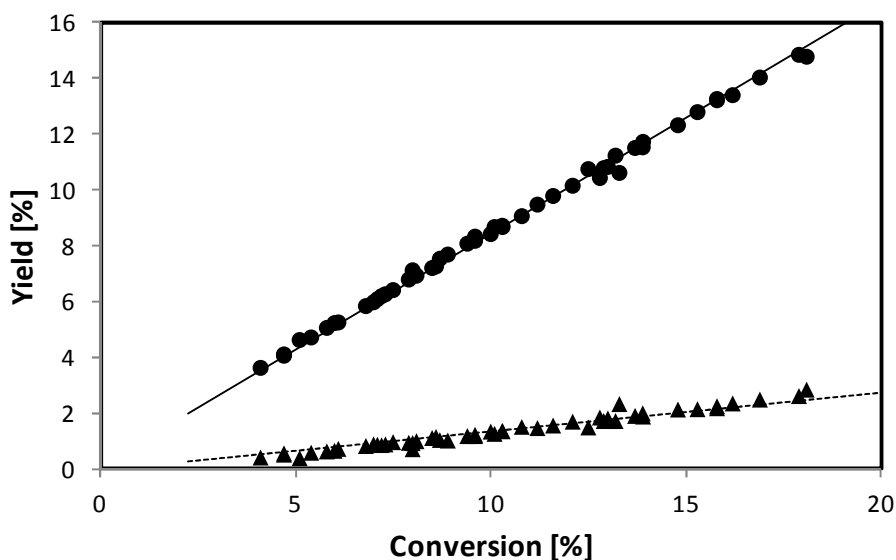
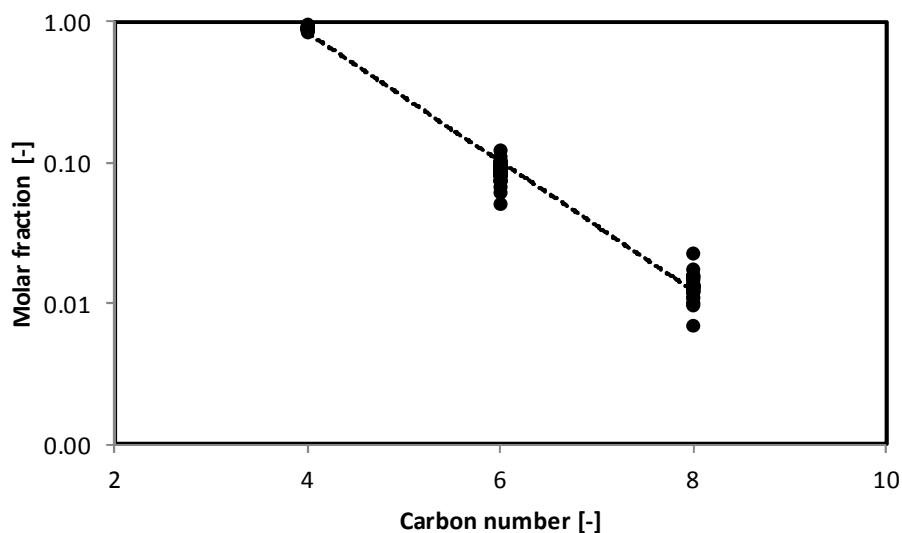


Figure 4-1: Ethene oligomerization product yields on 1.8wt% Ni-SiO<sub>2</sub>-Al<sub>2</sub>O<sub>3</sub> as function of ethene conversion. Symbols correspond to experimental data, lines correspond to model simulations, i.e., by integration of Eq. 2-21, with the corresponding net rates of formation as given by Eq. 4-27 and the parameter values as reported in Table 4-4; ●, full line: butene; ▲, dashed line: hexene.



**Figure 4-2: Experimental product distribution: molar fraction as function of carbon number. The full line shows the linear trend of the logarithm of the molar fraction of the components as function of their carbon number.**

In the whole range of reaction conditions tested, double bond isomerization was observed within the butene fraction and was found to establish thermodynamic equilibrium within this fraction. In general, 30 to 40% of the butenes were found as 1-butene depending on the reaction temperature. This thermodynamic equilibrium of the butene isomers was also experimentally observed by Espinoza et al. on a similar catalyst and at similar reaction conditions [2]. As can be seen from Figures 4-3 and 4-4, the effects of increasing space time, temperature and ethene partial pressure were as expected: they resulted in an increase of the ethene conversion.

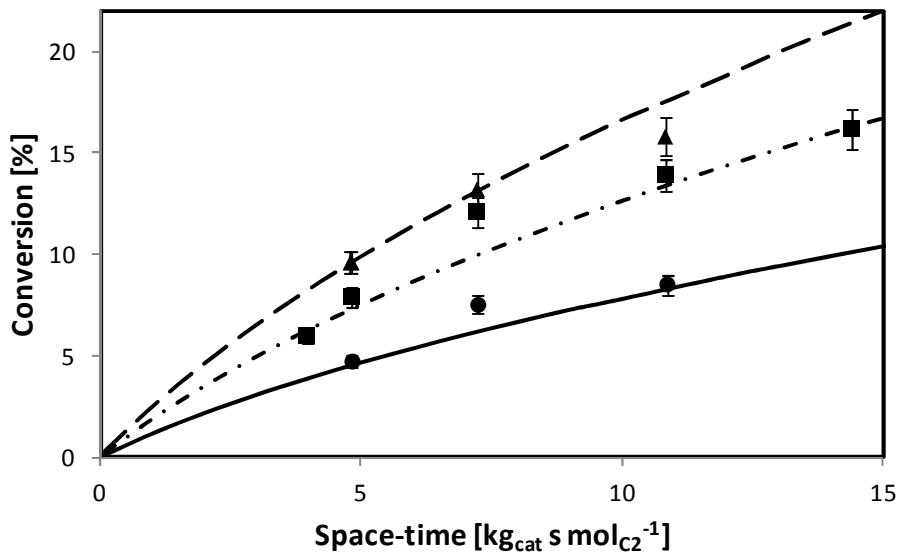


Figure 4-3: Ethene conversion on 1.8wt% Ni-SiO<sub>2</sub>-Al<sub>2</sub>O<sub>3</sub> as function of space time at different temperatures, at 3.5MPa total pressure and an ethene inlet partial pressure equal to 0.35 MPa. Symbols correspond to experimental data, lines correspond to model simulations, i.e., by integration of Eq. 2-21, with the corresponding net rates of formation as given by Eq. 4-27 and the parameter values as reported in Table 4-4; ●, full line: 443 K; ■, dash-dotted line: 473 K; ▲, dashed line: 493 K.

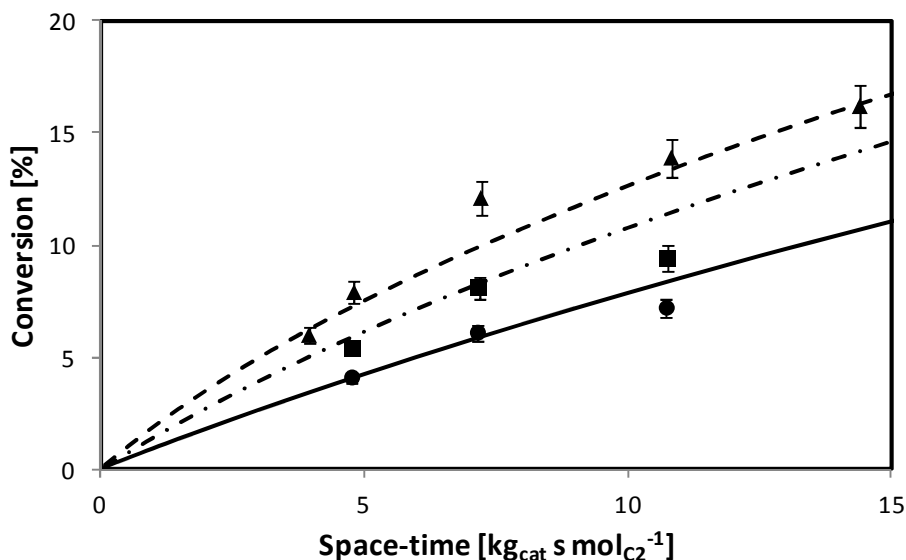


Figure 4-4: Ethene conversion on 1.8wt% Ni-SiO<sub>2</sub>-Al<sub>2</sub>O<sub>3</sub> as function of space time at different inlet ethene partial pressures, at 3.5 MPa total pressure and at 473K. Symbols correspond to experimental data, lines correspond to model simulations, i.e., by integration of Eq. 2-21, with the corresponding net rates of formation as given by Eq. 4-27 and the parameter values as reported in Table 4-4; ●, full line: 0.15 MPa; ■, dash-dotted line: 0.25 MPa; ▲, dashed line: 0.35 MPa.

As shown by Figures 4-3 and 4-4, both differential and integral behavior were observed. More specifically, at space times equal or lower than 7.4 kg<sub>cat</sub> s mol<sub>C2</sub><sup>-1</sup>, differential reactor behavior was obtained, allowing to obtain oligomerization rates in a straightforward

manner. In this space time range, a linear relationship between the oligomerization rate and ethene inlet partial pressure was found, see Figures 4-5.

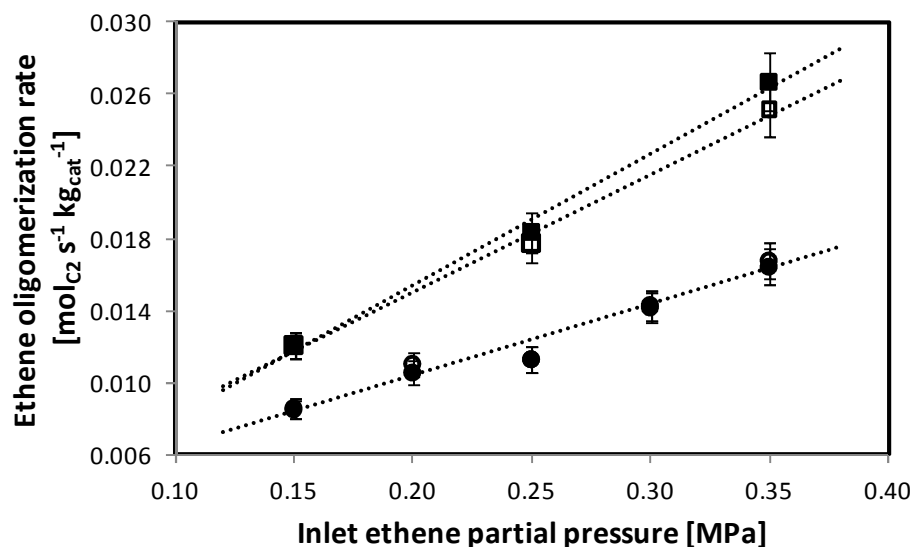


Figure 4-5: Ethene oligomerization rate on 1.8wt% Ni-SiO<sub>2</sub>-Al<sub>2</sub>O<sub>3</sub> as function of ethene inlet partial pressure at different space times and temperatures. Symbols correspond to experimental data, lines are determined by linear regression for each set of experimental conditions indicating the first order dependency on the reaction rate of the ethene inlet partial pressure; ●: 4.8 kg<sub>cat</sub> s mol<sub>C2</sub><sup>-1</sup> and 473 K; ○: 7.2 kg<sub>cat</sub> s mol<sub>C2</sub><sup>-1</sup> and 473 K; ■: 4.8 kg<sub>cat</sub> s mol<sub>C2</sub><sup>-1</sup> and 503 K; □: 7.2 kg<sub>cat</sub> s mol<sub>C2</sub><sup>-1</sup> and 503 K.

A similar observation was made on an amorphous nickel oxide silica-alumina by Kiessling and Froment [3]. Therefore, they proposed the use of an Eley-Rideal mechanism to describe the oligomerization of ethene on amorphous nickel oxide silica-alumina [3].

### 4.3 SEMK model construction

#### 4.3.1 Proposed mechanism for ethene oligomerization

Two mechanisms have already been proposed for alkene oligomerization on nickel complexes, i.e., degenerate polymerization and concerted coupling [4, 5]. Yet another mechanism, i.e., reductive isomerization only occurs in the presence of hydrogen [5].

It is reported that, for both mechanisms, alkene desorption occurs through  $\beta$ -hydride elimination which, hence, regenerates the active site [4], i.e., Ni-H. However, based on DFT calculations, Fan et al. [6] concluded that Ni-H regeneration through  $\beta$ -hydride elimination is energetically very demanding. These authors showed that regeneration would rather occur through  $\beta$ -hydride transfer to form a nickel-ethene species, which is then denoted as the actual catalytic site and which is agreement with the work by Speier et al. [7].

#### **4.3.1.1 Degenerate polymerization**

Degenerate polymerization, see Figure 4-6, starts with the coordination of an ethene molecule at a nickel hydride, leading to a nickel-ethene species (A). In a next step, the coordinated ethene molecule is inserted in the Ni-H bond (B). The formed  $\beta$ -agostic ethyl complex coordinates a second ethene molecule which results in a nickel-ethyl-ethene (C). Upon insertion of the coordinated ethene in the nickel-ethyl bond (D), the first oligomerization, c.q., dimerization has been established. As indicated above, the formed  $\beta$ -agostic alkyl, c.q., butyl, complex does not undergo  $\beta$ -hydride elimination, which would regenerate the Ni-H site, since it is energetically unfavorable [6]. Instead, another ethene molecule has to be coordinated by the complex, leading to a similar nickel-alkyl-ethene species as before in the catalytic cycle (E). The coordinated ethene in this species can either insert in the nickel-alkyl bond (F) or this species can undergo hydride transfer from the growing carbon chain to the nickel (G). The first leads to chain growth while the latter leads to the regeneration of the catalytic site, i.e., the nickel-ethene species, and the release of a 1-alkene. A  $\beta$ -agostic alkyl complex can also isomerize (H), leading to the formation of internal alkenes, see the left hand side of Figure 4-6.

The ratio of insertion to termination is reported to be temperature independent [5]. The main characteristics of the degenerate polymerization mechanism are that it, mainly, leads to an ASF product distribution and that it allows the formation of internal and branched alkenes [7].

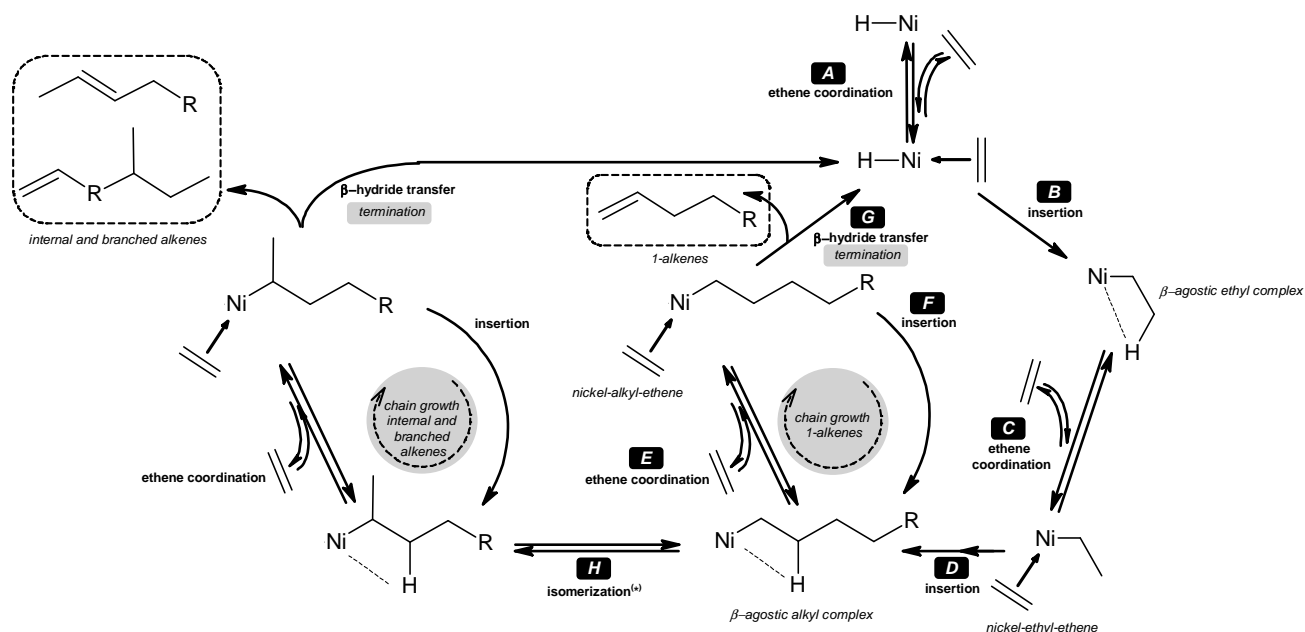


Figure 4-6: Proposed mechanism for ethene oligomerization on a heterogeneous nickel-based catalyst based on degenerated polymerization, <sup>(\*)</sup> the multi-elementary step isomerization is depicted as a elementary step for not to overload the figure.

#### 4.3.1.2 Concerted coupling

Concerted coupling, see Figure 4-7, starts with the coordination of an ethene molecule at a nickel-ion, resulting in a nickel-ethene species (A). In the next step, an additional ethene molecule is coordinated at the nickel-ethene species (B). Via oxidative coupling, the nickel-di-ethene species forms a metallacyclopentane (C) [4, 7]. In this metallacyclopentane, ethene can be inserted consecutively, leading to a metallacycloalkane with a larger ring structure (D). This metallacycloalkane is also susceptible to reductive elimination leading to a nickel-alkene species (E). Via the coordination of an additional ethene molecule (F) a nickel-alkene-ethene species is formed, which can release the alkene product via  $\beta$ -hydride transfer (G), regenerating the catalytic site, i.e., the nickel-ethene species.

In contrast to degenerate polymerization, concerted coupling generally results in the rather selective production of a single linear 1-alkene, of which the chain length depends on the stability of the metallacycle formed and, hence, on the metal-ion used as catalyst [7]. Moreover, it does generally not lead to double bond nor skeletal isomerization products [5, 7].



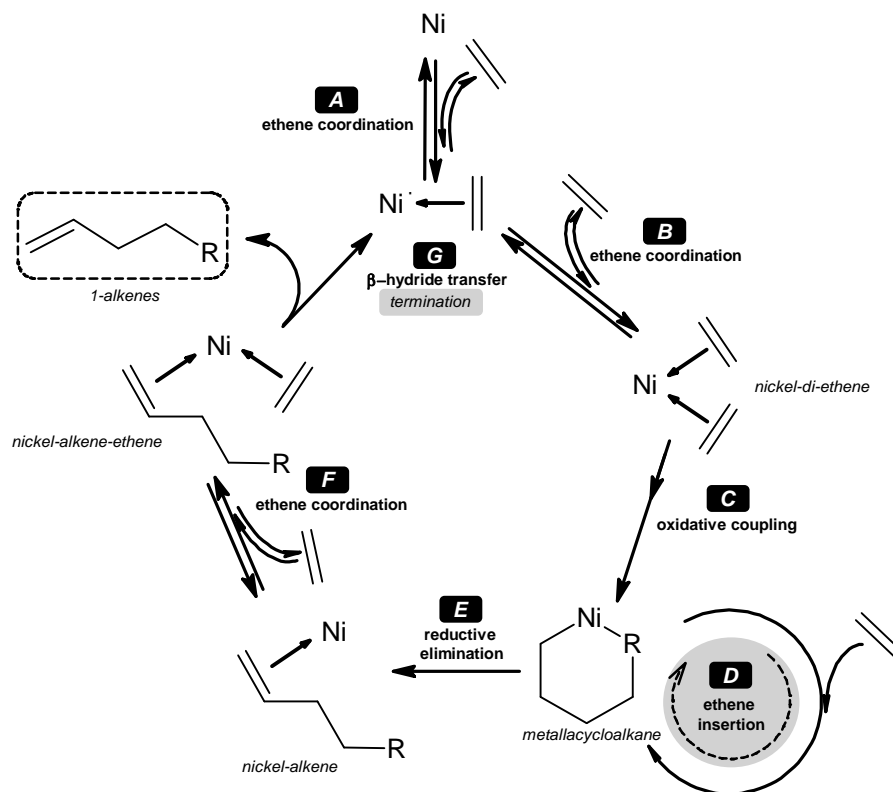


Figure 4-7: Proposed mechanism for ethene oligomerization on a heterogeneous nickel catalyst based on concerted coupling

#### 4.3.1.3 SEMK reaction mechanism

The actual oxidation state of the nickel ion is still a matter of debate, see section 2.1.1.2. Several studies have been performed by different groups indicating that either  $\text{Ni}^+$  [8-11],  $\text{Ni}^{2+}$  [12-17] or even a pair of Ni and  $\text{H}^+$  [18-20] is the active site catalyzing alkene, c.q., ethene, oligomerization. However, in this work, the constructed SEMK model does not critically depend on the oxidation state of the nickel ion. For further notation, the nickel ions will be denoted by  $\text{Ni}^{(+)}$ .

The experimental observations from this work, i.e., the temperature independence of the product distribution as well as its ASF character, see section 4.2, are in favor of degenerate polymerization mechanism. Moreover, concerted coupling has been reported to preferentially produced 1-alkenes with a specific length, see also the previous section, while experimentally components up to octenes were observed. Nevertheless, for both mechanisms, the elementary steps and the corresponding kinetic equations are very similar. In the proposed SEMK mechanism, 4 types of elementary steps were considered, i.e., activation of the catalyst precursor, coordination of an ethene molecule, insertion and termination. In Table 4-2, the corresponding steps for ethene oligomerization on a

heterogeneous nickel containing catalyst are listed as they occur in degenerate polymerization and coupling mechanism. Before any chemical interactions take place, physical adsorption of the alkenes at the catalyst surface, denoted as physisorption, occurs [3].

**Table 4-2: Reaction steps and kinetic parameters for ethene oligomerization on a heterogeneous nickel containing catalyst for the degenerate polymerization and concerted coupling mechanism**

SEMK reaction family	kinetic parameter	degenerate polymerization	concerted coupling
activation of the catalyst precursor	$K^a$	coordination and insertion of an ethene molecule leading to a $\beta$ -agostic ethyl complex	coordination of an ethene molecule leading a nickel-alkene species
coordination of an ethene molecule	$K^c$	leading to a nickel-alkyl-ethene species	leading to a nickel-alkene- ethene species
insertion	$k^{ins}$	insertion of the nickel-alkyl- ethene species	oxidative coupling, followed by reductive elimination.
termination	$k^{ter}$	$\beta$ -hydride transfer	

In short, nickel-alkyl/alkene-ethene species are subject to two competitive reactions, i.e., insertion and termination. The formation of internal alkenes can be attributed to either the occurrence of the degenerate polymerization mechanism or to the presence of (weakly) acid sites on which alkenes can subsequently undergo double bond isomerization via consecutive protonation/deprotonation reactions. The thermodynamic equilibrium within the internal alkenes was accounted for in the kinetic model by redistributing the net rate of formation of the alkenes according to the thermodynamic equilibrium at the reaction conditions considered, see section 4.4.1.3.

### 4.3.2 Rate equations

In the following, the rate equations for ethene oligomerization are derived in accordance with the mechanistic details as outlined in section 4.3.1. First, the pseudo steady state was assumed for all nickel ion species, i.e., their net rate of formation was set equal to zero:

$$R_{Ni^{(+)}(C_{2i})} = R_{Ni^{(+)}(C_2)(C_{2i})} = 0 \quad i = 1 \dots n + 1 \quad 4-1$$

in which  $R$  is the net rate of formation and  $Ni^{(+)}(C_{2i})$  and  $Ni^{(+)}(C_2)(C_{2i})$  are a nickel-alkene species and a nickel-alkyl/alkene-ethene species respectively.  $n$  equals the maximum number of insertions considered and, hence, the maximum carbon number of an alkene produced equals  $2n+2$ . This pseudo steady state approximation resulted in the following relationship between the insertion and termination reaction rates, depending on the carbon number:

$$r_i^{ins} = r_{i+1}^{ins} + r_i^{ter} \quad i = 1 \dots n-1 \quad 4-2$$

and

$$r_n^{ins} = r_n^{ter} \quad 4-3$$

From these equations, the concentration of the nickel-alkyl/alkene-ethene species can be determined as follows:

$$C_{Ni^{(+)}(C_2)(C_{2i})} = C_{Ni^{(+)}(C_2)(C_{2(i+1)})} \frac{k_{i+1}^{ins} + k_i^{ter}}{k_i^{ins}} \quad i = 1 \dots n-1 \quad 4-4$$

and

$$C_{Ni^{(+)}(C_2)(C_{2n})} = C_{Ni^{(+)}(C_2)(C_{2(n+1)})} \frac{k_n^{ter}}{k_n^{ins}} \quad 4-5$$

The net production rates of the alkenes were determined by the termination rate:

$$R_{C_{2(i+1)}} = k_i^{ter} C_{Ni^{(+)}(C_2)(C_{2(i+1)})} = k_i^{ter} C_{Ni^{(+)}(C_2)(C_2)} \prod_{j=1}^i \frac{k_j^{ins}}{k_{j+1}^{ins} + k_j^{ter}} \quad i = 1 \dots n-1 \quad 4-6$$

and

$$R_{C_{2(n+1)}} = k_n^{ter} C_{Ni^{(+)}(C_2)(C_{2(n+1)})} = k_n^{ter} C_{Ni^{(+)}(C_2)(C_2)} \frac{k_n^{ins}}{k_n^{ter}} \prod_{j=1}^{n-1} \frac{k_j^{ins}}{k_{j+1}^{ins} + k_j^{ter}} \quad 4-7$$

The concentration of the nickel-ethyl-ethene/nickel-di-ethene species was determined via the equilibrium coefficient for the coordination of an ethene molecule on a nickel-ethene species  $K^c$ :

$$C_{Ni^{(+)}(C_2)(C_2)} = K^c C_{Ni^{(+)}(C_2)} C_{C_2}^{phys} \quad 4-8$$

in which  $C_{C_2}^{phys}$  represents the concentration of physisorbed ethene. The concentration of the physisorbed alkenes, i.e.,  $C_{C_{2i}}^{phys}$ , was calculated via a Langmuir isotherm:

$$C_{C_{2i}}^{phys} = \frac{C_{sat} K_{C_{2i}}^{phys} p_{C_{2i}}}{1 + \sum_{j=1}^{n+1} K_{C_{2j}}^{phys} p_{C_{2j}}} \quad i = 1 \dots n+1 \quad 4-9$$

in which  $p_{C_{2i}}$  is the partial pressure of an alkene with carbon number  $2i$ . The ‘active site’ concentration, i.e., that of the nickel-ethene species,  $C_{Ni^{(+)}(C_2)}$ , was obtained from the activation equilibrium,  $K^a$ , i.e., coordination of a first ethene molecule on the nickel ion:

$$C_{Ni^{(+)}(C_2)} = K^a C_{Ni_{free}^{(+)}} C_{C_2}^{phys} \quad 4-10$$

The concentration of free nickel ions was determined via the active site balance:

$$C_{Ni_{tot}^{(+)}} = C_{Ni_{free}^{(+)}} + \sum_{i=1}^{n+1} C_{Ni^{(+)}(C_2)(C_{2i})} + \sum_{i=1}^{n+1} C_{Ni^{(+)}(C_{2i})} \quad 4-11$$

By defining the chain growth probability,  $\alpha$ , as:

$$\alpha_i = \frac{k_i^{ins}}{k_{i+1}^{ins} + k_i^{ter}} \quad i = 1 \dots n-1 \quad 4-12$$

and

$$\alpha_n = \frac{k_n^{ins}}{k_n^{ter}} \quad 4-13$$

and the combined chain growth probability, i.e.,  $\gamma$ , as:

$$\gamma_i = \prod_{j=1}^i \alpha_j \quad i = 1 \dots n \quad 4-14$$

the active site balance was rewritten as:

$$C_{Ni_{tot}^{(+)}} = C_{Ni_{free}^{(+)}} \left( 1 + K^a C_{C_2}^{phys} \left( 1 + K^c C_{C_2}^{phys} \left( 1 + \sum_{i=1}^n \gamma_i \left( 1 + \frac{1}{K^c C_{C_2}^{phys}} \right) \right) \right) \right) \quad 4-15$$

In this site balance, every term represents the concentration of a type of active species, i.e., from left to right: the free Ni<sup>(+)</sup> sites, the nickel-ethene species, the nickel-ethyl-ethene/nickel-di-ethene species, the nickel-alkene species and the nickel-alkyl/alkene-ethene species.

The combination of equations 4-6 to 4-15 resulted in the following expression for the net rate of formation of the alkenes:

$$R_{C_{2(i+1)}} = \frac{k_i^{ter} K^c K^a C_{Ni^{(+)}} (C_{C_2}^{phys})^2 \gamma_i}{1 + K^a C_{C_2}^{phys} \left( 1 + K^c C_{C_2}^{phys} \left( 1 + \sum_{j=1}^n \gamma_j \left( 1 + \frac{1}{K^c C_{C_2}^{phys}} \right) \right) \right)} \quad i = 1 \dots n \quad 4-16$$

### 4.3.3 Reaction network generation

For the model, a detailed reaction network, comprising all components and elementary reactions, was required. Since the manual determination of such elementary reaction networks may represent a gargantuan effort, especially when, in a later stage, acid catalyzed steps will be accounted for, an in-house reaction network generation program, ReNGeP [21] was used. In the framework of the present work, the latter was extended with the elementary reaction families of metal ion catalyzed oligomerization, i.e., insertion and termination by  $\beta$ -hydride transfer. In ReNGeP, elementary reactions are described by simple operations on matrices, that represent the reactants. In addition, the matrices are converted to vectors for subsequent use in the kinetic model [22]. Because in the present work only metal ion oligomerization, double bond isomerization and a maximum carbon number equal to 8 were considered, the reaction network was rather limited, i.e., a total of 16 species and 31 corresponding elementary steps.

### 4.3.4 Determination of the number of single events

In order to apply the Single-Event MicroKinetic (SEMK) methodology, the number of single events should be determined for the metal-ion catalyzed ethene oligomerization, see section 2.3. Ethene does not have any chiral atoms and, hence,  $n_{chir}$  equals 0. Because of the presence of  $\pi$ -electrons, no internal symmetry axis is present with respect to this double bond in alkenes heavier than ethene. In the gas phase, ethene has three external symmetry axes, i.e., one along each of the three Cartesian axes. When physisorbed, its rotational freedom is limited such that only a single symmetry axis remains.

The nickel-alkene species, i.e.,  $Ni^{(+)}(C_2)$ ,  $Ni^{(+)}(C_4)$ ,  $Ni^{(+)}(C_6)$  and  $Ni^{(+)}(C_8)$ , all have one chiral atom, i.e., the carbon atom bound to the nickel ion, and no external symmetry axis. For  $Ni^{(+)}(C_4)$ ,  $Ni^{(+)}(C_6)$  and  $Ni^{(+)}(C_8)$ , there exists one terminal  $CH_3$ -group which leads to

an internal symmetry number equal to 3. This results in global symmetry numbers equal to resp. 1/2 and 3/2 for  $Ni^{(+)}(C_2)$  and the heavier nickel-alkyl species, see Table 4-3.

The nickel-alkyl/alkene-ethene species, i.e.,  $Ni^{(+)}(C_2)(C_2)$ ,  $Ni^{(+)}(C_4)(C_2)$ ,  $Ni^{(+)}(C_6)(C_2)$  and  $Ni^{(+)}(C_8)(C_2)$ , all have two chiral atoms, i.e., the two end-carbon atoms bound to the nickel ion, and have no external symmetry axis. For  $Ni^{(+)}(C_4)(C_2)$ ,  $Ni^{(+)}(C_6)(C_2)$  and  $Ni^{(+)}(C_8)(C_2)$ , one terminal CH<sub>3</sub>-group is present, which leads to an internal symmetry number equal to 3. This leads to global symmetry numbers of resp. 1/4 and 3/4 for  $Ni^{(+)}(C_2)(C_2)$  and the higher nickel-alkyl/alkene-ethene species, see Table 4-3.

**Table 4-3: External, internal and global symmetry numbers and number of chiral atoms of the reactant species considered in the reaction network**

Species	$\sigma_{ext}$	$\sigma_{int}$	$n$	$\sigma_{gl}$
Ethene (gas phase)	2 x 2 x 2	1	0	8
Ethene (physisorbed)	2	1	0	2
$Ni^{(+)}(C_2)$	1	1	1	1/2
$Ni^{(+)}(C_4)$	1	3	1	3/2
$Ni^{(+)}(C_6)$	1	3	1	3/2
$Ni^{(+)}(C_8)$	1	3	1	3/2
$Ni^{(+)}(C_2)(C_2)$	1	1	2	1/4
$Ni^{(+)}(C_4)(C_2)$	1	3	2	3/4
$Ni^{(+)}(C_6)(C_2)$	1	3	2	3/4
$Ni^{(+)}(C_8)(C_2)$	1	3	2	3/4

For the calculation of the global symmetry number of the transition state, several possibilities exist, depending on the assumed transition state. An early transition state was assumed in all of the considered reaction families corresponding with a transition state resembling the reactant [6].

## 4.4 Model regression and assessment

### 4.4.1 Identification, classification and determination of the model parameters

According to the model proposed, a total of 2 equilibrium coefficients for activation and ethene coordination, i.e.,  $K^a$  and  $K^c$ , 2 rate coefficients, i.e.,  $k^{ins}$  and  $k^{ter}$ , and 4 physisorption equilibrium coefficients, i.e., one  $K^{phys}$  for each lump of alkenes with an identical carbon number, were to be determined. According to the transition state theory the rate coefficients were written as:

$$k = A \cdot e^{-E_a/RT} = \frac{k_B T}{h} e^{\Delta S^{0,\ddagger}/R} \cdot e^{-E_a/RT} \quad 4-17$$

While the equilibrium coefficients were expressed according to the van 't Hoff relation:

$$K = e^{\Delta_r S^0/R} \cdot e^{-\Delta_r H^0/RT} \quad 4-18$$

and, hence, per coefficient, 2 parameters were to be determined. A total of 16 parameter values was to be determined. The entropy changes were assessed a priori based on justified assumptions [23], see below. The remaining activation energies and reaction enthalpies were estimated by model regression to experimental data. In what follows, the determination of the various model parameters is discussed as well as the corresponding opportunities for further reaction mechanism refinement and model improvement.

#### 4.4.1.1 Physisorption

Upon physisorption of a species, its entropy loss was assumed to be equal to one third of its gas phase translational entropy. It corresponds to the loss of the translational mobility in the gas phase along the axis perpendicular to the catalyst surface, while preserving free mobility of the physisorbed species on the catalyst surface [24].

For every considered carbon number, a physisorption enthalpy was required. Rather than estimating 4 physisorption enthalpies independently, i.e., for ethene, butene, hexene and octene, a linear relationship between the physisorption enthalpy and the carbon number was assumed [25], resulting in the determination of only 2 physisorption parameters, i.e., the physisorption enthalpy of ethene,  $\Delta H_{C_2}^{phys}$ , and the enthalpy increment per two carbon atoms,  $\Delta\Delta H_{2C}^{phys}$ :

$$K_{C_{2i}}^{phys} = e^{-S_{trans}/3R} e^{-\left(\Delta H_{C_2}^{phys} + (i-1)\Delta\Delta H_{2C}^{phys}\right)/RT} \quad i = 1 \dots 4 \quad 4-19$$

#### 4.4.1.2 Nickel ion catalyzed oligomerization

The first two steps in the nickel ion catalyzed oligomerization following physisorption are nickel ion activation and ethene coordination at a nickel-alkene species. These two steps are structurally related since they both involve the binding of an ethene molecule on a nickel ion. Hence, an identical entropy loss was assumed. Because a coordinated species was assumed to have lost an amount of entropy corresponding to the loss of all translational degrees of freedom, the change in entropy upon coordination of a physisorbed species amounted to two thirds of the translational entropy of that component in the gas phase. The reaction enthalpies of the activation by coordination of ethene and the second coordination of ethene at the nickel-alkene species, however, were assumed not to be identical. The presence of a first ethene ligand after activation was allowed to affect the coordination enthalpy of the second ethene molecule. Hence, for both activation and coordination of a second ethene molecule, one parameter was to be determined, i.e.,  $\Delta H^a$  and  $\Delta H^c$ :

$$K^a = e^{-2S^{trans}/3R} \cdot e^{-\Delta H^a/RT} \quad 4-20$$

$$K^c = e^{-2S^{trans}/3R} \cdot e^{-\Delta H^c/RT} \quad 4-21$$

For insertion and termination, an early transition state was assumed, as already discussed in section 4.3.4. Consequently, the entropy change corresponding to transition state formation was set to zero. Per reaction family, one parameter was to be estimated, i.e., the corresponding activation energies  $E_a^{ins}$  and  $E_a^{ter}$ . The kinetic coefficients, based on the transition state theory, were as follows:

$$k^{ins} = \frac{k_B T}{h} e^{-E_a^{ins}/RT} \quad 4-22$$

$$k^{ter} = \frac{k_B T}{h} e^{-E_a^{ter}/RT} \quad 4-23$$

#### 4.4.1.3 Double bond isomerization

Double bond isomerization was experimentally observed to reach thermodynamic equilibrium during each experiment, see section 4.2. Based on the experimental



observations, degenerate polymerization was selected as the most probable reaction mechanism for ethene oligomerization, section 4.3.1.3. Via degenerate polymerization, double bond isomers can be formed by isomerization on the nickel sites, see section 4.3.1.1. However, double bond isomerization via consequent protonation and deprotonation on the weak acid sites of the amorphous  $\text{SiO}_2\text{-Al}_2\text{O}_3$ , see section 2.1.1.2, can also contribute to the formation of these double bond isomers. Due to the thermodynamic equilibrium which was always established, no additional parameters were required to account for double bond isomerization and it becomes irrelevant for the model which isomerization mechanism is actually operating. The required equilibrium coefficients were calculated using the Bensen's group contribution method [26].

#### ***4.4.1.4 Estimation of the reaction enthalpies and activation energies***

Table 4-4 gives an overview of the estimates for the remaining kinetic model parameters. The  $F$  value for the global significance of the model,  $F_s$ , amounted to  $1.1 \cdot 10^5$  which largely exceeds the corresponding tabulated  $F_s$  value. The model was determined to be adequate, with a calculated  $F_a$  value equal to 1.2 which is lower than the tabulated value of 1.6. This means that the differences between the model simulations and experimental observations can be ascribed solely to the experimental error and is not due to a systematic shortcoming of the model or parameter estimate. It was evident from the parameter estimates and their individual confidence intervals that all of them were statistically significant. The activation enthalpy had a much more negative value compared to the coordination enthalpy, i.e.,  $-125.3 \text{ kJ mol}^{-1}$  versus  $-48.4 \text{ kJ mol}^{-1}$ , and a much wider confidence interval. The corresponding physical interpretation is that the activation of the nickel ion is practically irreversible. Hence, any activation enthalpy value leading to a modeled complete transformation of nickel ions into active nickel-ethene species sufficed to obtain a good agreement between experimental data and model simulations. This complete transformation can also be correlated with the initial increase of the catalyst bed temperature when it was first exposed to ethene, see section 4.1.1. A simplified rate equation, accounting for this physical interpretation, was constructed and is discussed in the next section.

**Table 4-4: Reaction enthalpies and activation energies as well as statistical performance indicators, all at 95% confidence level, determined by non-linear regression of the model given by integration of Eq. 2-21 to the experimental data measured at the range of operating conditions given in Table 4-1. Left: according to the original kinetic model given for which the net rates of formation are given by Eq. 4-16; right: according to the revised kinetic model given for which the net rates of formation are given by Eq. 4-27.**

	Value [kJ mol <sup>-1</sup> ]	Value [kJ mol <sup>-1</sup> ]
$\Delta H_{C_2}^{phys}$	-6.8 ± 0.2	-7.2 ± 0.2
$\Delta\Delta H_{2C}^{phys}$	-12.3 ± 0.4	-12.3 ± 0.4
$\Delta H^a$	-125.3 ± 63.1	
$\Delta H^c$	-48.4 ± 0.4	-49.9 ± 0.6
$E_a^{ins}$	74.5 ± 0.4	76.3 ± 0.6
$E_a^{ter}$	66.0 ± 0.5	67.8 ± 0.6
Residual SSQ	110.9	111.9
$F_s$ (tabulated value)	1.1 10 <sup>5</sup> (3.1)	1.3 10 <sup>5</sup> (3.2)
$F_a$ (tabulated value)	1.2 (1.6)	1.2 (1.6)

#### 4.4.2 Revised model: fast and irreversible nickel ion activation

As in the original kinetic model, the concentration of the nickel-ethyl-ethene/nickel-di-ethene species was determined via the coordination equilibrium:

$$C_{Ni^{(+)}(C_2)(C_2)} = K^c C_{Ni^{(+)}(C_2)} C_{C_2}^{phys} \quad 4-24$$

In this case, it was assumed that all initially available nickel was instantaneously and irreversibly transformed into the nickel-ethene species under an ethene atmosphere, i.e.,  $K^a \gg \gg$ . Hence, after this initial coordination, the concentration of the nickel-ethene species equals the initial nickel ion concentration. The concentration of the nickel-ethene species was found via a nickel ion site balance:

$$C_{Ni^{(+)}(C_2)} = C_{Ni^{(+)}(C_2)} = \sum_{i=1}^{n+1} C_{Ni^{(+)}(C_2)(C_{2i})} + \sum_{i=1}^{n+1} C_{Ni^{(+)}(C_{2i})} \quad 4-25$$

Substitution of the combined chain growth probability,  $\gamma$ , and the coordination equilibria resulted in the following expression:

$$C_{Ni^{(+)}(C_2)} = C_{Ni^{(+)}(C_2)} \left( 1 + K^c C_{C_2}^{phys} \left( 1 + \sum_{i=1}^n \gamma_i \left( 1 + \frac{1}{K^c C_{C_2}^{phys}} \right) \right) \right) \quad 4-26$$

The combination of equations 4-6, 4-8 and 4-27 to 4-29 resulted in the net rate of formation of the alkenes for the simplified kinetic model:

$$R_{C_2(i+1)} = \frac{k_i^{ter} K^c C_{Ni^{(+)}} C_{C_2}^{phys} \gamma_i}{1 + K^c C_{C_2}^{phys} \left( 1 + \sum_{i=1}^n \gamma_i \left( 1 + \frac{1}{K^c C_{C_2}^{phys}} \right) \right)} \quad i = 1 \dots n \quad 4-27$$

In Table 4-4 an overview is also given of the parameter estimates for the revised kinetic model. The model had a 20% higher  $F_s$  value for the global significance than the original model. This increase stemmed from the reduction in number of parameters without pronounced effect on the residual sum of squares, see Table 4-4. As for the original model, the revised kinetic model was tested to be adequate with the calculated  $F_a$  value equal to 1.2. Similar parameter estimates and corresponding confidence intervals were obtained for the revised model compared to the original model, see Table 4-4.

### 4.4.3 Model parameter assessment

The activation energy for insertion and termination differed by about 10 kJ mol<sup>-1</sup>. In combination with an identical pre-exponential factor for both reactions, see section 4.4.1.2, this led to low chain growth probabilities around 0.1, see Table 4-5. The difference in activation energies between insertion and termination was sufficiently small for the chain growth probabilities to be practically constant in the investigated temperature range.

**Table 4-5: Chain growth probability  $\alpha$  as function of temperature as determined by Eqs. 4-12 and 4-13 calculated with the parameter values reported in Table 4-4.**

Temperature [K]	443	453	463	473	483	493	503
$\alpha$ [-]	0.090	0.095	0.099	0.103	0.107	0.112	0.116

The more termination is dominating insertion, corresponding with low chain growth probabilities, the less product selectivities depend on the reaction conditions. At these low chain growth probabilities, a relative change of 30%, i.e., the change of the chain growth probability in this work in the investigated temperature range, will not result in a noticeable change in the product distribution. This is illustrated with the following three theoretical Anderson Schulz Flory distributions, see equation 4-28 for which the product distribution is given by:

$$w_i = i(1 - \alpha)^2 \alpha^{i-1} \quad 4-28$$

in which  $w_i$  is the mass fraction of a component with carbon number  $i$ . From the theoretical ASF distributions it was clear that, indeed, for sufficiently small chain growth probabilities, e.g.,  $\alpha = 0.1$ , a relative deviation of 30% would not lead to a significant change in product distribution. The higher the chain growth probability, the more visible changes in the product distribution becomes, see Figure 4-8.

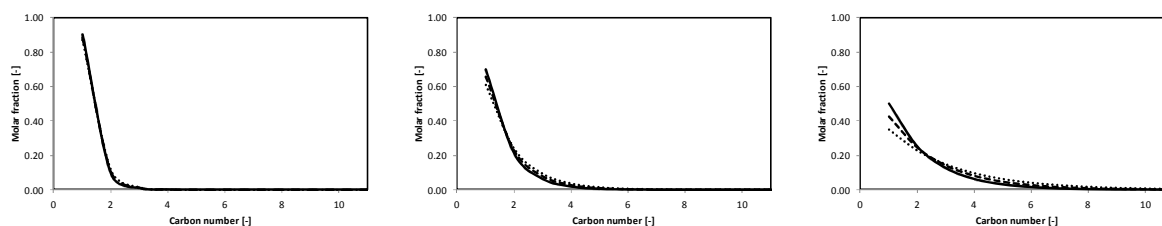


**Figure 4-8: Theoretical ASF distributions given by Eq. 4-31 for different chain growth probabilities  $\alpha$ . Full lines:  $\alpha_{ref}$ , dashed lines:  $1.15 \alpha_{ref}$ , dotted lines:  $1.30 \alpha_{ref}$ . Left:  $\alpha_{ref} = 0.1$ , middle:  $\alpha_{ref} = 0.3$ , right:  $\alpha_{ref} = 0.5$ .**

The above discussed behavior explains the apparent independence of the product selectivity from the reaction conditions, especially of the reaction temperature, as experimentally observed, see Figure 4-1.

With the obtained parameters estimates, the denominator of equation 4-27 amounted to 1.10 to 1.13 in the range of investigated reaction conditions. Additionally, the change in concentration of physisorbed components, as a function of the ethene inlet partial pressure was practically linear, see section 4.4.4. This was due to the relatively low surface coverage with physisorbed components and the small interval in which the inlet partial pressure of ethene was varied. Exhibiting such a behavior, the kinetic model was in agreement with the reported first order dependency of the reaction rate as function of ethene partial pressure by Kiessling and Froment [3].

The binary correlation coefficients between the parameter estimates were very similar for both the original and revised kinetic model. In Table 4-6, the binary correlation coefficients for the revised kinetic model are given. Overall, correlation coefficients below 0.95 were obtained, indicating that the corresponding parameters were not significantly correlated. Nevertheless, some of the correlation coefficients exhibited logic trends. The activation energies of insertion and termination were correlated positively, i.e., a correlation coefficient amounting to 0.94, meaning that an increase of one of the activation energies led to an increase of the activation energy of the other reaction. The positive correlation has

its origin in reproducing the observed independence of the product selectivity from the reaction conditions. Negative correlation coefficients were obtained between the coordination enthalpy and activation energies of insertion and termination, i.e., resp. -0.88 and -0.84. To obtain an identical overall temperature dependence, c.q., apparent activation energy, a decrease of the coordination enthalpy and, hence, an increase of the heat of coordination was compensated by an increase of the activation energy of both insertion and termination.

**Table 4-6: Binary correlation coefficient matrix as determined by non-linear regression by integration of Eq. 2-21, with the corresponding net rates of formation, Eq. 4-27, to the experimental data measured at the operating conditions given in Table 4-1.**

	$\Delta H_{C_2}^{phys}$	$\Delta\Delta H_{2C}^{phys}$	$\Delta H^c$	$E_a^{ins}$	$E_a^{ter}$
$\Delta H_{C_2}^{phys}$	1.00	-0.26	0.29	0.02	0.02
$\Delta\Delta H_{2C}^{phys}$	-0.26	1.00	-0.44	0.08	-0.02
$\Delta H^c$	0.29	-0.44	1.00	-0.88	-0.84
$E_a^{ins}$	0.02	0.08	-0.88	1.00	0.94
$E_a^{ter}$	0.02	-0.02	-0.84	0.94	1.00

#### 4.4.4 Kinetic model performance

As can be seen in Figure 4-1, the model was capable to simulate the linear dependence between product yield and conversion. The relatively small values of the chain growth probability, see Table 4-5, resulted in a high selectivity towards the dimers, c.q., butene, and a product selectivity which was independent of reaction conditions. Also, Figures 4-3 and 4-4 show the model performance with respect to the experimental data. Both the temperature and pressure effect were simulated adequately.

In Figures 4-9 and 4-10 several residual diagrams are shown. The ethene, butene, hexene and octene molar outlet flow rate were used as responses for the actual regression as discussed in section 4.1.2. The residual diagram for the butene molar outlet flow rate is given in Figure 4-9 as function of three independent variables, i.e., temperature (a), ethene inlet partial pressure (b) and space-time (c), and one dependent variable, i.e., the butene molar outlet flow rate (d). This response was simulated very well, as indicated by the random distribution of the simulated points around the x-axis.

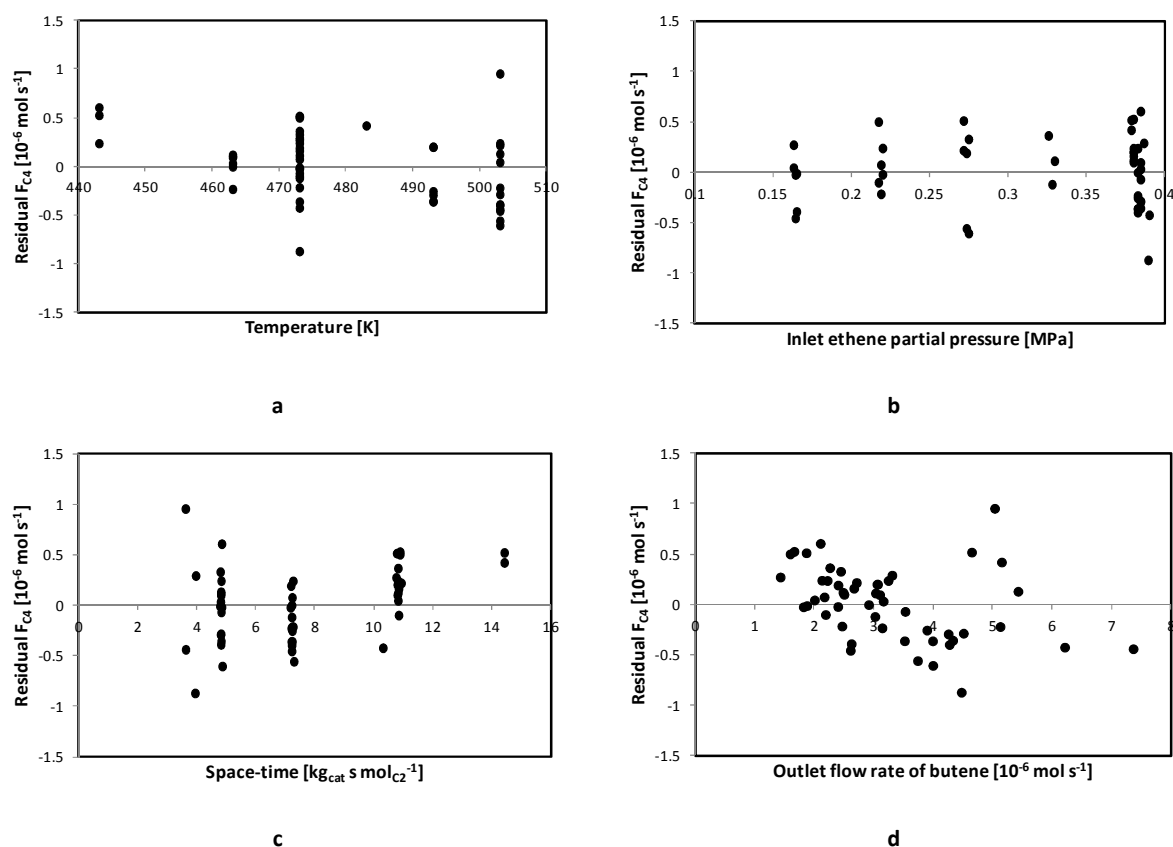


**Figure 4-9: Residual diagrams for the molar outlet flow rate of butene as function of temperature (a), inlet partial pressure of ethene (b), space-time (c) and molar flow rate of butene (d). Residuals are determined by integration of Eq. 2-21, with the corresponding net rates of formation, Eq. 4-27 and the parameter values reported in Table 4-4.**

The residual diagrams as function of ethene inlet partial pressure for the other modeled responses are given in Figure 4-10, i.e., ethene (a), hexene (b) and octene (c). These responses were simulated very well without any systematic deviation. Additionally, no deviation could be observed in any of the residual diagrams, which indicated the model's adequacy. The 1-butene molar outlet flow rate, which was not used during regression and only calculated via the thermodynamic equilibrium within the C<sub>4</sub> internal alkenes, was also well simulated and the corresponding residuals were independent of the operating conditions, see Figure 4-10d.

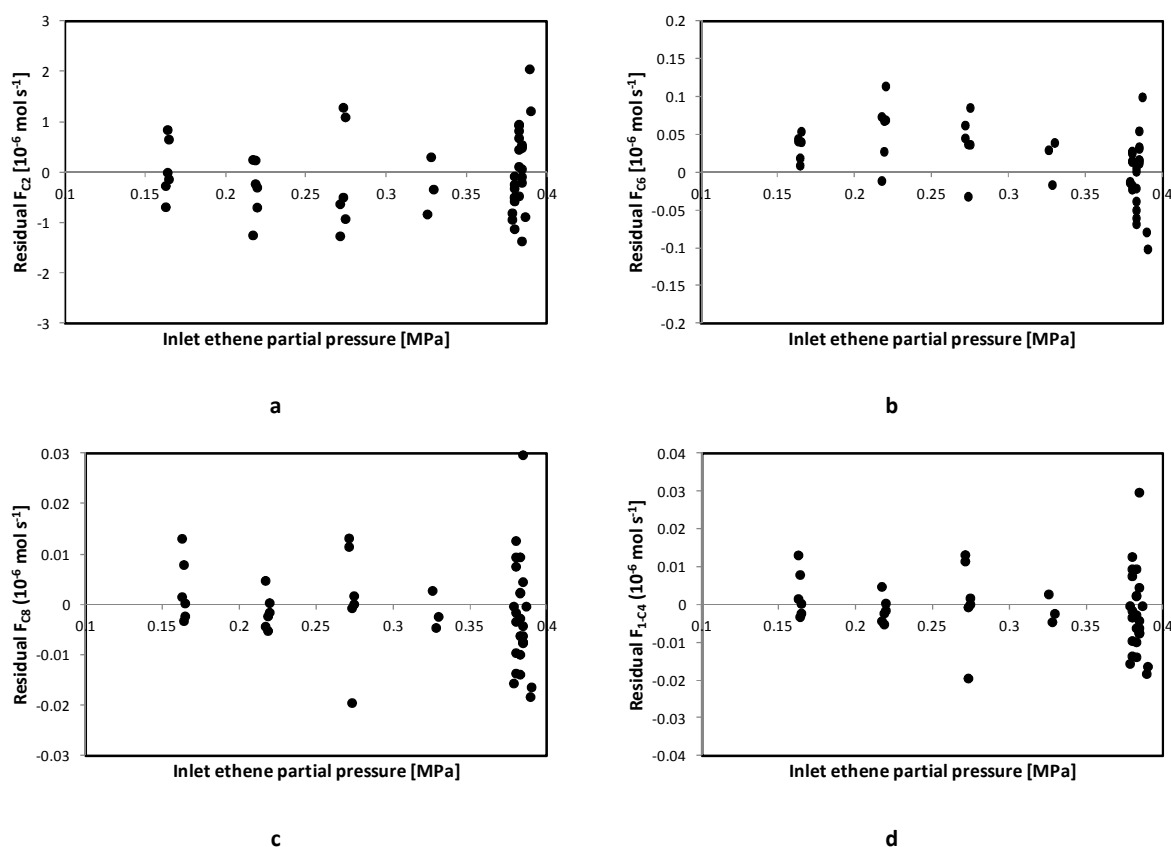


Figure 4-10: Residual diagrams for the molar outlet flow rate of ethene (a), hexene (b), octene (c) and 1-butene (d) as function of inlet partial pressure of ethene. Residual are determined by integration of Eq. 2-21, with the corresponding net rates of formation, Eq. 4-27 and the parameter values reported in Table 4-4.

#### 4.4.5 Physisorbed and chemisorbed species concentrations

Figures 4-11 and 4-12 show the total catalyst occupancy by physisorbed species and the corresponding fractions, as a function of the space time, the temperature and the ethene inlet partial pressure. The latter two effects were investigated at equal conversion, i.e., 13.4%. As can be seen on these figures, between 10% and 50% of the catalyst was occupied by physisorbed species in the investigated range of operating conditions. At space time equal to zero, about 10% of the catalyst was occupied, exclusively by ethene, while with increasing conversion, the physisorbed ethene fraction logically decreased while the heavier components that were formed, the octenes in particular, physisorbed more strongly, see Figure 4-11.

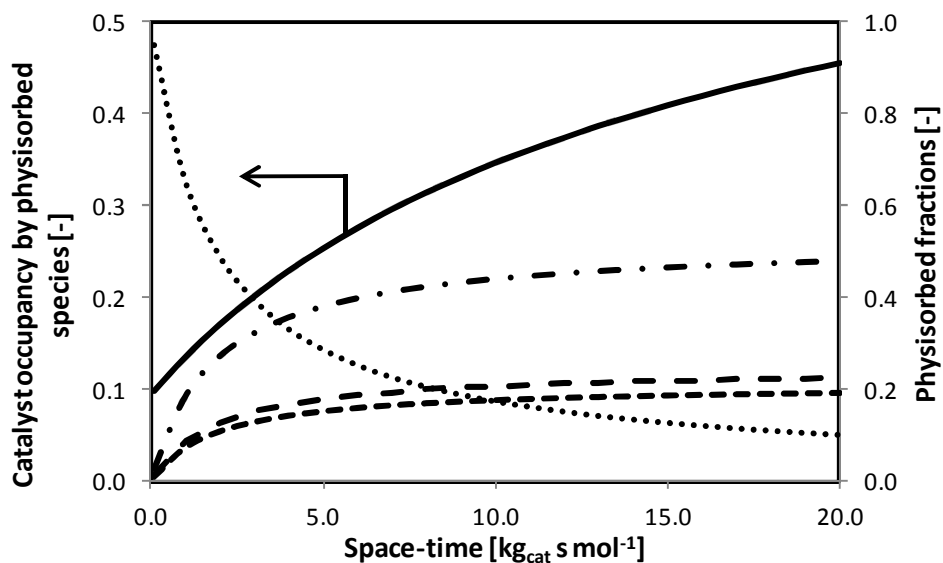


Figure 4-11: Catalyst occupancy by physisorbed species and the corresponding physisorbed fractions as a function of space-time at 473 K and an inlet ethene partial pressure equal to 0.35 MPa, calculated by integration of Eq. 2-21, with the corresponding net rates of formation, Eq. 4-27 and the parameter values reported in Table 4-4. Full line: catalyst occupancy by physisorbed species, dotted line: physisorbed fraction of ethene, short-dashed line: physisorbed fraction of butene, long-dashed line: physisorbed fraction of hexene, dashed dotted line: physisorbed fraction of octene.

With increasing temperature, physisorption became less pronounced, see Figures 4-12. Since physisorption is an exothermic process and was assumed to be in equilibrium, a temperature increase led to a shift in the physisorption equilibrium towards the gas phase molecules. Due to the low physisorption enthalpy of light components in comparison with heavier components, the physisorption equilibrium of the former were influenced less by a temperature increase compared to the latter. At equal conversion levels, this led to an increase of the physisorbed fraction of the most weakly physisorbed component, i.e., ethene, and a decrease of the physisorbed fraction of the stronger physisorbed components as function of the temperature.



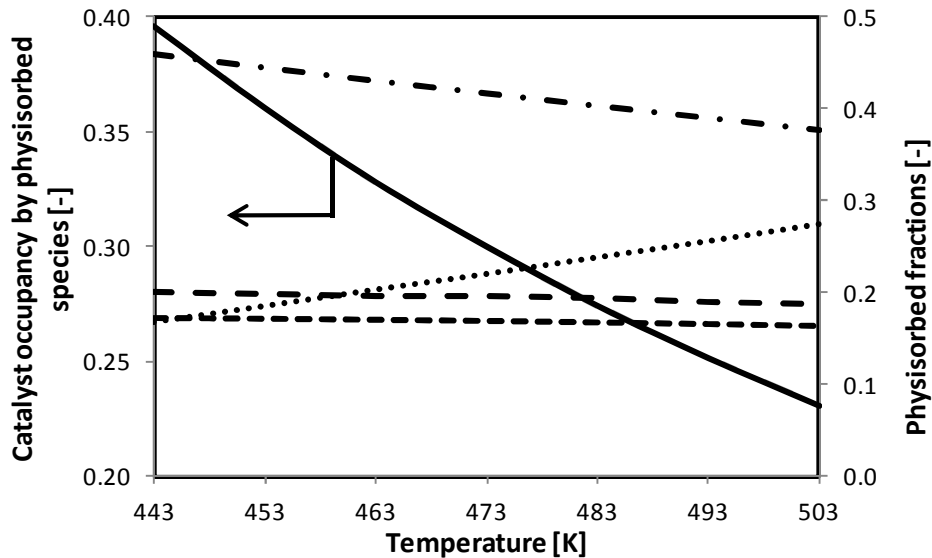


Figure 4-12: Catalyst occupancy by physisorbed species and the corresponding physisorbed fractions as a function of temperature at an inlet ethene partial pressure equal to 0.35 MPa at 13.4% conversion, calculated by integration of Eq. 2-21, with the corresponding net rates of formation, Eq. 4-27 and the parameter values reported in Table 4-4. Full line: catalyst occupancy by physisorbed species, dotted line: physisorbed fraction of ethene, short-dashed line: physisorbed fraction of butene, long-dashed line: physisorbed fraction of hexene, dashed dotted line: physisorbed fraction of octene.

Increasing the ethene inlet partial pressure, while maintaining an equal level of conversion, increased the catalyst occupancy by physisorbed species linearly. This was in accordance with the first order dependency of the reaction rate to the ethene partial pressure. The physisorbed fractions did not change appreciably since the relative change in partial pressure was equal for every component.

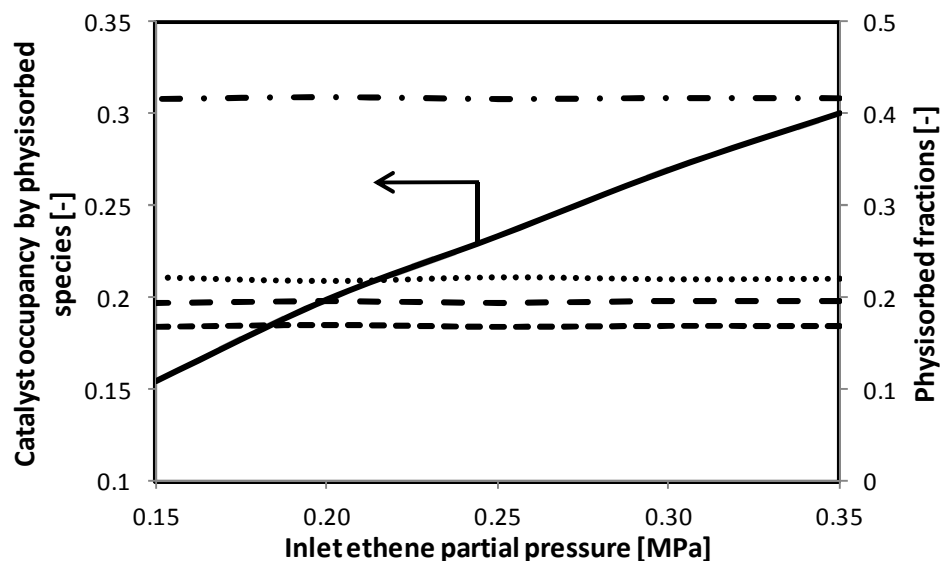


Figure 4-13: Catalyst occupancy by physisorbed species and the corresponding physisorbed fractions as a function of the inlet ethene partial pressure at 473 K, at 13.4% conversion, calculated by integration of Eq. 2-21, with the corresponding net rates of formation, Eq. 4-27 and the parameter values reported in Table 4-4. Full line: catalyst occupancy by physisorbed species, dotted line: physisorbed fraction of ethene, short-dashed line: physisorbed fraction of butene, long-dashed line: physisorbed fraction of hexene, dashed dotted line: physisorbed fraction of octene.

From the model, also information about the occurrence of the nickel ions, i.e., the fraction of nickel-alkene species and nickel-alkyl/alkene-ethene species, was retrieved. Under all the reaction conditions tested, the nickel ions were bound with at least one alkene species, see section 4.3.1. About 90% of the nickel ions were found as a nickel-ethene species. The coordination of an additional ethene species onto a nickel-alkene species was relatively weak. The corresponding equilibrium coefficient amounted to maximum  $10^{-3}$ , explaining why about 1000 times more nickel-alkene than nickel-alkyl/alkene-ethene species were determined by the model. Termination was 7 to 10 times faster than insertion and, hence, regeneration of nickel-ethene species was very fast, which also contributed to the abundance of the latter within the nickel ions.

## 4.5 Conclusions

Intrinsic ethene oligomerization kinetics were determined on an amorphous silica-alumina, impregnated with nickel ions. Due to the absence of strong acid sites, the catalytic activity towards oligomerization originated solely from the nickel ion sites and allowed the specific determination of the nickel ion catalyzed oligomerization kinetics. The products followed an Anderson Schulz Flory distribution with a particularly limited chain growth probability of

about 0.1. As a result, the nickel ion sites mainly dimerized ethene to butene. The product selectivities were independent of the operating conditions as can be expected from an insertion-termination mechanism exhibiting low chain growth probabilities. The reaction rate increased linearly with increasing ethene partial pressure.

A Single-Event MicroKinetic model for ethene oligomerization was constructed. On a fresh catalyst, ethene coordinated fast and irreversibly on the nickel ion sites, forming the active nickel-ethyl species, after which the insertion-termination mechanism started. Degenerate polymerization was determined to be the most likely reaction mechanism, but the occurrence of a concerted coupling mechanism could not be totally excluded. The kinetic parameters were all estimated with narrow confidence intervals and a precise physical meaning. The model itself was statistically tested to be significant and adequate and was able to describe all experimental data without any systematic deviations.

The catalyst occupancy by physisorbed species ranged from 10% to 50%, mainly comprising ethene and octene. There was a linear increase of the concentration of physisorbed components as function of the ethene partial pressure. About 90% of the nickel ions were found to be a nickel-ethene species, due to the rather weak coordination of an additional ethene species and the high rate of termination compared to insertion.

## 4.6 References

- [1] J. Patzlaff, Y. Liu, C. Graffmann, J. Gaube, *Applied Catalysis a-General*. 186 (1999) 109-119.
- [2] R.L. Espinoza, C.J. Korf, C.P. Nicolaidis, R. Snel, *Applied Catalysis*. 29 (1987) 175-184.
- [3] D. Kiessling, G.F. Froment, *Applied Catalysis*. 71 (1991) 123-138.
- [4] C. Lepetit, J.Y. Carriat, C. Bennett, *Applied Catalysis a-General*. 123 (1995) 289-300.
- [5] S.M. Pillai, M. Ravindranathan, S. Sivaram, *Chemical Reviews*. 86 (1986) 353-399.
- [6] L. Fan, A. Krzywicki, A. Somogyvari, T. Ziegler, *Inorganic Chemistry*. 35 (1996) 4003-4006.
- [7] F. Speiser, P. Braunstein, W. Saussine, *Accounts of Chemical Research*. 38 (2005) 784-793.
- [8] F.X. Cai, C. Lepetit, M. Kermarec, D. Olivier, *Journal of Molecular Catalysis*. 43 (1987) 93-116.
- [9] T.X. Cai, *Catalysis Today*. 51 (1999) 153-160.
- [10] A.A. Davydov, M. Kantcheva, M.L. Chepotko, *Catalysis Letters*. 83 (2002) 97-108.
- [11] I.V. Elev, B.N. Shelimov, V.B. Kazanskii, *Kinetics and Catalysis*. 25 (1984) 955-958.
- [12] L. Bonneviot, D. Olivier, M. Che, *Journal of Molecular Catalysis*. 21 (1983) 415-430.
- [13] A.K. Ghosh, L. Kevan, *Journal of Physical Chemistry*. 94 (1990) 3117-3121.
- [14] J. Heveling, C.P. Nicolaidis, M.S. Scurrell, *Applied Catalysis a-General*. 173 (1998) 1-9.

- [15] M. Lallemand, A. Finiels, F. Fajula, V. Hulea, *Applied Catalysis a-General*. 301 (2006) 196-201.
- [16] A. Martinez, M.A. Arribas, P. Concepcion, S. Moussa, *Applied Catalysis a-General*. 467 (2013) 509-518.
- [17] A.N. Mlinar, G.B. Baur, G.G. Bong, A. Getsoian, A.T. Bell, *Journal of Catalysis*. 296 (2012) 156-164.
- [18] V. Hulea, F. Fajula, *Journal of Catalysis*. 225 (2004) 213-222.
- [19] F.T.T. Ng, D.C. Creaser, *Applied Catalysis a-General*. 119 (1994) 327-339.
- [20] R. Spinicci, A. Tofanari, *Materials Chemistry and Physics*. 25 (1990) 375-383.
- [21] G.G. Martens, J.W. Thybaut, G.B. Marin, *Industrial & Engineering Chemistry Research*. 40 (2001) 1832-1844.
- [22] J.W. Thybaut, G.B. Marin, *Journal of Catalysis*. 308 (2013) 352-362.
- [23] J.A. Dumesic, D.F. Rudd, L.M. Aparicio, J.E. Rekoske, A.A. Trevino, *The Microkinetics of Heterogeneous Catalysis* American Chemical Society, Washington, DC, 1993.
- [24] G.G. Martens, G.B. Marin, J.A. Martens, P.A. Jacobs, G.V. Baroni, *Journal of Catalysis*. 195 (2000) 253-267.
- [25] J.F.M. Denayer, G.V. Baron, *Adsorption-Journal of the International Adsorption Society*. 3 (1997) 251-265.
- [26] S.W. Benson, J.H. Buss, *Journal of Chemical Physics*. 29 (1958) 546-572.

# Chapter 5

## Exploiting Bifunctional Heterogeneous Catalysts in Ethene Oligomerization: Guidelines for Rational Catalyst Design

---

In this work, ethene oligomerization is investigated on a bifunctional, heterogeneous catalyst, i.e., Ni-Beta zeolite. The experimental results indicate the presence of acid catalyzed reactions such as isomerization, oligomerization and cracking as evident from the formation of odd carbon numbered alkenes, e.g., propene and pentene. For modeling purposes, the SEMK model for metal-ion catalyzed ethene oligomerization, see chapter 4, is extended to account for these acid catalyzed elementary steps. Based on the SEMK model, a reaction path analysis is performed from which guidelines were derived for rational catalyst design aiming at the production of propene, linear 1-alkenes and gasoline.

## 5.1 Procedures

### 5.1.1 Experimental conditions

The experimental dataset was obtained on a Ni-Beta zeolite using the HTK-1 set-up as described in sections 2.1.1.3 and 2.1.2.2. Catalyst deactivation was observed from the exponential decrease in observed ethene conversion with time-on-stream. Therefore, the outlet molar composition was measured during 8 hours and an extrapolation was performed to zero time-on-stream to approximate the activity of a fresh catalyst. In between every run, the reactor was emptied and carefully cleaned.

Methane was not detected in the product stream and was fed as an internal standard to verify the carbon and mass balance which was always closed within  $\pm 5\%$ . The separation of the C<sub>5</sub>+ double bound isomer alkenes was not possible with the present analysis equipment. Therefore, the product outlet molar flow rates were lumped per carbon number. A clear distinction between different carbon numbered alkenes could be made up to octene. Additionally, only components up to octene were detected significantly. In total, 14 experiments including one repeat experiment, were performed. The range of investigated experimental conditions was chosen as such intrinsic kinetics were obtained, see section 2.1.2.2, and is given in Table 5-1.

**Table 5-1: Range of investigated experimental conditions for ethene oligomerization on Ni-Beta**

Temperature	Total pressure	Ethene partial pressure	Space-time
[K]	[MPa]	[MPa]	[kg <sub>cat</sub> s mol <sub>C<sub>2</sub></sub> <sup>-1</sup> ]
443 – 543	1.5 – 3.5	0.17 – 0.40	4.2 – 12.7

### 5.1.2 Definition of responses

In total, 7 responses were used, i.e., the lumped outlet molar flow rates per carbon number, ranging from ethene to octene.

## 5.2 Ethene oligomerization on bifunctional catalysts: experimental investigation

Due to catalyst deactivation with increasing time-on-stream, see section 5.1.1, the experimental dataset was limited to 14 well-selected points within the range of reaction conditions reported in Table 5-1. The experimental error was determined to be ca. 12%, which could mainly be attributed to the processing of the experimental data, including the extrapolation to zero time-on-stream. An example of this extrapolation is given in Figure 5-1, in which the measured ethene conversion and butene and hexene selectivities are plotted as function of time-on-stream. An exponential extrapolation to zero hour time-on-stream yielded the best overall fit for all experiments and was used to determine the initial catalyst behavior.

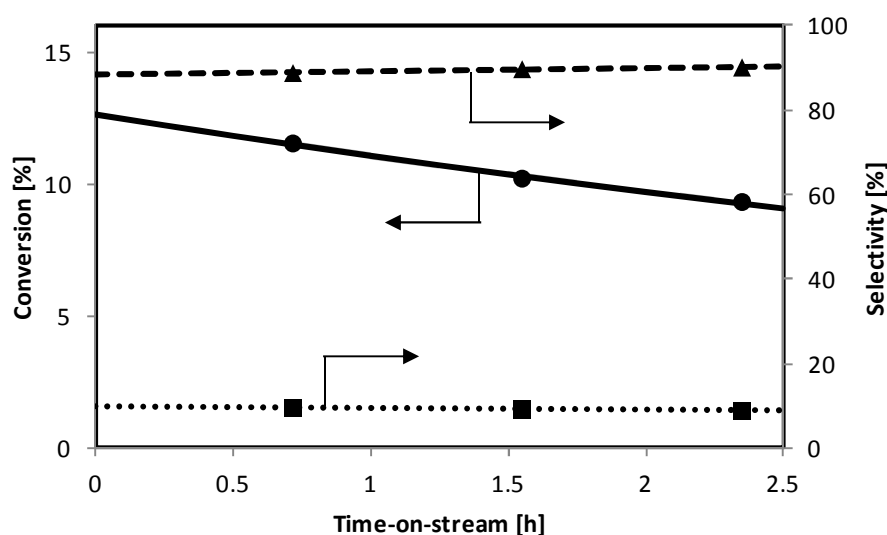


**Figure 5-1:** Ethene conversion and butene and hexene selectivity on 4.9wt% Ni-Beta as function of time-on-stream at 523 K,  $10.2 \text{ kg}_{\text{cat}} \text{ s mol}^{-1}$ , 2.5 MPa total pressure and an ethene inlet partial pressure equal to 0.25 MPa. Symbols correspond to experimental observations, lines are the exponential trend lines to determine the ethene conversion and product selectivities at zero hour time-on-stream. ●, full line: conversion, left axis; ▲, dashed line: butene selectivity, right axis; ■, dotted line: hexene selectivity, right axis.

The ethene oligomerization rate ranged from  $0.006$  to  $0.018 \text{ mol s}^{-1} \text{ kg}_{\text{cat}}^{-1}$ , which is slightly smaller than the ethene oligomerization rate on amorphous 1.8wt% Ni-SiO<sub>2</sub>-Al<sub>2</sub>O<sub>3</sub> at slightly milder reaction conditions, i.e.,  $0.007$  to  $0.027 \text{ mol s}^{-1} \text{ kg}_{\text{cat}}^{-1}$ , see section 4.2. Thermodynamic equilibrium was always obtained within the linear butene fraction, i.e., 1-butene, 2-cis-butene and 2-trans-butene, such as in previous work, see section 4.2. The

product distribution consisted mainly of butene and hexene, i.e., resp. 80-90% and 5-10%, while small amounts of odd carbon numbered alkenes were produced. Propene and pentene contributed for resp. ca. 0.1-1.0% and 0.2-2.5% to the product distribution. Heptene was only detected in trace amounts while octene was formed to a similar extent as propene. The even carbon numbered alkenes can reasonably be mainly related to oligomerization on the nickel-ion sites, while the acid sites are responsible for the production of the odd carbon numbered alkenes [1].

The space-time effect on the ethene conversion and product selectivities is shown in Figures 5-2 and 5-3. With increasing space-time and conversion, the butene selectivity decreases while the hexene selectivity remains more or less constant and other product selectivities increase. The butene formation from ethene is, hence, considered as the first step in the reaction mechanism and, correspondingly, butene can be regarded as a primary product. All other components are formed from butene via further oligomerization on the nickel-ion sites or oligomerization, isomerization and cracking on the acid sites and are secondary products.

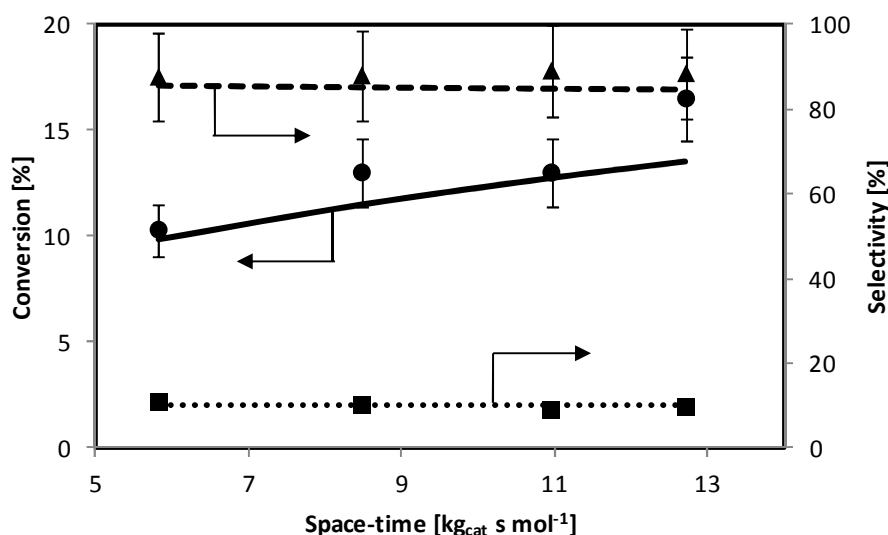


**Figure 5-2: Ethene conversion and butene and hexene selectivity on 4.9wt% Ni-Beta as function of space-time at 523 K, 3.0MPa total pressure and an ethene inlet partial pressure equal to 0.35 MPa. Symbols correspond to experimental observations, lines correspond to model simulations, i.e., integration of Eq. 2-21, with the corresponding net rates of formation as given by Eq. 5-15 and the parameter values as reported in Tables 5-5 and 5-6; ●, full line: conversion, left axis; ▲, dashed line: butene selectivity, right axis; ■, dotted line: hexene selectivity, right axis.**



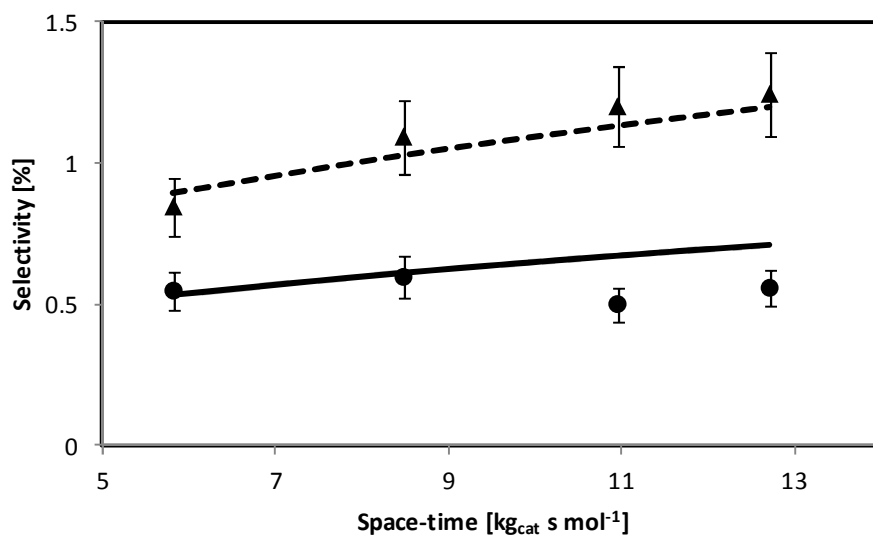


**Figure 5-3: Propene and pentene selectivity on 4.9wt% Ni-Beta as function of space-time at 523 K, 3.0 MPa total pressure and an ethene inlet partial pressure equal to 0.35 MPa. Symbols correspond to experimental observations, lines correspond to model simulations, i.e., integration of Eq. 2-21, with the corresponding net rates of formation as given by Eq. 5-15 and the parameter values as reported in Tables 5-5 and 5-6 ●, full line: propene; ▲, dashed line: pentene. M**

The temperature effect on the ethene conversion and propene and pentene selectivities is shown in Figure 5-4. With increasing temperature, the conversion increases from 5 to 15% and the propene and pentene selectivity increases from 0 to resp. 1% and 2%. This increase in selectivities cannot be attributed solely to a conversion effect. This becomes clear when inspecting Figure 5-3, indicating that a conversion increase from 10 to 15% only leads to an increase of less than 0.2% and 0.5% for resp. the propene and pentene selectivities. Similarly, the butene and hexene selectivity decreases slightly with increasing temperature (not shown). Higher temperatures seem to favor the formation of odd-carbon numbered components, probably through cracking of larger alkenes produced by oligomerization on either metal-ion and acid sites.

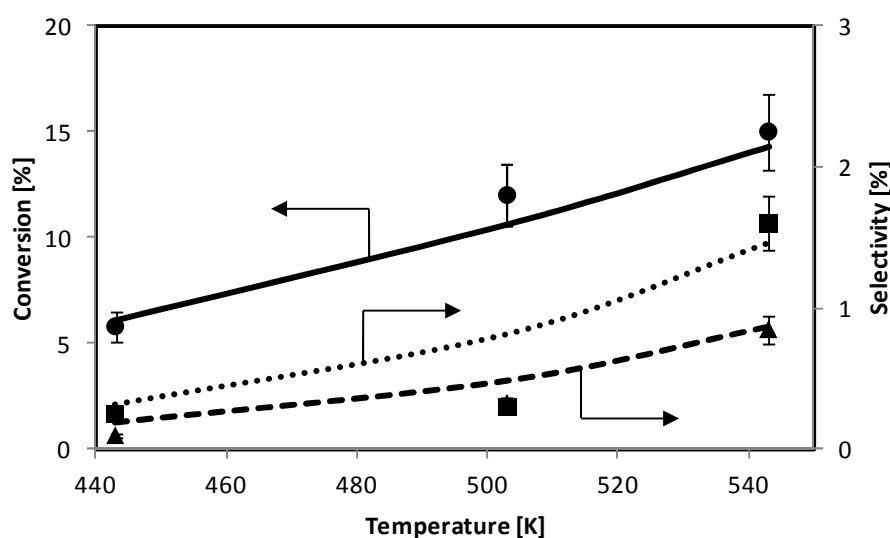


**Figure 5-4:** Ethene conversion and propene and pentene selectivity on 4.9wt% Ni-Beta as function of temperature at  $10.5 \text{ kg}_{\text{cat}} \text{ s mol}^{-1}$ , 3.0 MPa total pressure and an ethene inlet partial pressure equal to 0.35 MPa. Symbols correspond to experimental observations, lines correspond to model simulations, i.e., integration of Eq. 2-21, with the corresponding net rates of formation as given by Eq. 5-15 and the parameter values as reported in Tables 5-5 and 5-6; ●, full line: conversion, left axis; ▲, dashed line: propene selectivity, right axis; ■, dotted line: pentene selectivity, right axis.

## 5.3 Extension of the SEMK model for ethene oligomerization to bifunctional catalysts

### 5.3.1 Reaction network for ethene oligomerization on Ni-Beta zeolite

A reaction network for ethene oligomerization on Ni-Beta zeolite is based upon the reaction mechanism for metal-ion oligomerization proposed in section 4.3, and classical carbenium ion chemistry, see Figure 5-5.

In a first step, ethene is physisorbed from the gas bulk phase in the zeolite pores (A). Ethene protonates difficult at the acid sites under the relative mild conditions applied due to the unstable primary carbenium ion formed. Compared to secondary and tertiary carbenium ions, the concentration of primary carbenium ions would be negligible. A physisorbed ethene molecule rather coordinates at a nickel-ethene species. This nickel-ethene species acts as the active site for metal-ion oligomerization, see section 4.3.1. On the nickel-ethene species, a second ethene molecule is coordinated, leading to a nickel-di-ethene species (B). Insertion of one of the ethene groups into the bond between the nickel atom and the other ethene group leads to a nickel-butene species (C). Subsequently, another ethene molecule coordinates at this nickel-butene species (B), which can either lead to an increased number of insertions  $n_{ins}$  (C), i.e., chain growth to form hexene, octene... , or to releasing butene within the zeolite pores and recycling the active nickel-ethene species (D).

Butene can protonate on an acid site (E) and alkylate to form an octyl carbenium ion (F). This octyl carbenium ion can deprotonate (E) and desorb towards the bulk phase (A), however, it can also undergo other acid catalyzed reactions at the reaction conditions applied in this work such as isomerization via alkyl shift or pcp-branching (G) and cracking via  $\beta$ -scission towards smaller molecules such as propene and pentene (H). The rate equations for these elementary steps are derived in the following sections.

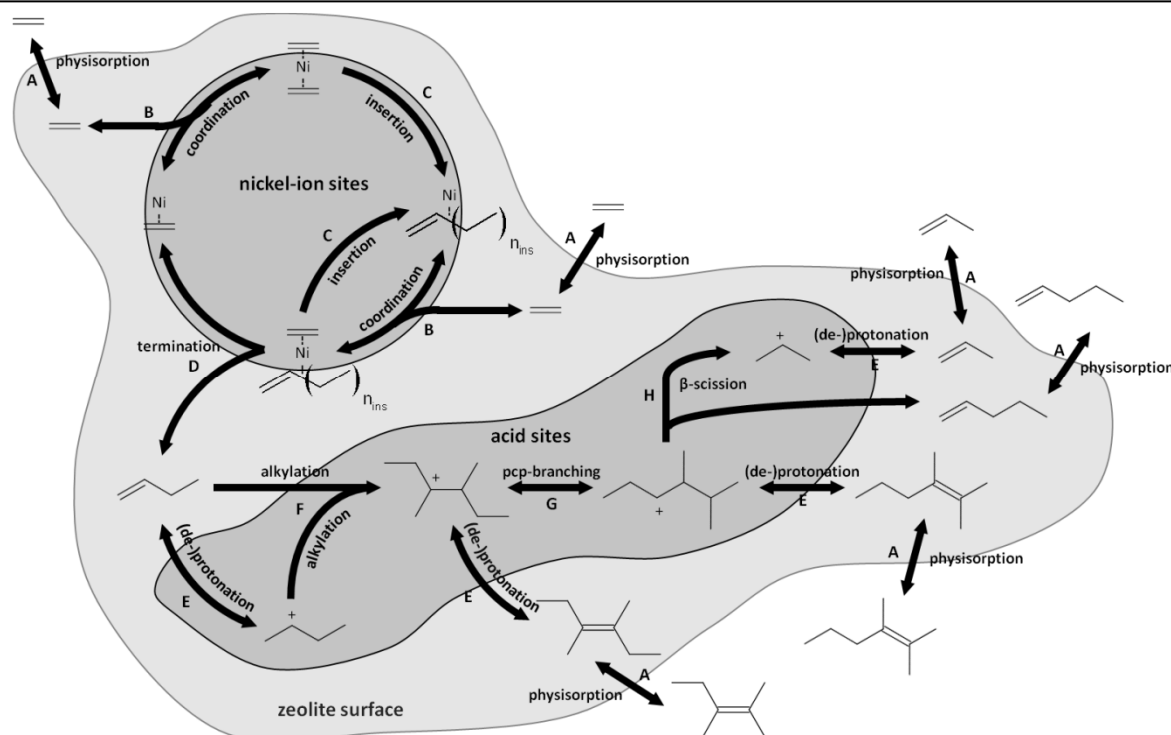


**Figure 5-5: Schematic representation of the ethene oligomerization reaction network involving Ni-ion oligomerization and acid catalyzed alkylation, isomerization and cracking.**

Such a detailed, elementary step based reaction network forms the basis of the kinetic model. The construction of such a complete network requires a gargantuan effort and, hence, has been done practically using an in-house computer software tool, i.e., ReNGeP [5]. In total, two separate reaction networks were generated of which one contains components limited to a carbon number of 8. This network was used for the regression of kinetic model to the experimental data, see section 5.4.2. The use of the small reaction network is valid since experimentally, only components up to octene were significantly detected. It also decreases the CPU time drastically.

For the reaction path analysis and consecutive catalyst optimization, see section 5.5, a reaction network with components up to  $C_{12}$  alkenes was used instead. The contribution of higher alkenes cannot be totally neglected at the higher conversion range investigated for the reaction path analysis and catalyst optimization. It was validated that with the parameters determined via regression, the deviation of the simulation results between the  $C_8$  and  $C_{12}$  network was less than 5%. In both reaction networks, the following elementary steps were considered: metal-ion oligomerization, protonation, deprotonation, pcp-

branching, 1,2 alkyl shift, alkylation and  $\beta$ -scission. To limit the number of components, the degree of branching was limited to 2. An overview of the size of both reaction networks is given in Table 5-2.

**Table 5-2: Overview of the reaction networks generated with ReNGeP for regression, reaction pathway analysis and catalyst design purposes.**

purpose of the reaction network	regression (max. $C_8$ )	reaction path analysis and catalyst design (max. $C_{12}$ )
number of alkenes	116	1220
number of carbenium ions	88	972
number of elementary steps		
metal-ion oligomerization	3	5
protonation	165	1985
deprotonation	165	1985
pcp-branching	158	1096
1,2 alkyl shift	58	668
alkylation	23	330
$\beta$ -scission	23	330

### 5.3.2 Physisorption in the zeolite pores

Prior to undergoing chain growth and skeletal rearrangement reactions, the alkenes physisorb in the zeolite pores. The physisorbed alkene concentrations,  $C_i^{phys}$ , depends on the saturation concentration  $C^{sat}$  and the fractional occupancy of alkene  $i$   $\theta_i$ :

$$C_i^{phys} = C^{sat} \theta_i \quad i = 1 \dots n_{ole} \quad 5-1$$

The fractional occupancy of alkene  $i$  on the zeolite surface is determined using a Langmuir isotherm:

$$\theta_i = \frac{K_i^{phys} p_i}{1 + \sum_{j=1}^{n_{ole}} K_j^{phys} p_j} \quad i = 1 \dots n_{ole} \quad 5-2$$

in which  $p_i$  is the partial pressure of alkene  $i$ . The saturation concentration,  $C^{sat}$ , is given by:

$$C^{sat} = \frac{\sum_{i=1}^{n_{ole}} \theta_i C_i^{sat}}{\sum_{i=1}^{n_{ole}} \theta_i} \quad 5-3$$

which accounts for potential differences in saturation concentration between molecules of different carbon number. The saturation concentration of alkene  $i$ ,  $C_i^{sat}$ , is calculated as:

$$C_i^{sat} = \frac{V_p}{V_{m,i}} \quad i = 1 \dots n_{ole} \quad 5-4$$

The pore volume  $V_p$  was determined experimentally, see section 2.1.1.3, while the molar volume of component  $i$ ,  $V_{m,i}$ , is calculated using the Hankinson-Brost-Thomson (HBT) method [6]. The physisorption coefficient,  $K_i^{phys}$ , is determined from the Henry coefficient  $H_i$  and the saturation concentration  $C_i^{sat}$ :

$$K_i^{phys} = \frac{H_i}{C_i^{sat}} \quad i = 1 \dots n_{ole} \quad 5-5$$

The Henry coefficient  $H_i$  can be expressed as an Arrhenius relation to account for the temperature dependence of the equilibrium:

$$H_i = e^{\frac{\Delta S_i^{phys}}{R}} e^{-\frac{\Delta H_i^{phys}}{RT}} \frac{C_i^{sat}}{2p^0} \quad i = 1 \dots n_{ole} \quad 5-6$$

The standard physisorption entropy,  $\Delta S_i^{phys}$ , is determined to amount to one third of the translational entropy of the corresponding component [7]. Physically, this means that after physisorption, translational movement in the zeolite pores is still allowed. The translational entropy,  $S_i^{trans}$ , is determined via the Sackur Tetrode equation [8].

For the standard physisorption enthalpy of alkene  $i$ , a linear dependence on the carbon number is assumed:

$$\Delta H_i^{phys} = \Delta H_{C_2}^{phys} + (a_{c,i} - 2) \cdot \Delta(\Delta H_C^{phys}) \quad i = 1 \dots n_{ole} \quad 5-7$$

in which  $\Delta(\Delta H_C^{phys})$  represents the standard physisorption enthalpy increment for one additional carbon atom, also see section 4.4.1.1 [9, 10].

### 5.3.3 Metal-ion catalyzed elementary steps

The SEMK model for ethene oligomerization on the nickel-ion sites has already been developed in chapter 4, see equation 4-27.

### 5.3.4 Acid catalyzed elementary steps

Acid sites result in the formation of reactive carbenium ions via protonation. Free carbenium ion chemistry is assumed to occur on these sites, i.e., pcp-branching (*pcp*), 1,2-alkyl shift (*as*), alkylation (*alk*) and cracking via  $\beta$ -scission (*bs*). The rates of these elementary steps, are calculated from the law of mass action and the SEMK methodology:

$$r_i^{pcp} = n_{e(i)}^{pcp} \tilde{k}_i^{pcp} C_{i^+} \quad 5-8$$

$$r_i^{as} = n_{e(i)}^{as} \tilde{k}_i^{as} C_{i^+} \quad 5-9$$

$$r_{i,j}^{alk} = n_{e(i)}^{alk} \tilde{k}_i^{alk} C_{i^+} C_j^{phys} \quad 5-10$$

$$r_i^{bs} = n_{e(i)}^{bs} \tilde{k}_i^{bs} C_{i^+} \quad 5-11$$

Protonation and deprotonation are assumed to be quasi-equilibrated [11]. Hence, the concentration of the carbenium ions  $C_{i^+}$  is given by:

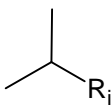
$$C_{i^+} = \frac{C_{H_{tot}^+} K_i^{pr} C_i^{phys}}{1 + C_{H_{tot}^+} \sum_{j=1}^{n_{ole}} K_j^{pr} C_j^{phys}} \quad 5-12$$

in which  $C_{H_{tot}^+}$  represents the total acid site concentration as determined by  $\text{NH}_3$ -TPD, see section 2.1.1.3. According to equation 5-12, one protonation equilibrium coefficient should be determined for each individual alkene. In order to decrease the total number of protonation equilibrium coefficients to be calculated, each coefficient is related to the single-event protonation equilibrium coefficient of a reference alkene,  $K_{ref}^{pr}$ , and the equilibrium isomerization coefficient between these two components,  $K_{i,ref}^{iso}$ :

$$K_i^{pr} = n_{e(i)}^{pr} \tilde{K}_{ref}^{pr} K_{i,ref}^{iso} \quad 5-13$$

In analogy to alkane hydrocracking, the reference alkenes are selected per carbon number and can protonate towards a secondary (s) or tertiary (t) carbenium ion [12], see Table 5-3.

**Table 5-3: Selection of the reference alkenes considered in Eq. 5-13**

carbon number	reference alkene	remarks
2	none	under the conditions applied, the protonation of ethene is very difficult
3	propene	
4	1-butene (s) and isobutene (t)	for C <sub>4</sub> , no component exists which lead to both a secondary and tertiary carbenium ion
≥5	2-methyl-2-alkene 	

As a result, the carbenium ion concentrations are calculated as follows:

$$C_{i^+} = \frac{C_{H_{tot}^+} n_{e(i)}^{pr} \tilde{K}_{ref}^{pr} K_{i,ref}^{iso} C_i^{phys}}{1 + C_{H_{tot}^+} \sum_{j=1}^{n_{ole}} n_{e(j)}^{pr} \tilde{K}_{ref}^{pr} K_{j,ref}^{iso} C_j^{phys}} \quad 5-14$$

### 5.3.5 Net rate of formation

The net rate of formation of an alkene,  $R_i$ , is determined as the sum of reaction rates  $r_i^j$ , in which alkene  $i$  or a corresponding carbenium ion is involved, times the stoichiometric coefficient with respect to alkene  $i$  or its corresponding reactive intermediate, i.e.,  $\alpha_i^j$ , see equation 5-15.

$$R_i = \sum_{j=1}^{n_r} \alpha_i^j r_i^j \quad 5-15$$

Herein,  $n_r$  stands for the total number of elementary reaction steps in the reaction network. As commented in section 5.2, thermodynamic equilibrium between the C<sub>4</sub> double isomers was observed. Hence, also for all alkenes of a higher carbon number, the double bound isomers were assumed to be in thermodynamic equilibrium. A summation over the net rates of formation of all components within an alkene lump, containing the double bound isomers, results in the corresponding net rate of formation of that lump, i.e.,  $R_i^{dbi}$ :



$$R_i^{dbi} = \sum_{j=1}^{n_{dbi}} R_j \quad 5-16$$

with  $n^{dbi}$  the number of double bound isomers in that lump. The thermodynamic equilibrium between the double bound isomers is determined by the thermodynamic equilibrium coefficient  $K_j$ . To determine this thermodynamic equilibrium coefficient, one reference alkene was chosen per lump, c.q., the 1-alkene. The thermodynamic equilibrium coefficient is calculated via by Bensen's group contribution method [13]. The net rate of formation of an alkene belonging to a lump is calculated from  $R_i^{dbi}$  by redistributing  $R_i^{dbi}$  over all alkenes in that lump according to the thermodynamic equilibrium coefficients  $K_j$ :

$$R_i = \frac{K_i}{\sum_{j=1}^{n_{dbi}} K_j} R_j^{dbi} \quad 5-17$$

## 5.4 Ethene oligomerization on bifunctional catalysts: assessment of acid activity

### 5.4.1 Determination of the model parameters

In the kinetic model derived in section 5.3, a number of rate and equilibrium coefficients are present for which a value needs to be determined. The temperature dependency of these coefficients can be adequately captured by means of an Arrhenius and van 't Hoff expression:

$$k = A e^{-E_a/RT} = \frac{k_B T}{h} e^{\Delta S_{\ddagger}^0/R} \cdot e^{-E_a/RT} \quad 5-18$$

$$K = e^{\Delta_r S^0/R} \cdot e^{-\Delta_r H^0/RT} \quad 5-19$$

with  $k_B$  and  $h$  resp. Boltzmann and Planck's constant,  $\Delta S_{\ddagger}^0$  the standard entropy change during transition state formation,  $\Delta_r S^0$  the standard reaction entropy,  $E_a$  the activation energy and  $\Delta_r H^0$  the standard reaction enthalpy. Hence, for every rate or equilibrium coefficient, two parameters are to be determined, i.e., a pre-exponential factor defined by an entropy change and a standard reaction enthalpy or activation energy.

#### 5.4.1.1 Pre-exponential factors

For the insertion and termination step during metal-ion oligomerization, an early transition state is assumed and, hence, the entropy change during transition state formation equals zero, as discussed in section 4.4.1.2. As a result, the corresponding pre-exponential factor can be obtained as:

$$A_i^{ins/ter} = \frac{k_B T}{h} \quad 5-20$$

A gas phase component which is coordinated at a nickel-alkene species site, has lost all of its degrees of translational freedom. One third of the translational entropy was assumed to be already lost during physisorption, see section 5.3.2, and, hence, two third of the translational entropy can be attributed to the coordination step, see section 4.4.1.2. Similarly, the entropy change during transition state formation in alkene protonation amounts to two third of the translational entropy.

For the acid catalyzed isomerization reactions, i.e., pcp-branching and 1,2 alkyl shift, also no entropy changes are assumed for during transition state formation:

$$A_i^{pcp/as} = \frac{k_B T}{h} \quad 5-21$$

During  $\beta$ -scission, a bond is elongated and eventually broken which corresponds to a gain of one degree of translation freedom. The corresponding pre-exponential factor is calculated as follows:

$$A_i^{bs} = \frac{k_B T}{h} e^{\frac{\Delta S_i^{trans}}{R}} \quad 5-22$$

For alkylation, the entropy change during transition state formation can be related to that for  $\beta$ -scission considering thermodynamic consistency, see section 5.4.1.3.

#### 5.4.1.2 Activation energies and standard reaction enthalpies

For the insertion and termination steps occurring as part of metal-ion oligomerization on an amorphous Ni-SiO<sub>2</sub>-Al<sub>2</sub>O<sub>3</sub>, values for the activation energies were already in chapter 4, see Table 4-4. Additionally, for the acid catalyzed reactions, activation energies for pcp-branching, 1,2 alkyl shift and  $\beta$ -scission were estimated by Vandegehuchte et al. [14] using experimental *n*-hexadecane hydrocracking data obtained on a Pt/H-Beta zeolite. The

activation energy for alkylation is determined from thermodynamic constraints, see section 5.4.1.3. All these kinetic descriptors remain fixed during the model regression.

The ethene standard physisorption enthalpy in the Ni-Beta zeolite pores,  $\Delta H_{C_2}^{phys}$ , and the standard physisorption enthalpy increment per carbon atom,  $\Delta(\Delta H_C^{phys})$  were retrieved from work on alkane physisorption by Denayer et al. [9, 10], i.e., resp. -22.6 and -10.0 kJ mol<sup>-1</sup>. The minor difference in molecular mass and structure of the alkenes in this work and of the alkanes in the work of Denayer et al., is assumed to be negligible. From the work of Vandegehuchte et al. [14], the alkene standard protonation enthalpy for secondary (s) carbenium ion formation, i.e.,  $\Delta H_s^{pr}$ , was determined to be 30 kJ mol<sup>-1</sup> higher than the alkene standard protonation enthalpy for tertiary (t) carbenium ion formation  $\Delta H_t^{pr}$ . This relationship was also implemented in the kinetic model.

In total, only 2 catalyst descriptors are estimated, i.e., the ethene standard coordination enthalpy at a nickel-alkene species,  $\Delta H^c$ , and the alkene standard protonation enthalpy for secondary (s) carbenium ion formation, i.e.,  $\Delta H_s^{pr}$ .

### 5.4.1.3 Thermodynamic consistency for alkylation and cracking

For each reversible reaction, the thermodynamic consistency between the forward (*f*) and reverse (*r*) reaction rate coefficient enables to relate the corresponding activation energies to each other via the standard reaction enthalpy  $\Delta_r H^0$ :

$$E_a^f + \Delta_r H^0 = E_a^r \quad 5-23$$

A similar relationship holds for the standard activation entropy:

$$\Delta S^f + \Delta_r S^0 = \Delta S^r \quad 5-24$$

As a result, the number of adjustable parameters can be significantly reduced, i.e., one activation energy per reaction pair provided that the reaction enthalpy and entropy can be calculated independently. Applied to alkylation and  $\beta$ -scission, this relationship becomes:

$$E_a^{alk} + \Delta H^{0,alk} = E_a^{bs} \quad 5-25$$

A schematic overview of the thermodynamic consistency accounted for between alkylation and  $\beta$ -scission is given in Figure 5-6.

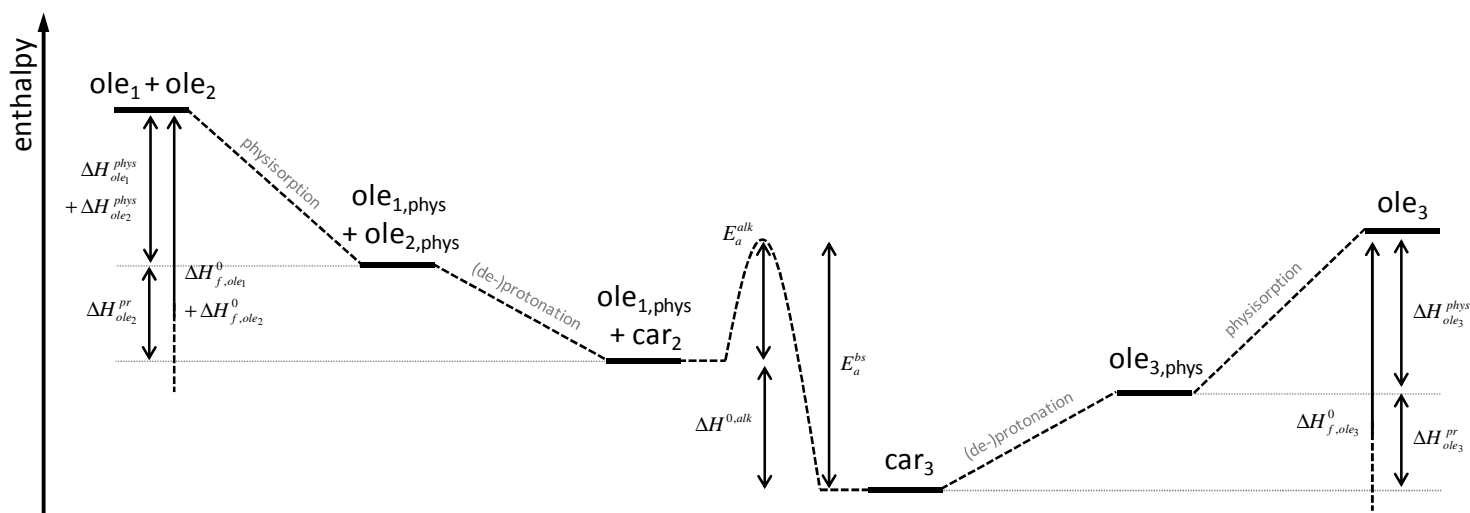


Figure 5-6: Energy diagram for alkylation and  $\beta$ -scission

Consider the alkylation of two alkenes,  $ole_1$  and  $ole_2$ , to form alkene 3,  $ole_3$ . The standard reaction enthalpy for alkylation,  $\Delta H^{0,alk}$ , can be calculated from the standard formation enthalpy  $\Delta_f H^0$  of the components involved, i.e., the physisorbed alkene 1,  $ole_{1,phys}$ , the carbenium ion of alkene 2,  $car_2$ , and the carbenium ion of alkene 3,  $car_3$ , see equation 5-26.

$$\Delta H^{0,alk} = \Delta_f H_{car_3}^0 - [\Delta_f H_{ole_{1,phys}}^0 + \Delta_f H_{car_2}^0] \quad 5-26$$

The standard formation enthalpies for these reactive intermediates can be determined from the standard formation enthalpy of the corresponding gas phase alkenes while accounting for stabilization by physisorption and protonation:

$$\Delta_f H_{ole_{1,phys}}^0 = \Delta_f H_{ole_1}^0 + \Delta H_{ole_1}^{phys} \quad 5-27$$

$$\Delta_f H_{car_2}^0 = \Delta_f H_{ole_2}^0 + \Delta H_{ole_2}^{phys} + \Delta H_{ole_2}^{pr} \quad 5-28$$

$$\Delta_f H_{car_3}^0 = \Delta_f H_{ole_3}^0 + \Delta H_{ole_3}^{phys} + \Delta H_{ole_3}^{pr} \quad 5-29$$

The standard enthalpy of formation has been determined by Benson's group contribution method [13]. The reaction entropy can be determined in a similar manner.

#### 5.4.1.4 Summary

In Table 5-4, an overview is given of all kinetic and catalyst descriptors required for the modeling of ethene oligomerization on Ni-Beta zeolite. More than 20 rate and equilibrium coefficients are required, each being determined by their corresponding pre-exponential factor and activation energy or standard reaction enthalpy. The pre-exponential factors are

quantified based on judicious assumptions regarding the entropy change during transition state formation. Due to the fundamental character of the model, a large number of kinetic and catalyst descriptors could be retrieved from literature. The introduction of thermodynamic consistency between alkylation and cracking through  $\beta$ -scission leads to the direct determination of the standard alkylation enthalpy and entropy. The only parameters to be determined are related to the catalyst descriptors. In total, there are only 2 catalyst descriptors to be estimated, i.e., the standard ethene coordination enthalpy at a nickel-ethene species,  $\Delta H^c$ , and the alkene standard protonation enthalpy for forming a secondary (s) carbenium ion,  $\Delta H_s^{pr}$ . The alkene standard protonation enthalpy for forming a tertiary (t) carbenium ion,  $\Delta H_t^{pr}$ , is determined via a linear relationship with the alkene standard protonation enthalpy for forming a secondary (s) carbenium ion, see section 5.4.1.2.

**Table 5-4: Overview of the kinetic and catalyst descriptors to be determined for the Single-Event MicroKinetic model for ethene oligomerization on Ni-Beta zeolite.**

kinetic descriptors	pre-exponential factor	activation energy
$\tilde{k}^{ins}$	determined using TST	see Table 4-4
$\tilde{k}^{ter}$	determined using TST	see Table 4-4
$\tilde{k}^{pcp}$ [s,s][s,t][t,s][t,t]	determined using TST	values from Vandegehuchte et al. [14]
$\tilde{k}^{as}$ [s,s][s,t][t,s][t,t]	determined using TST	values from Vandegehuchte et al. [14]
$\tilde{k}^{alk}$ [s,s][s,t][t,s][t,t]	calculated from $A^{bs}$ using thermodynamic considerations	calculated from $E_a^{bs}$ using thermodynamic considerations
$\tilde{k}^{bs}$ [s,s][s,t][t,s][t,t]	determined using TST	values from Vandegehuchte et al. [14]
catalyst descriptor	pre-exponential factor	standard reaction enthalpy
$\tilde{K}^c$	determined using TST	to be estimated: $\Delta H^c$

$\tilde{K}^{pr}$ [s][t]	determined using TST	to be estimated: $\Delta H_s^{pr}$ ( $\Delta H_t^{pr}$ is determined via a linear relationship with $\Delta H_s^{pr}$ [14])
$K^{phys}$	determined using TST	values from Denayer et al. [9, 10]

---

## 5.4.2 Estimation of the model parameters

The model parameters values are reported in Tables 5-5 and 5-6, of which 21 were determined from literature or thermodynamic consistency and 2 were estimated. Both standard reaction enthalpies were deemed to be significant as indicated by their respective confidence interval. The model was found to be globally significant with a calculated  $F_s$  value higher than 2700 which exceeds the tabulated  $F_s$  value of 4.0 more than two order of magnitude. Additionally, the model was determined to be adequate as indicated by the corresponding  $F_a$  value equal to 2.4 which is lower than the tabulated  $F_a$  value of 4.4. This implies that deviations of the model with respect to the experimental observations can be attributed to experimental errors only and are not due to any systematic shortcomings of the model itself. The binary correlation coefficient between  $\Delta H^c$  and  $\Delta H_s^{pr}$  amounts to only 0.03, which means that there is no correlation between these two parameters.

**Table 5-5: Catalyst descriptors as well as statistical performance indicators, all at 95% confidence level, determined by non-linear regression of the model given by integration of Eq. 2-21 in which the net rates of formation are given by Eq. 5-15 to the experimental data measured at the operating conditions given in Table 5-1. (a): values from [14] and (b): values from [9, 10]**

Type	Catalyst descriptor	Value (kJ mol <sup>-1</sup> )
nickel-ion sites	$\Delta H^c$	-80.3 ± 0.2
acid sites	$\Delta H_s^{pr}$	-40.1 ± 0.3
	$\Delta H_t^{pr}$	$\Delta H_s^{pr} - 30.0$ <sup>(a)</sup>
zeolite	$\Delta H_{C_2}^{phys}$	-22.6 <sup>(b)</sup>
support	$\Delta(\Delta H_C^{phys})$	-10.0 <sup>(b)</sup>

**Table 5-6: Kinetic descriptors used during the non-linear regression of the model given by integration of Eq. 2-21 in which the net rates of formation are given by Eq. 5-15 to the experimental data measured at the operating conditions given in Table 5-1. (a): values from Table 4-4, (b): values from [9, 10] and (c): determined via thermodynamic considerations**

Type	Kinetic descriptor	Value (kJ mol <sup>-1</sup> )			
nickel-ion sites	$E_a^{ins}$	76.3 <sup>(a)</sup>			
	$E_a^{ter}$	67.8 <sup>(a)</sup>			
	type	(s,s)	(s,t)	(t,s)	(t,t)
acid sites	$E_a^{as}$	79.8 <sup>(b)</sup>	74.8 <sup>(b)</sup>	(c)	104.5 <sup>(b)</sup>
	$E_a^{pcp}$	112.1 <sup>(b)</sup>	93.3 <sup>(b)</sup>	(c)	125.5 <sup>(b)</sup>
	$E_a^{bs}$	138.9 <sup>(b)</sup>	122.8 <sup>(b)</sup>	149.5 <sup>(b)</sup>	125.4 <sup>(b)</sup>
	$E_a^{alk}$	(c)	(c)	(c)	(c)

The alkene standard protonation enthalpy to form secondary carbenium ions is estimated significantly on  $-40.1 \text{ kJ mol}^{-1}$ . The absolute value of the alkene standard protonation enthalpy, however, is lower than the corresponding value obtained on a different H-Beta zeolite. This could be attributed to the nickel ions which are reported to be exchanged with the Brønsted acid sites [15], hence resulting in a lower overall acidity. As a result, relatively low reaction rates are simulated for the acid catalyzed reactions leading to low selectivities towards odd carbon numbered alkenes, see section 5.2.

The ethene standard coordination enthalpy at a nickel-alkene species equals  $-80.3 \text{ kJ mol}^{-1}$ , which is almost twice the value determined for the amorphous Ni-SiO<sub>2</sub>-Al<sub>2</sub>O<sub>3</sub> in previous work, i.e.,  $-49.9 \text{ kJ mol}^{-1}$ . From the reaction mechanism and corresponding rate equations proposed for metal-ion oligomerization, see equation 4-27, it is expected that the concentration of active nickel-di-ethene species will be much higher on the Ni-Beta than on the amorphous Ni-SiO<sub>2</sub>-Al<sub>2</sub>O<sub>3</sub>, resulting in a much higher oligomerization rate for the former compared to the latter. However, as discussed in section 5.2, the ethene oligomerization rate on Ni-Beta is of the same order of magnitude as observed on the amorphous Ni-SiO<sub>2</sub>-Al<sub>2</sub>O<sub>3</sub> at milder conditions. This lower activity is attributed to the difference in physisorption stabilization of the alkenes between both catalysts. On Ni-Beta, the higher alkenes physisorb

much stronger than on the amorphous Ni-SiO<sub>2</sub>-Al<sub>2</sub>O<sub>3</sub> as evident from the difference in standard physisorption enthalpy per additional carbon, i.e., -12.4 kJ mol<sup>-1</sup> compared to -6.1 kJ mol<sup>-1</sup>, see Table 4-4. Probably, the microporous character of Ni-Beta leads to a much stronger physisorption interaction due to a relative small distance between alkene and catalyst surface compared to the amorphous Ni-SiO<sub>2</sub>-Al<sub>2</sub>O<sub>3</sub> [9]. This difference in standard physisorption enthalpy leads to a much more pronounced competition of the higher alkenes with ethene for physisorption on the catalyst surface. As a result, the physisorbed ethene concentration decreases more quickly with increasing conversion on Ni-Beta than on the amorphous Ni-SiO<sub>2</sub>-Al<sub>2</sub>O<sub>3</sub> and, leading to a much faster decrease of the ethene oligomerization rate. This is illustrated in Figure 5-7 in which the ethene oligomerization rate on the Ni-Beta zeolite and the amorphous Ni-SiO<sub>2</sub>-Al<sub>2</sub>O<sub>3</sub> from chapter 4 is simulated at identical reaction conditions. Initially, i.e., at very low space-times, the ethene oligomerization rate on Ni-Beta is much higher than on amorphous Ni-SiO<sub>2</sub>-Al<sub>2</sub>O<sub>3</sub> which is caused by the stronger coordination of ethene at the nickel-ethene species, leading to a higher concentration of nickel-di-ethene species. At higher space-times, i.e., from 0.6 kg<sub>cat</sub> s mol<sub>C<sub>2</sub></sub><sup>-1</sup> on, the surface concentration of ethene is more strongly reduced by physisorbed oligomerization products on the Ni-Beta zeolite than on the amorphous Ni-SiO<sub>2</sub>-Al<sub>2</sub>O<sub>3</sub>.

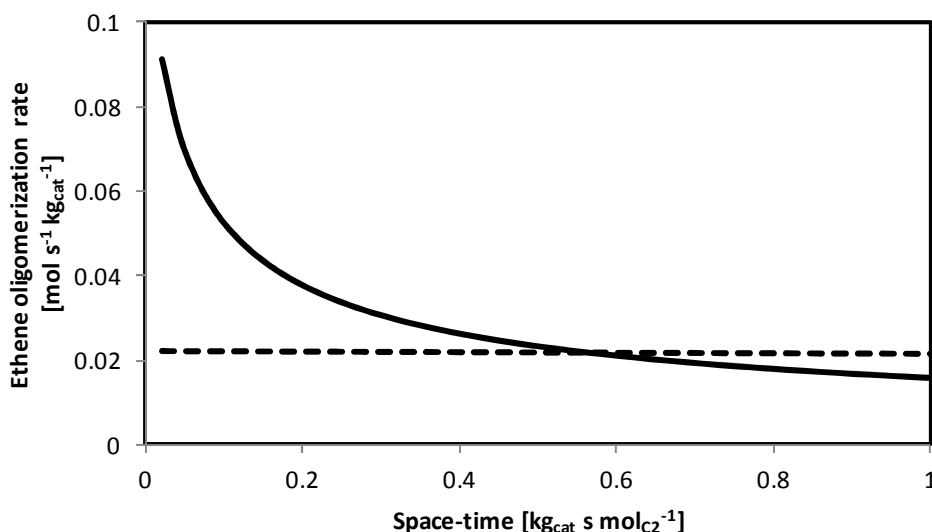


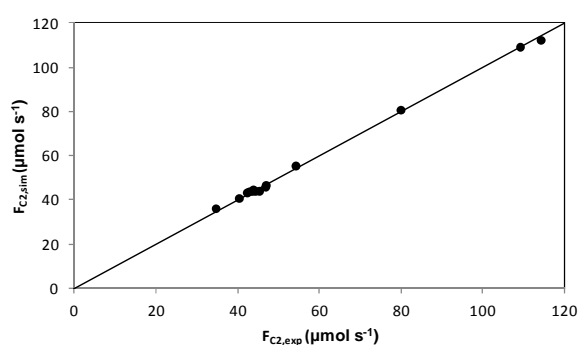
Figure 5-7: Simulated ethene oligomerization rates as function of space-time at 473 K and an inlet ethene partial pressure of 0.34 MPa. Full line: Ni-Beta zeolite, as determined by the model given by integration of Eq. 2-21 in which the net rates of formation is given by Eq. 5-15 with the parameter values given in Tables 5-5 and 5-6. Dashed line: Ni-SiO<sub>2</sub>-Al<sub>2</sub>O<sub>3</sub> as determined by the model given by integration of Eq. 2-21 in which the net rates of formation is given by Eq. 4-27 with the parameter values given in Table 4-4.



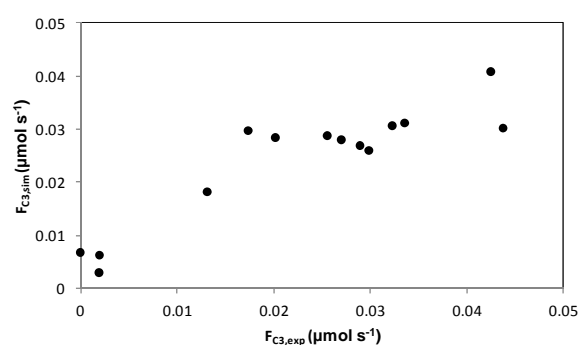
### 5.4.3 Kinetic model performance

The model performance was already assessed successfully by a statistical analysis of the model and kinetic parameters significance and model adequacy, see section 5.4.2. However, an additional analysis based on the residuals could reveal some extra information of the model performance.

As shown in Figures 5-2 to 5-4, the model is capable of adequately describing the major trends in the experimental data. For most experimental points, the model simulations are within the experimental error. In Figure 5-8, the parity diagrams for the molar outlet flow rates of ethene (a), propene (b), butene (c), pentene (d) and hexene (e) are depicted. In general, all parity diagrams indicate that the model is able to simulate the experimental observations quite satisfactorily. The parity diagram for the pentene molar flow rate exhibits the largest discrepancies between model and experiment. This is probably related to the reaction network used which is limited to alkenes with a maximum carbon number of 8. As a result, pentene could only have been produced by cracking of octyl ions. The expansion of the reaction network to heavier  $C_9+$  components would include the alkylation of pentene and additional cracking reactions towards pentene. However, given the adequacy, statistical significance and the physical sense of the model, this expansion is not required.

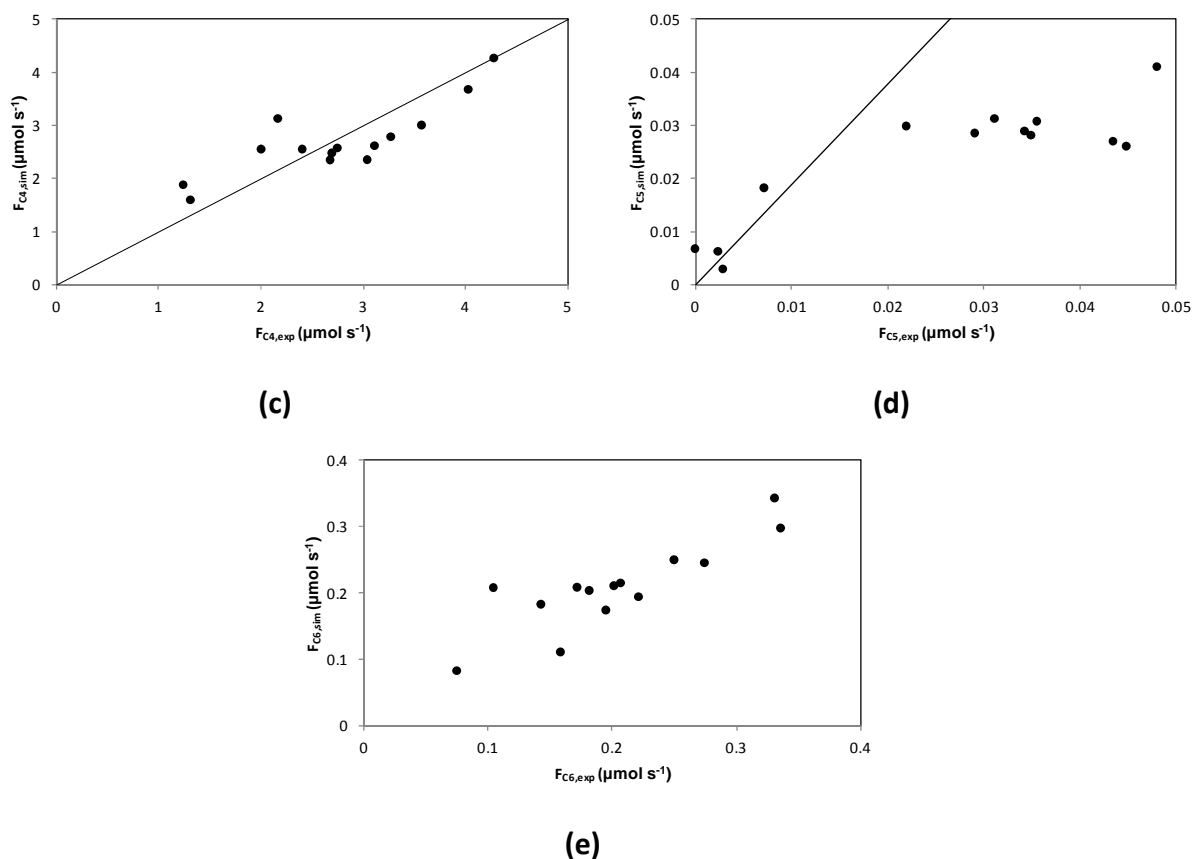


(a)



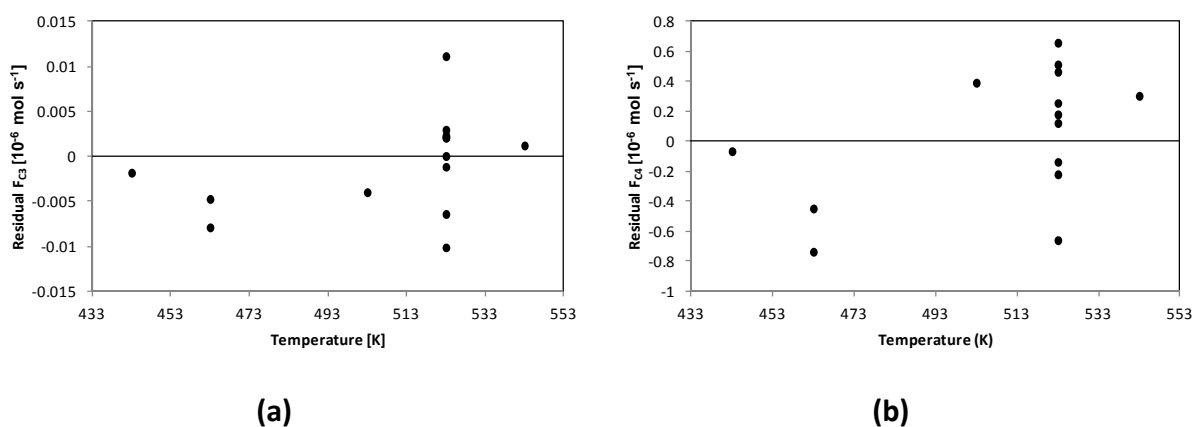
(b)

## Exploiting Bifunctional Heterogeneous Catalysts in Ethene Oligomerization: Guidelines for Rational Catalyst Design



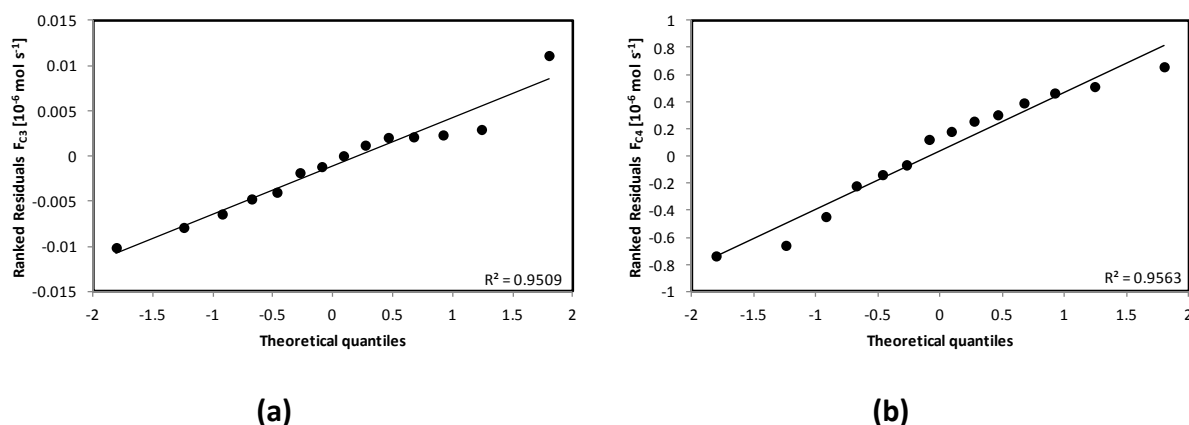
**Figure 5-8: Parity diagrams for the molar outlet flow rate of ethene (a), propene (b), butene (c), pentene (d) and hexene (e) as determined by integration of Eq. 2-21, with the corresponding net rates of formation, Eq. 5-15 and the parameter values reported in Tables 5-5 and 5-6.**

Figure 5-9 shows the residuals of the molar flow rates as function of the temperature of two components, i.e., propene (a) and butene (b), which are characteristic for resp. the acid and metal-ion catalyzed reaction steps. It is noticed that the residuals are randomly distributed over the x-axis and do not show any trend as function of the temperature.



**Figure 5-9: Residual figures for the molar outlet flow rate of propene (a) and butene (b) as function of temperature as determined by integration of Eq. 2-21, with the corresponding net rates of formation, Eq. 5-15 and the parameter values reported in Tables 5-5 and 5-6.**

The residuals were also tested on their statistical distribution using a normal probability figure as illustrated in Figure 5-10. For both propene (a) and butene (b), the linear regression of the ranked residuals is quite satisfactory, indicating that the residuals are distributed normally.



**Figure 5-10: Normal probability figures for the molar outlet flow rate of propene (a) and butene (b) as determined by integration of Eq. 2-21, with the corresponding net rates of formation, Eq. 5-15 and the parameter values reported in Tables 5-5 and 5-6.**

## 5.5 Catalyst design guidelines for chemicals and fuel production from ethene oligomerization

The bifunctional character of ethene oligomerization catalysts can be exploited to expand the targeted product slate towards other alkene fractions. The metal-ion sites produce mainly linear alkenes through an insertion-termination mechanism while the acid sites increase the degree of branching and enhance either the chain growth through alkylation or the production of smaller alkenes through cracking. In order to gain more insight in the synergy between both functionalities, a reaction path analysis is performed. To this purpose, the extended reaction network containing components up to  $C_{12}$  is used, see Table 5-2. In the reaction path analysis figures, see Figures 5-13, 5-15 and 5-17, the  $C_9+$  fraction is not shown due to the low amount of heavy alkenes formed and to improve the figures' readability. However, these heavier fractions may still significantly contribute to the product formation.

In sections 5.5.2 to 5.5.4, guidelines for rational catalyst design are proposed by performing a reaction path analysis and investigating the effect of different catalyst properties such as the number of and adsorption strength on acid and nickel-ion sites and the support. The

adsorption strength on the active acid and nickel-ion sites is quantified by resp. the alkene standard protonation and standard coordination enthalpy. The support intervenes via the physisorption enthalpy of the different alkenes in the pores. The adsorption, coordination and reaction entropies were determined in a support-independent manner, see sections 5.3.2 and 5.4.1.1, and, hence, is not varied.

### 5.5.1 Metal-ion versus acid catalyzed oligomerization: reaction path analysis

In total, 3 fractions are defined based on their economic value: linear 1-alkenes (excluding ethene), propene and gasoline, i.e., branched components with a carbon number ranging from 5 to 8. Several components, e.g., 2-butene and isobutene, are not included in any of these fractions. Hence, the summation of the selectivity towards these three fractions do not necessarily add up to 100%. Figure 5-11 shows the space-time effect on the ethene conversion and selectivity towards each of these fractions at 503 K and an ethene inlet partial pressure of 1.0 MPa. At low space-times and conversions, i.e., resp. lower than 50  $\text{kg}_{\text{cat}} \text{ s mol}^{-1}$  and 30% ethene conversion, mostly linear 1-alkenes are produced whereas at higher space-times these linear alkenes are isomerized and cracked on the acid sites, as indicated by the increase in propene and gasoline fraction, see resp. Figures 5-11 and 5-12.

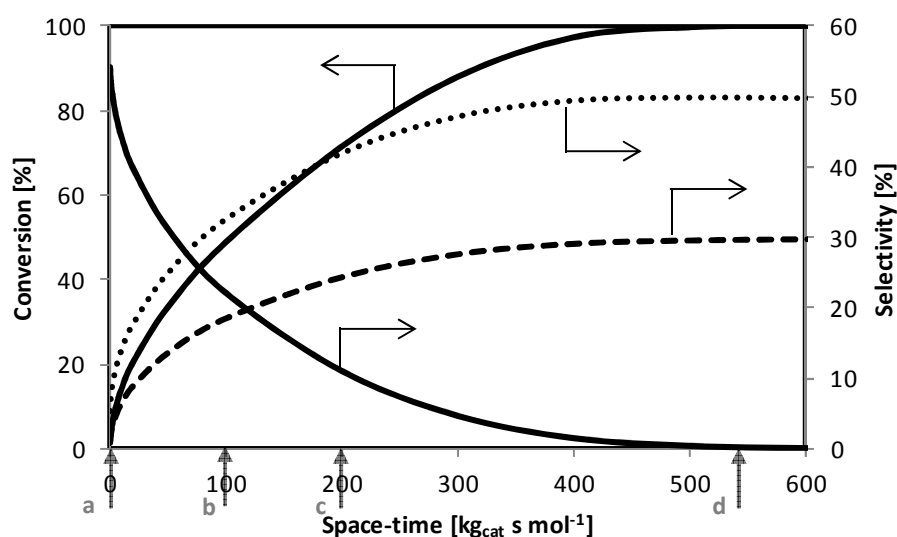
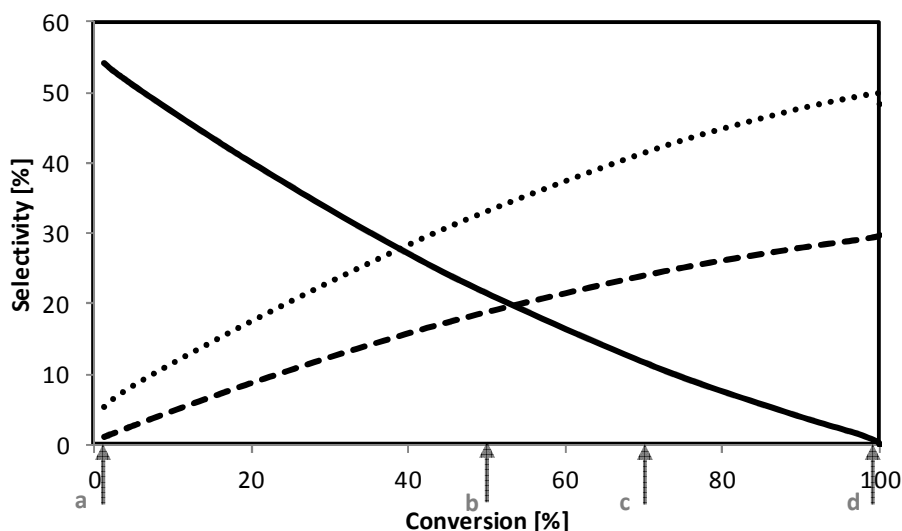


Figure 5-11: Ethene conversion and selectivity towards linear 1-alkenes (full line), gasoline (dotted line) and propene (dashed line) on Ni-Beta as function of space-time at 503 K and an ethene inlet partial pressure of 1.0 MPa as obtained by integration of Eq. 2-21, with the corresponding net rates of formation, Eq. 5-15 and the parameter values reported in Tables 5-5 and 5-6.

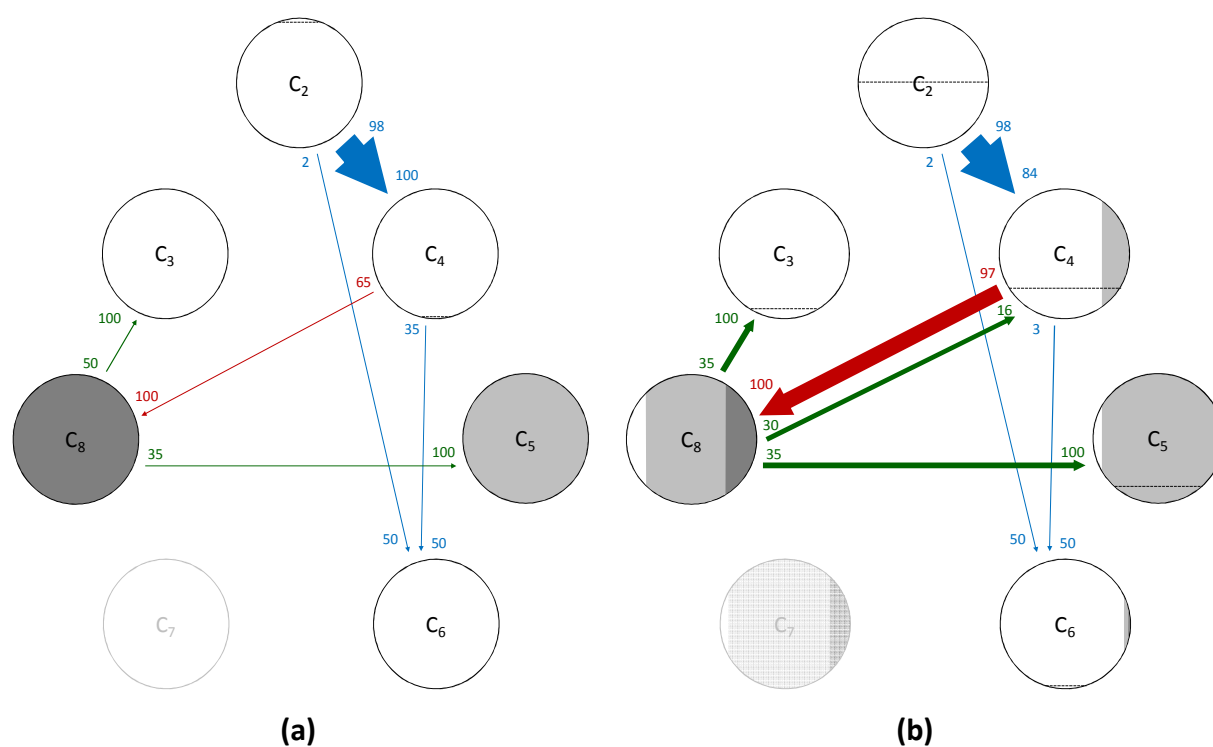


**Figure 5-12:** Selectivity towards linear 1-alkenes (full line), gasoline (dotted line) and propene (dashed line) as function of conversion on Ni-Beta at 503 K and an ethene inlet partial pressure of 1.0 MPa as obtained by integration of Eq. 2-21, with the corresponding net rates of formation, Eq. 5-15 and the parameter values reported in Tables 5-5 and 5-6.

Several reaction path analyses are shown in Figure 5-13 in which the space-time was varied at 503 K and an ethene inlet partial pressure of 1.0 MPa, corresponding to Figures 5-11 and 5-12. Four feed conversions were considered: 1% (a), 50% (b), 70% (c) and 99% (d), corresponding with (a), (b), (c) and (d) in Figures 5-11 and 5-12. At low space-times and conversions, see Figure 5-13(a), ethene dimerization to linear butenes on the nickel-ion sites constitutes the main reaction path as it is the primary step in the reaction network. There is a small fraction of hexene formed through the insertion of ethene in butene via the metal-ion oligomerization route. The dimerization of butene through alkylation results in a very low amount of dibranched octenes. With increasing conversion, see Figure 5-13(b-c), the acid sites contribute more and more to the overall reaction mechanism. Linear butenes are further dimerized on the acid sites via an alkylation step to form dibranched octenes. However, these dibranched octenes are highly susceptible to isomerization, hence the shift towards monobranched and even linear octenes. Also, the octenes rapidly undergo cracking to form propene, pentene and isobutene, leading to a shift in the butene composition and a low overall production of octenes as final products. At very high space-times and conversions, see Figure 5-13(d), the acid catalyzed reaction steps are of equal importance as the metal-ion oligomerization steps and cause a high degree of isomerization, alkylation and cracking with propene, isobutene and pentene as main products. However, experimental

## Exploiting Bifunctional Heterogeneous Catalysts in Ethene Oligomerization: Guidelines for Rational Catalyst Design

investigations on similar Ni-Beta catalysts indicated a much lower propene yield than simulated with the kinetic model [15]. Most probably, the modelled physisorption of higher olefins is too pronounced, resulting in a higher surface concentration of these species and, hence, a higher cracking rate and propene yield. Taking into account the effect of catalyst surface saturation on the physisorption competitiveness between different components should lead to an improved model description [14].



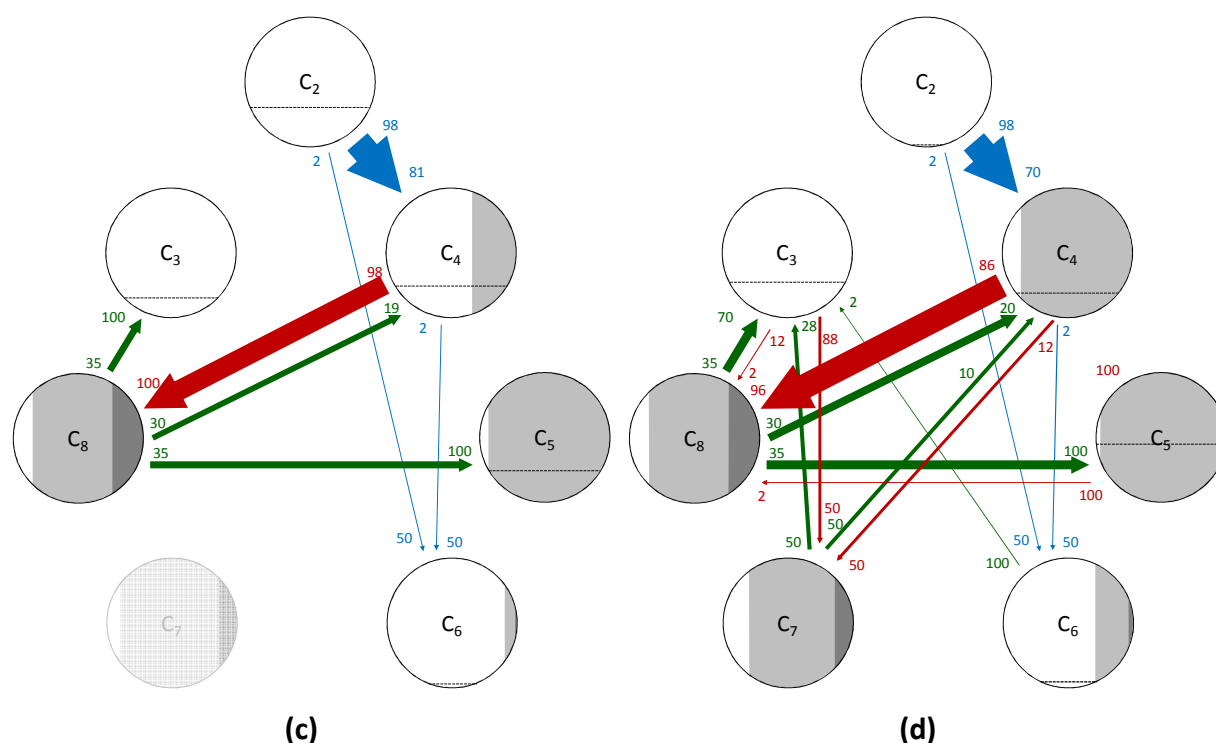


Figure 5-13: Reaction path analysis for ethene oligomerization on Ni-Beta at 503 K, an ethene inlet partial pressure of 1.0 MPa and a conversion of 1% (a), 50% (b), 70% (c) and 99% (d), see also Figures 5-11 and 5-12.

The model simulations were obtained by integration of Eq. 2-21, with the corresponding net rates of formation, Eq. 5-15 and the parameter values reported in Tables 5-5 and 5-6. The alkenes are lumped per carbon number. The height of the horizontal line in these circle is proportional to the mass fraction of the corresponding alkene lump. If no line is visible it indicates that the corresponding mass fraction is very small, i.e., less than 1%. However, these lump may still significantly contribute to the product formation. Additionally, alkene lumps in watermark indicate that its mass fraction is less than 0.1%. The vertical gray-scale code is used to differentiate between the different structural isomers, i.e., white: linear alkenes, light grey: monobranched alkenes and dark grey: dibranched alkenes. The surface area taken by these colors is proportional to the mass fraction of each structural isomer in the alkene lump. The color of the arrows indicate the reaction family: blue = metal-ion oligomerization, red = acid alkylation, green =  $\beta$ -scission. pcp-branching and alkyl shift are not explicitly shown as they only change the isomer distribution within an alkene lump. The size of the arrow is linearly proportional to the rate of the corresponding step. The numbers at the arrow head indicate the fraction of the lump which is produced via the corresponding step while numbers next to the arrow shaft indicate the fraction of the lump which is consumed via this step.

The temperature effect on the different fraction selectivities is shown in resp. Figures 5-14 and 5-15. The ethene conversion was constant at 50% and the ethene inlet partial pressure was equal to 1.0 MPa. At low temperatures, mainly linear 1-alkenes are produced which mainly consist out of linear butenes, see Figure 5-15(a), and are produced via the dimerization of ethene on the nickel-ion sites. With increasing temperature, see Figure 5-15(b), (c) and (d), the relative importance of the acid catalyzed reactions is increasing, leading to branched and cracking products. The relative increase of the cracking and isomerization reaction rate with increasing temperature compared to the metal-ion oligomerization can be related to the difference of their apparent activation energy values.

## Exploiting Bifunctional Heterogeneous Catalysts in Ethene Oligomerization: Guidelines for Rational Catalyst Design

For metal-ion oligomerization, assuming ethene dimerization, the apparent activation energy is determined as:

$$E_a^{ter} = \Delta H_{C_2}^{phys} + \Delta H^c + E_a^{ter} \quad 5-30$$

and is equal to ca.  $-35 \text{ kJ mol}^{-1}$ , see Table 5-6. For cracking an octene molecule the apparent activation energy is determined as:

$$E_a^{bs} = \Delta H_{C_2}^{phys} + 6\Delta(\Delta H_C^{phys}) + \Delta H_{s/t}^{pr} + E_a^{bs} \quad 5-31$$

and varies between  $-30$  to  $30 \text{ kJ mol}^{-1}$ , see Table 5-6, which is higher than the apparent activation energy for metal-ion oligomerization. Similarly, the apparent activation energy for alkylation of linear butenes amounts to ca.  $-20 \text{ kJ mol}^{-1}$ , see Table 5-6. which is slightly higher than the apparent activation for metal-ion oligomerization. As a result, these acid catalyzed reactions will dominate metal-ion oligomerization in the higher temperature range, resulting in a product spectrum containing odd-carbon numbered, branched alkenes, see Figure 5-15(d).

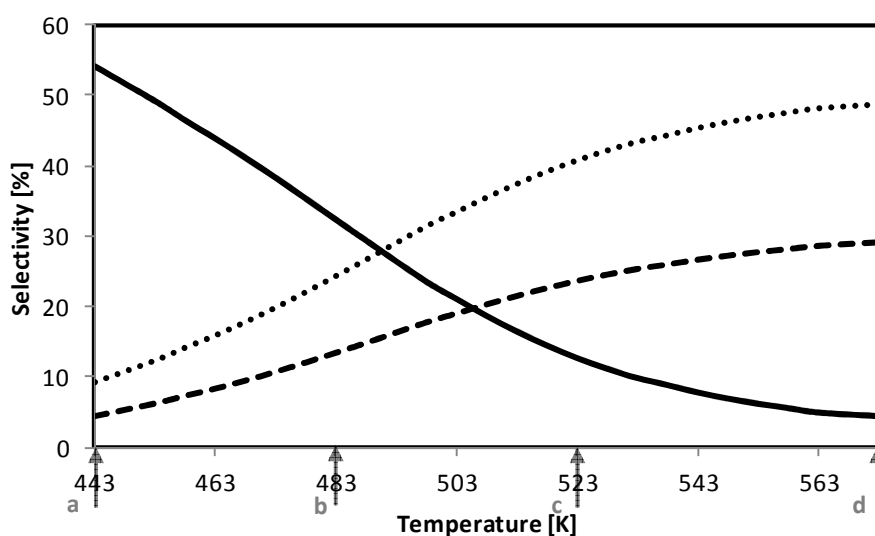


**Figure 5-14:** Selectivity towards linear 1-alkenes (full line), gasoline (dotted line) and propene (dashed line) as function of temperature at an ethene inlet partial pressure of 1.0 MPa and a conversion of 50% as obtained by integration of Eq. 2-21, with the corresponding net rates of formation as given by Eq. 5-15 and the parameter values as reported in Tables 5-5 and 5-6.



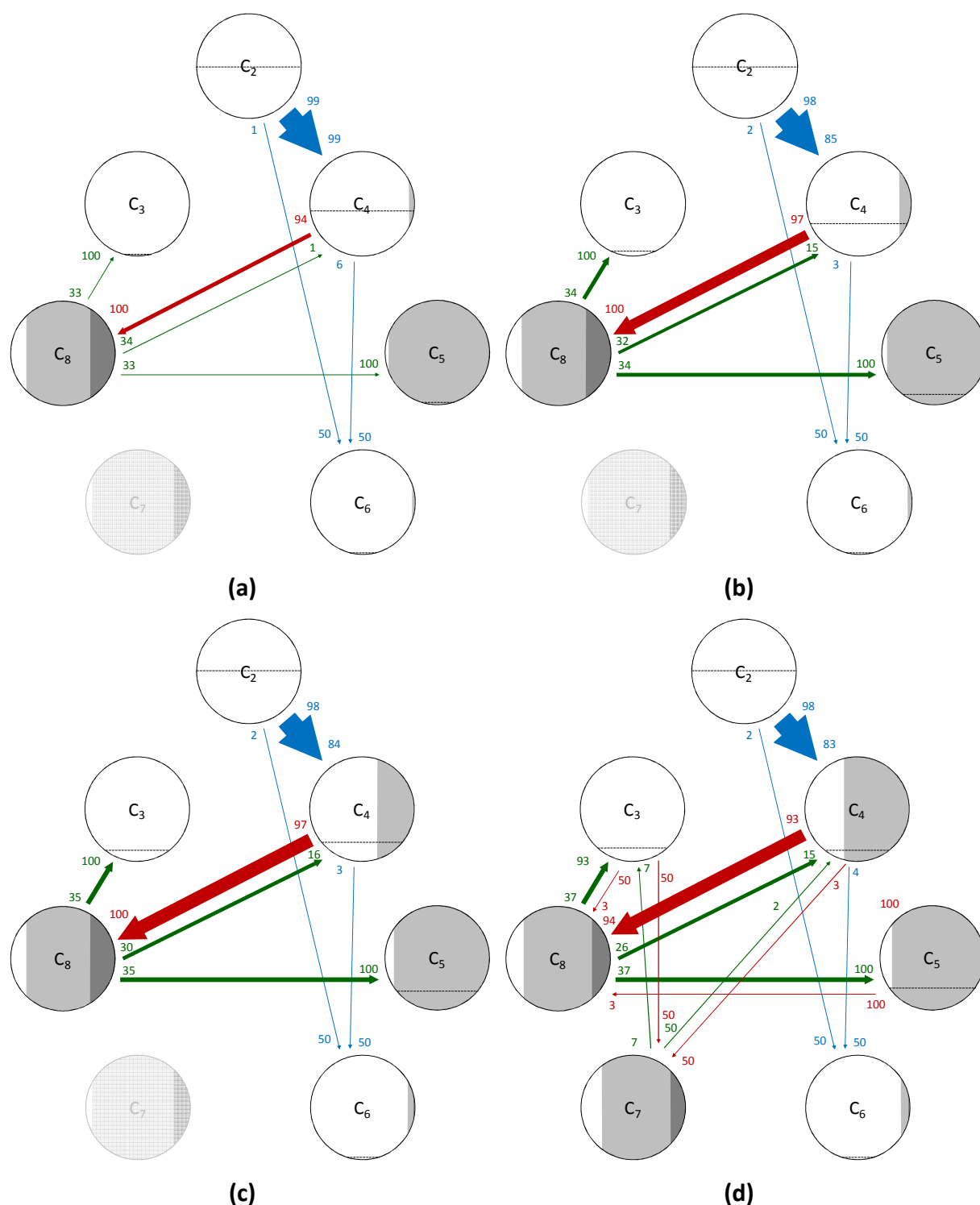


**Figure 5-15:** Reaction path analysis for ethene oligomerization on Ni-Beta at 50% ethene conversion, an ethene inlet partial pressure of 1.0 MPa and 443 K (a), 483 K (b), 523 K (c) and 573 K (d), corresponding with (a), (b), (c) and (d) in Figure 5-14. The model simulations were obtained by integration of Eq. 2-21, with the corresponding net rates of formation, Eq. 5-15 and the parameter values reported in Tables 5-5 and 5-6. The alkenes are lumped per carbon number. The height of the horizontal line in these circle is proportional to the mass fraction of the corresponding alkene lump. If no line is visible it indicates that the corresponding mass fraction is very small, i.e., less than 1%. However, these lump may still significantly contribute to the product formation. Additionally, alkene lumps in watermark indicate that its mass fraction is less than 0.1%. The vertical gray-scale code is used to differentiate between the different structural isomers, i.e., white: linear alkenes, light grey: monobranched alkenes and dark grey: dibranched alkenes. The surface area taken by these colors is proportional to the mass fraction of each structural isomer in the alkene lump. The color of

the arrows indicate the reaction family: blue = metal-ion oligomerization, red = acid alkylation, green =  $\beta$ -scission. pcp-branching and alkyl shift are not explicitly shown as they only change the isomer distribution within an alkene lump. The size of the arrow is linearly proportional to the rate of the corresponding step. The numbers at the arrow head indicate the fraction of the lump which is produced via the corresponding step while numbers next to the arrow shaft indicate the fraction of the lump which is consumed via this step.

## 5.5.2 Strength and concentration of the acid sites

In Figure 5-16, the effect of the acid site strength on the selectivity toward the fraction of linear 1-alkenes, gasoline, propylene is shown. For relatively weak acid sites with an alkene standard protonation enthalpy between  $-30$  and  $-40$   $\text{kJ mol}^{-1}$ , mainly linear 1-alkenes are produced. Both fractions can be directly related to the metal-ion oligomerization steps, i.e., the formation of 1-butene through ethene dimerization and the formation of higher linear alkenes through subsequent ethene insertions. With increasing strength of the acid sites, these linear alkenes are more easily transformed into branched and cracked products, as discussed in section 5.5. However, if the acid sites would become even stronger, the selectivity towards propene and gasoline will decrease due to a favored formation of isobutene via consecutive alkylation and cracking, as indicated by the reaction path analysis shown in Figure 5-17.

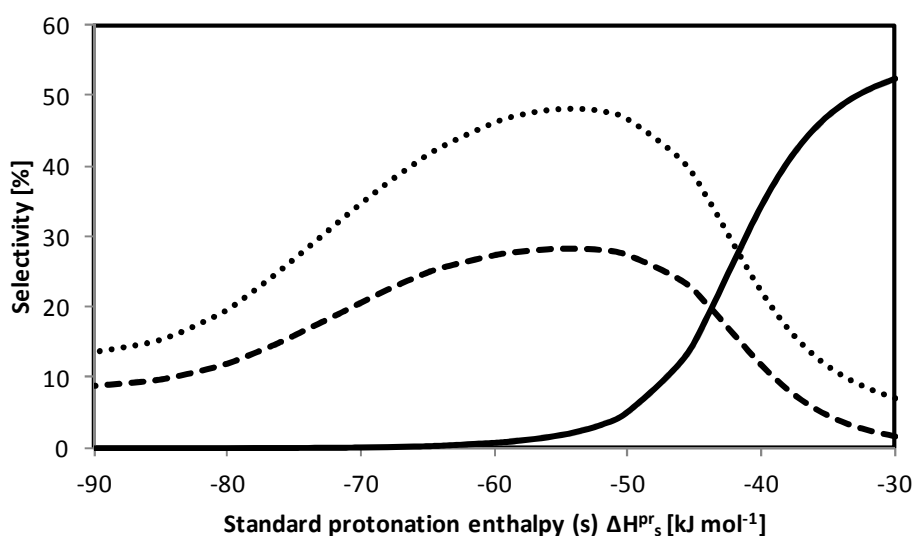


Figure 5-16: Selectivity towards linear 1-alkenes (full line), gasoline (dotted line) and propene (dashed line) on Ni-Beta as function of alkene standard protonation enthalpy (s) at 50% ethene conversion, 503 K and an ethene inlet partial pressure of 1.0 MPa as obtained by integration of Eq. 2-21, with the corresponding net rates of formation as given by Eq. 5-15 and the parameter values as reported in Tables 5-5 and 5-6. The alkene standard protonation enthalpy for the formation of tertiary carbenium ions is determined to be  $30$   $\text{kJ mol}^{-1}$  more negative than that of secondary carbenium ion formation.

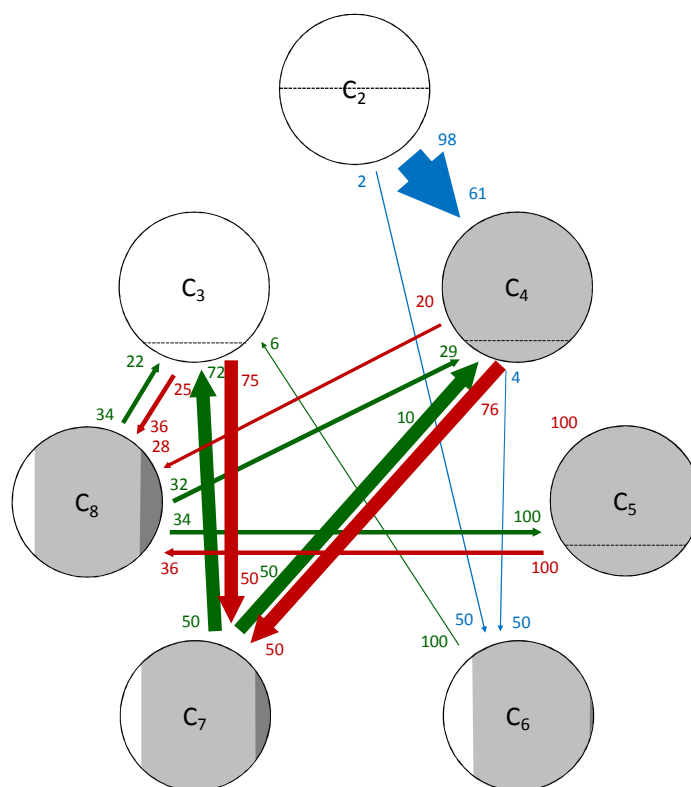
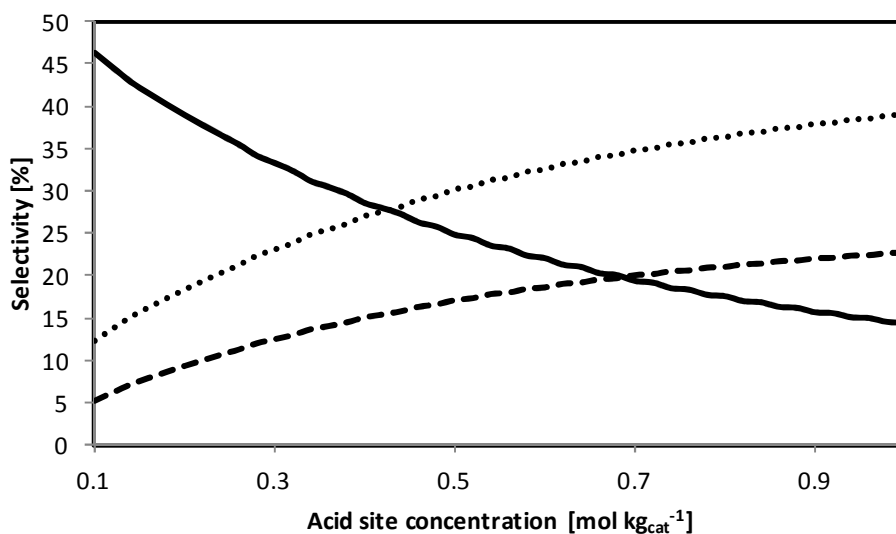


Figure 5-17: Reaction path analysis for ethene oligomerization on Ni-Beta at 50% ethene conversion, 503 K, an ethene inlet partial pressure of 1.0 MPa and an alkene standard protonation enthalpy ( $\Delta H^\circ$ ) equal to  $-80 \text{ kJ mol}^{-1}$ . The alkene standard protonation enthalpy for the formation of tertiary carbenium ions is determined to be  $30 \text{ kJ mol}^{-1}$  less.

The model simulations were obtained by integration of Eq. 2-21, with the corresponding net rates of formation, Eq. 5-15 and the parameter values reported in Tables 5-5 and 5-6. The alkenes are lumped per carbon number. The height of the horizontal line in these circles is proportional to the mass fraction of the corresponding alkene lump. If no line is visible it indicates that the corresponding mass fraction is very small, i.e., less than 1%. However, these lump may still significantly contribute to the product formation. Additionally, alkene lumps in watermark indicate that its mass fraction is less than 0.1%.

The vertical gray-scale code is used to differentiate between the different structural isomers, i.e., white: linear alkenes, light grey: monobranched alkenes and dark grey: dibranched alkenes. The surface area taken by these colors is proportional to the mass fraction of each structural isomer in the alkene lump. The color of the arrows indicate the reaction family: blue = metal-ion oligomerization, red = acid alkylation, green =  $\beta$ -scission. pcp-branching and alkyl shift are not explicitly shown as they only change the isomer distribution within an alkene lump. The size of the arrow is linearly proportional to the rate of the corresponding step. The numbers at the arrow head indicate the fraction of the lump which is produced via the corresponding step while numbers next to the arrow shaft indicate the fraction of the lump which is consumed via this step.

Considering the acid site concentration, see Figure 5-18, the relative importance of isomerization and cracking increases with the concentration. As a result, the fractions of propene and gasoline increases. As the acid site concentration affects the isomerization and cracking rates in a rather linear way, its effect is much less pronounced than that of the protonation enthalpy.



**Figure 5-18:** Selectivity towards linear 1-alkenes (full line), gasoline (dotted line) and propene (dashed line) on Ni-Beta as function of acid site concentration (s) at 50% ethene conversion, 503 K and an ethene inlet partial pressure of 1.0 MPa as obtained by integration of Eq. 2-21, with the corresponding net rates of formation as given by Eq. 5-15 and the parameter values as reported in Tables 5-5 and 5-6.

### 5.5.3 Ethene standard coordination enthalpy and nickel content

The effect of the ethene standard coordination enthalpy and nickel content is opposite to the effect of resp. acid site strength and concentration. Increasing the standard coordination enthalpy of ethene at a nickel-ion site, see Figure 5-19, or the nickel content, see Figure 5-20, results in an increased contribution of the metal-ion oligomerization steps mainly resulting in 1-butene. With decreasing standard coordination enthalpy and/or nickel content, acid catalysis becomes more important, leading to an increase in propene and gasoline selectivity.

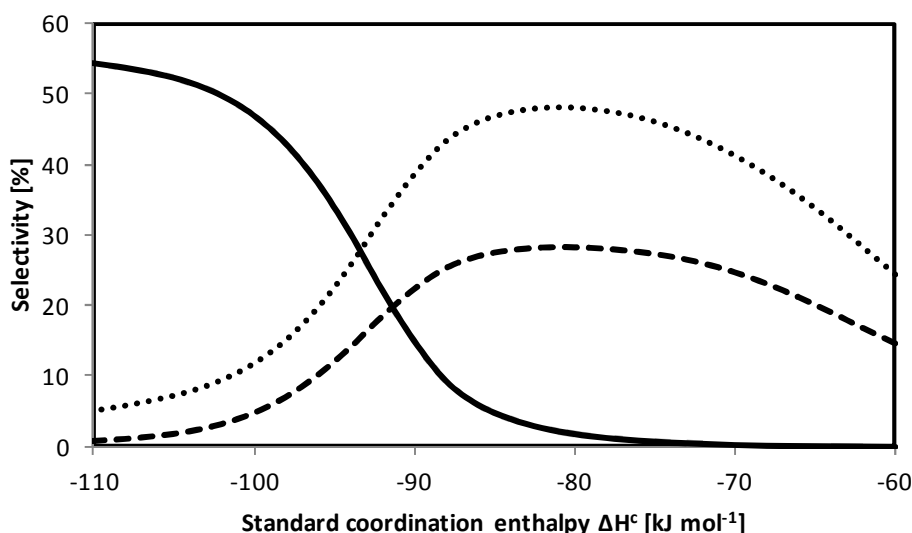


Figure 5-19: Selectivity towards linear 1-alkenes (full line), gasoline (dotted line) and propene (dashed line) on Ni-Beta as function of ethene standard coordination enthalpy at a nickel-ion site at 50% ethene conversion, 503 K and an ethene inlet partial pressure of 1.0 MPa as obtained by integration of Eq. 2-21, with the corresponding net rates of formation as given by Eq. 5-15 and the parameter values as reported in Tables 5-5 and 5-6.

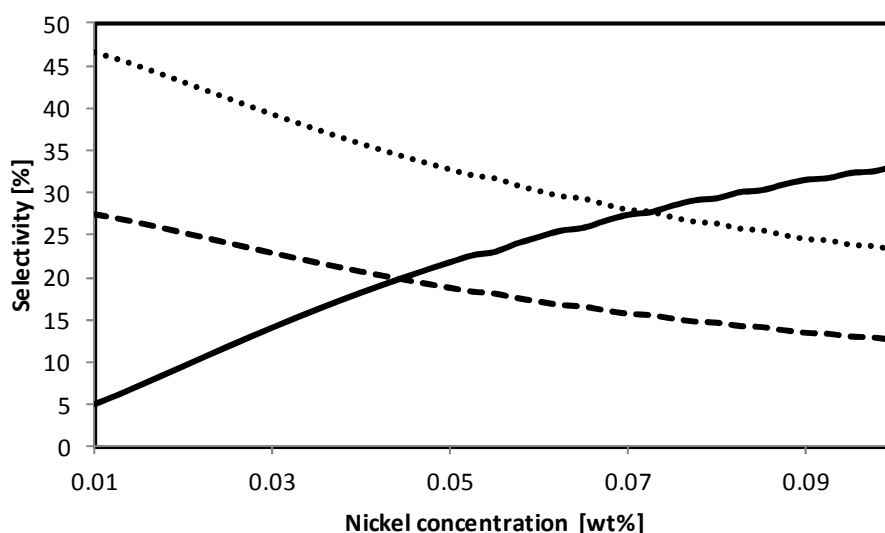


Figure 5-20: Selectivity towards linear 1-alkenes (full line), gasoline (dotted line) and propene (dashed line) on Ni-Beta as function of nickel content at 50% ethene conversion, 503 K and an ethene inlet partial pressure of 1.0 MPa as obtained by integration of Eq. 2-21, with the corresponding net rates of formation as given by Eq. 5-15 and the parameter values as reported in Tables 5-5 and 5-6.

### 5.5.4 Physisorption parameters

The effect of the support is assessed through the variation of the physisorption parameters, i.e., the standard physisorption enthalpy in particular. As benchmark, a USY support was considered which gives rise to a standard physisorption enthalpy equal to [10]:

$$\Delta H_i^{phys} = 6.44 a_{c,i} + 3.34 \quad 5-32$$

The resulting physisorption coefficients are rather low compared to those for Beta zeolite. Additionally, the increment per additional carbon atom is relatively low. Simulations showed that the ethene oligomerization rate on the 4.9wt% Ni-USY zeolite was at least one order of magnitude larger compared to the Ni-Beta zeolite. This can be attributed to a less pronounced contribution of the heavier alkenes to physisorption which, otherwise, would limit the conversion of ethene as discussed in section 5.4.2. Figures 5-21 and 5-22 show the effect of resp. temperature and conversion on the selectivities to the different product fractions. Qualitatively, the same trends as observed with Ni-Beta were simulated, see Figure 5-14, i.e., increasing temperatures and conversions reduce the selectivity to linear 1-alkenes while more gasoline and propene is produced. However, in the entire temperature range investigated, the major products formed remain linear 1-alkenes. The latter is again related to the less pronounced physisorption of heavier products which promote isomerization and cracking on the acid sites.

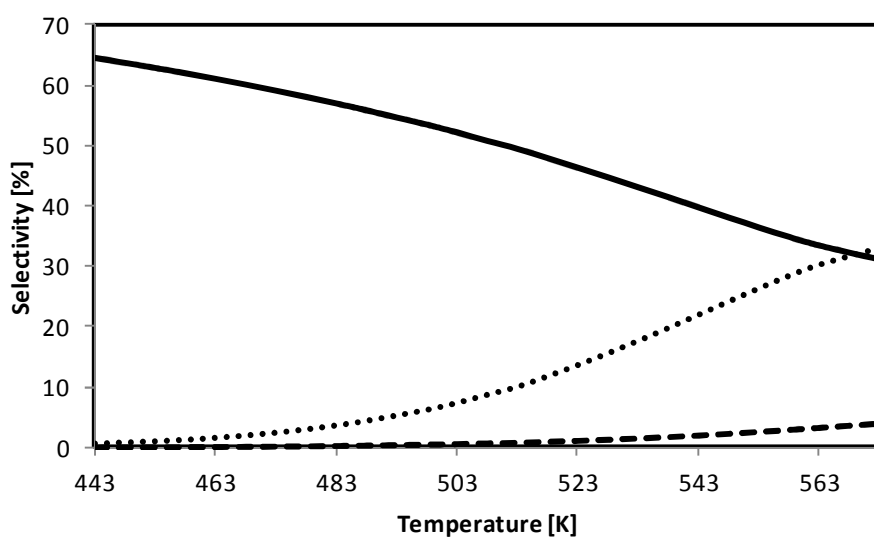


**Figure 5-21: Selectivity towards linear 1-alkenes (full line), gasoline (dotted line) and propene (dashed line) on Ni-USY as function of temperature at an ethene inlet partial pressure of 1.0 MPa and a conversion of 50% as obtained by integration of Eq. 2-21, with the corresponding net rates of formation as given by Eq. 5-15 and the parameter values as reported in Tables 5-5 and 5-6.**

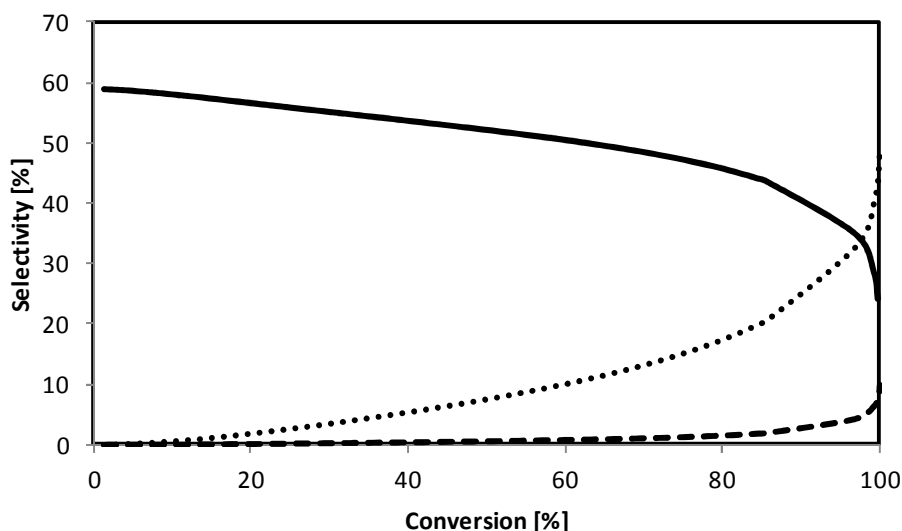


**Figure 5-22:** Selectivity towards linear 1-alkenes (full line), gasoline (dotted line) and propene (dashed line) as function of conversion on Ni-USY at 503 K and an ethene inlet partial pressure of 1.0 MPa as obtained by integration of Eq. 2-21, with the corresponding net rates of formation as given by Eq. 5-15 and the parameter values as reported in Tables 5-5 and 5-6.

## 5.6 Conclusions

Intrinsic ethene oligomerization kinetics were measured on a Ni-Beta zeolite. The main products were linear butenes and hexenes which are formed via subsequent ethene insertions on nickel-ion sites. As confirmed by  $\text{NH}_3$ -TPD, the zeolite contains acid sites which catalyze isomerization, alkylation and cracking reactions towards branched and odd carbon numbered alkenes. However, only a minor amount of odd carbon numbered alkenes were formed which indicated that the acid sites were only contributing marginally to the reaction network.

A catalytic cycle for the bifunctional catalyzed oligomerization of ethene was proposed involving ethene oligomerization, c.q., dimerization on the nickel-ion sites and consequent acid catalysis, i.e., alkylation, isomerization and cracking. This catalytic cycle was used for the construction of a Single-Event MicroKinetic model. Only two catalyst descriptors needed to be estimated by SEMK model regression to the experimental dataset. The kinetic model was tested to be significant and was able to simulate the experimental observations in an adequate manner. The parameter estimates were all highly significant and had a clear physical meaning. The standard physisorption enthalpy of gas phase alkenes on the zeolite surface was determined to be a linear function of the carbon number. The coordination of

ethene at a nickel-alkene species was considerably more strong than the protonation of the C<sub>3</sub>+ alkenes.

A reaction path analysis of ethene oligomerization on the Ni-Beta was performed using the kinetic model. Linear 1-alkenes are produced at low conversion and low temperature when the reaction mechanism is dominated by the metal-ion oligomerization route. Increasing the conversion and temperature leads to an increase in acid catalyzed reaction rates, leading to mainly gasoline and propene products. By adjusting the catalyst descriptor values, guidelines for catalyst design were uncovered. Mainly the ratios of the nickel-ion and acid site concentration and strength determine the product distribution. A catalyst with a high concentration of and strong nickel-ion sites gives primarily rise to the formation of linear 1-alkenes. With increasing acid site strength and concentration or decreasing nickel-ion site strength and concentration, the propene and gasoline fractions become larger. Eventually, a highly acidic catalyst would give rise to nearly exclusively isobutene through extended alkylation and subsequent cracking. The effect of the physisorption parameters was also investigated. A zeolite on which there is strong physisorption competition of the heavy to the lighter alkenes, will result in a less active catalyst due to the pronounced reduction in surface occupancy of ethene. However, this also increases the isomerization and cracking rate, and, hence, the selectivity towards propene and a gasoline fraction. A catalyst for which the competitive physisorption is less pronounced, will be more active and more selective to metal-ion oligomerization towards linear 1-alkenes.

## 5.7 References

- [1] J. Heveling, C.P. Nicolaides, M.S. Scurrall, *Catalysis Letters*. 95 (2004) 87-91.
- [2] M.A. Baltanas, K.K. Vanraemdonck, G.F. Froment, S.R. Mohedas, *Industrial & Engineering Chemistry Research*. 28 (1989) 899-910.
- [3] G.D. Svoboda, E. Vynckier, B. Debrabandere, G.F. Froment, *Industrial & Engineering Chemistry Research*. 34 (1995) 3793-3800.
- [4] J.W. Thybaut, G.B. Marin, *Journal of Catalysis*. 308 (2013) 352-362.
- [5] G.G. Martens, J.W. Thybaut, G.B. Marin, *Industrial & Engineering Chemistry Research*. 40 (2001) 1832-2144.
- [6] B.E. Poling, J.M. Prausnitz, J.P. O'Connell, *The Properties of Gases and Liquids*, McGraw-Hill Professional, 2000.



- [7] G.G. Martens, G.B. Marin, J.A. Martens, P.A. Jacobs, G.V. Baroni, *Journal of Catalysis*. 195 (2000) 253-267.
- [8] W.J. Moore, *Physical Chemistry*, Prentice-Hall, Englewood Cliffs, 1962.
- [9] J.F. Denayer, G.V. Baron, J.A. Martens, P.A. Jacobs, *Journal of Physical Chemistry B*. 102 (1998) 3077-3081.
- [10] J.F.M. Denayer, G.V. Baron, *Adsorption-Journal of the International Adsorption Society*. 3 (1997) 251-265.
- [11] J.M. Martinis, G.F. Froment, *Industrial & Engineering Chemistry Research*. 45 (2006) 954-967.
- [12] E. Vynckier, G.F. Froment, in: G. Astarita, S.I. Sandler (Eds.), *Kinetic and Thermodynamic Lumping of Multicomponent Mixtures*, Elsevier, 1991, p. 131.
- [13] S.W. Benson, J.H. Buss, *Journal of Chemical Physics*. 29 (1958) 546-572.
- [14] B.D. Vandegehuchte, J.W. Thybaut, A. Martinez, M.A. Arribas, G.B. Marin, *Applied Catalysis a-General*. 441 (2012) 10-20.
- [15] A. Martinez, M.A. Arribas, P. Concepcion, S. Moussa, *Applied Catalysis a-General*. 467 (2013) 509-518.



# Chapter 6

## Scale Up Chemicals and Fuel

### Production by Ethene

#### Oligomerization:

#### Industrial Reactor Design

---

In the present Chapter, an industrial reactor is designed for ethene oligomerization employing bifunctional, heterogeneous catalysts which comprise nickel-ions on an acid support such as amorphous silica-alumina or zeolites, i.e., MCM-41 and Beta. In contrast to ideal laboratory reactors, non-ideal hydrodynamics at the reactor scale and transport phenomena at the catalyst crystallite scale are much more likely to impact on the overall behavior and, hence, have to be accounted for. A simulation code is developed including the microkinetic model for ethene oligomerization developed in Chapters 4 and 5. Additionally, transport limitations and the formation of liquids due to condensation of heavy alkenes and their effects on the observed kinetics are included.

#### 6.1 Experimental setup for reactor model validation

The experimental data used to validate the simulation model were acquired on an oligomerization demonstration unit constructed at an industrial partner as described in section 2.1.2.3. The reaction conditions applied for these experiments were much more severe compared to those applied for the acquisition of the intrinsic kinetic data. The

catalyst used during this experimental campaign was the amorphous Ni-SiO<sub>2</sub>-Al<sub>2</sub>O<sub>3</sub> catalyst as described in section 2.1.1.2. The catalyst powder was pelletized, crushed and sieved to obtain a particle size of 1.0 to 2.0 10<sup>-3</sup> m. For each run, 20 g of catalyst, diluted with SiC as an inert, was loaded in the reactor. Prior to experimentation, the catalyst was pretreated for 16 hours in-situ under a nitrogen flow at atmospheric pressure at 673 K.

## 6.2 Multi-scale ethene oligomerization industrial reactor model

A graphical representation of the reactor model and the phenomena that are accounted for is given in Figure 6-1. The reactor model describes a tubular reactor with a specified length and diameter, i.e., resp.  $L_r$  and  $d_r$ . The inlet conditions are specified by the inlet molar flow rates of ethene  $F_{C_2}^0$  and nitrogen  $F_{N_2}^0$ , inlet temperature  $T^0$  and inlet total pressure  $p_{tot}^0$ . Several fixed beds, i.e., with catalyst masses  $W^1$ ,  $W^2$  and  $W^3$  and  $n_b$  the number of beds can be contained in the reactor with interbed heat exchange depicted by the temperatures  $T^1$  and  $T^2$ . It is possible to operate the reactor in an isothermal, adiabatic or heat exchange mode. In the heat exchange mode, the heat input  $Q$  is defined by a reactor wall temperature, i.e.,  $T^{wall}$ . The pressure drop along the axial reactor coordinate,  $\Delta p$ , can also be calculated. It is possible to determine, if any, liquids formation at the reaction conditions applied. If so, a so-called catalyst wetting efficiency,  $\eta_w$ , is calculated and resulting in a reduced catalyst surface area which is in contact with a gas phase. The reactor model is capable to account for intraparticle mass and heat transfer limitations inside a crystallite with diameter  $L_c$  in the direction of the diffusion path. This is represented in Figure 6-1 by the ethene coverage profile, i.e.,  $\theta_{C_2}$ , and temperature profile as function of the dimensionless crystallite diameter, i.e.,  $\xi_c$ . Also, the observed kinetics are highly depending on the catalyst properties, c.q., descriptors, such as the crystallite shape factor,  $s$ , crystallite diameter,  $d_c$ , thermal conductivity,  $\lambda_p$ , saturation concentration,  $C^{sat}$ , concentration of acid and nickel-ion sites,  $C_{H^+}$  and  $C_{Ni}$ , and standard enthalpies of physisorption,

protonation and coordination,  $\Delta H^{phys}$ ,  $\Delta H^{pr}$  and  $\Delta H^c$ . The reactor model does not account for external mass and heat transfer nor radial gradients at reactor scale.

Additionally, three parameters can be changed which aid in solving the set of partial differential equations, *PDEs*, of which the number of mesh points  $n_{mesh}$  is the most important in defining the number of points used to discretize the PDE's to a set of ODE's.

A number of output files, depending on the details required, is generated during the reactor simulation. All these output files report on various variables as a function of the reactor axial coordinate. Depending on the level of detail required for the simulation, this can include conversion, reactor temperature, pressure, product selectivities, wetting efficiency, liquid fraction and concentration and temperature profiles in a crystallite.

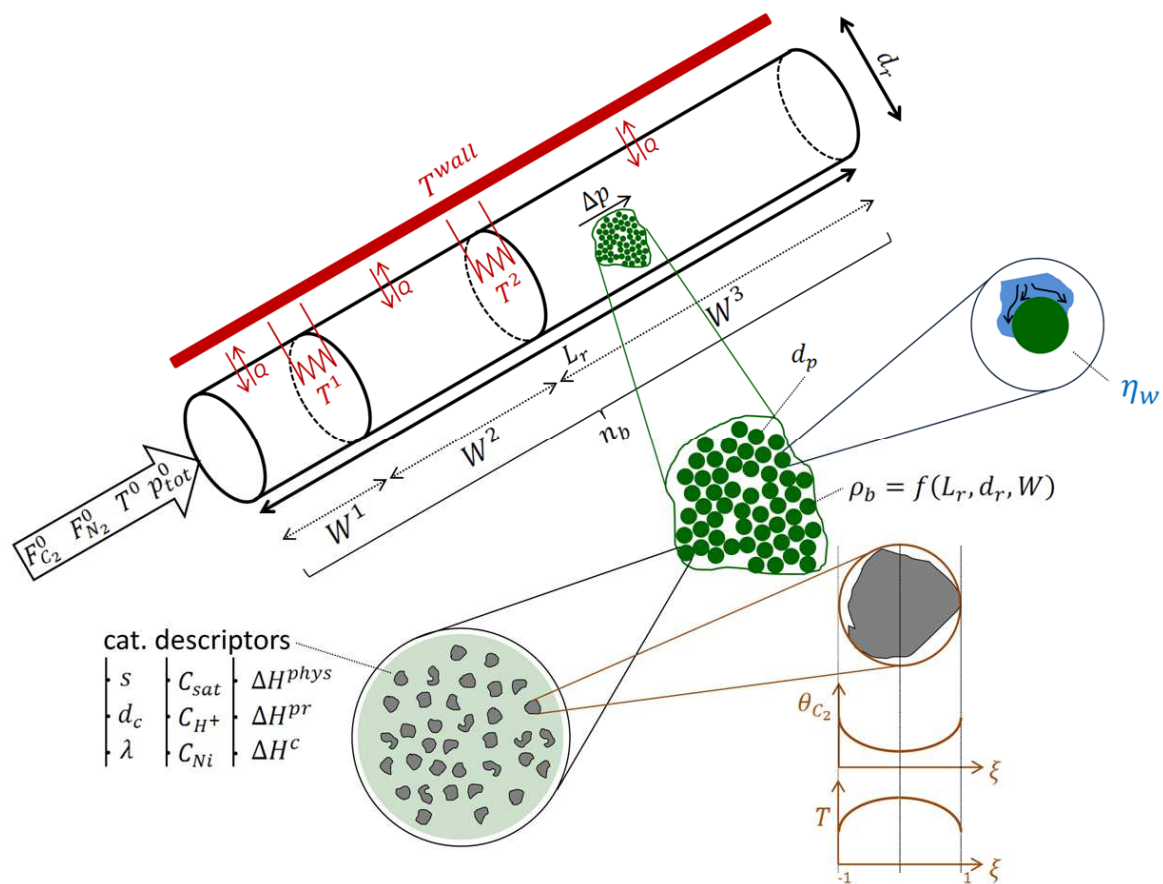


**Figure 6-1: Graphical representation of the industrial reactor model for the heterogeneous, bifunctional catalyst ethene oligomerization.**

Another graphical, more mathematical orientated, representation of the phenomena that can be accounted for by the reactor model is given in Figure 6-2. Four scales are considered: the reactor scale, the catalyst pellet scale, the catalyst particle scale and the nano scale. At the reactor scale which is comprises the mass, energy and impulse balance, see section

6.2.1. The effect of liquid formation on the simulated kinetics is situated at the catalyst pellet scale, see section 6.2.2. Mass and heat transfer phenomena are accounted for at the crystallite scale, see section 6.2.3. At nano scale the intrinsic kinetics are determined as described in Chapters 4 and 5, see section 6.2.4.

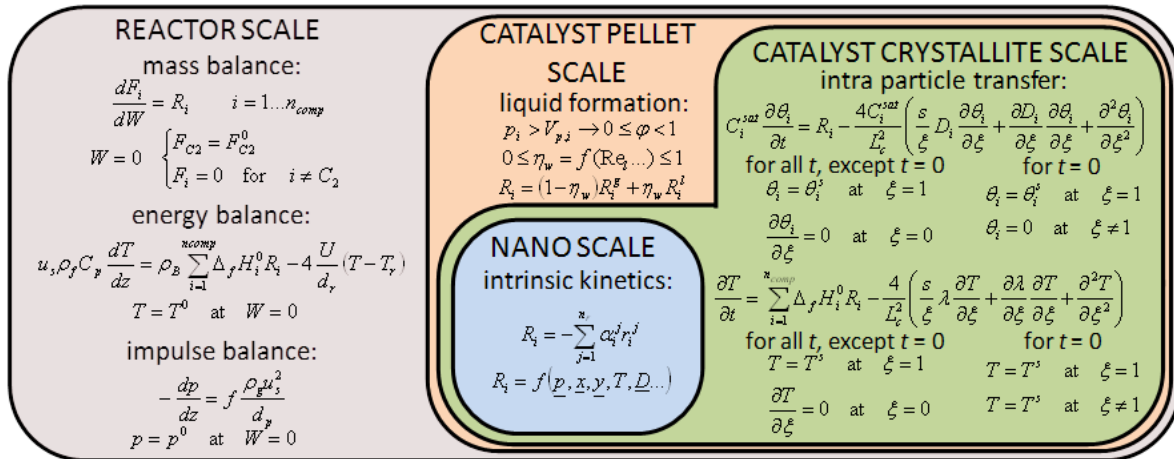


Figure 6-2: Mathematical representation of the industrial reactor model for the heterogeneous, bifunctional catalyst ethene oligomerization.

In order to solve this reactor model, a large number of physical properties are required, e.g., critical properties, heat capacity, viscosity, vapor pressure, ..., which often depend on the actual conditions at a point along the reactor axial coordinate. In appendix A, an overview is given of all correlations and methods used to determine these physical properties. Most of these properties are based upon the comprehensive book of Reid et al. [1]

## 6.2.1 Reactor scale

The reactor is described by means of three continuity equations, see equation 6-1, i.e., conservation of mass, see section 6.2.1.1, energy, see section 6.2.1.2, and momentum, see section 6.2.1.3.

$$IN = OUT + ACC - FORM \tag{6-1}$$

In this work, the industrial reactor is considered to be in steady state, hence accumulation is neglected resulting in the following continuity equation:

$$IN = OUT - FORM \tag{6-2}$$

### 6.2.1.1 Mass balance

For the reactor mass balance, see equation 6-2, the *IN* and *OUT* term correspond with the variation in the molar flow rate of every component over an infinitesimal amount of catalyst, i.e.,  $(F_i + dF_i) - F_i$  and the formation term *FORM* is represented by the net rate of formation  $R_i$  in the infinitesimal amount of catalyst:

$$dF_i = R_i dW \quad i = 1 \dots n_{ole} \quad 6-3$$

in which  $F_i$  is the molar flow rate of component  $i$ ,  $W$  is the catalyst mass,  $R_i$  is the net rate of formation of component  $i$  and  $n_{ole}$  is the number of alkenes considered in the reaction network.

The initial conditions for this set of differential equations are given by:

$$W = 0 \quad \begin{cases} F_{C_2} = F_{C_2}^0 \\ F_i = 0 \quad \text{for } i \neq C_2 \end{cases} \quad 6-4$$

The infinitesimal catalyst mass  $dW$  can be rewritten in terms of axial distance along the reactor, i.e.,  $z$ , via:

$$dW = A_r \rho_b dz \quad 6-5$$

in which  $A_r$  is the cross-sectional area of the reactor tube and  $\rho_b$  is the bed density of the reactor.

### 6.2.1.2 Energy balance

For the energy balance over the reactor, see equation 6-2, heat can enter (*IN*) and leave (*OUT*) the in two manners: either with components flow, i.e.,  $u_s \rho_f C_{p,f} [(T + dT) - T]$ , or via heat transfer with the reactor wall in an infinitesimal volume of the reactor, i.e.,

$4 \frac{U}{d_r} (T - T_r) dz$ . Heat can also be produced or consumed

(*FORM*) by the chemical reactions in an infinitesimal volume of the reactor, i.e.,

$$\rho_B \sum_{i=1}^{n_{ole}} \Delta_f H_i^0 R_i dz :$$

$$u_s \rho_f C_{p,f} dT = \rho_B \sum_{i=1}^{n_{ole}} \Delta_f H_i^0 R_i dz - 4 \frac{U}{d_r} (T - T_r) dz \quad 6-6$$

The initial condition for this differential equation is given by:

$$W = 0 \rightarrow T = T^0 \quad 6-7$$

$T$  is the temperature,  $\Delta_f H_i^0$  is the standard formation enthalpy of component  $i$ ,  $u_s$  is the superficial velocity through the reactor and  $\rho_f$  and  $C_{p,f}$  are resp. the density and the thermal capacity of the fluidum, i.e., gas, liquid or gas-liquid, all at the reactor conditions.  $U$  is the overall heat transfer coefficient and  $d_t$  is the diameter of the reactor tube.

- $\Delta_f H_i^0$  is determined using a group additivity method such as Benson's [2]
- $u_s$  is determined via the volumetric flow rate of the fluidum  $Q$  and the cross sectional area of the reactor:

$$u_s = \frac{Q^g + Q^l}{A_r} \quad 6-8$$

$Q^g$  and  $Q^l$  are the volumetric flow rate of the gaseous and liquid phase respectively which can be determined via the molar volume of both phases, see appendix A.

- $\rho_f$ , the density of the fluidum, is calculated as follows:

$$\rho_f = \frac{\sum_{i=1}^{n_{ole}} F_i M_i}{Q^g + Q^l} \quad 6-9$$

in which  $M_i$  is molecular mass of component  $i$ .

- $C_{p,f}$  and its temperature dependence are determined using thermodynamic data available from literature [1], see appendix A.
- The overall heat transfer coefficient  $U$  is assumed to be mainly determined by the heat transfer coefficient on the bed side, i.e.,  $\alpha_i$ :

$$\frac{1}{U} = \frac{1}{\alpha_i} \quad 6-10$$

The heat transfer coefficient on the bed side  $\alpha_i$  is determined by Leva's correlation [3]. For heating up the reaction mixture  $\alpha_i$  is found via:

$$\frac{\alpha_i d_r}{\lambda} = 0.813 \left( \frac{d_p J_m}{\mu} \right)^{0.9} e^{-6d_p/d_t} \quad 6-11$$



For cooling down the reaction mixture  $\alpha_i$  is found via:

$$\frac{\alpha_i d_r}{\lambda} = 3.50 \left( \frac{d_p J_m}{\mu} \right)^{0.7} e^{-4.6 d_p / d_t} \quad 6-12$$

$\lambda$  is the thermal conductivity of the fluidum flowing through the reactor and is determined as described in appendix A.  $d_r$  and  $d_p$  are the diameter of resp. the reactor and a catalyst pellet.  $J_m$  is the superficial mass flow rate and  $\mu$  is the dynamic viscosity, see appendix A.

### 6.2.1.3 Momentum balance

For the momentum balance over the reactor, see equation 6-2, the momentum over the reactor, i.e., *IN* and *OUT*, is given by the pressure profile  $-\frac{dp}{dz}$ . Momentum can be lost

(-*FORM*) throughout the reactor because of friction with the packed bed and is represented

by  $f \frac{\rho_f u_s^2}{d_p}$ :

$$-\frac{dp}{dz} = f \frac{\rho_f u_s^2}{d_p} \quad 6-13$$

$p$  is the total pressure in the reactor,  $\rho_f$  is the density of the fluidum,  $u_s$  is the superficial velocity of the fluidum,  $d_p$  is the catalyst pellet diameter and  $f$  is the friction factor.

- The friction factor  $f$  is determined by a correlation of Hicks [4]:

$$f = 6.8 \frac{(1 - \varepsilon_B)^{1.2}}{\varepsilon_B^3} \text{Re}^{-0.2} \quad 6-14$$

The bed porosity  $\varepsilon_B$  can be found via a correlation of Haughey and Beveridge [5]:

$$\varepsilon_B = 0.38 + 0.073 \left( 1 + \frac{\left( \frac{d_t}{d_p} - 2 \right)^2}{\left( \frac{d_t}{d_p} \right)^2} \right) \quad 6-15$$

while the Reynolds number of a fluid in a packed bed is given by:

$$\text{Re} = \frac{J_m d_p}{\mu(1 - \varepsilon_B)} \quad 6-16$$

- For two phase flow through a fixed bed, the friction factor can be determined by [6]:

$$f = \frac{1}{\kappa^{1.5}} \left( 31.3 + \frac{17.3}{\sqrt{\kappa}} \right) \quad 6-17$$

$\kappa$  is a dimensionless parameter given by:

$$\kappa = \frac{J_m^g}{J_m^l} \sqrt{\frac{\rho^l}{\rho^g}} (\text{Re}^l \text{We}^l)^{0.25} \quad 6-18$$

in which  $J_m^g$  is the gas superficial mass flow rate and  $\text{Re}^l$  and  $\text{We}^l$  are the Reynolds and Weber number of the liquid phase given by resp.:

$$\text{Re}_L = \frac{J_m^l d_p}{\mu^l} \quad 6-19$$

$$\text{We}_L = \frac{(J_m^l)^2 d_p}{\rho^l \sigma^l} \quad 6-20$$

$\sigma^l$  is the surface tension of the liquid fluidum, see appendix A.

## 6.2.2 Catalyst pellet scale – liquid formation

Throughout the catalyst bed, heavy components can be formed via oligomerization which can condense to form liquids. These liquids can partially or fully wet the surface of a catalyst pellet, which results in a shift in surface concentrations to heavier components. As a result, the simulated kinetics can be altered significantly.

To account for potential phase transition from gas to liquid phase, a parameter  $\varphi$  is introduced, which equals the molar ratio of the gas flow rate to the total flow rate:

$$\varphi = \frac{F^g}{F^{tot}} \quad 6-21$$

In practice for ethene oligomerization,  $\varphi$  equals 1 at the reactor inlet, and can, potentially, decrease along the axial reactor coordinate. The vapor liquid equilibrium is determined in a similar manner as described by the Grayson Streed model [7]. However, using this method at every point along the reactor axial coordinate would require a considerable amount of CPU time. Hence, before this method is actually invoked, the partial pressure of every component is compared with its vapor pressure. The Grayson Streed method is only effectively launched if the partial pressure of a component reaches 90% of its vapor pressure.

It can be expected that condensation in the micropores will occur even under conditions at which condensation will occur in larger pores and can be attributed to capillary effects. In this work, a difference is made between the microporous (subscript  $p$ ) and macroporous (subscript  $o$ ) surface area. The latter is referring to both macro and mesoporous surface area as the outer surface area. In order to account for the difference between the microporous and macroporous surface area, a weighted average is taken of the net rate of formation under the reaction conditions in the micropores and non-micropores, resp.  $R_{i,p}$  and  $R_{i,o}$ :

$$R_i = \frac{A_p R_{i,p} + A_o R_{i,o}}{A_p + A_o} \quad 6-22$$

The net rate of formation for every component in any point along the axial reactor coordinate can be written as function of the wetting efficiency, i.e.,  $\eta_w$ , which is the ratio of the wetted catalyst surface area and the total catalyst surface area:

$$R_{i,p} = R_{i,p}^g (1 - \eta_{w,p}) + R_{i,p}^l \eta_{w,p} \quad 6-23$$

$$R_{i,o} = R_{i,o}^g (1 - \eta_{w,o}) + R_{i,o}^l \eta_{w,o} \quad 6-24$$

in which  $R_i^g$  and  $R_i^l$  are the net rate of formation of component  $i$  resulting from the composition of resp. the gas and liquid phase.

Methods are described in literature in order to determine the wetting efficiency of micropores due to capillary condensation [8]. However, modeling these effects is typically quite CPU intensive. Therefore, it is assumed that the micropores are filled up instantaneously when any liquids are formed. This is translated mathematically into:

$$\eta_{w,p} = 1 \quad 6-25$$

$$R_{i,p} = R_{i,p}^l \quad 6-26$$

The wetting efficiency for the macroporous area  $\eta_{w,o}$  is described by a correlation proposed by Aldahhan et al. for trickle bed reactors at high pressure [9]:

$$\eta_{w,o} = 1.104 \text{Re}^{\frac{1}{3}} \left( \frac{1 + \frac{\Delta P}{z\rho^l g}}{Ga^l} \right)^{\frac{1}{9}} \quad 6-27$$

$\frac{\Delta P}{z}$  is the pressure gradient through the bed,  $g$  is the gravitational constant and  $Ga^l$  is the dimensionless liquid Galileo number determined by:

$$Ga^l = g \frac{d_p^3 \varepsilon_B^3}{(1 - \varepsilon_B)^3} \left( \frac{\rho^l}{\mu^l} \right)^2 \quad 6-28$$

The correlation proposed by Aldahhan is only applicable for trickle bed regime and, hence, at very low and high values of  $\varphi$ , a substantial deviation can be expected. Therefore, at the regimes with nearly only pure gas or liquid, the following linear correlation between  $\eta_{w,o}$  and  $\varphi$  is proposed:

$$\eta_{w,o} = 1 - \varphi \quad 6-29$$

## 6.2.3 Crystallite scale

### 6.2.3.1 Mass transfer limitations

To incorporate intraparticle diffusion limitations, for every component  $i$ , a one-dimensional transient mass balance over an infinitesimal volume of the crystallite is considered, see equation 6-30. It was preferred to solve this transient mass balance rather than a steady state mass balance because, in the case of second order differential equations, solving the latter balances is not guaranteed to lead to a solution.

$$C_i^{sat} \frac{\partial \theta_i}{\partial t} = R_i - \frac{4C_i^{sat}}{L_c^2} \left( \frac{s}{\xi} D_i \frac{\partial \theta_i}{\partial \xi} + \frac{\partial D_i}{\partial \xi} \frac{\partial \theta_i}{\partial \xi} + \frac{\partial^2 \theta_i}{\partial \xi^2} \right) \quad 6-30$$

$C_i^{sat}$  is the saturation concentration of component  $i$ ,  $L_c$  is the crystallite diameter in the direction of the diffusion path,  $\xi$  is the dimensionless length of the crystallite, i.e.,

$\xi = \frac{2r_c}{L_c} = \frac{d_c}{L_c}$ ,  $s$  is the crystallite shape factor, i.e., 0, 1 or 2 for resp. a slab, cylinder or

sphere,  $D$  is the intraparticle diffusion coefficient and  $\theta$  is the fractional occupancy of the catalyst surface by the component considered.  $R$ , the net rate of formation, is affected by the shape of the crystallite assumed and is determined as follows:

$$R_i = \frac{s+1}{2n_{mesh}} \sum_{j=1}^{n_{mesh}} (R(r_{c,j})r_{c,j}^s + R(r_{c,j+1})r_{c,j+1}^s) \quad 6-31$$

For this set of partial differential equations, the following boundary and initial conditions were considered:

- for all  $t$ , except  $t=0$

$$\begin{aligned} \theta_i &= \theta_i^s \quad \text{at} \quad \xi = 1 \\ \frac{\partial \theta_i}{\partial \xi} &= 0 \quad \text{at} \quad \xi = 0 \end{aligned}$$

- for  $t=0$

$$\begin{aligned} \theta_i &= \theta_i^s \quad \text{at} \quad \xi = 1 \\ \theta_i &= 0 \quad \text{at} \quad \xi \neq 1 \end{aligned}$$

$\theta_i^s$  is the fractional occupancy by component  $i$  of the catalyst surface at the outer surface of the crystallite.

These sets of partial differential equations are solved by a finite difference method. The partial differential equation is discretized over the dimensional length of the crystallite  $\xi$  over a user-defined number of mesh points,  $n_{mesh}$ . Every partial differential equation is rewritten as a set of  $n_{mesh}$  ordinary differential equations. These equations are solved until steady state which is defined as the maximum relative deviation allowed of the concentration profile between two time integration steps in the reactor model, e.g., 0.1%.

In Figures 6-3 and 6-4, the effect of the number of mesh points on the coverage profile of ethene in a crystallite, catalyst effectiveness  $\eta$  and CPU time needed to determine the initial concentration profile is shown. Increasing the number of mesh points, leads to a better and smoother description of the coverage profile, see Figure 6-3. However, by increasing the number of mesh points with one, a total of  $n_{comp}$  ordinary differential equations are added to the set of equations to be solved. This leads to an exponential increase of CPU time needed to determine the coverage profile of every component in the catalyst particle, see Figure 6-4. Additionally, the catalyst effectiveness as function of the number of mesh points was nearly constant already when using 10-15 mesh points.

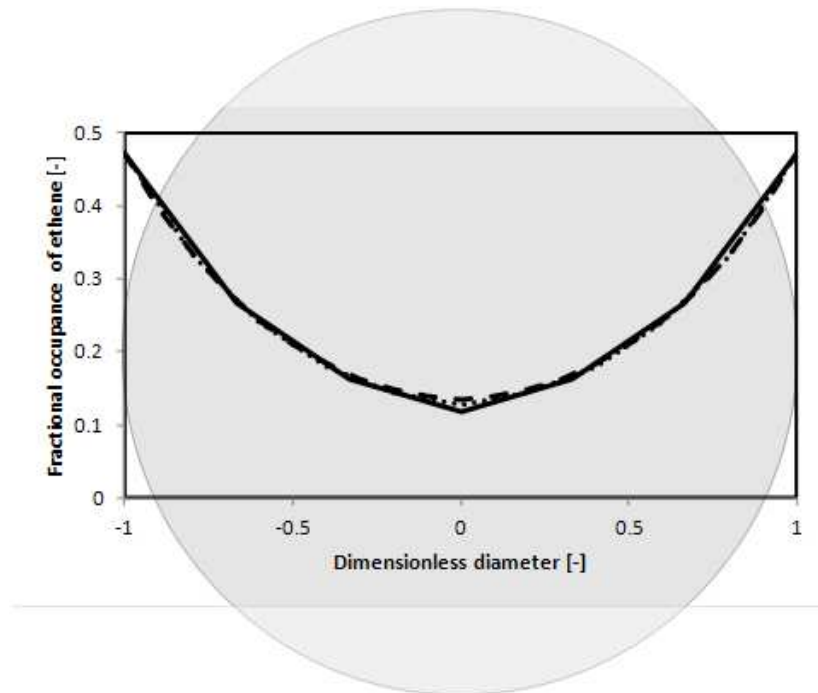


Figure 6-3: Fractional coverage of ethene in a catalyst particle as function of the number of mesh points, used for discretizing the partial differential equations describing these profiles, at the reactor inlet (no conversion): full line: 3 mesh points, small dashed line: 5 mesh points, dotted line: 10 mesh points. The inlet temperature is equal to 503 K, the inlet partial pressure and molar flow rate of ethene is equal resp. 1.0 MPa and. The diffusion coefficient for ethene is taken equal to  $10^{-16} \text{ m}^2 \text{ s}^{-1}$  for illustration purposes.

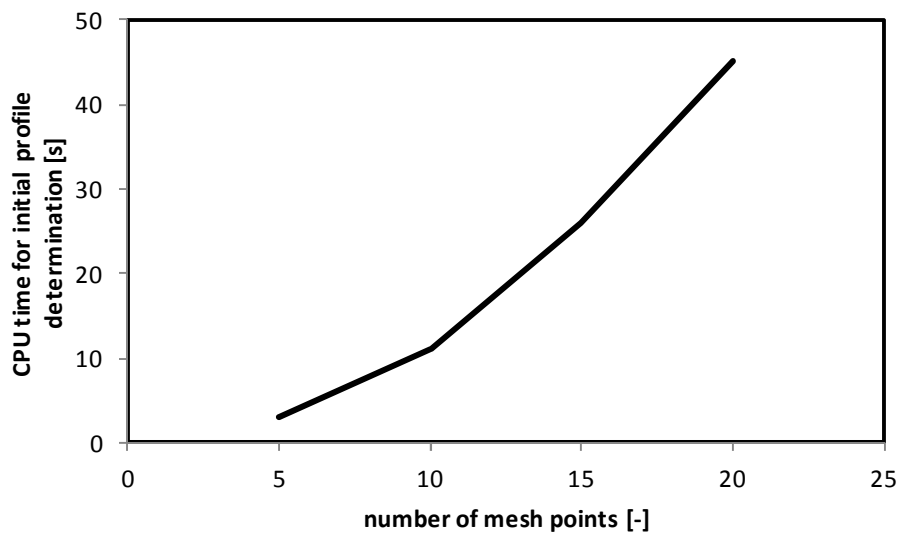


Figure 6-4: Time needed to determine the initial concentration profile as function of the number of mesh points, used for discretizing the partial differential equations describing these profiles, at the reactor inlet (no conversion). The inlet temperature is equal to 503 K, the inlet partial pressure and molar flow rate of ethene is equal resp. 1.0 MPa and  $37.2 \text{ mol s}^{-1}$ . The catalyst used is Ni-Beta. The diffusion coefficient for ethene is taken equal to  $10^{-16} \text{ m}^2 \text{ s}^{-1}$  for illustration purposes.

### 6.2.3.2 Energy transfer limitations

In order to account for temperature gradients in a catalyst particle, an analogous balance as equation 6-30 is considered for intraparticle heat transfer limitations:

$$\frac{\partial T}{\partial t} = \sum_{i=1}^{n_{ole}} \Delta_f H_i^0 R_i - \frac{4}{L_c^2} \left( \frac{s}{\xi} \lambda \frac{\partial T}{\partial \xi} + \frac{\partial \lambda}{\partial \xi} \frac{\partial T}{\partial \xi} + \frac{\partial^2 T}{\partial \xi^2} \right) \quad 6-32$$

with the following boundary and initial conditions:

- for all  $t$ , except  $t=0$

$$T = T^s \quad \text{at} \quad \xi = 1$$

$$\frac{\partial T}{\partial \xi} = 0 \quad \text{at} \quad \xi = 0$$

- for  $t=0$

$$T = T^s \quad \text{at} \quad \xi = 0 \dots 1$$

## 6.2.4 Nanoscale – intrinsic kinetics description

At the nanoscale, i.e., at the scale of the active sites, the kinetics are described by the intrinsic kinetic models developed in Chapters 4 and 5. For every component, the net rate of formation is calculated as a function of the local reaction conditions, i.e., surface coverage, temperature...

## 6.2.5 Experimental validation of the reactor model

A limited number of well chosen experiments were performed by an industrial OCMOL partner on the experimental set-up described in section 6.1. The experimental results are compared to the model predictions for validation purposes.

The space-time effect on the ethene conversion is shown in Figure 6-5. There is a good agreement between the experimental observations and the simulation results. The absence of repetition experiments makes it difficult to find a solid explanation for this effect, however, given the trend in conversion versus space time, this experimental point seems to be situated at a lower value than would be expected.

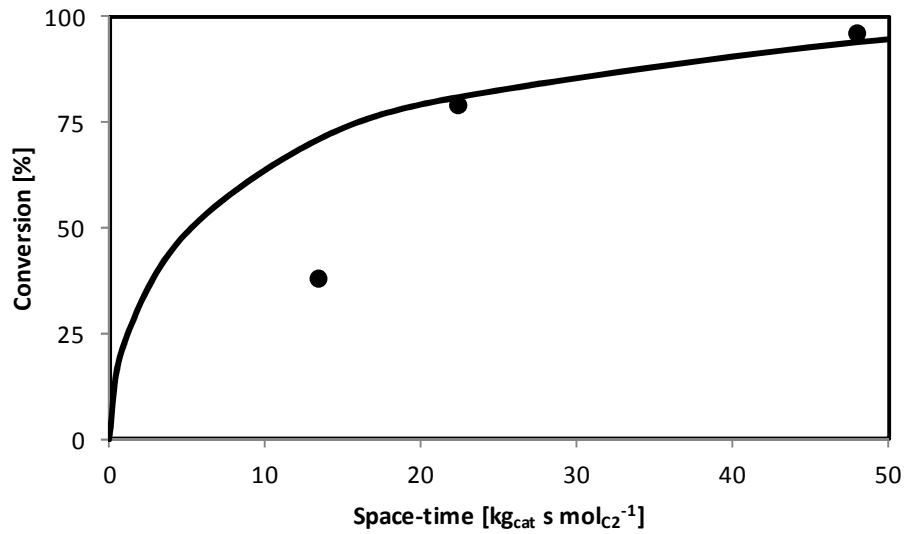


**Figure 6-5:** Ethene conversion as function of space-time on Ni-SiO<sub>2</sub>-Al<sub>2</sub>O<sub>3</sub> at 493 K, 3.5 MPa total pressure and 2.6 MPa inlet ethene pressure; black line: simulation results as obtained using the simulation model for an industrial oligomerization reactor, see equations 6-3, 6-6 and 6-14.

The temperature effect on the ethene conversion is shown in Figure 6-6. There is a very good agreement between the two experimental observations and the simulation results. Also, from this figure it is obvious that increasing the reaction temperature will result in an increased observed reaction rate.

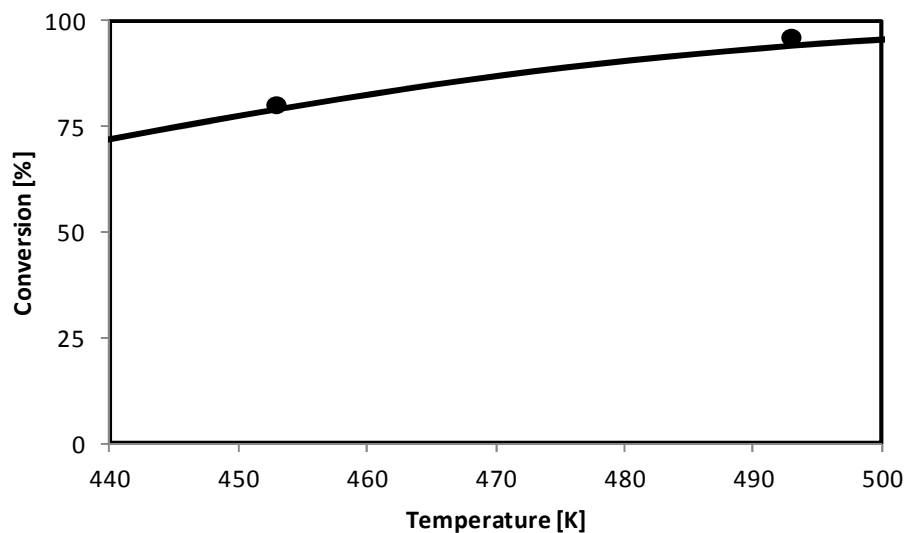


**Figure 6-6:** Ethene conversion on Ni-SiO<sub>2</sub>-Al<sub>2</sub>O<sub>3</sub> as function of temperature at 48.0 kg<sub>cat</sub> s mol<sub>C<sub>2</sub></sub><sup>-1</sup>, 3.5 MPa total pressure and 2.6 MPa inlet ethene pressure; black line: simulation results as obtained using the simulation model for an industrial oligomerization reactor, see equations 6-3, 6-6 and 6-14.

The effect of the ethene inlet molar fraction and total pressure is shown in Figures 6-7 and 6-8. Even while there are no significant trends obtained in the obtained conversion with the



ethene inlet molar fraction and the total pressure, the absolute value of the simulated conversion is in excellent agreement with the observed conversion.

Again, there is a very good agreement between the experimental observations and simulation results. Increasing the ethene inlet molar fraction increases the observed reaction rate, see Figure 6-7. The low variation of the simulation conversion as function of the ethene inlet molar fraction is attributed to the high conversion level applied. However, changing the total pressure while maintaining a constant ethene pressure does not affect the observed reaction rate as shown in Figure 6-8.

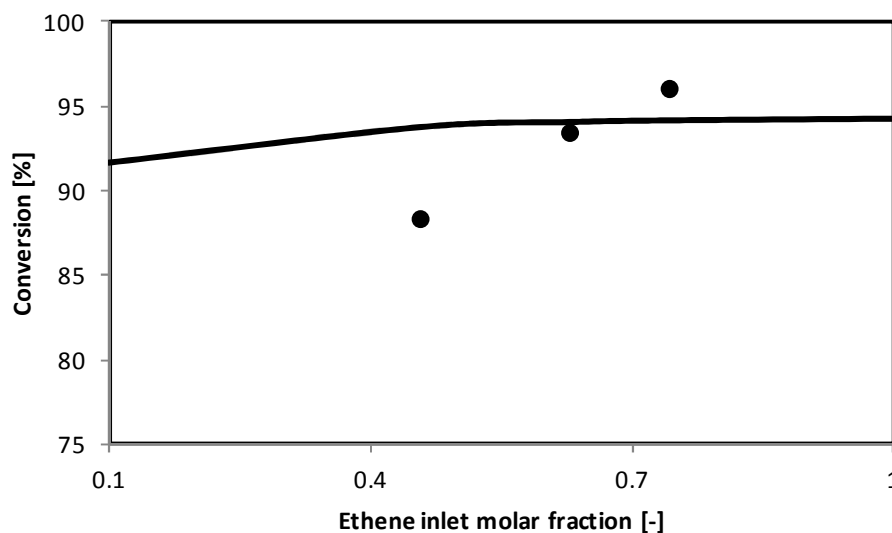
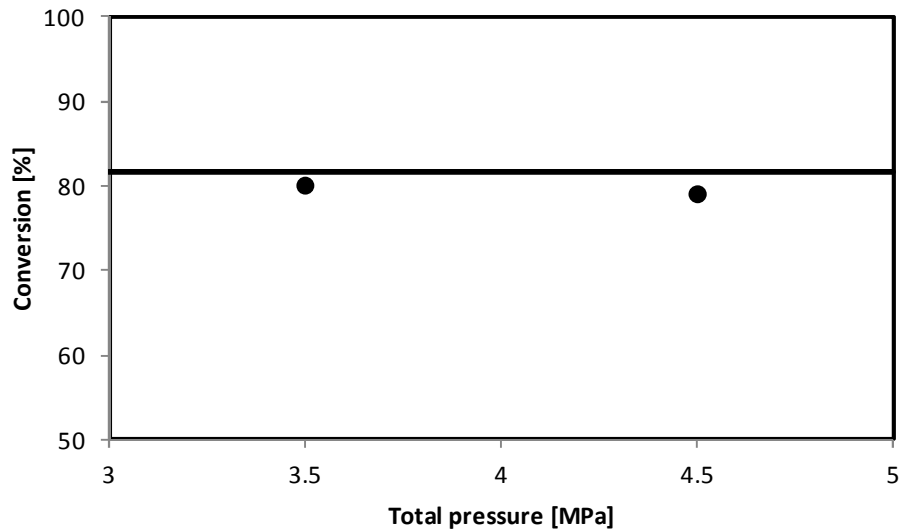
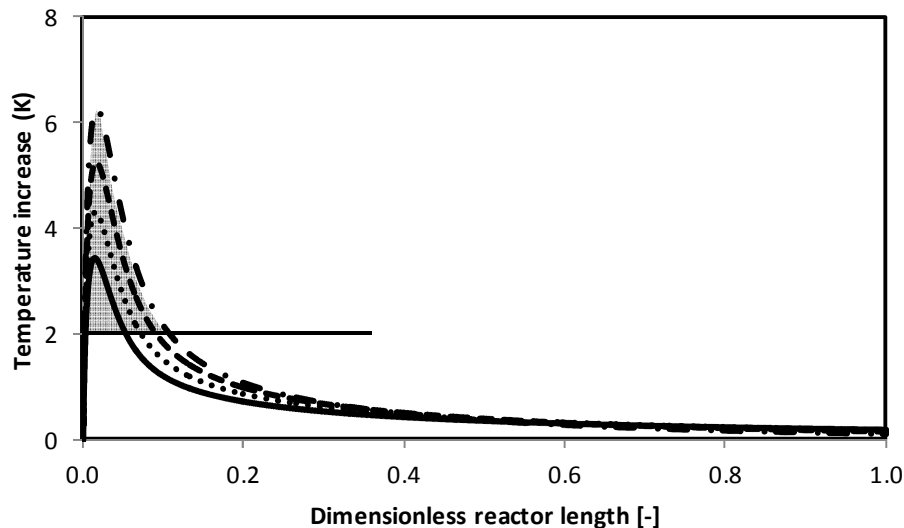


Figure 6-7: Ethene conversion on Ni-SiO<sub>2</sub>-Al<sub>2</sub>O<sub>3</sub> as function of ethene inlet molar fraction at 48.0 kg<sub>cat</sub> s mol<sub>C<sub>2</sub></sub><sup>-1</sup>, 493 K and 3.5 MPa total pressure; black line: simulation results as obtained using the simulation model for an industrial oligomerization reactor, see equations 6-3, 6-6 and 6-14.



**Figure 6-8: Ethene conversion on Ni-SiO<sub>2</sub>-Al<sub>2</sub>O<sub>3</sub> as function of total pressure at 22.4 kg<sub>cat</sub> s mol<sub>C<sub>2</sub></sub><sup>-1</sup>, 493 K and 2.6 MPa inlet ethene pressure; black line: simulation results as obtained using the simulation model for an industrial oligomerization reactor, see equations 6-3, 6-6 and 6-14.**

The isothermicity of the reactor in the pilot plant was also verified. As for the previous simulations, the reactor dimensions and inert used to dilute the catalyst bed was taken into account. From simulations, the temperature increase due to the exothermal oligomerization reaction, varied between ca. 3 to 6K, depending on the inlet and reactor wall temperature. Increasing the inlet and reactor wall temperature results in a larger temperature increase in the catalyst bed. However, this 'hot spot' is situated near the inlet and is small, i.e., less than 10% of the reactor length. After this 'hot spot', the temperature is within 2K of the reactor wall as experimentally determined, see section 6.1.



**Figure 6-9: Temperature increase during operation of the pilot plant reactor using the Ni-SiO<sub>2</sub>-Al<sub>2</sub>O<sub>3</sub> as function of the dimensionless reactor length as obtained using the simulation model for an industrial oligomerization reactor, see equations 6-3, 6-6 and 6-14, at 3.5 MPa total pressure and 2.6 MPa inlet ethene pressure for different reactor wall temperatures: full line: 443 K, dotted line: 453 K, dashed line: 473 K, dashed-dotted line: 493 K. The inlet temperature was taken equal to the reactor wall temperature.**

The pressure drop over the catalyst bed was less than <1% and could be neglected. Intracrystalline diffusion effects did not influence the observed kinetics, i.e., the catalyst effectiveness was higher than 0.99. Additionally, no liquids were formed in the reactor. Probably, this is related to the catalyst used which has a very high selectivity to butenes and leads to a very limited production of heavy components. From the simulation results, it was clear that quasi intrinsic kinetics were experimentally measured. The model parameters that may require further tuning could be identified via an experimental design.

### 6.3 Design of an industrial oligomerization reactor

In order to simulate an industrial oligomerization reactor, the reaction conditions were based on the design guidelines as put forward by the OCMOL project. In that project, a total methane capacity of 100 kTon per annum was envisaged. Taking into account state-of-the-art catalysts for the oxidative coupling of methane and separation units, a maximum production of ca. 30 kTon per annum ethene is to be expected. Accounting for 8000 h time on stream per annum, an ethene inlet flow rate of 37.2 mol s<sup>-1</sup> to the oligomerization reactor is achieved. The reaction temperature could vary between 423 to 573 K and the total pressure was maximum 3.5 MPa. The catalyst properties used for the following

simulations are those of the Ni-Beta catalyst as described in section 2.1.1.3. The effect of different heating regimes, reactor geometry, liquid formation and mass transport limitations are discussed in the following sections. A final design for an industrial ethene oligomerization reactor is given in section 6.3.5.

### 6.3.1 Effect of heating regime

The effect of operating the industrial ethene oligomerization reactor in an adiabatic compared to an isothermal mode is shown in Figure 6-10. Due to the exothermicity of the oligomerization reactor, the temperature increases with ca. 20 K up to 5 ton<sub>cat</sub>. Also no significant temperature differences in the catalyst pellets are simulated. Hereafter, the temperature decreases steadily. Since heat exchange is not allowed in an adiabatic operation, this temperature decrease can only be attributed to endothermic reactions. From a catalyst mass of 5 ton, energetically, endothermic cracking is contributing more than exothermic oligomerization, resulting in the temperature decrease. This is also illustrated in Figure 6-11 which shows the temperature profile and yield of 1-alkenes, propene and gasoline throughout the catalyst bed. While 1-alkenes are clearly the primary products and are formed through exothermic oligomerization, propene and gasoline are secondary products which are formed through endothermic cracking of the oligomers, see Chapter 5. At the maximum 1-alkenes yield, the oligomerization and cracking rates are identical. Because of the similar global heat effects by both reactions, the endothermicity of the cracking is compensated by the exothermicity of the oligomerization at the same point, explaining why the maximum 1-alkene yield coincides with that obtained for the temperature. After this maximum, cracking of oligomers to propene and gasoline will dominate the reaction pathways leading to a temperature decrease. Because the temperature throughout the reactor exceeds the inlet temperature, an adiabatic operation will require less catalyst to obtain a similar conversion level in an isothermal operation, see Figure 6-10. The temperature increase, however, is not sufficiently high to justify the use of a multi fixed bed reactor. The absence of acid functionality on the ethene oligomerization catalyst, e.g., the Ni-SiO<sub>2</sub>-Al<sub>2</sub>O<sub>3</sub> catalyst used in Chapter 4, results in a larger adiabatic temperature increase, see Figure 6-12. Since acid sites are required to catalyze the cracking of oligomers, no major endothermic reactions can occur.

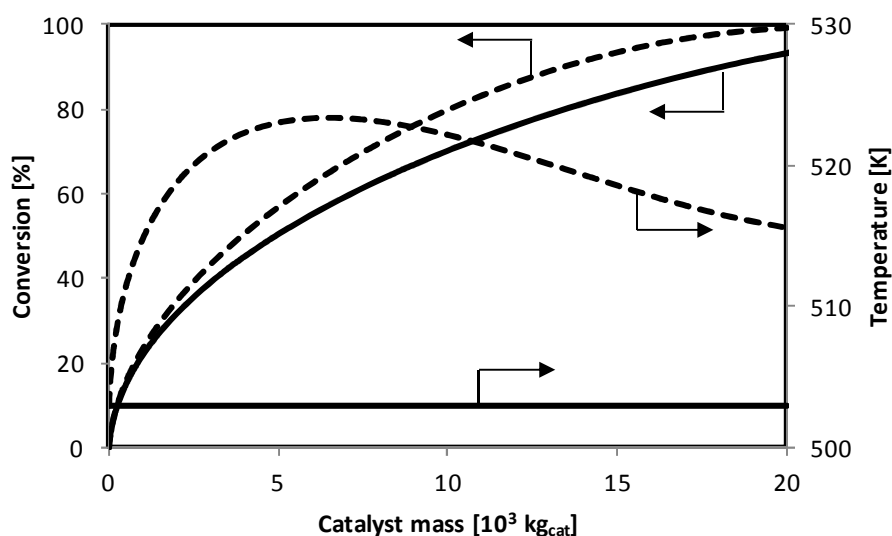


Figure 6-10: Ethene conversion (left axis) and reactor temperature (right) as function of the Ni-Beta catalyst mass, i.e., axial reactor coordinate as obtained using the simulation model for an industrial oligomerization reactor, see equations 6-3, 6-6 and 6-14, at 503 K inlet temperature, 1.0 MPa inlet ethene pressure and an inlet ethene molar flow rate equal to  $37.2 \text{ mol s}^{-1}$ , full line: isothermal case, dashed lines: adiabatic case.

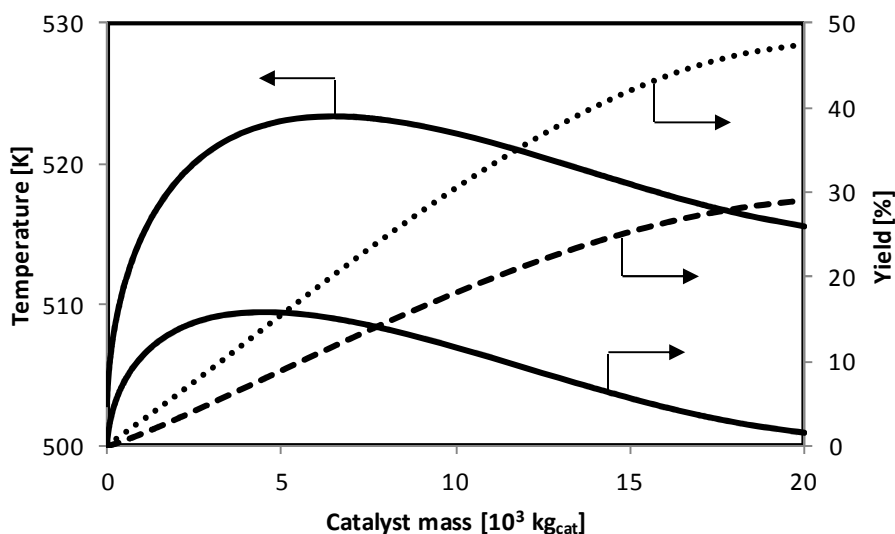
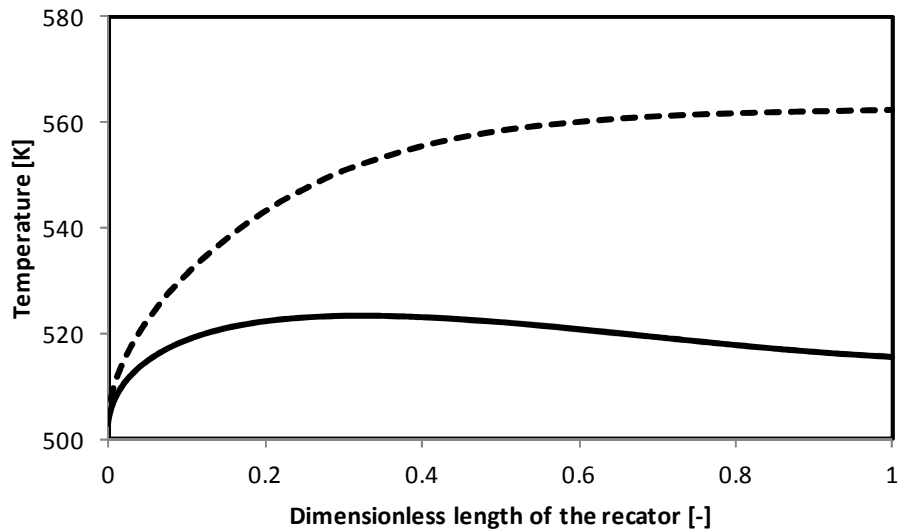


Figure 6-11: Reactor temperature (left axis) and product yield (right) as function of the Ni-Beta catalyst mass, i.e., axial reactor coordinate as obtained using the simulation model for an adiabatic industrial oligomerization reactor, see equations 6-3, 6-6 and 6-14, at 503 K inlet temperature, 1.0 MPa inlet ethene pressure and an inlet ethene molar flow rate equal to  $37.2 \text{ mol s}^{-1}$ , full line, left axis: reactor temperature; full line, right axis: 1-alkene yield; dashed line: propene yield; dotted line: gasoline yield.



**Figure 6-12:** Reactor temperature as function of axial reactor coordinate as obtained using the simulation model for an adiabatic industrial oligomerization reactor, see equations 6-3, 6-6 and 6-14, at 503 K inlet temperature, 1.0 MPa inlet ethene pressure and an inlet ethene molar flow rate equal to  $37.2 \text{ mol s}^{-1}$ , full line: Ni-Beta, dashed lines: Ni-SiO<sub>2</sub>-Al<sub>2</sub>O<sub>3</sub>.

The isothermal and adiabatic operation of the reactor represents two extremes concerning heating operating. Figure 6-13 illustrates the temperature profile throughout the catalyst bed in the intermediate case where heat transfer to the catalyst bed is considered via a cooling medium at a constant temperature of 503 K. The heat is originating both from the catalyst bed, i.e., reaction enthalpy, as the reactor wall. A temperature maximum is obtained around  $2 \text{ ton}_{\text{cat}}$ , corresponding with equal heat production and removal. After this maximum, the reactor temperature decreases as more energy is removed than there is produced through reactor since cracking is becoming dominant to oligomerization as discussed in previous paragraphs.

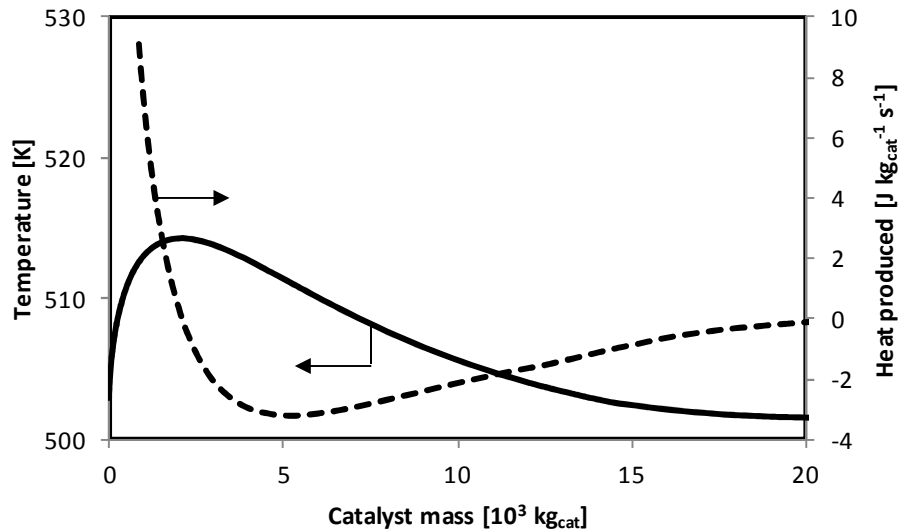


Figure 6-13: Reactor temperature (left axis) and heat produced (right axis) as function of the Ni-Beta catalyst mass, i.e., axial reactor coordinate as obtained using the simulation model for a heat exchanging industrial oligomerization reactor, see equations 6-3, 6-6 and 6-14, at 503 K inlet temperature, a constant cooling medium temperature of 503 K, 1.0 MPa inlet ethene pressure and an inlet ethene molar flow rate equal to  $37.2 \text{ mol s}^{-1}$ , full line: reactor temperature, dashed line: produced heat.

### 6.3.2 Effect of the reactor geometry on the temperature profile and pressure drop

Changing the reactor geometry of a tubular fixed bed reactor, i.e., the length to diameter ratio, mainly affects the heat transfer from the catalyst bed. In order to avoid too pronounced hot spots in the reactor, the length to diameter should be chosen sufficiently high, see Figure 6-14. However, this causes the pressure drop to increase as a function of the ratio between the catalyst pellet diameter and that of the reactor tube. However, under the reaction conditions investigated, the pressure drop is negligible when the reactor and pellet diameter differ less than 2 orders of magnitude, see Figure 6-15.

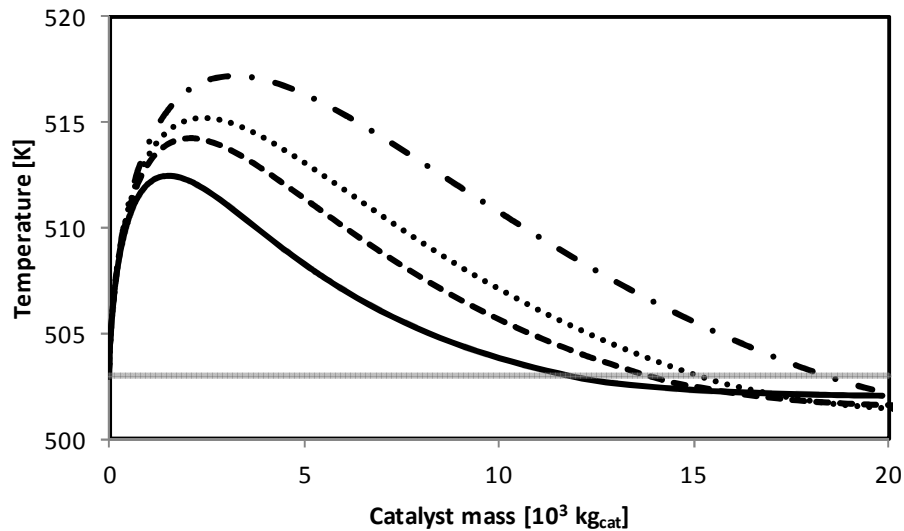


Figure 6-14: Reactor temperature as function of the Ni-Beta catalyst mass, i.e., axial reactor coordinate as obtained using the simulation model for a heat exchanging industrial oligomerization reactor with varying length to diameter ratio ( $L_r/d_r$ ), see equations 6-3, 6-6 and 6-14, at 503 K inlet temperature, 1.0 MPa inlet ethene pressure and an inlet ethene molar flow rate equal to  $37.2 \text{ mol s}^{-1}$ , full line:  $L_r/d_r = 15$ , dashed line:  $L_r/d_r = 10$ , dotted line:  $L_r/d_r = 8$ , dashed-dotted line:  $L_r/d_r = 5$ .

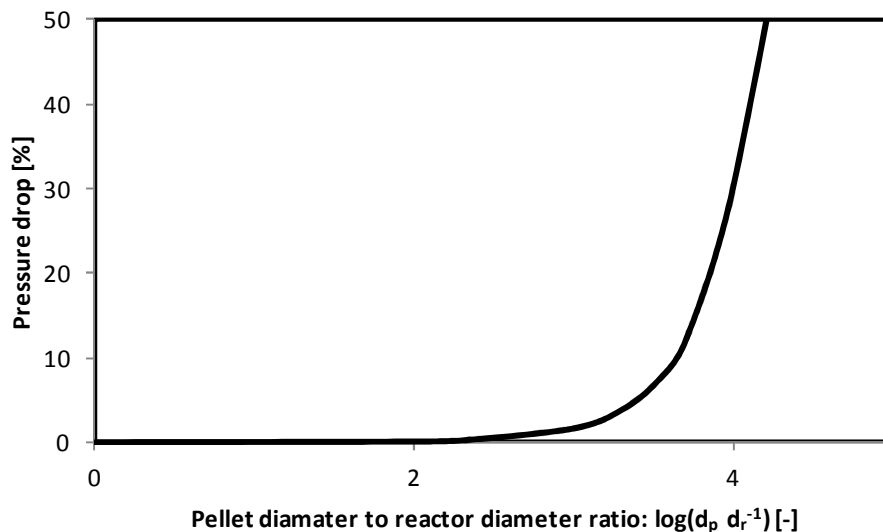


Figure 6-15: Pressure drop as function of the catalyst pellet to reactor diameter ratio as obtained using the simulation model for an isothermal industrial oligomerization reactor using the Ni-Beta catalyst, see equations 6-3, 6-6 and 6-14, at 503 K inlet temperature, 1.0 MPa inlet ethene pressure and an inlet ethene molar flow rate equal to  $37.2 \text{ mol s}^{-1}$ .

### 6.3.3 Effect of liquid formation on the conversion of ethene

At sufficiently low temperatures, high pressures or high ethene conversions, condensation of heavy alkenes formed by oligomerization is most likely, potentially causing a change in the observed reaction kinetics. These possible effects are illustrated in this paragraph. Four



different catalysts are considered, i.e., a macroporous catalyst ( $A_o > 100A_p$ ) which contains either only nickel-ion sites (type I) or both acid and nickel-ions sites (type II) and a microporous catalyst ( $A_p > 100A_o$ ) containing either only nickel-ion sites (type III) or both acid and nickel-ions sites (type IV), see Table 6-1. In order to clearly see the effect of liquid formation, the simulated reaction temperature was limited to 393 K while the ethene inlet pressure was 10.0 MPa. These relatively mild conditions led to the need for a large catalyst amount in order to obtain sufficient ethene conversion, i.e., ca.  $10^5 \text{ ton}_{\text{cat}}$ .

**Table 6-1: Overview of the catalyst types simulated to study the effect of liquid formation on the observed kinetics for ethene oligomerization.**

	macroporous ( $A_o > 100A_p$ )	microporous ( $A_p > 100A_o$ )
nickel-ion sites only	type I	type III
acid and nickel-ion sites	type II	type IV

Figure 6-16 shows the ethene conversion as function of the catalyst mass simulated when using a catalyst containing only nickel-ions as active sites (types I and III) compared to a reference case in which the liquid formation was not simulated (full line). The evolution of the wetting efficiency and molar gas fraction through the catalyst bed is shown in Figures 6-17 and 6-18 for both catalyst types. Condensation of heavy components begins around  $12 \cdot 10^4 \text{ ton}_{\text{cat}}$ , see Figures 6-17 and 6-18. In case of a microporous catalyst (type III), the observed rate of disappearance of ethene is greatly reduced as seen by the conversion plateau in Figure 6-16. For the macroporous catalyst (type I), liquid formation seems not to have a major effect on the conversion profile, see Figure 6-16. When liquids are formed, the micropores are assumed to instantaneously fill up with liquids. In case of a microporous catalyst, the total surface area is dominated by the microporous area and, hence, liquid formation rapidly leads to a complete wetting, see Figure 6-18. Only Ni-ion sites are present on the simulated catalyst which are only active towards ethene insertion. The liquid phase consists mainly of heavy alkenes which are not active on the Ni-ion site, leading to a sudden decrease of the observed rate of disappearance of ethene. For the macroporous catalyst, the wetting efficiency increases gradually with the phase composition, see Figure 6-17. Although the dry surface area containing the Ni-ions is decreasing steadily, the rate of disappearance of ethene remains quasi constant. This can be explained by the higher ethene partial pressure which is maintained in the gas phase because of the condensation of

the heavier compounds. Hence, as long as the decrease in dry surface area is sufficiently compensated by these higher ethene partial pressures the overall reaction rate does not vary to such a pronounced extent. This compensation leads to a conversion profile which is very similar in case liquid formation is not simulated for a macroporous catalyst. Liquid formation has no effect on the product distribution when using the type I and III catalyst due to their typical ASF product distribution, see chapter 4.

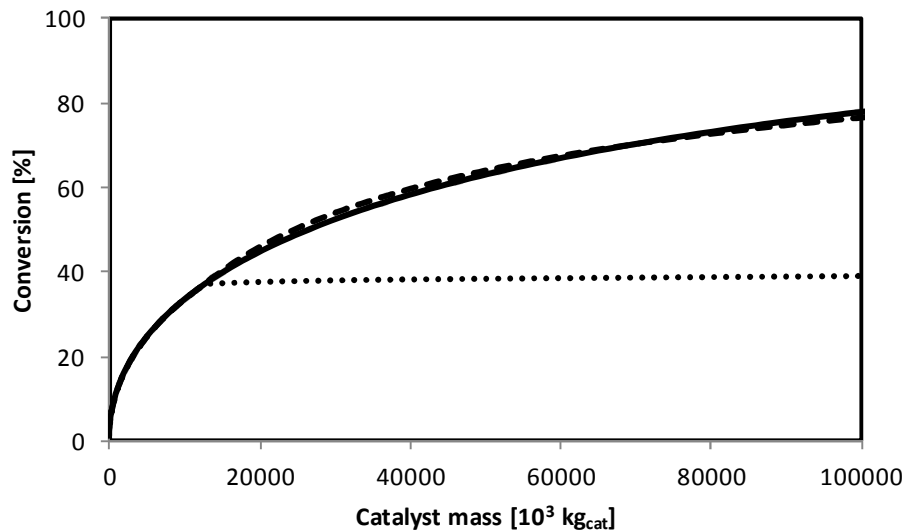


Figure 6-16: Ethene conversion as function of the catalyst mass, i.e., axial reactor coordinate as obtained using the simulation model for an isothermal industrial oligomerization reactor see equations 6-3, 6-6 and 6-14, for a Ni-Beta catalyst containing only Ni-ion sites (type I and III) at 393 K inlet temperature, 10.0 MPa inlet ethene pressure and an inlet ethene molar flow rate equal to  $37.2 \text{ mol s}^{-1}$ . Full line: ignoring liquid formation, dashed line:  $A_{\text{macro}} = 100 A_{\text{micro}}$  (type I), dotted line:  $A_{\text{micro}} = 100 A_{\text{macro}}$  (type III)

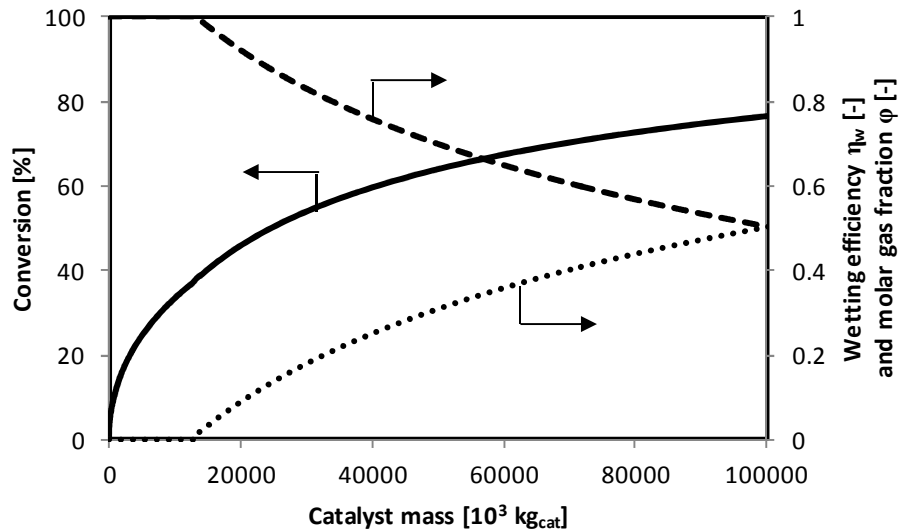


Figure 6-17: Ethene conversion (left) and wetting efficiency and phase molar gas fraction (right) as function of the catalyst mass, i.e., axial reactor coordinate as obtained using the simulation model for an isothermal industrial oligomerization reactor see equations 6-3, 6-6 and 6-14, for a Ni-Beta catalyst containing only Ni-ion sites having a macroporous surface area which highly exceeds the microporous surface area, i.e.,  $A_{\text{macro}} = 100 A_{\text{micro}}$  (type I), at 393 K inlet temperature, 10.0 MPa inlet ethene pressure and an inlet ethene molar flow rate equal to  $37.2 \text{ mol s}^{-1}$ . Full line: ethene conversion, dashed line: molar gas phase fraction, dotted line: wetting efficiency

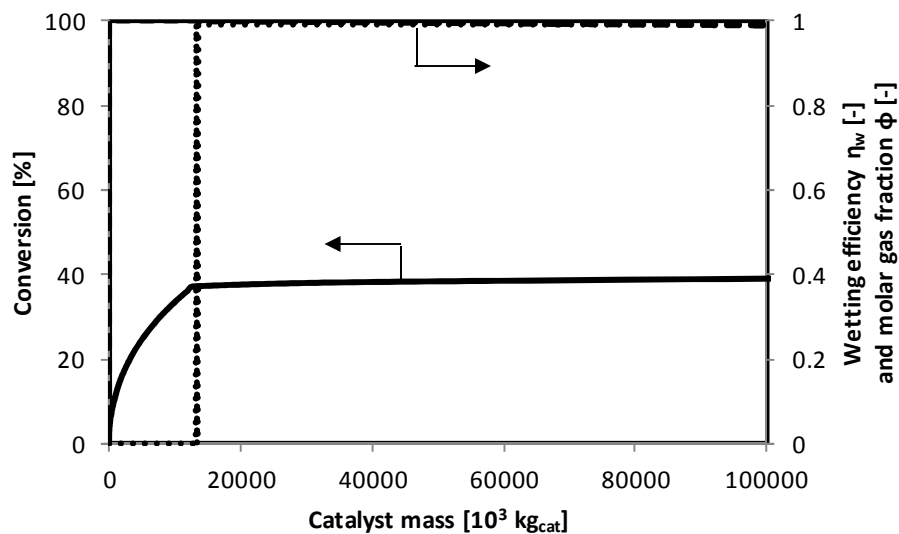
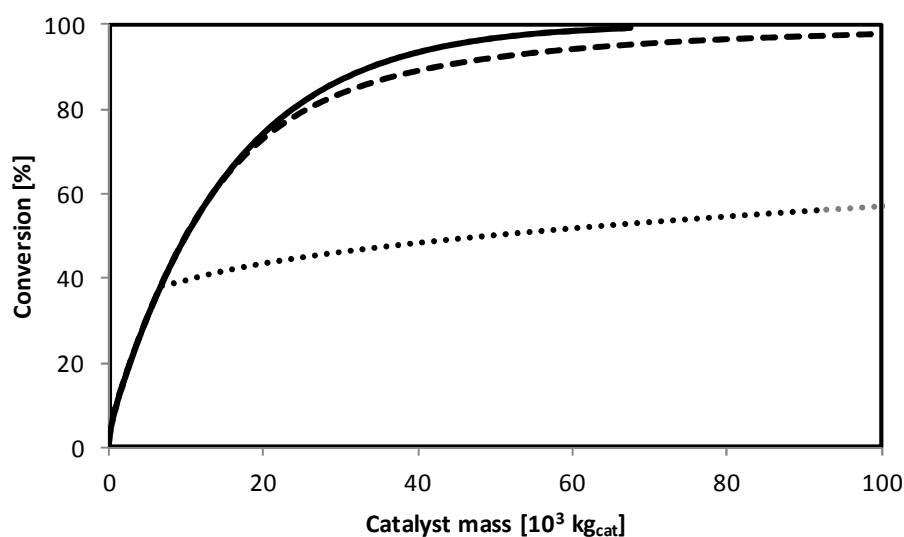


Figure 6-18: Ethene conversion (left) and wetting efficiency and phase molar gas fraction (right) as function of the catalyst mass, i.e., axial reactor coordinate as obtained using the simulation model for an isothermal industrial oligomerization reactor see equations 6-3, 6-6 and 6-14, for a Ni-Beta catalyst containing only Ni-ion sites having a microporous surface area which highly exceeds the macroporous surface area, i.e.,  $A_{\text{micro}} = 100 A_{\text{macro}}$  (type III), at 393 K inlet temperature, 10.0 MPa inlet ethene pressure and an inlet ethene molar flow rate equal to  $37.2 \text{ mol s}^{-1}$ . Full line: ethene conversion, dashed line: molar gas phase fraction, dotted line: wetting efficiency

In Figure 6-19 to 6-22, the ethene conversion and selectivity towards 1-alkenes, propene and gasoline is shown in case a bifunctional catalyst, i.e., containing acid and Ni-ion sites, is used. The conversion profile as shown in Figure 6-19 is very similar to the one shown in Figure 6-16. However, in case of the bifunctional microporous catalyst (type III), some catalyst activity is preserved compared to the total activity loss on the microporous catalyst containing only Ni-ion sites (type IV). In the former, the micropores, filled with liquid, also contain acid sites which are still able to convert, c.q., crack, the heavy oligomers into lighter alkenes. This leads to an increased production of propene and gasoline, see Figure 6-21, at the expense of the oligomers, e.g., 1-alkenes, see Figure 6-20. The production of light components causes the gas fraction not to decrease as rapidly as expected, leading to a less steep increase of the wetting efficiency and, hence a larger ethene oligomerization rate. This effect is also present, but to a lesser extent in case of using a macroporous catalyst (type II).



**Figure 6-19: Ethene conversion as function of the catalyst mass, i.e., axial reactor coordinate as obtained using the simulation model for an isothermal industrial oligomerization reactor see equations 6-3, 6-6 and 6-14, for a Ni-Beta catalyst containing acid and Ni-ion sites (type II and IV) at 393 K inlet temperature, 10.0 MPa inlet ethene pressure and an inlet ethene molar flow rate equal to  $37.2 \text{ mol s}^{-1}$ . Full line: ignoring liquid formation, dashed line:  $A_{\text{macro}} = 100 A_{\text{micro}}$  (type II), dotted line:  $A_{\text{micro}} = 100 A_{\text{macro}}$  (type IV)**

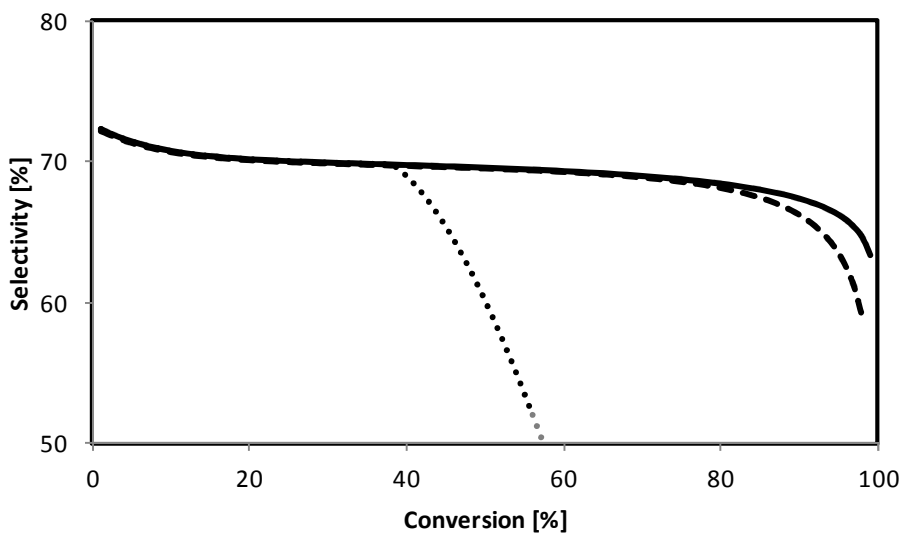


Figure 6-20: 1-alkene selectivity as function of ethene conversion using the simulation model for an isothermal industrial oligomerization reactor see equations 6-3, 6-6 and 6-14, for a Ni-Beta catalyst containing acid and Ni-ion sites (type II and IV) at 393 K inlet temperature, 10.0 MPa inlet ethene pressure and an inlet ethene molar flow rate equal to  $37.2 \text{ mol s}^{-1}$ . Full line: ignoring liquid formation, dashed line:  $A_{\text{macro}} = 100 A_{\text{micro}}$  (type II), dotted line:  $A_{\text{micro}} = 100 A_{\text{macro}}$  (type IV)

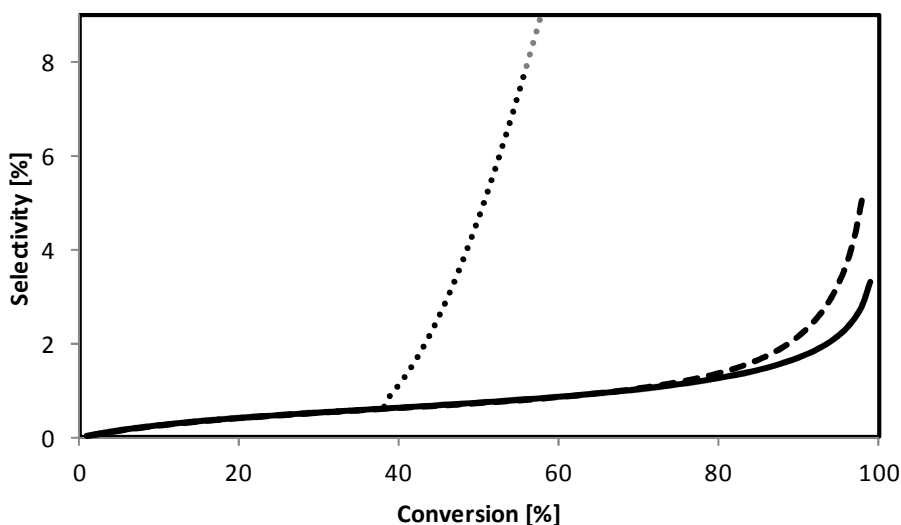


Figure 6-21: Propene selectivity as function of ethene conversion using the simulation model for an isothermal industrial oligomerization reactor see equations 6-3, 6-6 and 6-14, for a Ni-Beta catalyst containing acid and Ni-ion sites (type II and IV) at 393 K inlet temperature, 10.0 MPa inlet ethene pressure and an inlet ethene molar flow rate equal to  $37.2 \text{ mol s}^{-1}$ . Full line: ignoring liquid formation, dashed line:  $A_{\text{macro}} = 100 A_{\text{micro}}$  (type II), dotted line:  $A_{\text{micro}} = 100 A_{\text{macro}}$  (type IV)

### 6.3.4 Effect of the shape factor on the coverage profile of ethene in a catalyst particle

Mass transport limitations can greatly affect the overall catalyst performance, c.q., effectiveness. For illustration purposes, the effect of the shape factor  $s$  of the catalyst particle is shown in Figure 6-22. Three different catalyst particle geometries are considered, i.e., a slab ( $s = 0$ ), a cylinder ( $s = 1$ ) and a sphere ( $s = 2$ ). For these three geometries, a catalyst effectiveness of resp. 0.52, 0.73 and 0.84 is obtained. The spherical geometry has the best performance since components can diffuse in all three dimensions in the catalyst pellet, compared to only two and even one for resp. the cylinder and slab. A spherical geometry thus leads to a less steep concentration profile compared to the other geometries, see Figure 6-22. The knowledge of the actual diffusion coefficients and effects of zeolite geometry should enhance the description of mass transport phenomena.

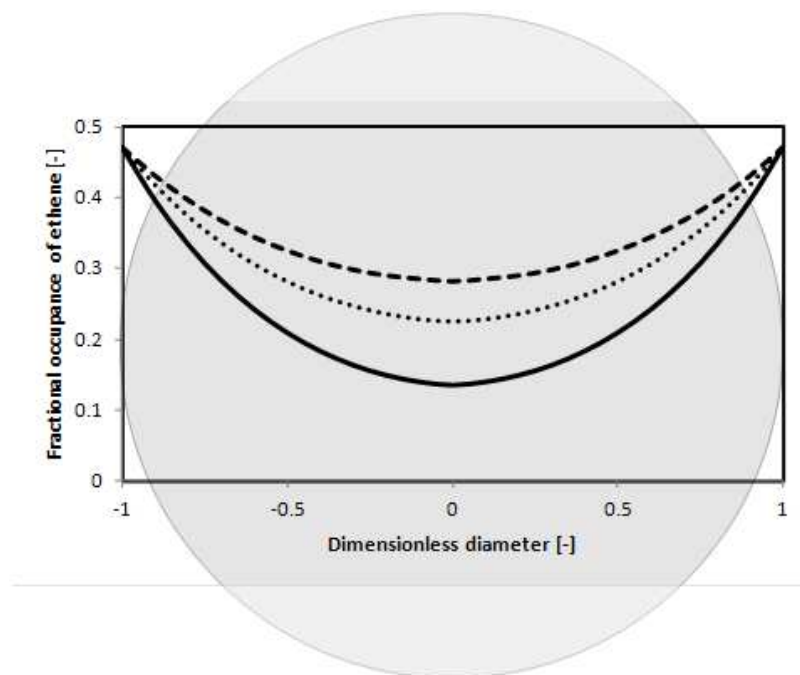


Figure 6-22: Fractional coverage of ethene in a Ni-Beta catalyst particle as function of the shape factor  $s$ , at the reactor inlet (no conversion): full line: slab ( $s=0$ ), dotted line: cylinder ( $s=1$ ), dashed line: sphere ( $s=2$ ).

The inlet temperature is equal to 503 K, the inlet partial pressure and molar flow rate of ethene is equal resp. 1.0 MPa and. The diffusion coefficient for ethene is taken equal to  $10^{-16} \text{ m}^2 \text{ s}^{-1}$  for illustration purposes.

### 6.3.5 Final industrial reactor design

Taking into account the effects described in the previous sections, a final design for an industrial ethene oligomerization is proposed. As already mentioned, the inlet flow rate of

ethene amounts to 30 kTon per annum, which equals  $37.2 \text{ mol s}^{-1}$ . The temperature and ethene inlet partial pressure were taken as high as possible within the operating window of the OMCOL project, i.e., resp. 573 K and 3.5 MPa. No diluent is sent with the reactants into the reactor. An ethene conversion of 95% was aimed at. Figure 6-23 shows the conversion and temperature profile for a single fixed bed adiabatic reactor since the temperature increase is limited to 20 K. The desired ethene conversion is reached at a catalyst mass of 8.2 ton. The catalyst density amounts to ca.  $1200 \text{ kg m}^{-3}$  and the bed porosity equals ca. 0.3. If a reactor length to diameter ratio of ca. 10 is assumed, this corresponds to a reactor length of 10.5 m, a reactor diameter of 1.0 m and a total reactor volume of  $8.9 \text{ m}^3$ . The yield towards 1-alkenes, propene and gasoline is shown in Figure 6-24. At 95% ethene conversion, the yield towards 1-alkenes, propene and gasoline is limited to resp. 4%, 30% and 40%. The remaining 26% is constituted of other fractions, such as iso-butene. Preliminary simulations showed that recycling of any of the components and fractions did not result in a remarkable product yield increase. Under the reaction conditions applied, no liquids were formed and the pressure drop ( $d_p = 1\text{-}2 \text{ m}^{-2}$ ) and intracrystalline transport limitations were negligible, i.e., <1%. If liquids would be formed, the yield towards 1-alkenes and gasoline can be increased slightly, i.e., resp. to 5% and 46%, at a cost of propene production. However, this comes at the cost of having to apply much higher space-times, and hence use more catalyst to obtain a similar conversion level.

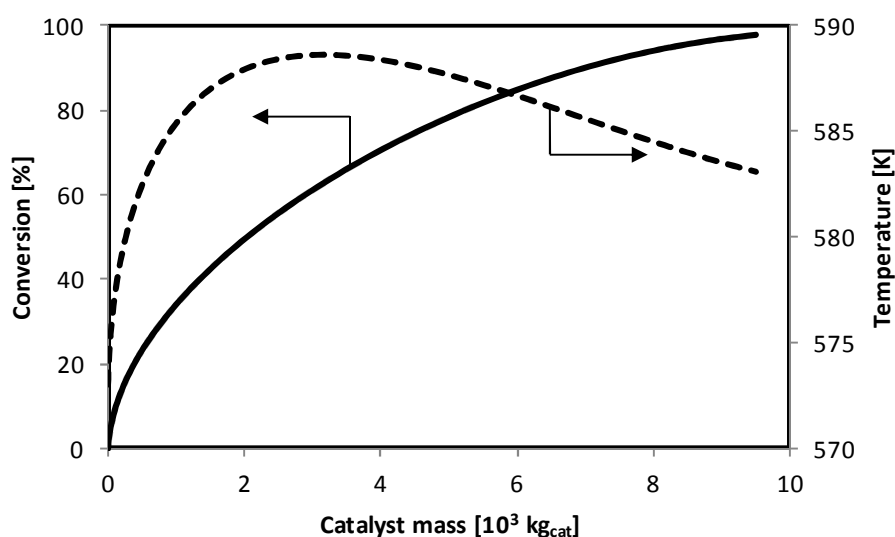


**Figure 6-23:** Ethene conversion (left axis) and reactor temperature (right) as function of the Ni-Beta catalyst mass, i.e., axial reactor coordinate as obtained using the simulation model for an adiabatic industrial oligomerization reactor, see equations 6-3, 6-6 and 6-14, at 573 K inlet temperature, 3.5 MPa inlet ethene pressure and an inlet ethene molar flow rate equal to  $37.2 \text{ mol s}^{-1}$

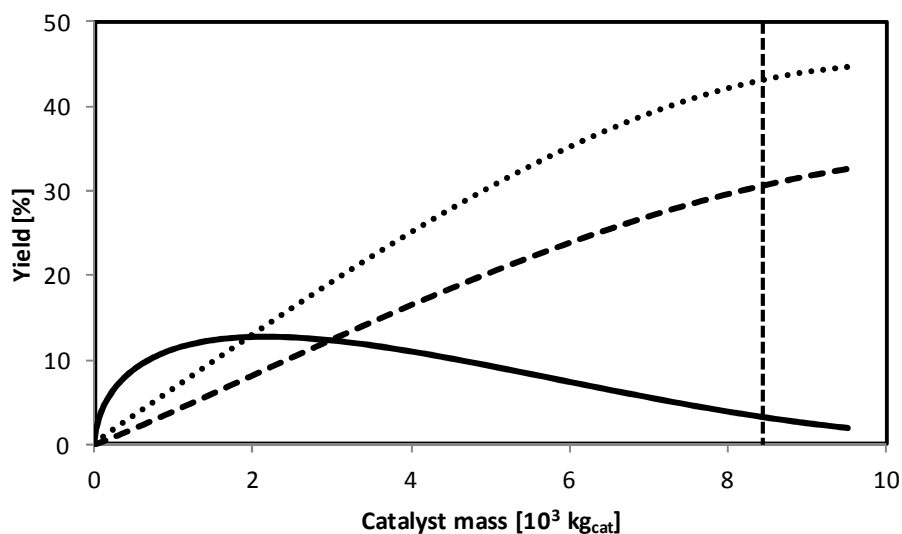


Figure 6-24: Product yield as function of the Ni-Beta catalyst mass, i.e., axial reactor coordinate as obtained using the simulation model for an adiabatic industrial oligomerization reactor, see equations 6-3, 6-6 and 6-14, at 573 K inlet temperature, 3.5 MPa inlet ethene pressure and an inlet ethene molar flow rate equal to  $37.2 \text{ mol s}^{-1}$ ; full line: 1-alkenes, dashed line: propene, dotted line: gasoline.

## 6.4 Conclusions

A model for simulating an industrial ethene oligomerization reactor was constructed. A microkinetics based scheme rather than a global kinetics one was implemented at the core of this model to gain more insight in the effect of varying reactor operation conditions and geometry on the observed kinetics. The reactor model is capable of simulating different reactor configurations, i.e., single versus multi fixed bed with interbed cooling and or heating, including reactor geometry, i.e., length and diameter. Also the effect of different heating regimes is accounted for: isothermal, adiabatic or heating exchanging. Intraparticle mass and heat transfer effects can be added to the simulation at the cost of CPU time. If expected, pressure drop effects and the influence of liquid formation can be included in the calculations. Also the catalyst properties can be adjusted, i.e., both physical, e.g., diameter and shape factor, concentration of active sites, etc., and chemical, e.g., physisorption enthalpy, etc.

Using a catalyst containing only Ni-ion sites as active sites, leads to an ASF product distribution but also to a high temperature increase when operating the reactor adiabatically. A bifunctional catalyst leads to a less pronounced temperature increase due to the occurrence of endothermic cracking reactions. Also the product distribution is distinctly different on a bifunctional catalyst compared to a monofunctional one with the formation of



highly branched and odd-carbon numbered products. The reactor geometry, i.e., length to diameter ratio, should be chosen wisely in order to minimize hot-spots if needed when operating in heat-exchanging mode and to avoid too large pressure drops. The formation of liquids can greatly enhance product yields in case a microporous, bifunctional catalyst is used. The liquids in the micropores are relatively easy transformed into propene and a gasoline fraction since this liquid fraction is enriched in heavy alkenes. The ethene conversion increases more moderately at such conditions, however. A final design for an industrial ethene oligomerization reactor was proposed based upon the requirements and operating window of the OCMOL project.

## 6.5 References

- [1] R.C. Reid, J.M. Prausnitz, B.E. Poling, *The Properties of Gases and Liquids* (4th ed.), 1988.
- [2] S.W. Benson, J.H. Buss, *Journal of Chemical Physics*. 29 (1958) 546-572.
- [3] M. Leva, *Chem. Eng.* 56 (1949) 115-124.
- [4] R.E. Hicks, *Industrial & Engineering Chemistry Fundamentals*. 9 (1970) 500-&.
- [5] D.P. Haughey, *Beveridg.Gs, Canadian Journal of Chemical Engineering*. 47 (1969) 130-&.
- [6] F. Larachi, A. Laurent, N. Midoux, G. Wild, *Chemical Engineering Science*. 46 (1991) 1233-1246.
- [7] R. Torres, J.C. de Hemptinne, I. Machin, *Oil & Gas Science and Technology*. 68 (2013) 217-233.
- [8] J. Wood, L.F. Gladden, F.J. Keil, *Chemical Engineering Science*. 57 (2002) 3047-3059.
- [9] M.H. Aldahhan, M.P. Dudukovic, *Chemical Engineering Science*. 50 (1995) 2377-2389.



# Chapter 7

## Catalyst Design for

## Ethylbenzene Dealkylation and

## Xylene Isomerization

---

In this chapter, a fundamental kinetic model of the single-event type (SEMK) is constructed for ethylbenzene dealkylation and xylene isomerization on a bifunctional catalyst, Pt/HZSM-5. It accounts for the acid-catalyzed reactions involved, i.e., (de-)protonation, intra- and intermolecular isomerization, resp. 1,2 methyl-shift and transalkylation, and hydrodealkylation, i.e.,  $\beta$ -scission, as well as for the metal catalyzed hydrogenation reactions.

### 7.1 Procedures

#### 7.1.1 Experimental conditions

The experimental dataset was obtained on a Pt/H-ZSM-5 zeolite as described in section 2.1.1.4 by Shell in a fixed bed reactor, see section 2.1.2.3. With the Si/Al ratio of the catalyst equal to 15, the concentration of the acid sites is calculated as  $1.7 \text{ mol kg}^{-1}$  [1]. The catalyst contained a minimal quantity of Pt to avoid deactivation by coking. However, these metallic sites also result in some, undesired, hydrogenation of the aromatic feed. The range of reaction conditions tested is give in Table 7-1. The temperature and pressure were varied between 623 and 673 K and 0.4 and 1.2 MPa. The feed flow contained metaxylene, orthoxylene, ethylbenzene and hydrogen, but no paraxylene. The ethylbenzene-

ortho-xylene-metaxylene (EB/OX/MX) molar feed ratio was equal to 0.18/0.35/1. The inlet molar feed ratio of hydrogen to aromatic components ranged from 1 to 5. The space time varied between 0.1 to 0.6 kg<sub>cat</sub> mol<sup>-1</sup> s.

**Table 7-1: Range of experimental conditions for xylene isomerization on Pt/H-ZSM-5**

Temperature [K]	Total pressure [MPa]	EB/OX/MX molar feed ratio [-]	H <sub>2</sub> to aromatic molar feed ratio [-]	Space time [kg <sub>cat</sub> s mol <sup>-1</sup> ]
623 – 673	0.4 – 1.2	0.18/0.35/1.00	1.0 – 0.5	0.1 – 0.6

### 7.1.2 Reactor model

Since the experiments have been performed in a set up comprising an ideal plug flow reactor and are also free of transport limitations at pellet scale, a 1-dimensional, isothermal and pseudo homogeneous reactor, see equation 2-21.

### 7.1.3 Definition of responses

In total, six representative responses are considered, i.e., the conversion of ethylbenzene, the selectivity for benzene, the conversion of xylene, the mass fraction of (produced) toluene, the mass fraction of the C<sub>9</sub>+ fraction and the approach to equilibrium for paraxylene production, each of these responses being affected by specific adjustable model parameters, see below.

The mass fraction of component  $i$ ,  $w_i$ , is calculated as follows:

$$w_i = \frac{F_i \cdot M_i}{\sum_{j=1}^{n_{comp}} F_j \cdot M_j} \quad 7-1$$

with  $M_j$  the molecular mass of component  $j$ .

The approach to equilibrium,  $ATE$ , of component  $i$  in lump  $B$  is defined as the approximation of the experimental molar outlet fraction of component  $i$  in lump  $B$  to the equilibrium molar outlet fraction of  $i$  in lump  $B$ . In this context, a lump is defined as a group of isomers.

$$ATE_{i,B} = \frac{\frac{F_i}{\sum_{j=1}^{n_{comp,B}} F_j}}{\frac{F_i^{eq}}{\sum_{j=1}^{n_{comp,B}} F_j^{eq}}} = \sum_{j=1}^{n_{comp,B}} K_{j,i} \frac{F_i}{\sum_{j=1}^{n_{comp,B}} F_j} \quad 7-2$$

with  $K_{j,i}$  the equilibrium coefficient between component  $j$  and  $i$ . In practice this  $ATE$  is calculated for paraxylene within the xylene mixture, i.e., excluding ethylbenzene.

## 7.2 Xylene isomerization on Pt/H-ZSM-5: proposed reaction network and observed behavior

ZSM-5 zeolites with significantly different properties and resulting catalytic behavior have been reported for a variety of chemical conversions. Among others, ZSM-5 is applied in processes such as methanol conversion to olefins, hydrocracking, xylene isomerization, amination, catalytic cracking... [2]. Depending on the feed to be converted, ZSM-5 type zeolites may exhibit pronounced shape selective properties due to their microporous structure consisting of 10-member sinusoidal rings with dimensions 5.1 by 5.5 nm and 5.3 by 5.6 nm [3]. Particularly for ethylbenzene dealkylation and xylene isomerization, high selectivities towards paraxylene have been reported for some ZSM-5 samples [4-8]. On other ZSM-5 samples near thermodynamic equilibrium for the xylene mixture was found to be established, making shape selectivity irrelevant in those cases [9]. The ZSM-5 zeolite investigated in the current work did not exhibit any evidence for shape selectivity towards paraxylene at the investigated operating conditions, i.e., the xylene outlet mixture almost approached thermodynamic equilibrium with an  $ATE$  of approximately 99%. As a result, no shape selectivity effects are accounted for in the model.

Due to the bifunctional character of the catalyst, both acid and metal catalyzed reactions have to be considered in the reaction network. However, the acid catalyzed reactions determine the effluent composition to a large extent. The following acid catalyzed

elementary reactions have been considered in a mixture consisting of xylene isomers and ethylbenzene: alkyl shift, transalkylation and dealkylation. The paring reaction has been proposed by Al-Khattaf as possible reaction pathway towards benzene and light alkenes, mainly propene [10]. However, in this work, ethane was the abundant light hydrocarbon originating from ethylbenzene dealkylation and C<sub>10+</sub> components were only formed to a minor extent [11]. Therefore, the paring reaction was not included in the reaction network. The most likely mechanism for ethylbenzene isomerization into xylenes consecutively requires aromatic hydrogenation, acid catalyzed isomerization and cycloalkane dehydrogenation [12]. Because aromatic hydrogenation was experimentally found to be of minor importance at the investigated conditions, ethylbenzene isomerization into xylenes was not considered. The molar outlet fraction of cycloalkanes is also low in comparison with the amount formed at thermodynamic equilibrium, i.e., 5-10%. In the paragraphs 7.2.1.1 to 7.2.1.4, the mechanisms of the reaction families considered in the network are discussed in some more detail. Paragraph 7.2.1.5 discusses the overall reaction network considered, including some constraints imposed on the considered components. In paragraph 7.2.2, the experimental observations are discussed.

## 7.2.1 Elementary steps and reaction network of xylene isomerization on Pt/H-ZSM-5

### **7.2.1.1 Alkyl shift**

In principle both methyl and ethyl shifts may occur within the elementary reaction family of the alkyl shifts. Both 1,2 and 1,3 alkyl shifts have been reported on H-ZSM-5 zeolites [13]. The experiments performed as part of the current work were at conditions where the thermodynamic equilibrium was approached for the xylene mixture. From the elementary reaction families considered in the overall network, alkyl shifts are the fastest and, hence, it is practically impossible to discriminate between 1,2 and 1,3 alkyl shifts. Because a 1,3 alkyl shift is equivalent with two consecutive 1,2 alkyl shifts it is sufficient to include the 1,2 alkyl shifts only. A schematic representation of an alkyl shift of a dialkyl substituted aromatic component is given in Figure 7-1.

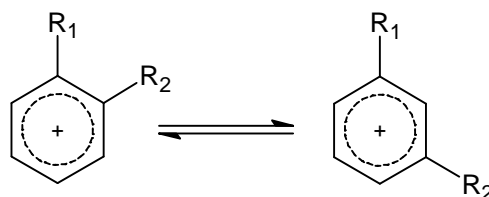


Figure 7-1: Schematic representation of alkyl shift of a dialkyl substituted aromatic component

### 7.2.1.2 Dealkylation

The dealkylation of ethylbenzene and xylenes can proceed either through an acid catalyzed mechanism or a metal catalyzed mechanism, i.e., hydrogenolysis. With the catalyst used and at the operating conditions considered, hydrogenolysis can be neglected [14]. Dealkylation of xylenes through acid catalysis can be neglected too. The extremely low stability of the product methyl ion results in huge activation energies for this elementary reaction family such that its contribution to the overall conversion is negligible. With respect to de-ethylation, which also involves a rather unstable primary carbenium ion, but less unstable than the methyl ion produced by de-methylation, it has been reported that the product alkene, i.e., ethylene, can be instantaneously hydrogenated to ethane in the presence of platinum and hydrogen [14]. A schematic overview of dealkylation of an alkyl substituted aromatic component is given in Figure 7-2.

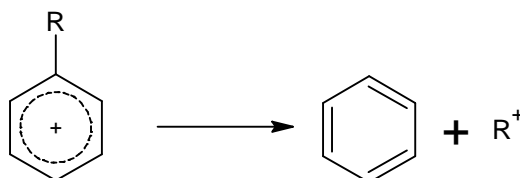


Figure 7-2: Schematic overview of dealkylation of an alkyl substituted aromatic component

### 7.2.1.3 Transalkylation

Within the transalkylation reaction family, i.e., intermolecular isomerization, a distinction is made between transmethylation and transethylation. Transmethylation is reported to occur at temperatures exceeding 573 K. Several mechanisms for transmethylation are described in the literature, the one proposed by Guisnet et al. [15] being the most accepted. In this bimolecular mechanism, an aromatic component interchanges a methyl group with an aromatic carbenium ion. Globally, the aromatic carbenium ion loses its charge and a methyl group which both migrate to the aromatic component. The formation of the benzylic carbocation intermediate is selected as the rate-determining step, which provided the most globally significant kinetic model. A schematic overview of transalkylation between two metaxylene molecules is given in Figure 7-3.

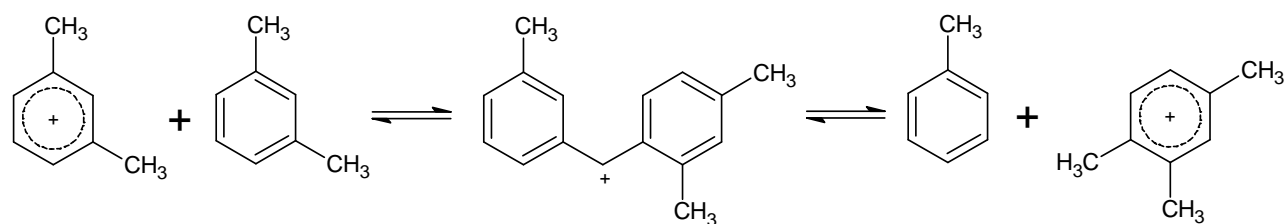


Figure 7-3: Schematic overview of transalkylation between two metaxylene molecules

Because of steric hindrance of the transition state in the medium sized pores of the catalyst, it can reasonably be assumed that transethylation can only occur via a dealkylation-realkylation route. Due to the rapid hydrogenation of the ethylene molecules formed [14], the reethylation step is very unlikely and, hence, trans-ethylation is neglected in the reaction mechanism. This is justified by the absence of diethyl benzene components in the reactor effluent.

#### 7.2.1.4 Hydrogenation

Hydrogenation of aromatic components only accounts for less than 1% of the conversion of the feed mixture. Hence, because the hydrogenation of aromatics is clearly not the major reaction family in the isomerization of xylene, this reaction is described using a conventional, literature reported Langmuir Hinshelwood/Hougen Watson type mechanism [16], see paragraph 7.3.2, rather than using the single-event methodology [17]. A schematic overview of the total hydrogenation of a dialkyl substituted aromatic component is given in Figure 7-4.

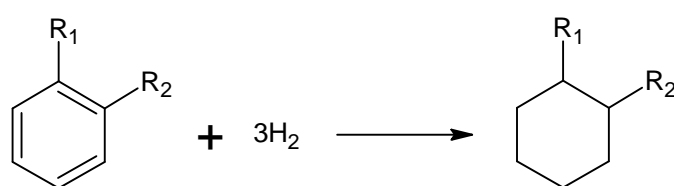


Figure 7-4: Schematic overview of the total hydrogenation of a dialkyl substituted aromatic component

#### 7.2.1.5 Overall reaction network

The reaction network is generated automatically by means of an in-house computer algorithm [18-20]. In this algorithm, the molecules are represented using matrices and arrays. Elementary reactions are represented by performing simple operations on the reactant matrices. The arrays form a simplified representation of the molecules used for storage of the automatically generated reaction network.



The reaction network is the result of a compromise between accounting for sufficient detail and limiting the extent of the network to what is relevant for the description of the observed data. Considering the discussions in the previous paragraphs, the following assumptions are made:

- a. alkyl shift (intramolecular isomerization, *ms*): only 1,2 methyl shifts are included and 1,3 methyl shift and ethyl shifts are neglected due to the experimental approximation of thermodynamic equilibrium between the xylene isomers. 1,2 ethyl shifts are not included, see f,
- b. dealkylation ( $\beta$ -scission, *da*): demethylation is neglected due to the very high instability of the methylcarbocations formed. Only de-ethylation is considered, with the ethylene formed instantaneously being hydrogenated into ethane,
- c. transalkylation (intermolecular isomerization, *ta*): transethylation is not accounted for due to steric hindrance of the transition state in the pores of H-ZSM-5. Only transmethylation is considered,
- d. hydrogenation (*hyd*): complete hydrogenation of the aromatic components is taken into account, i.e., no cycloalkenes are considered.

Some further assumptions are made in order to keep the size of the reaction network between reasonable limits and in accordance with the experimental observations:

- e. the aromatic components can have a maximum of three substituent groups, leading to a maximum carbon number equal to 10, e.g., 2-ethyl-metaxylene,
- f. only one ethyl substituent per component is allowed. As a result, all necessary alkyl shift isomerization reactions can be captured via 1,2 methyl shifts,
- g. endocyclic  $\beta$ -scissions are not implemented due to the high stability of the aromatic rings. Moreover, with respect to acyclic components in the reactor effluent, only the C<sub>2</sub> fraction which can be formed by exo-cyclic  $\beta$ -scission from ethylbenzene was considered,
- h. protonation and deprotonation of aromatic components are assumed to be in quasi-equilibrium,

- i. the isomerization of cycloalkanes, e.g., cyclohexane to methyl-cyclopentane, was also neglected.

In total, 1 alkane, 18 cycloalkanes, 18 aromatics and 78 aromatic carbenium ions are generated by 18 aromatic hydrogenations, 113 transalkylations, 78 (x2) aromatic (de-)protonations, 24 methyl shifts and 16 exocyclic  $\beta$ -scissions. The corresponding overall reaction network is graphically represented in Figure 7-5.

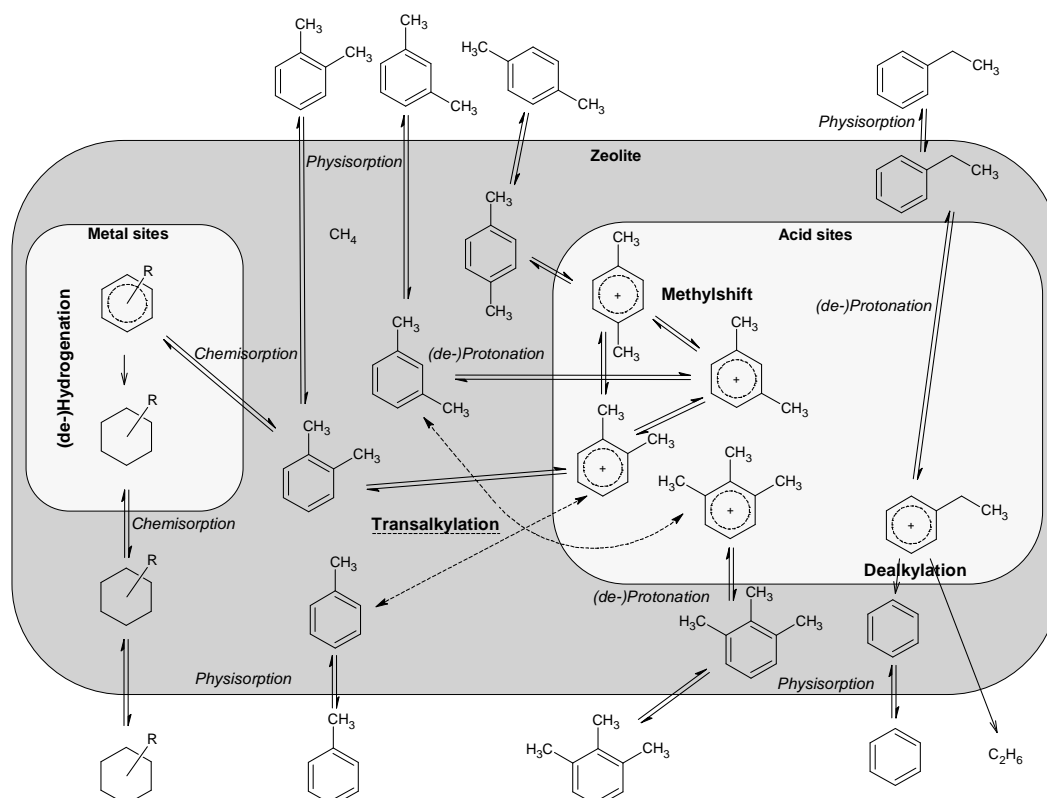


**Figure 7-5: Visual representation of the reaction network for xylene isomerization on a bifunctional catalyst. A gas phase aromatic component can physisorb on the catalyst surface followed by a possible interaction with either acid or metal sites. Depending on the nature of the active site, acid catalyzed isomerization or scission or metal catalyzed hydrogenation occurs. Products formed leave the active sites and desorb from the catalyst surface.**

## 7.2.2 Observed behavior of xylene isomerization on Pt/H-ZSM-5

In Table 7-2 the investigated inlet and correspondingly obtained outlet ranges of molar fractions are given. It follows from Table 7-2 that the relative importance of the reaction families is as follows: methyl shift > dealkylation >> transalkylation >> hydrogenation. Since almost no xylenes are lost and thermodynamic equilibrium within the xylenes is practically achieved, methyl shift reactions, i.e., intramolecular isomerizations, are identified as the

main reaction that is occurring. Ethylbenzene conversions range from 30 % up to near 100 %. As a result, also dealkylation is a very important reaction family, however, somewhat less important compared to methyl shifts given the lower ethylbenzene fraction in the feed than the xylenes fraction. Transalkylation, i.e., intermolecular isomerization and responsible for the xylene losses, only proceeds to a little extent, as evidenced by the low quantities formed of toluene and heavy components. From the reactions discussed above, hydrogenation is occurring to the lowest extent as this can be clearly seen by the very low molar outlet fractions of hydrogenated products, i.e., cycloalkanes. This hydrogenation activity is the result of a compromise between avoiding coke formation by hydrogenation of coke precursors and limiting aromatics, c.q., benzene, losses to cycloalkanes.

**Table 7-2: Molar fractions of the components at the inlet and the outlet of the reactor for xylene isomerization on a bifunctional Pt/H-ZSM-5 catalyst**

	$y^0$ [%]	$y_{min}^{outlet}$ [%]	$y_{max}^{outlet}$ [%]
$C_6H_6$	0.0	4.1	10.0
$C_7H_8$	0.0	0.3	3.7
EB	12.0	0.8	7.6
XYL (PX)	88.0 (0.0)	81.2 (18.4)	87.0 (19.7)
$C_9+$ (aro)	0.0	0.8	3.2
cyclohexane	0.0	0.2	1.1

### 7.3 The Single-Event MicroKinetic model for xylene isomerization on Pt/H-ZSM-5

Using the single-event concept, the number of rate coefficients required to describe the chemical kinetics in complex mixtures is reduced drastically, see section 2.4. In the case of aromatic components, the positive charge transferred by the active site towards the hydrocarbon reactant is assumed to be delocalized over the aromatic ring structure and, hence, no distinction is made between secondary and tertiary aromatic carbenium ions. Given the elementary reaction families considered as discussed in Section 7.2, these assumptions result in a total number of four single-event rate coefficients, i.e., one equilibrium coefficient for (de)protonation,  $\tilde{K}^{pr}$ , and three rate coefficients for methyl shifts,  $\tilde{k}^{ms}$ , transalkylation,  $\tilde{k}^{ta}$ , and dealkylation,  $\tilde{k}^{da}$ . For the hydrogenation kinetics, a

rate coefficient,  $k^{hyd}$ , is used in accordance with the literature proposed Langmuir Hinshelwood/Hougen Watson mechanism, see paragraph 7.3.2.

### 7.3.1 Acid-catalyzed reaction rates

By applying the law of mass action, the following expressions are obtained for the reaction rates of the acid catalyzed elementary reaction steps, i.e., methyl shift, dealkylation and transalkylation:

$$r_i^{ms/da} = n_{e(i)}^{ms/da} \tilde{k}^{ms/da} C_{A_i^+} \quad 7-3$$

$$r_{i,j}^{ta} = n_{e(i,j)}^{ta} \tilde{k}^{ta} C_{A_j} C_{A_i^+} \quad 7-4$$

The concentration of the aromatic carbenium ions is related to the concentration of the physisorbed aromatic components via a Langmuir expression for the (de-)protonation equilibrium in which  $C_{H_{tot}^+}$  represents the total concentration of acid sites.

$$C_{A_i^+} = \frac{C_{H_{tot}^+} K_{A_i}^{pr} C_{A_i}}{1 + C_{H_{tot}^+} K_{A_i}^{pr} C_{A_i}} \quad 7-5$$

The protonation coefficient of the component considered can be related to the protonation coefficient of a reference component via the isomerization coefficient between these two components [21]. This leads to the following expression for the concentration of protonated aromatics:

$$C_{A_i^+} = \frac{C_{H_{tot}^+} n_{e(i)}^{pr} K_{A_i, A_{ref}}^{iso} \tilde{K}_{A_{ref}}^{pr} C_{A_i}}{1 + C_{H_{tot}^+} n_{e(i)}^{pr} K_{A_i, A_{ref}}^{iso} \tilde{K}_{A_{ref}}^{pr} C_{A_i}} \quad 7-6$$

In turn, the concentration of physisorbed aromatic components on the zeolite surface is expressed through another Langmuir isotherm expressing the physisorption equilibrium, in which  $C^{sat}$  is the saturation concentration of the physisorbed component:

$$C_{A_i} = \frac{C^{sat} K_{A_i}^{phys} p_{A_i}}{1 + \sum_{j=1}^{n_{comp}} K_{A_j}^{phys} p_{A_j}} \quad 7-7$$

The Langmuir physisorption coefficient can be calculated as the ratio of the Henry coefficient  $H$  and the saturation concentration  $C^{sat}$  of the component considered:

$$K_{A_i}^{phys} = \frac{H_i}{C^{sat}} \quad 7-8$$

The Henry coefficient can be written as an Arrhenius type equation, see Eq. 7-9, in which the contribution of the entropy term and the saturation concentration is grouped as a pre-exponential factor,  $A^{phys}$ , see Eq. 7-10.

$$H = e^{\frac{\Delta S^{phys}}{R}} \cdot e^{-\frac{\Delta H^{phys}}{RT}} \cdot \frac{C^{sat}}{2 \cdot p^0} \quad 7-9$$

$$H = A^{phys} \cdot e^{-\frac{\Delta H^{phys}}{RT}} \quad 7-10$$

Normally, one physisorption coefficient per component has to be considered. However, as the individual components in the reaction network are structurally related, it is sufficient to introduce a single physisorption coefficient per carbon number. This leads to the following expression for the physisorbed aromatics concentration:

$$C_{A_i} = \frac{C^{sat} K_{A_i}^{phys} p_{A_i}}{1 + \sum_{a_c=6}^{10} K_{a_c}^{phys} \sum_{j=1}^{n_{comp}} p_{A_{j,a_c}}} \quad 7-11$$

The saturation concentration can be calculated via the method proposed section 5.3.2. Combining equations 7-3 to 7-11, expressions for the reaction rates for methyl shift, transalkylation and dealkylation can be obtained:

$$r_i^{ms/da} = n_{e(i)}^{ms/da} \tilde{k}^{ms/da} \frac{C_{H_{tot}^+} n_{e(i)}^{pr} K_{A_i, A_{ref}}^{iso} \tilde{K}_{A_{ref}}^{pr} \frac{C^{sat} K_{A_i}^{phys} p_{A_i}}{1 + \sum_{a_c=6}^{10} K_{a_c}^{phys} \sum_{j=1}^{n_{comp}} p_{A_{j,a_c}}}}{1 + C_{H_{tot}^+} n_{e(i)}^{pr} K_{A_i, A_{ref}}^{iso} \tilde{K}_{A_{ref}}^{pr} \frac{C^{sat} K_{A_i}^{phys} p_{A_i}}{1 + \sum_{a_c=6}^{10} K_{a_c}^{phys} \sum_{j=1}^{n_{comp}} p_{A_{j,a_c}}}} \quad 7-12$$

$$r_{i,k}^{ta} = n_{e(i,k)}^{ta} \tilde{k}^{ta} \frac{C^{sat} K_{A_k}^{phys} p_{A_k}}{1 + \sum_{a_c=6}^{10} K_{a_c}^{phys} \sum_{j=1}^{n_{comp}} p_{A_{j,a_c}}} \frac{C_{H_{tot}^+} n_{e(i)}^{pr} K_{A_i, A_{ref}}^{iso} \tilde{K}_{A_{ref}}^{pr} \frac{C^{sat} K_{A_i}^{phys} p_{A_i}}{1 + \sum_{a_c=6}^{10} K_{a_c}^{phys} \sum_{j=1}^{n_{comp}} p_{A_{j,a_c}}}}{1 + C_{H_{tot}^+} n_{e(i)}^{pr} K_{A_i, A_{ref}}^{iso} \tilde{K}_{A_{ref}}^{pr} \frac{C^{sat} K_{A_i}^{phys} p_{A_i}}{1 + \sum_{a_c=6}^{10} K_{a_c}^{phys} \sum_{j=1}^{n_{comp}} p_{A_{j,a_c}}}} \quad 7-13$$

### 7.3.2 Hydrogenation rate

For the hydrogenation kinetics, a rate equation of the Langmuir Hinshelwood/Hougen Watson type, as developed by Thybaut et al. [16], is used, see equation 7-17. Here, a rate-

determining step is implemented in the global hydrogenation mechanism, i.e., the  $i^{\text{th}}$  hydrogen addition.  $K_j$  represents the equilibrium coefficient for the atomic hydrogen addition on the Pt surface, for which the pre-exponential is set equal to 0.5 and the surface reaction enthalpy is calculated according to  $-2\Delta H_{H_2}^{\text{phys}} - 74 \text{ kJ mol}^{-1}$  as reported by Saeys et al. [22].

$$r_k^{\text{hyd}} = \frac{C_m k_i^{\text{hyd}} \left( \prod_{j=1}^i K_j \right) K_A^{\text{chem}} \left( K_{H_2}^{\text{chem}} \right)^{i/2} p_{A_k} p_{H_2}^{i/2}}{\left( 1 + K_A^{\text{chem}} \sum p_{A_k} + \sqrt{K_{H_2}^{\text{chem}} p_{H_2}} \right)^2} \quad 7-14$$

### 7.3.3 Net rates of formation

The net rate of formation of a component is calculated from the summation of the reaction rates of all elementary steps in which the components or the corresponding carbenium ions are produced or consumed:

$$R_{A_i} = \sum r_{A_i}^{\text{ms/da}} + \sum r_{A_i, Q}^{\text{ta}} + \sum r_{A_i}^{\text{hyd}} \quad 7-15$$

$$R_{\text{naft}_i} = \sum r_{A_i}^{\text{hyd}} \quad 7-16$$

$$R_{C_2} = \sum r_{A_i}^{\text{da}} \quad 7-17$$

## 7.4 Xylene isomerization on Pt/H-ZSM-5: kinetic modeling

### 7.4.1 Determination of the model parameters

In total, 3 single-event rate coefficients, 1 hydrogenation rate coefficient and 1 (de-)protonation equilibrium coefficient need to be determined:

$$K^{\text{pr}} = e^{\frac{\Delta S^{\text{pr}}}{R}} e^{\frac{\Delta H^{\text{pr}}}{RT}} = e^{\frac{-(\Delta S^{\text{trans}} + \Delta S^{\text{phys}})}{R}} e^{\frac{\Delta H^{\text{pr}}}{RT}} \quad 7-18$$

$$\tilde{k}^{\text{ms/ta/da}} = A^{\text{ms/ta/da}} e^{\frac{E_a^{\text{ms/ta/da}}}{RT}} C_{H_{\text{tot}}^+} \quad 7-19$$

$$k^{\text{hyd}} = A^{\text{hyd}} e^{\frac{E_a^{\text{hyd}}}{RT}} C_m \quad 7-20$$

With respect to the hydrogenation mechanism, rate equations with the different surface hydrogen addition reactions as the rate-determining step have been tested. With respect to the kinetic descriptors, the pre-exponential factors are calculated based on transition state

theory and making judicious assumptions on the differences in mobility of the species involved as reactant and transition state, see paragraph 7.4.1.1. The activation energies of the elementary reaction families are estimated from regression, see paragraph 7.4.1.3. As for the catalyst descriptors, the parameters used for the physisorption equilibrium are determined based on reported values, see paragraph 7.4.1.2, and the protonation enthalpy is estimated from regression, see paragraph 7.4.1.3.

#### 7.4.1.1 Calculation of the pre-exponential factors

The pre-exponential factors are calculated from transition state theory [23]:

$$A = \frac{k_B T}{h} e^{-\frac{\Delta S^\ddagger}{R}} \quad 7-21$$

with  $k_B$  the Boltzmann constant and  $h$  the Planck constant. By assessing the entropy difference between the reacting species and that in the transition state, a priori values can be obtained for the pre-exponential factors.

For methyl shift reactions, only the internal migration of a methyl group occurs which can reasonably be assumed not to affect the entropy. Hence, no global change in the number of degrees of freedom or entropy needs to be accounted for:

$$A^{ms} = \frac{k_B T}{h} \quad 7-22$$

During dealkylation, the elongation of the bond which is breaking can be regarded as a gain in entropy corresponding to one translational degree of freedom, which is in agreement with assumptions made in previous work for acyclic  $\beta$ -scissions [23].

$$A^{da} = \frac{k_B T}{h} e^{\frac{\Delta S^{trans}}{3R}} \quad 7-23$$

For transalkylation, a physisorbed aromatic component is coupled with an aromatic carbenium ion. During the formation of the transition state, the physisorbed molecule loses all remaining degrees of freedom, which corresponds to the protonation entropy  $\Delta S^{pr}$  and can be calculated as  $\Delta S^{trans} - (-\Delta S^{phys})$  while one translational degree of freedom is gained by the elongation of the new bond between the two molecules:

$$A^{ta} = \frac{k_B T}{h} e^{-\frac{(\Delta S^{trans} + \Delta S^{phys}) + \frac{\Delta S^{trans}}{3}}{R}} \quad 7-24$$

In Table 7-3, the calculated pre-exponential factors at 623 K are given. Because of the entropy gain during dealkylation, the corresponding pre-exponential factor is several orders of magnitude larger than the other pre-exponential factors. The net entropy loss during transalkylation results in a comparatively smaller pre-exponential factor.

**Table 7-3: Calculated pre-exponential factors for methyl shift, dealkylation and transalkylation using equations 7-22 to 7-24 at 623.15K.**

Pre-exponential factor	Calculated value
$A^{ms} [s^{-1}]$	$7.94 \cdot 10^{13}$
$A^{da} [s^{-1}]$	$3.74 \cdot 10^{18}$
$A^{ta} [mol \cdot kg_{cat}^{-1} \cdot s^{-1}]$	$1.69 \cdot 10^{12}$

For hydrogenation, the pre-exponential factors, i.e., for the chemisorption of hydrogen and an aromatic and the hydrogenation step, are taken from literature [16] and are given in Table 7-4.

**Table 7-4: Pre-exponential factors for the hydrogenation kinetics based on a Langmuir Hinshelwood/Hougen Watson type rate equation as used in the kinetic model for xylene isomerization on a bifunctional Pt/H-ZSM-5 catalyst [16]**

Pre-exponential factor	
$K_A^{chem}$	$1.0 \cdot 10^{-12} [Pa^{-1}]$
$K_{H_2}^{chem}$	$1.0 \cdot 10^{-10} [Pa^{-1}]$
$k^{hyd}$	$1.0 \cdot 10^{15} [s^{-1}]$

#### 7.4.1.2 Calculation of the physisorption parameters

The physisorption enthalpy was calculated using experimental values as reported by Denayer [24], see Table 7-5. It is assumed that the difference in physisorption enthalpy, between a *n*-alkane and the aromatic component with the same carbon number on a ZSM-5 zeolite is equal to the difference in physisorption enthalpy between these two components on a USY zeolite. Using this method, the physisorption enthalpies of benzene, toluene and xylene on ZSM-5 are calculated, see Table 7-5. The value for the physisorption enthalpy of benzene on ZSM-5 is close to what is calculated using quantum mechanical methods, i.e., 79 kJ mol<sup>-1</sup> [25]. The physisorption enthalpies of C<sub>9</sub>H<sub>12</sub> and C<sub>10</sub>H<sub>14</sub> on ZSM-5 were obtained by linearly extrapolating the values obtained for the lower carbon number compounds.



**Table 7-5: Physisorption enthalpies for linear alkanes and aromatic components on USY and ZSM-5 zeolite. Physisorption enthalpies for linear alkanes on USY and ZSM-5 zeolite and for aromatics on USY zeolite are reported by Denayer [24]. Physisorption enthalpies for aromatics on ZSM-5 as used in the kinetic model for xylene isomerization on a bifunctional Pt/H-ZSM-5 catalyst are calculated via (\*) and (\*\*).**

	$\Delta H^{phys}$ [kJ mol <sup>-1</sup> ]		$\Delta H^{phys}$ [kJ mol <sup>-1</sup> ]		
	USY [24]	ZSM-5 [24]	USY [24]	ZSM-5 (used in the model)	
<i>n</i> -C <sub>6</sub>	43.3	68.8	C <sub>6</sub> H <sub>6</sub>	50.2	75.7 <sup>(*)</sup>
<i>n</i> -C <sub>7</sub>	50.3	79.6	C <sub>7</sub> H <sub>8</sub>	58.4	87.7 <sup>(*)</sup>
<i>n</i> -C <sub>8</sub>	56.5	90.7	C <sub>8</sub> H <sub>10</sub>	63.6	97.8 <sup>(*)</sup>
			C <sub>9</sub> H <sub>12</sub>	-	109.2 <sup>(**)</sup>
			C <sub>10</sub> H <sub>14</sub>	-	120.2 <sup>(**)</sup>

\* Calculated via:  $\Delta H_{TOL, ZSM-5}^{phys} = \Delta H_{n-C_7, ZSM-5}^{phys} + \left( \Delta H_{TOL, USY}^{phys} - \Delta H_{n-C_7, ZSM-5}^{phys} \right)$

\*\* Calculated via linear extrapolation

The pre-exponential factor for physisorption,  $A^{phys}$ , is calculated from the physisorption entropy, see equations 7-9 and 7-10. The latter is determined assuming that one degree of freedom is lost during physisorption, see section 4.4.1.1. The calculated pre-exponential factors are slightly lower than those reported by Denayer on a Y zeolite [24], resulting from a more negative physisorption entropy, i.e., more stabilization, in a medium pore zeolite, e.g., ZSM-5, than in a large pore zeolite, e.g., Y.

#### 7.4.1.3 Estimation of the activation energies and protonation enthalpy

In total, 5 parameters are to be estimated by regression, i.e., the protonation enthalpy ( $\Delta H^{pr}$ ) for the aromatic carbenium ion formation, the activation energies for methyl shift ( $E_a^{ms}$ ), dealkylation ( $E_a^{da}$ ), transalkylation ( $E_a^{ta}$ ) and the activation energy for hydrogenation ( $E_a^{hyd}$ ). Initial guesses for these model parameters have been obtained from the literature [22, 26-28] and lead to a reasonable agreement between experimentally observed and model calculated responses. The chemisorption enthalpies for aromatics and hydrogen on the metallic sites are taken from literature [16] and are not adjusted during the data regression.

The estimated parameter values, along with the corresponding  $t$  values are reported in Table 7-6.

**Table 7-6: Parameter estimates with their 95% confidence intervals and corresponding  $t$  and  $F$  values obtained after regression of the kinetic model of xylene isomerization to the experimental data obtained on a bifunctional Pt/H-ZSM-5 catalyst in which for the hydrogenation kinetics the first hydrogen addition is taken as the rate determining step ( $i=1$ ). Literature reported values and ranges are included for comparison. The model consists of the reactor model (equation 2-21), the reaction rate equations (equations 7-12 to 7-14) and the net rates of formation (equations 7-15 to 7-17). Values denoted with \* are taken from literature and are not estimated.**

	Estimated value ( $i=1$ )[kJ mol <sup>-1</sup> ]	$t$ value	Reported value [kJ mol <sup>-1</sup> ]
$\Delta H^{pr}$	$-86.8 \pm 3.3$	26.1	-60 to -100 [28]
$E_a^{ms}$	$138.4 \pm 3.2$	43.4	132 [26]
$E_a^{da}$	$198.4 \pm 3.1$	63.6	-
$E_a^{ta}$	$129.1 \pm 3.2$	40.4	112 to 121, 139 [27]
$E_a^{hyd}$	$72.6 \pm 0.6$	115.9	75 [22]
$\Delta H_A^{chem}$	*	-	70 [16]
$\Delta H_{H_2}^{chem}$	*	-	42 [16]
$F_s$ value	$2.97 \cdot 10^4$	Tabulated $F_s$ value	3.20
		Tabulated $t$ value	1.976

The  $F_s$  value for the global significance of the regression is much higher than the tabulated value, implying that the regression is globally significant. In addition, each of the individual parameters is estimated significantly as evidenced by their  $t$  values, see Table 7-6. A rather strong correlation is obtained between the activation energies of all acid catalyzed reactions, most probably via the standard protonation enthalpy. The highest absolute correlation, amounting to 0.999 is obtained between the protonation enthalpy and the dealkylation activation energy. Such a value can be understood from the catalytic cycle in which ethylbenzene undergoes dealkylation into benzene and ethane. At the investigated operating conditions, this is a practically irreversible reaction in which a surface intermediate formed by protonation ( $\Delta H^{pr}$ ) reacts through dealkylation ( $E_a^{da}$ ). If the simulated surface concentration becomes higher because of a more negative protonation enthalpy, the dealkylation activation energy will compensate for this by becoming higher. Moreover, the activation energy for dealkylation is the only adjustable parameter that is exclusively related to the ethylbenzene conversion response. The high correlation coefficients between the protonation enthalpy and the activation energies for methyl shift

and transalkylation are explained in a similar way. However, since these activation energies are related to several responses and because the reactions concerned are reversible, the correlation between these activation energies and the protonation enthalpy is somewhat less pronounced. When the protonation enthalpy is not adjusted by regression, the correlation between the activation energies of the acid catalyzed reactions completely disappears, see Table 7-7.

**Table 7-7: Correlation coefficient matrix from the regression of the experimental data to the proposed kinetic model for xylene isomerization on a bifunctional Pt/H-ZSM-5 catalyst. The model consists of the reactor model (equation 2-21), the reaction rate equations (equations 7-12 to 7-14) and the net rates of formation (equations 7-15 to 7-17). The protonation enthalpy not included as estimated parameter.**

	$E_a^{ms}$	$E_a^{da}$	$E_a^{ta}$	$E_a^{hyd}$
$E_a^{ms}$	1.00	0.07	0.10	-0.02
$E_a^{da}$	0.07	1.00	0.35	-0.40
$E_a^{ta}$	0.10	0.35	1.00	-0.67
$E_a^{hyd}$	-0.02	-0.40	-0.67	1.00

## 7.4.2 Kinetic model performance

The parity diagrams for each of the responses described in section 7.1.3, i.e., the conversion of ethylbenzene and xylene, the selectivity of ethylbenzene towards benzene, the molar outlet flow of toluene and C<sub>9</sub>+-aromatic components and the approach to equilibrium for paraxylene, are given in Figure 7-6.

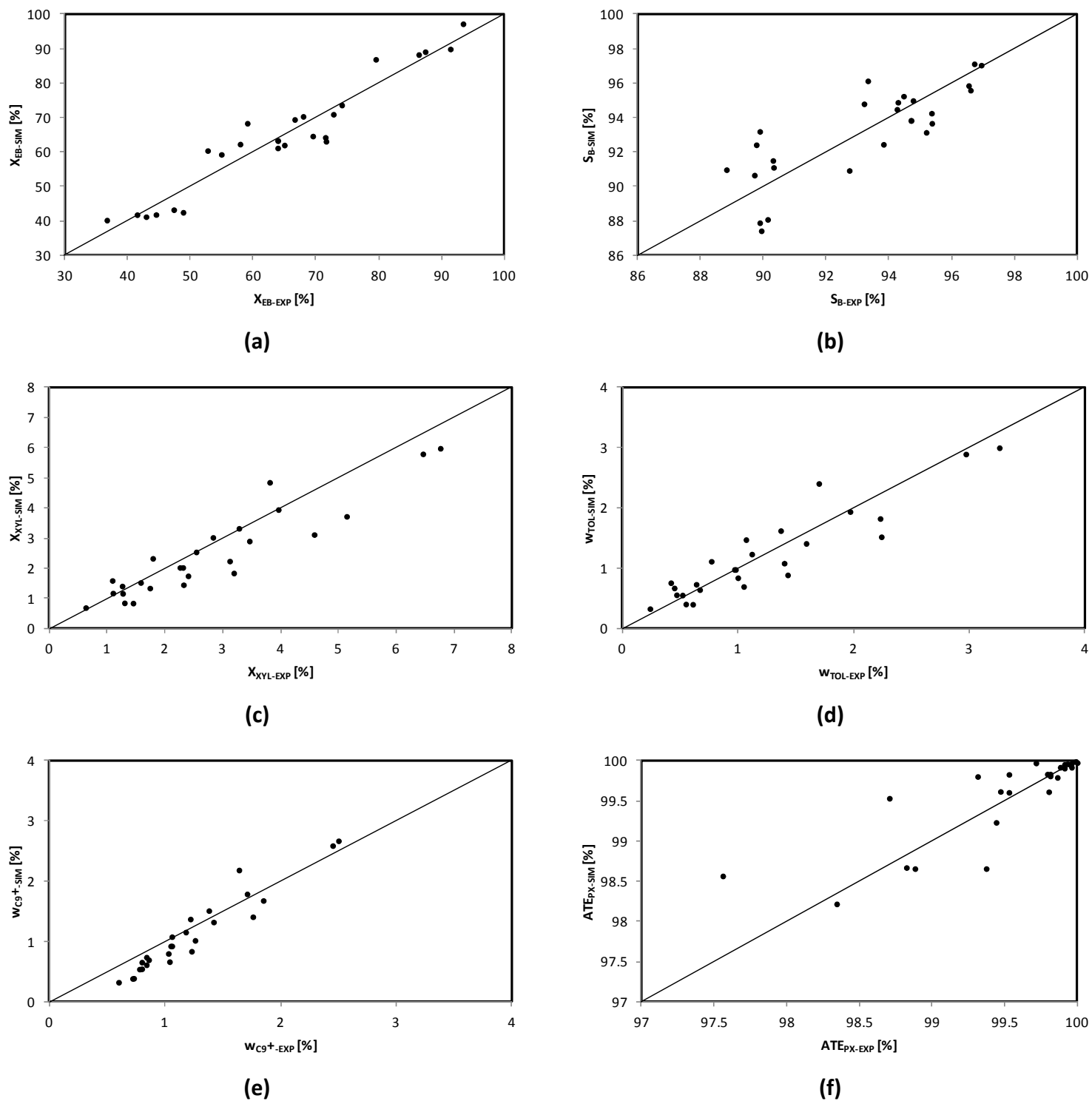


Figure 7-6: Parity diagrams for the responses of the kinetic model for xylene isomerization on a bifunctional Pt/H-ZSM-5 catalyst: conversion of ethylbenzene (a), benzene selectivity (b), conversion of xylene (c), mass fraction of toluene (d), mass fraction of  $C_9+$ -components (e) and approach to equilibrium (ate) of paraxylene (f). The parity diagrams are obtained using equations 1 to 4 with the molar outlet flow rates determined by the kinetic model consisting of the reactor model (equation 2-21), the reaction rate equations (equations 7-15 to 7-17) and the net rates of formation (equations 7-18 to 7-20). See Table 7-6 for the estimated parameter values and their 95% confidence interval.

Since the ethylbenzene conversion is affected most directly by dealkylation and this activation energy is estimated significantly, the corresponding response is modeled well. The same holds for the approach to equilibrium for paraxylene by isomerization. This response mostly depends on the intramolecular isomerization, for which the activation energy is estimated highly significant. The xylene conversion and mass fraction of toluene and C<sub>9</sub>+fractions are directly related to transalkylation. The first two are modeled in satisfactory manner, while the slight systematic deviation in the latter, i.e., underpredicted at low values and overpredicted at high values, can be attributed to the restrictions made within the reaction network, i.e., the maximum carbon number and the intermolecular isomerization in which only methyl transfer was considered and no ethyl transfer was allowed. Shape selectivity effects induced by the pore geometry on the large structures involved in intermolecular isomerization also constitute a possible cause. The benzene selectivity is described within an allowable range of uncertainty, regarding the global rate equation that has been used for describing the hydrogenation kinetics.

## 7.5 Discussion

All parameter estimates, i.e., activation energies and protonation enthalpy, are in agreement with literature reported values. The protonation enthalpy, -86.8 kJ mol<sup>-1</sup>, lies within the range for unsaturated hydrocarbons within zeolites, between -60 kJ mol<sup>-1</sup> and -100 kJ mol<sup>-1</sup>, as reported by Demuth et al [28]. The activation energy for methyl shift, 138.4 kJ mol<sup>-1</sup>, approaches the DFT calculated value for xylene isomerization 132 kJ mol<sup>-1</sup>, as reported by Choe [26]. For transalkylation, the activation energy of 129.1 kJ mol<sup>-1</sup> is close to the range as proposed by Clarck et al., i.e., 112 kJ mol<sup>-1</sup> to 121 kJ mol<sup>-1</sup> which was obtained by assuming a diphenylmethane-mediated reaction pathway [27]. The same authors also proposed a methoxide-mediated reaction pathway for which an activation energy of 139 kJ mol<sup>-1</sup> was obtained. The activation energy for hydrogenation, i.e., 72.6 kJ mol<sup>-1</sup>, is very close to the reported value by Saeys et al., i.e., 75 kJ mol<sup>-1</sup> [22].

In contrast to the order of the relative importance for the reactions, see paragraph 7.2.2, the following order of the activation energies has been obtained, see Table 7-6: dealkylation >> methyl shift > transalkylation >> hydrogenation. Qualitatively, these activation energies follow a logical order, i.e., dealkylation requires the highest activation energy due to the

bond cleavage between the side chain and the aromatic ring and the formation of a rather unstable ethylcarbenium ion, with an activation energy amounting to 198.4 kJ mol<sup>-1</sup>. The activation energy for transalkylation is slightly lower than the activation energy for methyl shift.

The difference in ranking of the reactions according to the relative importance or to the activation energies is explained by major differences in the pre-exponential factors, see Table 7-8. The activation energy of dealkylation largely exceeds that of methyl shift. However, the entropy gain in the case of dealkylation compared to the identical entropy of the transition state and the reactant in the case of a methyl shift leads to a significantly higher pre-exponential factor for dealkylation than for methyl shift, finally resulting in comparable reaction rates at the investigated operating conditions. Similarly, the difference in importance between methyl shift and transalkylation is explained. During the formation of the transition state of transalkylation, entropy is lost, resulting in a pre-exponential factor which is about 10<sup>5</sup> times lower than the pre-exponential factor of methyl shift. The low reaction rate for hydrogenation can be explained by the minor amount of metal sites compared to the total concentration of acid sites. The ethylene formed by ethylbenzene dealkylation is also strongly competing with the aromatics for the metal sites on the Pt surface. Moreover, the investigated temperature range in this work is far beyond that in which a maximum hydrogenation rate can be expected [16].

**Table 7-8: Relative pre-exponential factors as determined in the kinetic model for xylene isomerization on a bifunctional Pt/H-ZSM-5 catalyst, linked to the changes in entropy during the formation of the transition state**

	state	
	$\Delta S$	$A$
DA	> 0	$10^5 A_{\text{ref}}$
MS	0	$A_{\text{ref}}$
TA	< 0	$10^{-5} A_{\text{ref}}$
HYD	-	$10^{-6} A_{\text{ref}}$

The best regression results have been obtained assuming the first hydrogen addition to be rate determining, with an  $F_s$  value over 10<sup>4</sup>. This result is clearly different from the results obtained by Thybaut et al. [16] who have found the 3<sup>rd</sup> or the 4<sup>th</sup> surface hydrogen addition step to be rate determining. This apparent contradiction may be explained, however, by differences in catalytic material and, mainly, in operating conditions used. The hydrogen to hydrocarbon inlet molar ratio is rather low, i.e., 1 to 4, compared to 5 to 10 in [16]. More

importantly, the temperature is much higher, i.e., 623 to 673 K in this work compared to 423 to 498 K previously in [16]. This temperature effect will result in lower surface concentrations of the reactive intermediates and can result in a forward shift of the rate-determining step in the hydrogenation reaction mechanism as evidenced by the evolution of the hydrogen partial reaction order with the temperature [16]. Also, the competition between ethylene and aromatics for hydrogenation on the metal sites could be contributing to this observation.

## 7.6 Identification of an optimal catalyst for xylene isomerization

Having determined the kinetic and the catalyst descriptor values with the SEMK model for xylene isomerization, the latter descriptors can be the subject of a performance optimization while the kinetic descriptors are inherent to the elementary reaction families considered and, hence, invariable. By investigating the effect of the catalyst descriptors on the simulated performance, an optimized catalyst can be identified. The protonation enthalpy is taken as the most relevant catalyst descriptor to vary. It corresponds with the acid strength of the active sites. Whereas, for the present case, not assuming any shape selectivity effects, the physisorption properties can reasonably be assumed not to vary much with the Si/Al ratio of the zeolite considered [29], the acid strength of the active sites, quantified by the standard protonation enthalpy, will evolve with this Si/Al ratio as will the total acid site concentration. Because a change in the acid site concentration can be compensated by a change in the space time, it is the effect of the protonation enthalpy that has been investigated in a wide range from  $-60 \text{ kJ mol}^{-1}$  to  $-110 \text{ kJ mol}^{-1}$ , which includes the value obtained by regression, i.e.,  $-86.8 \text{ kJ mol}^{-1}$ , see Table 7-6. The reaction conditions used in the simulation are given in Table 7-9.

**Table 7-9: Reaction conditions used in the investigation of the effect of the protonation enthalpy and the total acid site concentration on the simulated catalyst performance. The model consists of the reactor model (equation 2-21), the reaction rate equations (equations 7-15 to 7-17) and the net rates of formation (equations 7-18 to 7-20). All parameter estimates, except the value for the protonation enthalpy, from Table 7-6 are used as input for the simulations.**

$F_{MX}^0$ [mol s <sup>-1</sup> ]	4.73 10 <sup>-3</sup>
$F_{OX}^0$ [mol s <sup>-1</sup> ]	1.67 10 <sup>-3</sup>
$F_{EB}^0$ [mol s <sup>-1</sup> ]	0.87 10 <sup>-3</sup>
T [K]	633–673
p [MPa]	1.00
$W / F_{C_8H_{10}}^0$ [kg <sub>cat</sub> mol <sup>-1</sup> s]	0.14

The three most relevant responses have been considered, i.e., the approach to equilibrium for paraxylene, the benzene yield and the xylene conversion. It is clear that the first two responses are to be maximized while the last is to be minimized. Hence, a profit function  $\Psi$  is defined, as the product of the benzene yield and the approach to equilibrium for paraxylene divided by the xylene conversion. The evolution of the three response values as well as of the profit function with the protonation enthalpy is given in Figure 7-7 at three different temperatures. For the approach to equilibrium for paraxylene, see Figure 7-7a, a threshold standard protonation enthalpy of about -70 kJ mol<sup>-1</sup>, is needed to initiate the xylene isomerization and between -80 to -85 kJ mol<sup>-1</sup> is required to reach the equilibrium. With increasing temperature, isomerization will occur at the same rate with slightly less negative standard protonation enthalpies to reach the same approach to equilibrium for paraxylene.



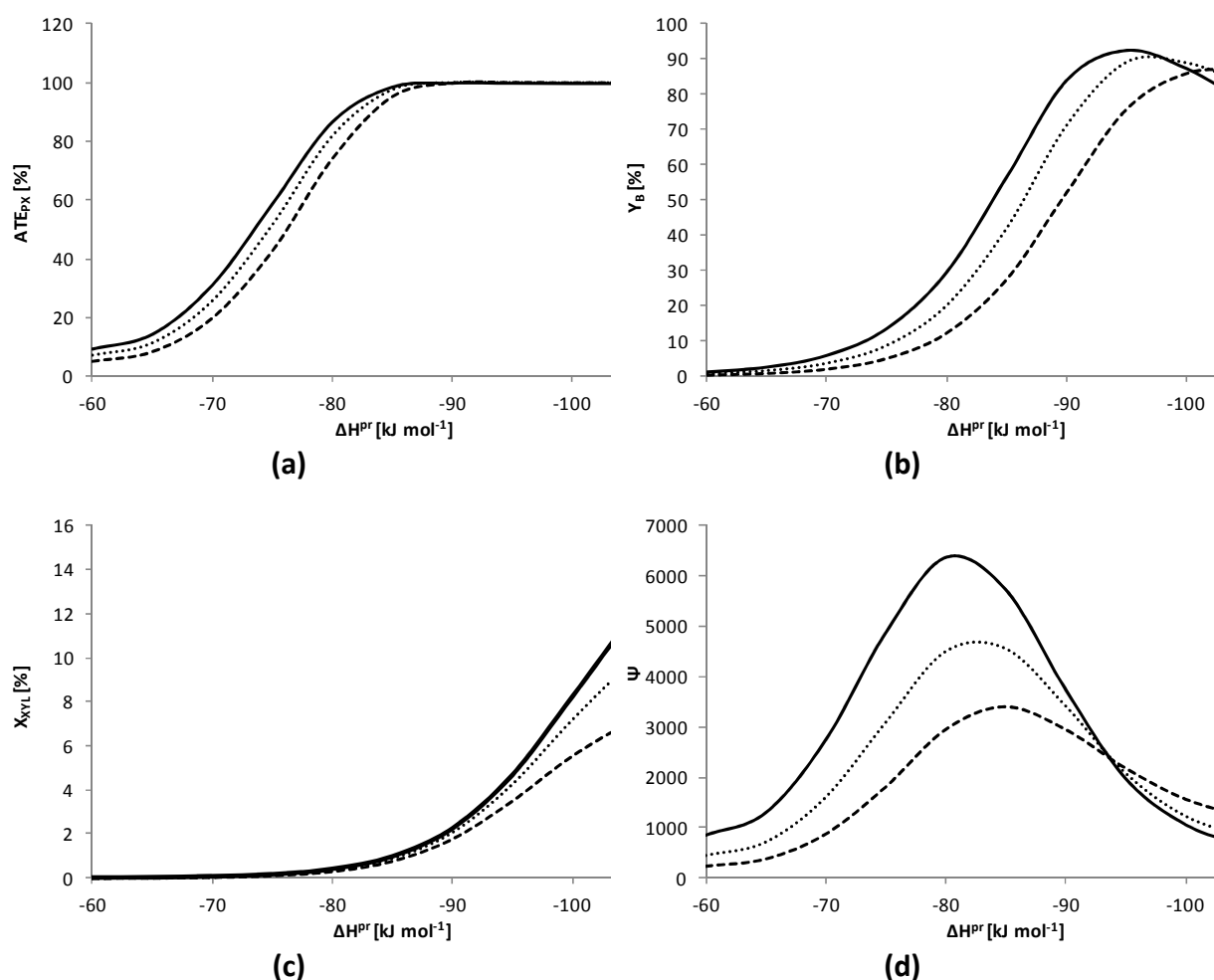


**Figure 7-7: Simulated approach to equilibrium for paraxylene (a), benzene yield (b), xylene conversion (c) and profit function  $\Psi=ab/c$  (d) as function of protonation enthalpy at the reaction conditions as defined in Table 7-9. Full line: at 673 K and 1.0 MPa; dotted line: at 653 K and 1 MPa; dashed line: 633 K and 1.0 MPa.**

With increasing acid strength of the sites, i.e., more negative standard protonation enthalpies, the benzene yield is increasing mainly due to the increase of the conversion of ethylbenzene to benzene by dealkylation, see Figure 7-7b. However, a maximum around -90 to -100  $\text{kJ mol}^{-1}$  is reached. Increasing the acid strength of the sites even more, results in a decrease of the benzene yield, because side reactions such as transalkylation are becoming more important. Analogous as with the approach to equilibrium for paraxylene, an increase of the reaction temperature requires less strong acid sites, i.e., less negative standard protonation enthalpies, to have the same benzene yield. Because of the higher activation energy for dealkylation than for isomerization, this simulated temperature effect is more pronounced.

For the conversion of xylenes, due to transalkylation reactions, a threshold standard protonation enthalpy between  $-90$  to  $-100$   $\text{kJ mol}^{-1}$  is required to initiate xylene, i.e., in the same range of standard protonation enthalpies for which a maximum is obtained in the benzene yield, see Figure 7-7c. Again, increasing the temperature results in the same level of conversion of xylene with weaker acid sites.

All these observations are combined in the profit function  $\Psi$ , which is visualized in Figure 7-7d. On a catalyst with only weak acid sites, corresponding to a protonation enthalpy less negative than  $-60$   $\text{kJ mol}^{-1}$ , few activity is observed corresponding to a low profit. With increasing acid strength of the active sites, corresponding to standard protonation enthalpies between  $-60$  and  $-80$   $\text{kJ mol}^{-1}$ , the profit function increases because both the approach to equilibrium and the benzene yield increase, while the xylene conversion remains practically negligible. At the investigated operating conditions, with even stronger acid sites, corresponding to standard protonation enthalpies beyond  $-80$  to  $-85$   $\text{kJ mol}^{-1}$ , xylene conversion becomes non-negligible, leading to a decrease of the profit function. At even more negative standard protonation enthalpies, below  $-90$   $\text{kJ mol}^{-1}$ , also the benzene yield decreases, leading to an even more pronounced decrease of the profit function  $\Psi$ . The maximum in the profit function significantly increases with the reaction temperature. It is a consequence of the significantly higher activation energy for dealkylation, compared to transalkylation. The activation energy of the latter reaction is comparable to that of the isomerization and, hence, no important temperature effect on isomerization versus transalkylation is simulated. The use of higher temperatures, i.e.,  $673$  K, combined with a catalysts having acid sites of moderate strength, i.e., standard protonation enthalpies between  $-80$  and  $-85$   $\text{kJ mol}^{-1}$  are identified as leading to the optimal xylene isomerization and ethylbenzene dealkylation behavior. The present catalyst, with an estimated standard protonation enthalpy amounting to  $-86.8$   $\text{kJ mol}^{-1}$ , see Table 7-6, is very close to this optimal range.

In the present example, the set of variable catalyst descriptors does not include shape selectivity descriptors, which severely restricts the ability to *tune* the catalyst. The use of shape selective catalyst, e.g., ZSM-22 or other ZSM-5 samples, would give a much greater flexibility to increase the selectivity towards the valuable products [30], but goes beyond the scope of the present thesis.

## 7.7 Conclusions

A fundamental Single-Event MicroKinetic (SEMK) model has been constructed for industrial “ethylbenzene dealkylation / xylene isomerization” on a Pt/H-ZSM-5 catalyst. The model is able to adequately reproduce the experimental observations in terms of ethylbenzene conversion, xylenes conversion, benzene selectivity, toluene and C<sub>9+</sub> mass fraction, approach to equilibrium. All model parameters are statistically and physically significant, i.e., the obtained estimates are in line with literature reported values.

The overall product distribution is mainly governed by methyl shift and dealkylation reactions while xylene losses via transalkylation and hydrogenation are minimal. The relative importance of the various reaction families is confirmed by the obtained activation energies and pre-exponential factors. The high activation energy for dealkylation is compensated by a high pre-exponential factor, leading to a rate coefficient which is comparable to that of methyl shift at the considered operating conditions. Transalkylation, on the other hand, has a much lower pre-exponential factor than the methyl shift due to the net entropy loss during transition state formation resulting in a lower rate coefficient. The lesser extent of the hydrogenation reactions is attributed to the limited number of Pt metal sites as well as to the high temperature and correspondingly low surface concentration of the reactive intermediates. Also the competition between ethylene and the aromatics for the Pt metal sites may contribute to this phenomenon.

The application of the SEMK methodology towards xylene isomerization and ethylbenzene dealkylation illustrates its versatility in the assessment of complex reaction kinetics in general and that of acid catalyzed reactions in particular. A limited effort on the extension of the methodology suffices for the development of an adequate model that can be used in the simulation of industrial reactors and/or the design of new and improved catalysts was shown. Catalysts with acid sites of moderate strength and used at higher temperatures optimize the isomerization and dealkylation behavior versus transalkylation.

## 7.8 References

- [1] K.Y. Wang, X.S. Wang, G. Li, *Catalysis Communications*. 8 (2007) 324-328.
- [2] *Zeolites and Ordered Mesoporous Materials: Progress and Prospects*, Elsevier, 2005.
- [3] Database of Zeolite Structures, <http://www.iza-structure.org/databases/>, 2009.
- [4] F. Bauer, E. Bilz, A. Freyer, *Applied Catalysis a-General*. 289 (2005) 2-9.

- [5] N.Y. Chen, *Industrial & Engineering Chemistry Research*. 40 (2001) 4157-4161.
- [6] A. Iliyas, S. Al-Khattaf, *Chemical Engineering Journal*. 107 (2005) 127-132.
- [7] J.H. Kim, T. Kunieda, M. Niwa, *Journal of Catalysis*. 173 (1998) 433-439.
- [8] S. Morin, P. Ayrault, S. ElMouahid, N.S. Gnep, M. Guisnet, *Applied Catalysis a-General*. 159 (1997) 317-331.
- [9] T.C. Tsai, I. Wang, C.K. Huang, S.D. Liu, *Applied Catalysis a-General*. 321 (2007) 125-134.
- [10] S. Al-Khattaf, A. Iliyas, A. Al-Amer, T. Inui, *Journal of Molecular Catalysis a-Chemical*. 225 (2005) 117-124.
- [11] R.F. Sullivan, R.P. Sieg, G.E. Langlois, C.J. Egan, *Journal of the American Chemical Society*. 83 (1961) 1156-&.
- [12] Y.S. Hsu, T.Y. Lee, H.C. Hu, *Industrial & Engineering Chemistry Research*. 27 (1988) 942-947.
- [13] S. Al-Khattaf, N.M. Tukur, A. Al-Amer, *Industrial & Engineering Chemistry Research*. 44 (2005) 7957-7968.
- [14] J.M. Silva, M.F. Ribeiro, F.R. Ribeiro, E. Benazzi, M. Guisnet, *Applied Catalysis a-General*. 125 (1995) 1-14.
- [15] M. Guisnet, N.S. Gnep, S. Morin, *Microporous and Mesoporous Materials*. 35-6 (2000) 47-59.
- [16] J.W. Thybaut, M. Saeys, G.B. Marin, *Chemical Engineering Journal*. 90 (2002) 117-129.
- [17] T. Bera, J.W. Thybaut, G.B. Marin, *Industrial & Engineering Chemistry Research*, In Press, doi: 10.1021/ie200541q.
- [18] G.F. Froment, *Catalysis Today*. 52 (1999) 153-163.
- [19] G.G. Martens, J.W. Thybaut, G.B. Marin, *Industrial & Engineering Chemistry Research*. 40 (2001) 1832-2144.
- [20] G. Lozano-Blanco, J.W. Thybaut, K. Surla, P. Galtier, G.B. Marin, *Oil & Gas Science and Technology-Revue de l'Institut Francais du Petrole*. 61 (2006) 489-496.
- [21] E. Vynckier, G.F. Froment, in: G. Astarita, S.I. Sandler (Eds.), *Kinetic and Thermodynamic Lumping of Multicomponent Mixtures*, Elsevier, 1991, p. 131.
- [22] M. Saeys, M.F. Reyniers, J.W. Thybaut, M. Neurock, G.B. Marin, *Journal of Catalysis*. 236 (2005) 129-138.
- [23] G.G. Martens, G.B. Marin, J.A. Martens, P.A. Jacobs, G.V. Baroni, *Journal of Catalysis*. 195 (2000) 253-267.
- [24] J.F. Denayer, W. Souverijns, P.A. Jacobs, J.A. Martens, G.V. Baron, *Journal of Physical Chemistry B*. 102 (1998) 4588-4597.
- [25] R. Rungtirisakun, B. Jansang, P. Pantu, J. Limtrakul, *Journal of Molecular Structure*. 733 (2005) 239-246.
- [26] J.C. Choe, *Chemical Physics Letters*. 435 (2007) 39-44.
- [27] L.A. Clark, M. Sierka, J. Sauer, *Journal of the American Chemical Society*. 126 (2004) 936-947.
- [28] T. Demuth, P. Raybaud, S. Lacombe, H. Toulhoat, *Journal of Catalysis*. 222 (2004) 323-337.
- [29] J.F. Denayer, G.V. Baron, P.A. Jacobs, J.A. Martens, *Physical Chemistry Chemical Physics*. 2 (2000) 1007-1014.
- [30] I.R. Choudhury, J.W. Thybaut, P. Balasubramanian, J.F.M. Denayer, J.A. Martens, G.B. Marin, *Chemical Engineering Science*. 65 (2010) 174-178.

# Chapter 8

## Conclusions and Future Work

---

An intrinsic kinetics based methodology for multi-scale modeling of chemical reactions has been developed, applied and validated. Intrinsic kinetics are used to construct (micro)kinetic models with a sound physical meaning and clear statistical significance. Microkinetic models tend to account for a large number of components, intermediates and elementary steps. This opens up opportunities for model based catalyst design and multi-scale modeling but requires an increased computational effort. The Single-Event MicroKinetic methodology is at hand to keep the number of adjustable parameters and the computational effort for regression within tractable limits.

As a proof of concept, the methodology was first developed for *n*-hexane hydroisomerization kinetics on Pt/H-ZSM-5. Because of the limited number of components and elementary steps and the correspondingly rather simple rate equations, it can be used as a case study in a tutorial for newcomers in the field of reaction engineering. The trade-off between physical meaning and statistical significance resulted in *LHHW*-type rate equations that could practically adequately simulate the experimental data. Limited deviations due to mass transport effects, which were not sufficiently relevant to account for in this example case, were at the origin of the ultimate non-adequacy of the model.

The methodology was subsequently applied to intrinsic ethene oligomerization kinetics. Experimental datasets were acquired on two different Ni-ion containing heterogeneous catalysts, i.e., Ni-SiO<sub>2</sub>-Al<sub>2</sub>O<sub>3</sub> and Ni-Beta. Based on the experimental observations, analogies from homogeneous oligomerization catalysis and free carbenium ion chemistry, a SEMK model was proposed. The SEMK model was regressed to the experimental data to determine the unknown parameters. Only a limited number of parameters were allowed to vary, i.e., the unknown kinetic descriptors for the metal-ion oligomerization steps, and the catalyst descriptors. All other descriptor values such as the activation energies for the acid

catalyzed steps were taken from literature. Through model discrimination, the nickel-ethyl species was determined to be most probably the actual active species for ethene oligomerization. All parameter estimates were statistically significant and had a sound physical meaning. Relatively low chain growth probabilities were determined corresponding to the very selective dimerization of ethene on the nickel-ion sites. Oligomer products do not undergo further chain growth on the nickel-ions. A too strong adsorption of the heavier oligomers result in a decrease in oligomerization rate which is ascribed to a decreasing ethene surface concentration. The resulting model was capable of adequately describing the experimental data obtained on both catalysts. Based on this SEMK model, a reaction path analysis was performed in order to elucidate the main reaction pathways. Although acid sites were present on the catalysts studied, they contributed only marginally to the product spectrum through isomerization and cracking. The reaction path analysis eventually lead to several guidelines for catalyst design, tailored to the production of 1-alkenes, propene and gasoline. The product spectrum is mainly determined by the ratio of the concentration and strength of the acid and nickel-ion sites. The SEMK model was also used in the construction of an industrial reactor model. This industrial reactor model included phenomena which are absent at well-performed lab-scale experiments, e.g., transport phenomena, pressure drop, condensation... Using this reactor model, an industrial reactor was designed which can operate within the limits of the *OCMOL* project.

Xylene isomerization on Pt/H-ZSM-5 was the third bifunctionally catalyzed reaction that was investigated in this work. A limited, but well-designed experimental dataset from Shell was used to regress the SEMK model which was extended with reaction families such as transalkylation and dealkylation to account for the occurring chemistry. Again, all catalyst and kinetic descriptors were estimated significantly and had a sound physical meaning. Via a profit function accounting for the paraxylene and benzene yield and xylene losses, it could be demonstrated that the investigated catalyst exhibited practically the desired steady-state kinetics behavior.

A PhD maybe is the end of a specific research project but seldom constitutes the culmination of an entire research programme. It rather generates new opportunities and perspectives for future work.

Efforts should be made to extend or at least verify if the systematic methodology for kinetic modeling to other engineering domains. The author is convinced that the concepts and methodology described in this work are employable in other domains than reaction engineering. The case study on *n*-hexane hydroisomerization developed for illustrating the systematic methodology for kinetic modeling should be distributed as much as possible, i.e., through publication(s), master student courses and tailored specialty courses. The case study illustrates some very particular and difficult concepts using a well described, well known reaction.

The work on ethene oligomerization could be extended by performing some experiments in which one of the main products, e.g., butene, is used as (co-)feed. Not only will this lead to a better understanding of the underlying reaction network but also to an improved estimation of some of the kinetic parameters. Additionally, the effect of pore geometries could be investigated. The particular structure of some zeolites, e.g., ZSM-5 and ZSM-22 zeolite, potentially influences the resulting catalyst performance as it proved to do so with other chemical reactions, e.g., hydrocracking. This could also be applied to the work on xylene isomerization, in which the influence of shape-selectivity effects originating from the ZSM-5 framework was not explicitly accounted for. The methodology for investigating the effect of pore geometry has already been developed and successfully applied in the LCT and described in literature. However, its application on ethene oligomerization and xylene isomerization would require an amount of time corresponding to one PhD project.





# Appendix A: Properties of Pure Components and Mixtures

---

In this appendix, an overview is given of all the methods to calculate the properties of pure components and mixtures as needed in the reactor model described in Chapter 6. In the reactor model, reference components are chosen to limit the number of physical properties to be determined. One reference component per carbon number is selected, i.e., the linear 1-alkene.

## A.1 Pure component properties

Table A-1 gives the pure reference components critical properties, i.e., critical temperature  $T_c$ , pressure  $p_c$ , volume  $V_c$  and compressibility factor  $Z_c$ , other properties, i.e., boiling point  $T_b$ , acentric factor  $\omega$ , molar volume parameter for the HBT correlation  $V^*$ , molecular mass  $M_w$  and dipole moment  $D$  for the reference components. Additionally, the critical properties of nitrogen can also be found in the table.

**Table A-1: Critical and other properties of the linear 1-alkenes used as reference components, \* determined by extrapolation**

	$T_c$	$T_b$	$p_c$	$V_c$	$Z_c$	$\omega$	$V^*$	$M_w$	$D$
	[K]	[K]	[bar]	[cm <sup>3</sup> mol <sup>-1</sup> ]	[-]	[-]	[l mol <sup>-1</sup> ]	[g mol <sup>-1</sup> ]	[debye]
C <sub>2</sub>	282	169	50.4	130	0.280	0.088	0.131	28	0.0
C <sub>3</sub>	365	225	46.0	181	0.274	0.145	0.183	42	0.4
C <sub>4</sub>	420	267	40.2	240	0.277	0.192	0.237	56	0.3
C <sub>5</sub>	470	303	35.3	300	0.310	0.282	0.295	70	0.4
C <sub>6</sub>	504	337	31.7	350	0.260	0.285	0.351	84	0.4
C <sub>7</sub>	537	374	28.3	440	0.280	0.394	0.411	98	0.3
C <sub>8</sub>	567	394	27.7	464	0.260	0.388	0.471	112	0.3

C <sub>9</sub>	592	420	23.4	580	0.280	0.433	0.533	126	0.3*
C <sub>10</sub>	615	444	22.0	650	0.280	0.498	0.601	140	0.3*
C <sub>11</sub>	637	466	19.9	735*	0.280*	0.530	0.668	154	0.3*
C <sub>12</sub>	657	487	18.5	825*	0.280*	0.564	0.734	168	0.3*
N <sub>2</sub>	126	77	33.9	90	0.290	0.039	-	28	0.0

### A.1.1 Heat capacity for gasses

Table A-2 gives the coefficients used to determine the heat capacity of gaseous reference components at a certain temperature  $T$  via:

$$C_p = A + BT + CT^2 + DT^3 \quad \text{A-1}$$

**Table A-2: Coefficients for the determination of the heat capacity of the reference components, see Eq. A-1.**

	$C_p$ [J mol <sup>-1</sup> K <sup>-1</sup> ]			
	$A$	$B$	$C$	$D$
C <sub>2</sub>	3.806	1.566 10 <sup>-1</sup>	-8.348 10 <sup>-5</sup>	1.755 10 <sup>-8</sup>
C <sub>3</sub>	3.710	2.345 10 <sup>-1</sup>	-1.160 10 <sup>-4</sup>	2.205 10 <sup>-8</sup>
C <sub>4</sub>	-2.994	3.532 10 <sup>-1</sup>	-1.990 10 <sup>-4</sup>	4.463 10 <sup>-8</sup>
C <sub>5</sub>	-1.340 10 <sup>-1</sup>	4.329 10 <sup>-1</sup>	-2.317 10 <sup>-4</sup>	4.681 10 <sup>-8</sup>
C <sub>6</sub>	-1.749	5.309 10 <sup>-1</sup>	-2.903 10 <sup>-4</sup>	6.054 10 <sup>-8</sup>
C <sub>7</sub>	-3.303	6.297 10 <sup>-1</sup>	-3.512 10 <sup>-4</sup>	7.607 10 <sup>-8</sup>
C <sub>8</sub>	-4.099	7.239 10 <sup>-1</sup>	-4.036 10 <sup>-4</sup>	8.675 10 <sup>-8</sup>
C <sub>9</sub>	-3.718	8.122 10 <sup>-1</sup>	-4.509 10 <sup>-4</sup>	9.705 10 <sup>-8</sup>
C <sub>10</sub>	-4.664	9.077 10 <sup>-1</sup>	-5.058 10 <sup>-4</sup>	1.095 10 <sup>-7</sup>
C <sub>11</sub>	-5.585	1.003	-5.602 10 <sup>-4</sup>	1.216 10 <sup>-7</sup>
C <sub>12</sub>	-6.544	1.098	-6.155 10 <sup>-4</sup>	1.341 10 <sup>-7</sup>
N <sub>2</sub>	3.150 10 <sup>1</sup>	-1.357 10 <sup>-2</sup>	2.680 10 <sup>-5</sup>	-1.168 10 <sup>-8</sup>

### A.1.2 Heat capacity for liquids

For liquids, the heat capacity of a liquid at 293 K can be determined using the Chueh-Swanson group contribution method [1]. The temperature dependency of the heat capacity for the liquid component is given by:

$$C_{p,i}^l = C_{p,i}^0 + R \left( 1.45 + \frac{0.45}{1-T_{r,i}} + 0.25\omega_i \left( 17.11 + 25.2 \frac{(1-T_{r,i})^{1/3}}{T_{r,i}} + \frac{1.742}{1-T_{r,i}} \right) \right) \quad \text{A-2}$$

### A.1.3 Vapor pressure

Table A-3 gives the coefficients and number of equation used for the determination of the vapor pressure of the reference components.

$$V_{p,i} = p_{c,i} \exp \left( \frac{T_{c,i}}{T} \left( A \left( 1 - \frac{T}{T_{c,i}} \right) + B \left( 1 - \frac{T}{T_{c,i}} \right)^{1.5} + C \left( 1 - \frac{T}{T_{c,i}} \right)^{3.0} + D \left( 1 - \frac{T}{T_{c,i}} \right)^{6.0} \right) \right) \quad \text{A-3}$$

$$V_{p,i} = \exp \left( A - \frac{B}{T + C} \right) \quad \text{A-4}$$

**Table A-3: Coefficients for the determination of the vapor pressure of the reference components, see Eqs. A-3 and A-4, \* determined by extrapolation**

	$V_p$ [bar]				
	$A$	$B$	$C$	$D$	eq.
$C_2$	-6.32055	1.16819	-1.55935	-1.83552	32
$C_3$	-6.64231	1.21857	1.81005	-2.48212	32
$C_4$	-6.88204	1.27051	-2.26284	-2.61632	32
$C_5$	-7.04875	1.17813	2.45105	2.21727	32
$C_6$	-7.76467	2.29843	-4.44302	0.89947	32
$C_7$	-8.26875	3.02688	6.18709	4.33049	32
$C_8$	9.2352	3134.97	-58.00	-	33
$C_9$	-8.30824	2.03357	5.42753	0.95331	32
$C_{10}$	9.05778	3.06154	7.07236	4.20695	32
$C_{11}$	9.05778*	3.06154*	7.07236*	4.20695*	32
$C_{12}$	9.05778*	3.06154*	7.07236*	4.20695*	32

## A.2 Mixing rules for (critical) properties

### A.2.1 Critical temperature

To determine the critical temperature of a liquid mixture, i.e.,  $T_{c_m}^l$ , the Chueh-Prausnitz rules are recommended [1]:

$$T_{c_m}^l = \sum_{i=1}^{n_{comp}} \sum_{j=1}^{n_{comp}} \phi_i \phi_j T_{c,ij} \quad \text{A-5}$$

$$\phi_i = \frac{x_i V_{c,i}}{\sum_{j=1}^{n_{comp}} x_j V_{c,j}} \quad \text{A-6}$$

$$T_{c,ij} = (1 - k_{ij}) \sqrt{T_{c,i} T_{c,j}} \quad \text{A-7}$$

$$(1 - k_{ij}) = \frac{8 \sqrt{V_{c,i} V_{c,j}}}{\left( V_{c,i}^{1/3} + V_{c,j}^{1/3} \right)^3} \quad \text{A-8}$$

To determine the critical temperature of a gas mixture, i.e.,  $T_{c_m}^g$ , Yorzane recommended the following rules [1]:

$$T_{c_m}^g = \frac{\sum_{i=1}^{n_{comp}} \sum_{j=1}^{n_{comp}} y_i y_j V_{c,ij} T_{c,ij}}{V_{c_m}^g} \quad \text{A-9}$$

$$T_{c,ii} = T_{c,i} \quad \text{A-10}$$

$$T_{c,ij} = \sqrt{T_{c,i} T_{c,j}} \quad \text{A-11}$$

$$V_{c,ii} = V_{c,i} \quad \text{A-12}$$

$$V_{c,ij} = \frac{1}{8} \left( V_{c,i}^{1/3} + V_{c,j}^{1/3} \right)^3 \quad \text{A-13}$$

## A.2.2 Critical volume of gas mixtures

To determine the critical volume of a gas mixture, i.e.,  $V_{c_m}^g$ , Yorzane recommended the following rules [1]:

$$V_{c_m}^g = \sum_{i=1}^{n_{comp}} \sum_{j=1}^{n_{comp}} y_i y_j V_{c,ij} \quad \text{A-14}$$

$$V_{c,ii} = V_{c,i} \quad \text{A-15}$$

$$V_{c,ij} = \frac{1}{8} \left( V_{c,i}^{1/3} + V_{c,j}^{1/3} \right)^3 \quad \text{A-16}$$

## A.2.3 Critical compressibility factor of gas mixtures

To determine the critical compressibility factor of a gas mixture, i.e.,  $Z_{c_m}$ , Yorzane recommended the following rule [1]:

$$Z_{c_m} = 0.291 - 0.08 \omega_m \quad \text{A-17}$$

### A.2.4 Critical pressure of gas mixtures

To determine the critical pressure of a gas mixture, i.e.,  $p_{c_m}$ , Yorizane recommended the following rule [1]:

$$p_{c_m} = \frac{Z_{c_m} RT_{c_m}}{V_{c_m}} \quad \text{A-18}$$

### A.2.5 Molecular mass of mixtures

To determine the critical molecular mass of a gas or liquid mixture, i.e.,  $M_m$ , Yorizane recommended resp. the following rules [1]:

$$M_m^g = \sum_{i=1}^{n_{comp}} y_i M_i \quad \text{A-19}$$

$$M_m^l = \sum_{i=1}^{n_{comp}} x_i M_i \quad \text{A-20}$$

### A.2.6 Acentric factor of mixtures

To determine the acentric factor of a gas or liquid mixture, i.e.,  $\omega_m$ , Yorizane recommended resp. the following rules [1]:

$$\omega_m^g = \sum_{i=1}^{n_{comp}} y_i \omega_i \quad \text{A-21}$$

$$\omega_m^l = \sum_{i=1}^{n_{comp}} x_i \omega_i \quad \text{A-22}$$

## A.3 Volumetric flow rates

$Q^g$  is the volumetric gas flow rate and is determined by assuming an ideal gas:

$$Q^g = \frac{RT \sum_{i=1}^{n_{comp}} F_i^g}{p} \quad \text{A-23}$$

with  $R$  the universal gas constant and  $p$  the total pressure at a certain point in the reactor.

$Q^l$  is the volumetric liquid flow rate and is determined via its molar volume  $V_m^l$ , see paragraph A-4:

$$Q_l = V_m^l \sum_{i=1}^{n_{comp}} F_i^l \quad \text{A-24}$$

## A.4 Molar volume

### A.4.1 Molar volume of liquid components

The molar volume of a pure liquid component  $V_{m,i}^l$  can be determined by the Hankinson-Brost-Thomson (HBT) correlation:

$$V_{m,i}^l = V_{R,i}^{(0)} V_i^* (1 - \omega_i V_{R,i}^{(\delta)}) \quad \text{A-25}$$

$$V_{R,i}^{(0)} = 1 + a(1 - T_{r,i})^{1/3} + b(1 - T_{r,i})^{2/3} + c(1 - T_{r,i}) + d(1 - T_{r,i})^{4/3} \quad \text{A-26}$$

$$V_{R,i}^{(\delta)} = \frac{e + fT_{r,i} + gT_{r,i}^2 + hT_{r,i}^3}{T_{r,i} - 1.00001} \quad \text{A-27}$$

The coefficient values of  $a$  to  $h$  can be found in Table A-4.

**Table A-4: Coefficients used in the determination of the molar volume of a pure liquid components, see Eqs. A-25 to A-27.**

$a$	-1.52816	$b$	1.43907
$c$	-0.81466	$d$	0.190454
$e$	-0.296123	$f$	0.386914
$g$	-0.0427258	$h$	-0.0480645

### A.4.2 Molar volume of liquid mixtures

The molar volume of a liquid mixture  $V_m^l$  is given by the modified Rackett equation:

$$V_m^l = R \left( \sum_{i=1}^{n_{comp}} \frac{x_i T_{c,i}}{p_{c,i}} \right) Z_{RA_m}^{(1+(1-T_r)^{2/7})} \quad \text{A-28}$$

$x_i$  is the molar fraction of component  $i$  in the liquid phase,  $T_c$  is the critical temperature,  $p_c$  is the critical pressure,  $Z_{RA_m}$  is the mean Rackett compressibility factor and  $T_r$  is the reduced temperature given by:

$$T_r = \frac{T}{T_{c_m}} \quad \text{A-29}$$

in which  $T_{c_m}$  is the mean critical temperature, see paragraph A.2.1.

The mean Rackett compressibility factor  $Z_{RA_m}$  is calculated as:

$$Z_{RA_m} = \sum_{i=1}^{n_{comp}} x_i Z_{RA,i} \quad \text{A-30}$$

The Rackett compressibility factor for component  $i$ ,  $Z_{RA,i}$ , is given by:

$$Z_{RA,i} = 0.29056 - 0.08775\omega_i \quad \text{A-31}$$

with  $\omega$  the Pitzer acentric factor.

## A.5 Heat capacity of mixtures

### A.5.1 Heat capacity of gas or liquid mixtures

Assuming an ideal gas or liquid mixture, the resp. heat capacity  $C_{p_m}^g$  or  $C_{p_m}^l$  of this mixture is given by:

$$C_{p_m}^g = \sum_{i=1}^{n_{comp}} \frac{y_i M_i}{\sum_{j=1}^{n_{comp}} y_j M_j} C_{p,i} \quad \text{A-32}$$

$$C_{p_m}^l = \sum_{i=1}^{n_{comp}} \frac{x_i M_i}{\sum_{j=1}^{n_{comp}} x_j M_j} C_{p,i} \quad \text{A-33}$$

in which the heat capacity of component  $i$ ,  $C_{p,i}$ , is determined as described in paragraph A.1.

### A.5.2 Heat capacity of gas-liquid mixtures

If a two phase (2p) fluidum is encountered, its heat capacity  $C_{p_m}^{2p}$  is determined as:

$$C_{p_m}^{2p} = \gamma C_{p_m}^g + (1 - \gamma) C_{p_m}^l \quad \text{A-34}$$

with  $\gamma$  being the mass fraction of the gas phase to the total mass of the fluidum.

## A.6 Thermal conductivity

### A.6.1 Thermal conductivity of gas components

The thermal conductivity of a gas component is given by the method of Chung et al. [1]:

$$\lambda_i^g = \frac{31.2 \mu_i^0 \Psi_i}{M_i} \left( \frac{1}{G_{2,i}} + B_{6,i} \frac{V_{c,i}}{6V_{m,i}} \right) + q_i B_{7,i} \left( \frac{V_{c,i}}{6V_{m,i}} \right)^2 \sqrt{T_{r,i}} G_{2,i} \quad \text{A-35}$$

$\mu_i^0$  is the low pressure gas viscosity of component  $i$ .  $\Psi_i$  is a parameter defined as:

$$\Psi_i = 1 + \alpha_i \left( \frac{0.215 + 0.28288\alpha_i - 1.061\beta_i + 0.26665Z_i}{0.6366 + \beta_i Z_i + 1.061\alpha_i \beta_i} \right) \quad \text{A-36}$$

in which:

$$\alpha_i = \frac{C_{v,i}}{R} - \frac{3}{2} \quad \text{A-37}$$

$$\beta_i = 0.7862 - 0.7109\omega_i + 1.3168\omega_i^2 \quad \text{A-38}$$

$$Z_i = 2.0 + 10.5T_{r,i}^2 \quad \text{A-39}$$

$q_i$  is given by:

$$q_i = 3.586 \cdot 10^{-3} \sqrt{\frac{T_{c,i}}{M_i}} \frac{1}{V_{c,i}^{2/3}} \quad \text{A-40}$$

The parameters  $G_{1,i}$  and  $G_{2,i}$  are calculated as:

$$G_{1,i} = \frac{1 - 0.5 \frac{V_{c,i}}{6V_{m,i}}}{\left(1 - \frac{V_{c,i}}{6V_{m,i}}\right)^3} \quad \text{A-41}$$

$$G_{2,i} = \frac{\frac{B_1}{V_{c,i}} \left(1 - e^{-B_4 \frac{V_{c,i}}{6V_{m,i}}}\right) + B_{2,i} G_{1,i} e^{-B_5 \frac{V_{c,i}}{6V_{m,i}}} + B_{3,i} G_{1,i}}{B_{1,i} B_{4,i} + B_{2,i} + B_{3,i}} \quad \text{A-42}$$

The  $B$  factors are determined using equation A-43 and the coefficients from Table A-5:

$$B_i = a_i + b_i\omega + c_i\mu_r^4 + d_i\kappa \quad \text{A-43}$$

**Table A-5: Coefficients used to determine  $B_i$  to calculate the thermal conductivity of a gas component, see Eq. A-43.**

$i$	$a_i$	$b_i$	$c_i$	$d_i$
1	2.4166	0.74824	-0.91858	121.72
2	-0.50924	-1.5094	-49.991	69.983
3	6.6107	5.6207	64.760	27.039
4	14.543	-8.9139	-5.6379	74.344
5	0.79274	0.82019	-0.69369	6.3173
6	-5.8634	12.801	9.5893	65.529
7	91.089	128.11	-54.217	523.81



## A.6.2 Thermal conductivity of gas mixtures

For determining the thermal conductivity of a gas mixture,  $\lambda_m^g$ , equation A-32 is applicable if the mixing and combination rules described in equations A-58 to A-77 are applied [1].

## A.6.3 Thermal conductivity of liquid components

The thermal conductivity of a liquid component can be approximated by the following correlation as proposed by Latini et al. [1]:

$$\lambda_i^l = \frac{A^* T_b^\alpha (1 - T_r)^{0.38}}{M^\beta T_c^\gamma T_r^{1/6}} \quad \text{A-44}$$

The coefficient values of  $A^*$  and  $\alpha$  to  $\gamma$  can be found in Table A-6.

**Table A-6: Coefficient used for the determination of the thermal conductivity of a liquid olefin, see Eq.A-44.**

$A^*$	$\alpha$	$\beta$	$\gamma$
0.0361	1.2	1.0	0.167

## A.6.4 Thermal conductivity of liquid mixtures

The thermal conductivity of a liquid mixture can be determined by Li's method [1]:

$$\lambda_m^l = \sum_{i=1}^{n_{comp}} \sum_{j=1}^{n_{comp}} \phi_i \phi_j \lambda_i^l \quad \text{A-45}$$

$$\lambda_{ij}^l = \frac{2}{\left( \frac{1}{\lambda_i^l} + \frac{1}{\lambda_j^l} \right)} \quad \text{A-46}$$

$$\phi_i = \frac{x_i V_{m,i}^l}{\sum_{j=1}^{n_{comp}} x_j V_{m,j}^l} \quad \text{A-47}$$

## A.6.5 Thermal conductivity of gas-liquid mixtures

If a two phase (2p) fluidum is encountered, its thermal capacity  $\lambda_m^{2p}$  is determined as:

$$\lambda_m^{2p} = \gamma \lambda_m^g + (1 - \gamma) \lambda_m^l \quad \text{A-48}$$

with  $\gamma$  being the mass fraction of the gas phase to the total mass of the fluidum.

## A.7 Viscosity

### A.7.1 Viscosity of gas components

The viscosity of a gas component can be determined applying the method of Chung et al. [1]:

$$\mu_i^g = \mu_i^* \frac{36.344 \sqrt{M_i T_{c,i}}}{V_{c,i}^{2/3}} \quad \text{A-49}$$

in which

$$\mu_i^* = \frac{\sqrt{T_i^*}}{\Omega_{v,i}} \left( F_{c,i} \left( \frac{1}{G_{2,i}} + E_{6,i} \frac{\rho_i^g V_{c,m,i}}{6} \right) \right) + \mu_i^{**} \quad \text{A-50}$$

and

$$\mu_i^{**} = E_{7,i} \left( \frac{\rho_i^g V_{c,m,i}}{6} \right)^2 G_{2,i} e^{\left( E_{8,i} + \frac{E_{9,i}}{T_i^*} + \frac{E_{10,i}}{(T_i^*)^2} \right)} \quad \text{A-51}$$

The coefficients  $G_{1,i}$  and  $G_{2,i}$  are given by:

$$G_{1,i} = \frac{1 - 0.5 \frac{\rho_i^g V_{c,m,i}}{6}}{\left( 1 - \frac{\rho_i^g V_{c,m,i}}{6} \right)^3} \quad \text{A-52}$$

$$G_{2,i} = \frac{E_{1,i} \left( \frac{1 - e^{-E_{4,i} \frac{\rho_i^g V_{c,m,i}}{6}}}{\frac{\rho_i^g V_{c,m,i}}{6}} \right) + E_{1,i} G_{1,i} e^{E_{5,i} \frac{\rho_i^g V_{c,m,i}}{6}} + E_{3,i} G_{1,i}}{E_{1,i} E_{4,i} + E_{2,i} + E_{3,i}} \quad \text{A-53}$$

The parameters  $T_i^*$ ,  $F_{c,i}$  and  $\Omega_{v,i}$  are calculated as:

$$T_i^* = 1.2593 T_{r,i} \quad \text{A-54}$$

$$F_{c,i} = 1 - 0.2756 \omega_i + 0.059035 \mu_{r,i}^4 + \kappa_i \quad \text{A-55}$$

$$\Omega_{v,i} = \frac{1.16145}{(T_i^*)^{0.14874}} + 0.52487 e^{-0.77320 T_i^*} + 2.16178 e^{-2.43787 T_i^*} \quad \text{A-56}$$

The  $E$  factors are determined using equation A-57 and the coefficients in Table A-7:

$$E_i = a_i + b_i \omega + c_i \mu_r^4 + d_i k \quad \text{A-57}$$

**Table A-7: Coefficients used to determine  $E_i$  to calculate the viscosity of a gas component, see Eq. A-57.**

$i$	$a_i$	$b_i$	$c_i$	$d_i$
1	6.324	50.412	-51.680	1189.0
2	$1.210 \cdot 10^{-3}$	$-1.154 \cdot 10^{-3}$	$-6.257 \cdot 10^{-3}$	0.03728
3	5.283	254.209	-168.48	3898.0
4	6.623	38.096	-8.464	31.42
5	19.745	7.630	-14.354	31.53
6	-1.900	-12.537	4.985	-18.15
7	24.275	3.450	-11.291	69.35
8	0.7972	1.117	0.01235	-4.117
9	-0.2382	0.06770	-0.8163	4.025
10	0.06863	0.3479	0.5926	-0.727

## A.7.2 Viscosity of gas mixtures

For determining the viscosity of a gas mixture,  $\mu_m^g$ , equation A-49 is applied if the following mixing and combination are applied [1]:

$$\sigma_m^3 = \sum_{i=1}^{n_{comp}} \sum_{j=1}^{n_{comp}} y_i y_j \sigma_{ij}^3 \quad \text{A-58}$$

$$T_m^* = \frac{T}{\left(\frac{\epsilon}{k}\right)_m} \quad \text{A-59}$$

$$\left(\frac{\epsilon}{k}\right)_m = \frac{\sum_{i=1}^{n_{comp}} \sum_{j=1}^{n_{comp}} y_i y_j \left(\frac{\epsilon_{ij}}{k}\right) \sigma_{ij}^3}{\sigma_m^3} \quad \text{A-60}$$

$$M_m = \frac{\sum_{i=1}^{n_{comp}} \sum_{j=1}^{n_{comp}} y_i y_j \left(\frac{\epsilon_{ij}}{k}\right) \sigma_{ij}^2 \sqrt{M_{ij}}}{\left(\frac{\epsilon_{ij}}{k}\right)_m \sigma_m^2} \quad \text{A-61}$$

$$\omega_m = \frac{\sum_{i=1}^{n_{comp}} \sum_{j=1}^{n_{comp}} y_i y_j \omega_{ij} \sigma_{ij}^3}{\sigma_m^3} \quad \text{A-62}$$

$$\mu_m^4 = \sigma_m^3 \sum_{i=1}^{n_{comp}} \sum_{j=1}^{n_{comp}} \frac{y_i y_j \mu_i^2 \mu_j^2}{\sigma_{ij}^3} \quad \text{A-63}$$

$$\kappa_m = \sum_{i=1}^{n_{comp}} \sum_{j=1}^{n_{comp}} y_i y_j k_{ij} \quad \text{A-64}$$

$$\sigma_{ij} = \sqrt{\sigma_i \sigma_j} \quad \text{A-65}$$

$$\sigma_{ii} = \sigma_i = 0.809 V_{c_i}^{1/3} \quad \text{A-66}$$

$$\frac{\varepsilon_{ij}}{k} = \sqrt{\frac{\varepsilon_i}{k} \frac{\varepsilon_j}{k}} \quad \text{A-67}$$

$$\frac{\varepsilon_{ii}}{k} = \frac{\varepsilon_i}{k} = \frac{T_{c_i}}{1.2593} \quad \text{A-68}$$

$$\omega_{ij} = \frac{\omega_i + \omega_j}{2} \quad \text{A-69}$$

$$\omega_{ii} = \omega_i \quad \text{A-70}$$

$$k_{ij} = \sqrt{k_i k_j} \quad \text{A-71}$$

$$k_{ii} = k_i \quad \text{A-72}$$

$$M_{ij} = \frac{2M_i M_j}{M_i + M_j} \quad \text{A-73}$$

$$F_{c_m} = 1 - 0.275 \omega_m + 0.059035 \mu_{r_m}^4 + \kappa_m \quad \text{A-74}$$

$$T_{c_m} = 1.2593 \left( \frac{\varepsilon}{k} \right)_m \quad \text{A-75}$$

$$V_{c_m} = \left( \frac{\sigma_m}{0.809} \right)^3 \quad \text{A-76}$$

$$\mu_{r_m} = \frac{131.3 \mu_m}{\sqrt{V_{c_m} T_{c_m}}} \quad \text{A-77}$$

### A.7.3 Viscosity of liquid components

The effect of pressure on the saturated liquid viscosity at vapor pressure  $p_{vp}$ , i.e.,  $\mu_{SL,i}^l$ , can be described according to Lucas et al. [1]:

$$\mu_i^l = \mu_{SL,i}^l \frac{D_i \left( \frac{\Delta P_{r,i}}{2.118} \right)^{A_i}}{1 + C_i \omega_i \Delta P_{r,i}} \quad \text{A-78}$$

$$A_i = 0.9991 - \frac{4.674 \cdot 10^{-4}}{1.0523 T_{r,i}^{-0.03877} - 1.0513} \quad \text{A-79}$$

$$D = \frac{0.3257}{(1.0039 - T_{r,i}^{2.573})^{0.2906}} - 0.2086 \quad \text{A-80}$$

$$C_i = -0.07921 + 2.1616 T_{r,i} - 13.4040 T_{r,i}^2 + 44.1706 T_{r,i}^3 - 84.8291 T_{r,i}^4 + 96.1209 T_{r,i}^5 - 59.8127 T_{r,i}^6 + 15.6719 T_{r,i}^7 \quad \text{A-81}$$

$$\Delta P_{r,i} = \frac{P - P_{vp,i}}{P_{c,i}} \quad \text{A-82}$$

The effect of temperature on the viscosity of a liquid component  $\mu_i^l$  is described as [1]:

$$\left( \mu_i^l \right)^{-0.2661} = \left( \mu_{K,i}^l \right)^{-0.2661} + \frac{T - T_K}{233} \quad \text{A-83}$$

with  $\mu_{K,i}^l$  being the viscosity of liquid component  $i$  at a temperature of  $T_K$  Kelvin.

#### A.7.4 Viscosity of liquid mixtures

The viscosity of a liquid mixture can be determined using the method of Grunberg and Nissan [1]:

$$\mu_m^l = \exp \left( \sum_{i=1}^{n_{comp}} x_i \ln \mu_i^l + \sum_{i=1}^{n_{comp}} \sum_{j=1}^{n_{comp}} x_i x_j G_{ij} \right) \quad \text{A-84}$$

$G_{ij}$  is an interaction parameter and is function of components  $i$  and  $j$  and the temperature.

A value for  $G_{ij}$  at 298 K can be obtained via a group contribution method proposed by Isdale et al. [1].

$$G_{ij} = \Sigma \Delta_i - \Sigma \Delta_j + W \quad \text{A-85}$$

$$G_{ii} = 0 \quad \text{A-86}$$

In which  $\Sigma \Delta_i$  are the group contribution  $W$  is given by:

$$W = \frac{0.3161(N_i - N_j)^2}{N_i + N_j} - 0.1188(N_i - N_j) \quad \text{A-87}$$

in which  $N_i$  is the number of carbon atoms in component  $i$ .

### A.7.5 Viscosity of gas-liquid mixtures

If a two phase (2p) fluidum is encountered, its viscosity  $\mu_m^{2p}$  is determined as:

$$\mu_m^{2p} = \gamma \mu_m^g + (1 - \gamma) \mu_m^l \quad \text{A-88}$$

with  $\gamma$  being the mass fraction of the gas phase to the total mass of the fluidum.

## A.8 Surface tension

### A.8.1 Surface tension of liquid components

The surface tension of a liquid components, i.e.,  $\sigma_i^l$ , can be calculated as [1]:

$$\sigma_{L,i} = P_c^{2/3} T_c^{1/3} Q (1 - T_r)^{11/9} \quad \text{A-89}$$

in which  $Q$  is given by:

$$Q = 0.1196 \left( 1 + \frac{\frac{T_b}{T_c} \ln \left( \frac{P_c}{1.01325} \right)}{1 - \frac{T_b}{T_c}} \right) - 0.279 \quad \text{A-90}$$

### A.8.2 Surface tension of liquid mixtures

The surface tension of liquid mixture is determined as [1]:

$$\sigma_m^l = \sum_{i=1}^{n_{comp}} x_i \sigma_i^l \quad \text{A-91}$$

## A.9 References

- [1] R.C. Reid, J.M. Prausnitz, B.E. Poling, The Properties of Gases and Liquids (4th ed.), 1988.



